REMOTE DETERMINATION OF SUSPENDED SEDIMENT SIZE AND CONCENTRATION BY MULTI-FREQUENCY ACOUSTIC BACKSCATTER

CENTRE FOR NEWFOUNDLAND STUDIES

TOTAL OF 10 PAGES ONLY
MAY BE XEROXED

(Without Author's Permission)

JINYU SHENG, M. Sc.

REMOTE DETERMINATION OF SUSPENDED SEDIMENT SIZE AND CONCENTRATION BY MULTI-FREQUENCY ACOUSTIC BACKSCATTER

BY

Jinyu Sheng, M.Sc.

A thesis submitted to the School of Graduate
Studies in partial fulfillment of the
requirements for the degree of
Doctor of Philosophy

Department of Physics
Memorial University
February 1991

St John's Newfoundland Canada

National Library of Canada
Bibliothèque nationale du Canada

Canadian Theses Service
Service des thèses canadiennes

Ottawa, Canada
K1A 0N4

The author has granted an irrevocable non-exclusive licence allowing the National Library of Canada to reproduce, loan, distribute or sell copies of his/her thesis by any means and in any form or format, making this thesis available to interested persons.

The author retains ownership of the copyright in his/her thesis. Neither the thesis nor substantial extracts from it may be printed or otherwise reproduced without his/her permission.

L'auteur a accordé une licence irrévocable et non exclusive permettant à la Bibliothèque nationale du Canada de reproduire, prêter, distribuer ou vendre des copies de sa thèse de quelque manière et sous quelque forme que ce soit pour mettre des exemplaires de cette thèse à la disposition des personnes intéressées.

L'auteur conserve la propriété du droit d'auteur qui protège sa thèse. Ni la thèse ni des extraits substantiels de celle-ci ne doivent être imprimés ou autrement reproduits sans son autorisation.

ISBN 0-315-65305-1

SUBJECT CATEGORIES

Dissertation Abstracts International is arranged by broad, general subject categories. Choose the ***one*** listed below (capital letters) which most nearly describes the general content of your dissertation. If the major subject category has sub-fields under it, and ***only*** if it does, please choose ***one*** (small letters). (Ex.: ECONOMICS, Theory). Enter subject category on Item 7 of Agreement Form.

HUMANITIES

IA COMMUNICATIONS AND THE ARTS
- ARCHITECTURE
- CINEMA
- FINE ARTS
- INFORMATION SCIENCE
- JOURNALISM
- LIBRARY SCIENCE
- MASS COMMUNICATIONS
- MUSIC
- SPEECH
- THEATER

IIA EDUCATION
- EDUCATION
  - General
  - Administration
  - Adult
  - Agricultural
  - Art
  - Audiovisual
  - Business
  - Community and Social
  - Community Colleges
  - Curriculum and Instruction
  - Early Childhood
  - Elementary
  - Finance
  - Guidance and Counseling
  - Health
  - Higher
  - History
  - Home Economics
  - Industrial
  - Language and Languages
  - Mathematics
  - Middle School
  - Minorities
  - Music
  - Personality Development and Mental Hygiene
  - Philosophy
  - Physical
  - Preschool
  - Programmed Instruction
  - Psychology
  - Religion
  - Sciences
  - Secondary
  - Social Sciences
  - Special
  - Teacher Training
  - Teaching Machines
  - Tests and Measurements
  - Theory and Practice
  - Vocational

IIIA LANGUAGE, LITERATURE AND LINGUISTICS
- LANGUAGE
  - General
  - Ancient
  - Linguistics
  - Modern
- LITERATURE
  - General
  - Classical
  - Comparative
  - Medieval
  - Modern
  - American
  - Asian
  - Dutch and Scandinavian
  - English
  - Germanic
  - Latin American
  - Romance
  - Russian and East European
  - Slavic and Finno-Ugrian

IVA PHILOSOPHY, RELIGION AND THEOLOGY
- PHILOSOPHY
- RELIGION
  - General
  - Clergy
  - History
  - Music
  - Philosophy
- THEOLOGY

VA SOCIAL SCIENCES
- ACCOUNTING
- AMERICAN STUDIES
- ANTHROPOLOGY
  - Archaeology
  - Cultural
  - Physical
- BANKING
- BUSINESS ADMINISTRATION
- ECONOMICS
  - General
  - Agricultural
  - Commerce-Business
  - Finance (includes Public Finance)
  - History
  - Theory
- FOLKLORE
- HISTORY
  - General
  - Ancient
  - Medieval
  - Modern
  - Black
  - Church
  - Africa
  - Asia
  - Australia and Oceania
  - Canada
  - Europe
  - Latin America
  - United States
- HISTORY OF SCIENCE
- LAW
- MANAGEMENT
- MARKETING
- POLITICAL SCIENCE
  - General
  - International Law and Relations
  - Public Administration
- PUBLIC RELATIONS
- RECREATION
- SOCIAL GEOGRAPHY
- SOCIAL STRUCTURE
- SOCIAL WORK
- SOCIOLOGY
  - General
  - Community Organization
  - Criminology
  - Demography
  - Educational
  - Individual and Family Studies
  - Industrial
  - Labor Relations
  - Public Welfare
  - Race Relations
  - Social Problems
  - Statistics–Research Methods
  - Theory
- TRANSPORTATION
- URBAN AND REGIONAL PLANNING
- WOMEN'S STUDIES

SCIENCES

IB BIOLOGICAL SCIENCES
- AGRICULTURE
  - General
  - Animal Culture
  - Animal Pathology
  - Forestry & Wildlife
  - Plant Culture
  - Plant Pathology
  - Plant Physiology
  - Range Management
  - Wood Technology
- AGRONOMY
- ANATOMY
- BIOLOGICAL OCEANOGRAPHY
- BIOLOGY
- BIOPHYSICS
  - General
  - Medical
- BIOSTATISTICS
- BOTANY
- ECOLOGY
- ENTOMOLOGY
- GENETICS
- LIMNOLOGY
- MICROBIOLOGY
- PHYSIOLOGY
- RADIATION BIOLOGY
- VETERINARY SCIENCE
- ZOOLOGY

IIB EARTH SCIENCES
- GEOCHEMISTRY
- GEODESY
- GEOLOGY
- GEOPHYSICS
- HYDROLOGY
- MINERALOGY
- PALEOBOTANY
- PALEONTOLOGY
- PALEOZOOLOGY
- PHYSICAL GEOGRAPHY
- PHYSICAL OCEANOGRAPHY

IIIB HEALTH AND ENVIRONMENTAL SCIENCES
- ENVIRONMENTAL SCIENCES
- FOOD TECHNOLOGY
- HEALTH SCIENCES
  - General
  - Audiology
  - Chemotherapy
  - Dentistry
  - Education
  - Hospital Management
  - Human Development
  - Hygiene
  - Immunology
  - Medicine & Surgery
  - Mental Health
  - Nursing
  - Nutrition
  - Pathology
  - Pharmacy
  - Public Health
  - Radiology
  - Recreation
  - Speech Pathology
- HOME ECONOMICS
- PHARMACOLOGY

IVB PHYSICAL SCIENCES
- PURE SCIENCES
  - CHEMISTRY
    - General
    - Analytical
    - Biological
    - Inorganic
    - Nuclear
    - Organic
    - Pharmaceutical
    - Physical
    - Polymer
    - Radiation
    - Water
  - MATHEMATICS
  - PHYSICS
    - General
    - Acoustics
    - Astronomy & Astrophysics
    - Atmospheric Science
    - Atomic
    - Electronics and Electricity
    - Elementary Particles and High Energy
    - Fluid and Plasma
    - Molecular
    - Nuclear
    - Optics
    - Radiation
    - Solid State
  - STATISTICS
- APPLIED SCIENCES
  - APPLIED MECHANICS
  - ASTRONAUTICS
  - COMPUTER SCIENCE
  - ENGINEERING
    - General
    - Aerospace
    - Agricultural
    - Automotive
    - Biomedical
    - Chemical (includes ceramics and fuel)
    - Civil
    - Electronics and Electrical
    - Heat and Thermodynamics
    - Hydraulic
    - Industrial
    - Marine
    - Materials Science
    - Mechanical
    - Metallurgy
    - Mining
    - Nuclear
    - Petroleum
    - Sanitary and Municipal
    - System Science
  - OPERATIONS RESEARCH
  - PLASTICS TECHNOLOGY
  - TEXTILE TECHNOLOGY

VB PSYCHOLOGY
- PSYCHOLOGY
  - General
  - Clinical
  - Experimental
  - Industrial
  - Physiological
  - Psychobiology
  - Social

ABSTRACT

Suspended sediment concentration and size are obtained simultaneously from multi-frequency acoustic profiling data collected in the nearshore zone with the newly developed Remote Acoustic Sediment TRANsport (RASTRAN) System 1. It appears to be the first time that both suspended sediment size and concentration have been obtained in the ocean from acoustic profiling data. The inversion method for data analysis is based on a semi-empirical expression for the scattering cross section of sand. Straight stainless steel wires are used as standard targets to determine the acoustic sounder sensitivities. Laboratory measurements, with a suspended sediment jet, and four periods of field measurements from Stanhope Beach, Prince Edward Island are analysed. It is demonstrated that in the laboratory measurements the systematic error is about +12% in concentration, and about -19% in size. The RASTRAN concentration data from the field experiments are in reasonably good agreement with Optical Backscattering Sensor (OBS) measurements at the same height above bottom. The time-mean profiles of particle concentration for the four selected field runs follow a power law in the nearbed region, above which the concentration profile can be expressed mainly by an exponential function. Suspended particle sizes are more uniform than concentration in the vertical. Both size and concentration profiles vary significantly with the wave energy level. The vertical profile of sediment eddy diffusivity K_s is calculated from the time-mean profiles of particle concentration and size by assuming a balance on average between vertical diffusion and settling. It is shown that the sediment eddy diffusivity is a linear function of height in the

nearbed region, then decreases slightly with height. It is demonstrated that the horizontal wave flux affects the total suspended sediment transport, while the vertical wave flux has important effects on the vertical profiles of sediment eddy diffusivity. By eliminating the effects of vertical wave flux from K_s, it is found that the vertical profile of eddy diffusivity due to turbulence is analogous to the profile of eddy viscosity proposed by Smith and McLean.

ACKNOWLEDGEMENTS

I am greatly indebted to my supervisor Dr. Alex Hay for suggesting this thesis topic to me and his guidance and encouragement throughout this project. I would like to express my thanks to Mr. Eugene Colbourne for participating in the laboratory and field experiments. Without his contribution the data in this thesis could never have been collected. I gratefully acknowledge the efforts of many members of Dalhousie University, University of Toronto, and Memorial University of Newfoundland in mounting the RASTRAN frame under the cold seawater at Stanhope Beach, Prince Edward Island. I am also grateful to Dr. Richard Greatbatch and Dr. Brad De Young and other faculty members in the Department for their advice.

I especially thank Dr. A. K. Bowen, Dr. K. Thompson, and Mr. D. Hazen in Dalhousie University for their cooperation in making UDATS data available to us.

I am deeply appreciative of the personal financial assistance from the Memorial University of Newfoundland in the form of a University Fellowship (1986-1988) and NSERC-Industry Fellowship (1989-1990), and from Dr. Hay's strategic grant funded by Natural Sciences and Engineering Research Council of Canada.

Finally, I wish to thank my wife Wu Xi for her understanding and encouragements during my graduate studies.

TABLE OF CONTENTS

LIST OF FIGURES

LIST OF TABLES

LIST OF SYMBOLS

SYMBOL	DESCRIPTION AND/OR DEFINITION AS APPLICABLE	REFERENCE PAGE
a	particle radius	21
a_g	geometric mean radius	64
a_o	effective radius of a circular transducer	29
a_o^*	actual radius of a circular transducer	29
a_w	cylinder radius	35
A	acoustic system constant	24
A_n	Eq. (3.33)	37
c	speed of sound in surrounding fluid	19
$c\,\tau/2$	range width of the detected volume	19
d	particle diameter	18
D	transducer directivity	21
D_{13}	depth difference between the pair of 1 and 5 MHz transducers	120
D_{23}	depth difference between the pair of 2.25 and 5 MHz transducers	120
D_{yz}	mean relative systematic error	88
$f_\infty(x)$	form factor for sand particles	21
f_{max}	wave frequency at the maximum power spectral density	97

$f_w(z_w)$	form factor for an infinite cylinder	37
$F(n(a), \lvert f_\infty \rvert)$	Eq. (3.14)	24
g	acceleration due to gravity	191
h_{ripple}	ripple height	177
H	water depth	192
i	$=\sqrt{-1}$	35
$J_1(\ )$	cylindrical Bessel function of order 1	29
$J_n(\ )$	cylindrical Bessel function of order n	38
k	von Karman's constant	201
k_c	compression wavenumber in the fluid	21
k_c'	compression wavenumber in the cylinder	38
k_s'	shear wavenumber in the cylinder	38
K'	sediment eddy diffusivity due to turbulence	160
$K_f(r)$	proportionality constant	53
K_s	$=K_w+K'$, sediment eddy diffusivity	160
K_w	sediment eddy diffusivity due to wave motion	160
$K_\Gamma(a_w)$	proportionality constant	56
K_μ	molecular diffusivity	158
L	effective length of the cylinder in a continuous system	34
L_p	effective length of the cylinder in a pulsed system	34
m_w'	turbulent fluctuation of mass concentration	158
M	mass concentration of suspended particles	22
M_i^e	rough estimated mass concentration at the range r_i	82
M_o	mass concentration at the centerline of the jet	67

M_{OBS}	time mean concentration detected by OBS	133
M_R	time mean concentration detected by RASTRAN	133
M_w'	wave induced mass concentration	158
$n(a)$	normalized particle size distribution	22
N	number of particles per unit volume	22
$N_n(\ )$	cylindrical Neumann function of order n	38
OBS	Optical Backscattering Sensor	5
p_i	pressure amplitude of incident wave	21
p_s	backscattered pressure amplitude	21
$\hat{p}_s$	root mean square scattered pressure amplitude from a cloud of suspended particles	22
p_w	backscattered pressure amplitude from a finite cylinder	39
$p_{w,max}$	maximum backscattered pressure from a finite cylinder in a pulsed system	45
p_o	on-axis pressure amplitude at r_o	21
PSD	Power Spectral Density	96
q	volume flow per unit length	36
$\overline{q}$	suspended sediment transport rate by the mean flow	182
q_t	suspended sediment transport rate in the cross-shore direction	181
q_w	suspended sediment transport rate due to wave orbital motion	182
Q	volume flow rate	35
r	distance from the transducer to the detected volume	21
	perpendicular distance from the cylinder to the field point	37
r_s	distance from the spherical source to any field point	36

r_o	reference distance along the acoustic axis	21
RASTRAN	Remote Acoustic Sediment TRANsport	7
R_c	critical range for the farfield	30
R_{yz}	correlation coefficient of linear regression	88
s_w'	$=k_s' a_w$	38
S	acoustic system sensitivity	24
S_w	$=Ap_o r_o$	50
t_w	averaged wave period	108
T	water temperature	19
TVG	Time Variable Gain	24
$\mathbf{u}$	turbulent fluctuation vector of particle velocity	158
u_*	bottom friction velocity	201
$U_{1/3}$	significant cross-shore wave velocity near the bed	107
U_{max}	maximum cross-shore wave velocity near the bed	107
$\mathbf{U}_t$	particle velocity vector	158
$\bar{\mathbf{U}}$	time mean particle velocity vector	158
$\mathbf{U}_w'$	wave induced particle velocity vector	158
VHF	vertical-form index of the ripple	174
V_o	detected voltage at the centerline of the jet	67
W_G	settling velocity of a spherical particle	161
W_s	settling velocity of natural sand particles	161
x	$=k_c a$	21
x_w	$=k_c a_w$	37
x_w'	$=k_c' a_w$	38

z	height from bottom	191
Z_{max}	perpendicular distance from the acoustic axis to the intersection of the cylinder and the pulse front at $t=2r/c+\tau/2$	42
α_n	Eq. (3.35)	38
α_o	attenuation coefficient in water	21
α_s	attenuation coefficient due to the suspended particles in water	21
$\bar{\alpha}_s$	$=\int_o^\infty \alpha_s\, n(a)\, da$	82
β	angle with respect to the acoustic axis	22
β_m	angle corresponding to the first zero of D	29
β_n	Eq. (3.35)	38
β_o	half power beamwidth	29
Γ	Eq. (3.55)	45
$\delta(\beta')$	Eq. (3.22)	32
δ_b	thickness of the wave boundary layer	201
δ_{linear}	thickness of the linear region of K_s	177
δ_n	Eq. (3.35)	38
Δr_B	temporal variation in bed positions	179
ϵ	$=\frac{M}{\rho_o'}$, volume concentration of suspended particles	22
ϵ_n	Neumann number	37
ς	$=c\tau\left[\alpha_o+\bar{\alpha}_s\right]$	24
η_n	phase shift of the n th partial wave	37
Θ	argument of the complex function Γ	46

κ	$\int_0^{\beta_m} D^4 \sin\beta d\beta$	23
λ	wavelength of the sound wave in the fluid	21
μ	molecular shear viscosity of water	161
ξ	$=\bar{\alpha}_s / k_c \epsilon$	82
ρ_o	density of water	27
ρ_o'	grain density of the particles	22
ρ_w'	mass density of the cylinder	36
σ_g	geometric standard deviation	64
τ	pulse duration	19
Φ_n	Eq. (3.36)	38
ψ	$=L/\sqrt{2r\lambda}$, ratio of the effective length of the cylinder to the diameter of the first Fresnel zone of the receiver	34
ω	angular frequency	23

CHAPTER 1 INTRODUCTION

The central objective of this thesis is to demonstrate that a multi-frequency acoustic system can be used to obtain vertical profiles of the absolute concentration and the mean size of suspended particles remotely. This problem is of great practical significance. To calculate the suspended sediment transport rate, it is necessary to be able to predict the profile of particle concentration throughout the water depth. Continuous sampling of vertical profiles with high accuracy and resolution is possible using sophisticated acoustic techniques. Results from existing acoustic systems depend, however, when inverting the detected voltage to suspended sediment concentration, on presupposing that the size distribution of the suspended particles is invariant in time and space. It was recognized a long time ago that the general utility of single-frequency acoustic instruments is hampered by this assumption [Huntley, 1982; Hay and Heffler, 1983]. In order to explore fully the dynamics of sediment transport, it is needed to monitor simultaneously the suspension concentration and the size distribution, which requires a multi-frequency system.

1.1 Suspended Sediment Transport

In recent years great attention has been paid to the resuspension of bottom sediments in the coastal and continental shelf regions due to its great importance with regard to offshore oil development, coastal defence, flood prevention,

navigation, and harbor management, to name only a few such areas of concern. Sediment transport in unidirectional flow has been studied extensively during the last five decades [Einstein, 1950; Smith and Hopkins, 1972; Smith, 1977; Smith and McLean, 1977a, and b], and is now fairly well understood. Sediment transport is still under investigation for pure wave conditions [Hom-ma *et al.*, 1965; Kennedy and Locher, 1972; Wang and Liang, 1975; Nakato *et al.*, 1977, Sleath, 1982], and the basic mechanics of sediment resuspension by waves has not been fully revealed. It is even much less studied in the condition of combined waves and currents, which is most likely the case in the aforementioned regions, due to the difficulty in understanding of the interaction of waves and currents with the seabed [Smith, 1977; Grant and Madsen, 1979, 1982; Glenn, 1983; Vincent and Green, 1990].

Sediment transport, in general, can be in the form of the suspended load or bedload, depending on the size of the bed material particles and the flow conditions. Suspension occurs when the grains, once they are entrained in the flow, are diffused upward by a random succession of upward impulses imparted by turbulent eddies while at the same time settling back toward the bed under the influence of gravity. Bedload is the mode of transport of sediment, in which the particles move by rolling or hopping distances of a few grain diameters under the influence of the lift and drag forces imparted to them by the near bed flow. There are considerable uncertainties about the relative importance of bedload and suspended load transport in the coastal and continental shelf regions [Huntley and Bowen, 1989]. It is generally believed, however, that the suspension transport mechanism is the most efficient aspect of sediment movement for fine sand, specifically under pure wave conditions [Smith and Hopkins, 1972; Smith, 1977],

and that the proper computation of suspension transport rate is a critical part of sediment transport models [Drake and Cacchione, 1989]. In this thesis we deal only with the suspended sediment transport problem.

In the past, a variety of formulae to calculate suspended sediment transport rates has been constructed from the fluid dynamical characteristics of the near bottom flow, an extensive review of such formulae was given by Kajima and Katori [1988]. It is very difficult, in the absence of reliable data, to assess the accuracy of these and other predictive formulae. It can be expected, however, that they will only provide rough estimates of suspended sediment transport rates under complex natural conditions, since suspended load transport is a nonlinear, two phase flow problem, in which there is considerable negative feedback between the moving sediment grains and the near bed flow [Dyer and Soulsby, 1988]. An alternate way, which has great potential, is to carry out numerical calculations starting with the mass conservation equations for sediment and water and the momentum conservation equations for turbulent, near bottom flow [Smith, 1977; Adams and Weatherly, 1981; Dally and Dean, 1984; Sheng and Villaret, 1989]. The lack of accurate data from nature, however, makes it impossible to effect direct quantitative or even qualitative tests of model results [Sandermann and Klocher, 1983]. It is clear that such verification procedures are essential to progress in understanding suspended sediment transport mechanics and thereby carrying out reliable suspended load transport calculations. Furthermore, to attain this goal, methods to obtain accurate measured suspended sediment concentration data must be developed.

1.2 Techniques for Measuring Suspended Sediment

The existing measurement techniques employed in the coastal and continental shelf regions generally fall into two categories: direct methods and indirect methods. The former refers to those in which the actual suspended sediment concentration or size is determined from a sample taken directly from the fluid. The latter refer to those in which the particle concentration or size is determined indirectly from a physical quantity, which depends on the concentration and size. Direct methods include bottle sampling [e.g. Drake *et al.*, 1980], mechanical sampling [Downing *et al.*, 1981], pump and hose sampling [e.g. Renger, 1986], and sediment trap methods [e.g. Moody *et al.*, 1987]. Direct methods suffer from several problems: sampling is possibly only at discrete points and, usually, only at discrete times; the time resolution is usually poor; the apparatus modifies modifying the flow field. Moreover, direct methods are tedious and time-consuming for the amount of data which they yield. Indirect methods, such as optical methods and acoustic methods, on the other hand, have the advantage of being labour-saving, having fast-response, and providing an effectively continuous output.

The principle of optical and acoustic methods is that radiation passing through water is modified by the processes of attenuation and scattering by water itself and by sand particles and dissolved matter in the water. Two kinds of optical devices are currently available: the transmissometer, which measures the attenuation of a light beam along its path [e.g. Brenninkmeyer, 1976; Drake, 1971; Cacchione and Drake, 1979; Spinrad, 1983], and the nephelometer, which monitors the scattered intensity from particles in suspension [e.g. Thornton and

Morris, 1978; Drake *et al.*, 1980; Downing *et al.*, 1981]. The nephelometer detecting the backscattered intensity is particularly called the Optical Backscatter Sensor, or OBS [e.g. Downing *et al.*, 1981; Hanes and Huntley, 1986]. It has been demonstrated that optical techniques, especially of the second kind, are well suited to the fast-response measurements required in the nearshore wave-dominated zone. However, they still have the disadvantage of being intrusive and sampling only at discrete, fixed points.

Several acoustic systems have been used until now.

1. The 3 MHz Acoustic Concentration Meter (henceforth "ACM"), which was described first by Huff and Friske [1980]. It was used in several field experiments for the study of sediment transport in the coastal and continental shelf regions [Young *et al.*, 1982; Vincent *et al.*, 1982; Hanes *et al.*, 1988]. A similar instrument, operating at 2.8 MHz, has been used by Vincent and Green [1990]. The ACM system demonstrated that it was capable of measuring concentration profiles of suspended sediments in the marine bottom boundary layer [Young *et al.*, 1982; Vincent *et al.*, 1982; Hanes *et al.*, 1988], monitoring local seabed microtopography during a storm [Hanes *et al.*, 1988], and observing wave-induced vortex entrainment of sediment from a rippled bed, which governs the net suspended sediment flux [Vincent and Green, 1990].

2. The 3 MHz Acoustic Sediment Profiler (henceforth "ASP") [Bedford *et al.*, 1982; Libicki *et al.*, 1987; Libicki *et al.*, 1989]. It was deployed in the benthic boundary layer to measure suspended sediments [Libicki *et al.*, 1989]. It should be pointed out that the acoustic transceivers in the ASP and in the ACM are same, but other configurations in the two systems are different. The detected

range of the ASP is in the transition region [Libicki *et al.*, 1989]. The characteristics of the transition region are more complicated than those of the far-field, and a generally accepted explicit expression for the scattered pressure in this region is not available. All of those make the problem more difficult, because the calibration relation obtained at a specific range from the transducer is not necessarily freely applicable to other ranges.

3. The Acoustic Backscattering System (henceforth "ABSS") [Orr and Hess, 1978; Hess and Bedford, 1985; Lynch *et al.*, 1987]. It is a dual-frequency system with 5 MHz unit looking downward and the 500 kHz unit looking upward. It was modified from a standard high frequency backscatter sonar to make it suitable for long term remote deployments in the deep ocean.

The above three acoustic systems monitor profiling backscattered signals, and among them the ACM and the ASP are single-frequency systems. The ABSS, on the other hand, was operated at two different frequencies, but it is still different from the multi-frequency system to be discussed in this thesis. This is because our system can simultaneously detect acoustic signals at several different frequencies scattered from particles suspended in the same water column, whereas the ABSS cannot.

Besides these three acoustic profiling systems, there is another acoustic device available, which is the 4.5 MHz Ultrasonic Sand Transport Meter (henceforth "USTM") [Jansen, 1979; Schaafsma and der Kinderen, 1986]. This instrument monitors the particle concentration and velocity simultaneously and thus the transport of suspended sand particles. Two versions of USTM are available, that is, one dimensional (1-D) USTM and two dimensional (2-D) USTM. The 1-D

USTM measured backscattering and attenuation together. Its shortcoming is that the maximum measurable concentration in the linear region is 5 g/l, which is too low for the practical application. The 2-D USTM almost completely corrects for the scattering attenuation, which is an advantage over other systems. The main disadvantage of 2-D USTM is, however, that it can only measure the concentration at a single position at a time.

All of the above mentioned acoustic techniques really demonstrate that the acoustic methods can be used for quantitative remote detection of suspended particle concentration with minimal disturbance to the flow field, which in conjunction with similar measurements of currents, could provide direct measurements of suspended sediment transport rate [Huntley and Bowen, 1989].

1.3 Current Situation

While the existing acoustic systems have exhibited the potential of the acoustic approach to measure the near-seabed concentrations in the offshore and continental regions, there are many questions still unanswered, particularly the difficulty in interpreting the relationship between the scattered acoustic signal and the particle concentration and size.

Hay *et al.* [1988] have developed a multi-frequency Remote Acoustic Sediment TRANsport system, called the RASTRAN System 1. The purpose of this thesis is to demonstrate that it is possible using this system, with a suitable inversion method, to measure the actual suspended sediment concentration and the mean particle size simultaneously.

The basic idea is that the scattered acoustic signal depends on the size distribution, the acoustic frequency, and the number of particles in the detected volume. At a given range, the parameters of the size distribution and the concentration can be extracted from signals detected by acoustic transceivers operating simultaneously at different frequencies, providing that the system sensitivity, and the differential and total scattering cross-sections (i.e. the backscatter form factor and the scattering attenuation) of natural sand particles are quantitatively known. If the acoustic system can provide continuous output for the whole detected range, then vertical profiles of concentration and size distribution can be obtained.

1.4 Thesis Outline

The RASTRAN system is described in Chapter 2, with descriptions of the laboratory calibration setup and of the field site configuration. The acoustic scattering theories for both a cloud of suspended particles and a cylinder of finite length (used as a standard target) in water are discussed in Chapter 3, in which a simple expression relating the acoustic output and particle properties is obtained. The estimated value of the acoustic system constant is determined in Chapter 4 by using the standard targets. The acoustic characteristics of natural sand particles are considered in Chapter 5. The inversion method to convert the acoustic output to the actual concentration and the size of the sediments in suspension is introduced in Chapter 6. The laboratory results and field measurements are presented and discussed in Chapter 7 and Chapter 8, respectively, with the conclusions in Chapter 9.

CHAPTER 2 RASTRAN SYSTEM AND SETUP

2.1 The RASTRAN System

The RASTRAN system [Hay *et al.*, 1988], as shown in Figure 2.1, is composed of four Mesotech Model 810 immersible sounders with frequencies of 1, 2.25 and 5 MHz, coupled to EXADAC, an Expandable Acoustic Data Acquisition System, which consists of a LeCroy model 6810 programmable 12-bit resolution, 4-channel transient recorder, a model 8501 programmable clock in a CAMAC crate, a GPIB controller, a microcomputer and a Thorne/EMI 9900 9-track streaming tape drive (Figure 2.2).

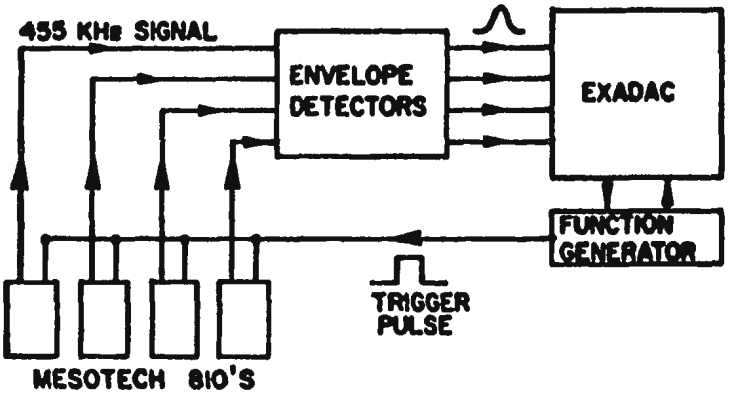

Figure 2.1. Block diagram of RASTRAN system [Hay *et al.*, 1988].

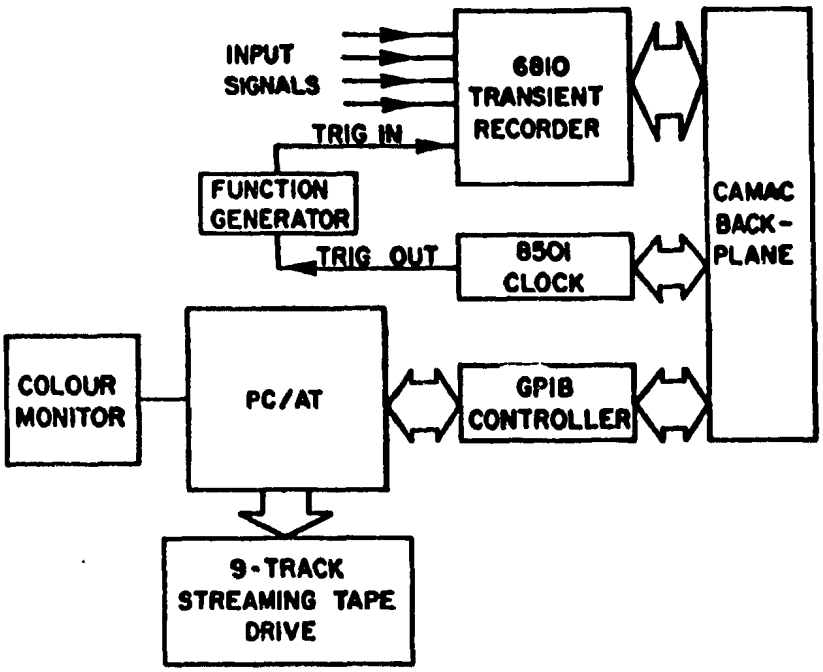

Figure 2.2. EXADAC: Block diagram [Hay *et al.*, 1988].

The Model 810 sounders are powered externally and are triggered by a function generator. The backscattered signals received by the sounders are heterodyned down to 455 kHz with the bandwidth of 50 to 100 kHz, and then pass from the sounders to an envelope detector, in which the signals are filtered and rectified. A user-selected number of backscatter profiles, usually four, are digitized at 200 kHz and stored in the transient recorder at 10 to 12 ms intervals. These data are transferred from the crate to the microcomputer, in which the averaging over the selected number of profiles and over each range bin is performed to yield a single ensemble-averaged profile with 2 cm range resolution. For a typical 4-ping ensemble average, this means an average of 20 digitized points at a ensemble-averaged profile acquisition rate of better than 6 Hz. Data can be displayed using color graphics either as time series of backscatter at

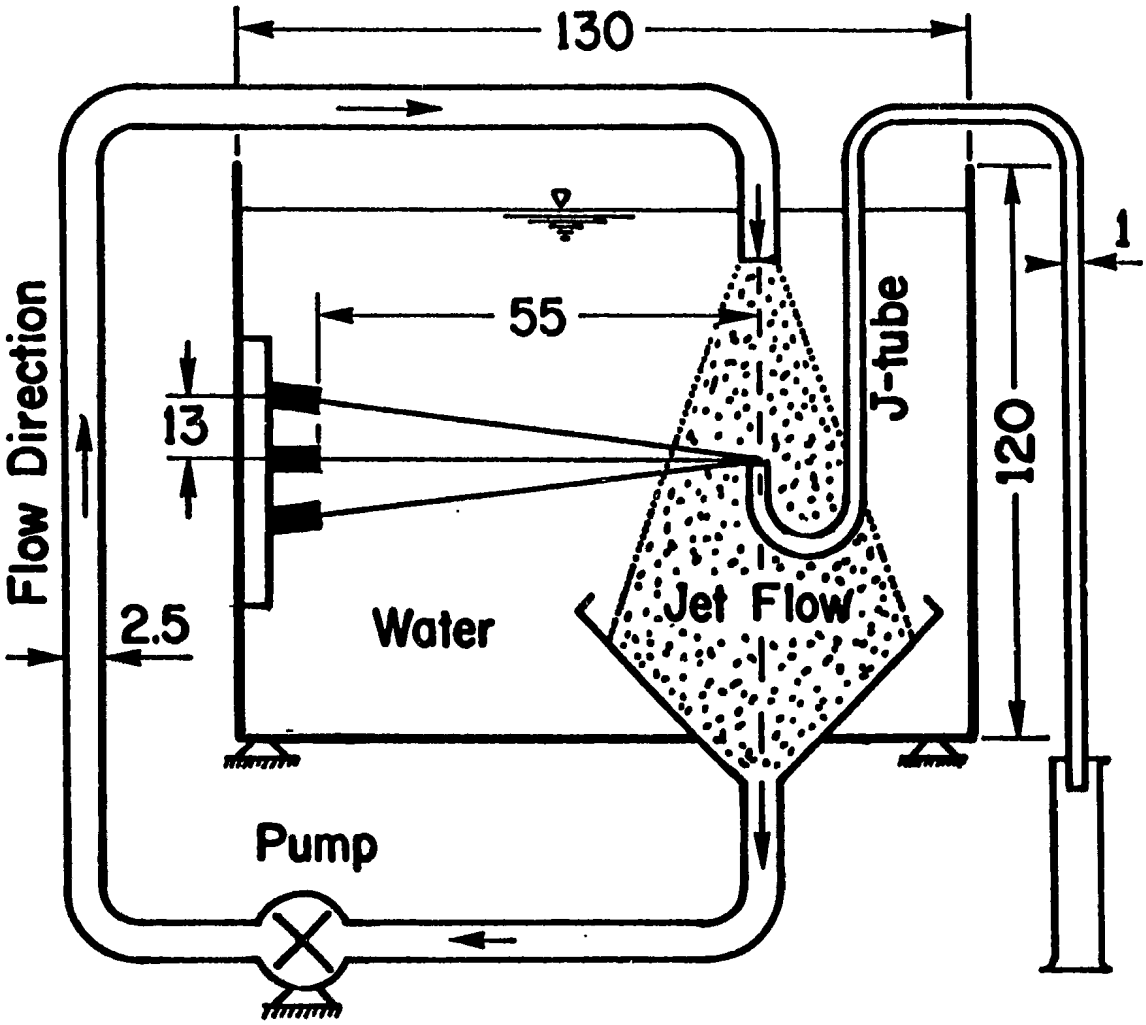

Figure 2.3. Schematic diagram of test tank arrangement. Distances are in cm.

selected ranges or as acoustic images color-coded with respect to backscatter amplitude, intensity or concentration.

2.2 Laboratory Callbration Setup

A special purpose tank was developed to calibrate the Model 810 sounders in the laboratory [Hay, 1991]. A schematic diagram of the calibration setup is given in Figure 2.3. The water tank is 1.3 m long, 0.9 m wide and 1.2 m deep. For the sediment calibrations, a submersible nozzle, connected to a pump by a hose, was fixed at about 10 cm down below the water surface. The metal cone projecting downwards from the tank bottom was connected to the pump intake by another hose. Water-sediment mixtures were pumped around the circuit, being injected downwards from the nozzle to form a suspended sediment jet. Calibration experiments can be performed simultaneously on three sounders mounted on the frame as shown in Figure 2.3. The three sounders were adjusted to have their axes aligned on a common point at the center of the jet (Figure 2.3).

To calibrate the response of the acoustic system as a function of suspended sand concentration and size distribution, the actual concentrations in the suspension jet are required. These were measured by suction, in which water samples were siphoned from the jet into a 1 liter graduated cylinder, the volume measured, and then sand particles weighed after they were dried. By calculating the ratio of the mass of the dried sand to the volume of the mixture, the sample concentration was obtained. However, the ratio of the sample concentration to the actual concentration in the jet, called the efficiency of a suction method, is not

always equal to unity. It has been demonstrated that this efficiency depends on the geometry of the suction tube, the orientation of the tube in the flow, the jet flow itself and the intake velocity. The efficiency, however, tends towards unity if the suction and jet flow are in line and the ratio of the intake velocity to the jet flow itself is greater than 3 [e.g. Bosman *et al.*, 1987]. The above conditions were satisfied by using the J-type tube and setting the level difference between the J-tube intake and siphon outlet to be more than 1 m in our calibration system. Four suction samples were taken at each concentration in order to to obtain the average concentration and to estimate experimental errors.

For testing with straight wires, which were used as standard targets and for alignment, the jet nozzle was replaced by a movable frame, on which the wire was mounted.

2.3 Field Site Configuration

The RASTRAN system was deployed in the nearshore zone at Stanhope Lane, Prince Edward Island in October and November 1989, as part of collaborative experiments with Dalhousie University and the University of Toronto designed to improve understanding of the mechanics of sediment transport.

The beach at Stanhope Lane is located on the central north coast of Prince Edward Island, facing north into the open Gulf of St. Lawrence, as shown in Figure 2.4. It is aligned roughly east-west and is characterized by an almost continuous shelving sandy beach over a sandstone peddle pavement with variable width, backed in places by extensive dune deposits and elsewhere by low rock or till

cliffs [Forbes, 1987; Hanes and Vincent, 1987]. The sand on the beach is well sorted with mean grain sizes in the range of 0.16-0.30 mm. The coarser material occurs on the beachface and the finer on the nearshore bars to seaward. The bottom profile off Stanhope Lane Beach, presented in Figure 2.5, indicates three major shore-parallel bars at about 100 m, 200 m, and 380 m from the baseline. The deployment location of the RASTRAN system was seaward of the second sand crest (see Figure 2.5).

The detailed configuration of the RASTRAN system in the field experiment is shown in Figure 2.6, in which four acoustic sounders operating at three different frequencies were mounted on a frame anchored to the seabed about 95 cm from the bottom. The 1 and 5 MHz sounders, and one of the 2.25 MHz sounders were 22-23 cm apart in the horizontal, and the other 2.25 MHz sounder was deployed 1.45 m farther onshore from the first. All sounders were connected to the shore-based data acquisition and control system by armored cables. Three OBS's were mounted on the seaward frame at heights of 5, 10, and 15 cm respectively above the bottom, while three electromagnetic flowmeters were mounted on the same frame at heights of 20, 50 and 100 cm respectively above the bottom (see Figure 2.6b). The same number of OBS's and flowmeters were also mounted on the shoreward end of the frame in the manner similar to those on the seaward end. It must be pointed out that the heights of all sensors from the bottom were variable owing to the movable seabed. All signals, with the exception of the RASTRAN acoustic data, were also recorded on the Dalhousie University UDATS, which stands for Underwater Digitization and Transmission System [Hazen *et al.*, 1988].

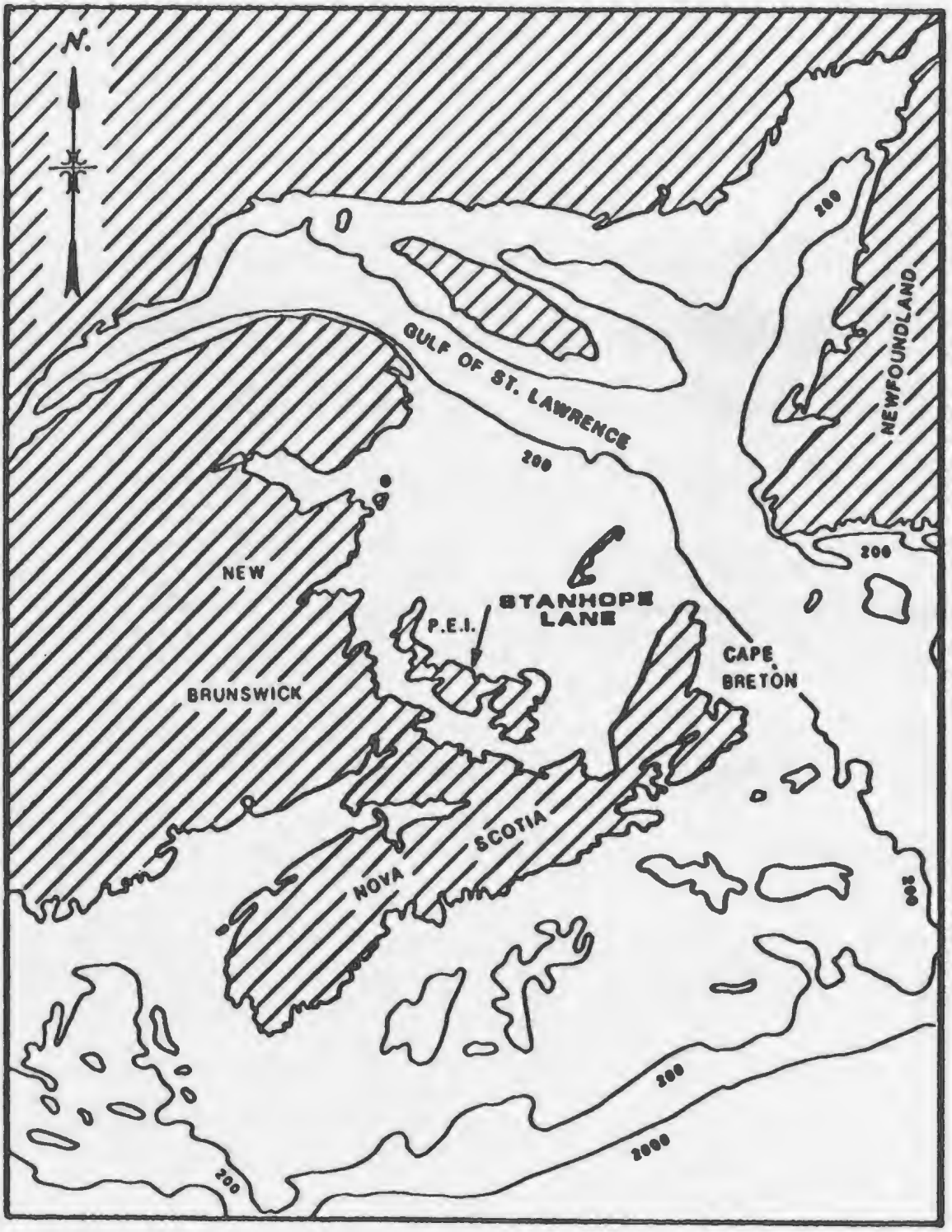

Figure 2.4. The site of the 1989 field experiment [from Willis, 1987].

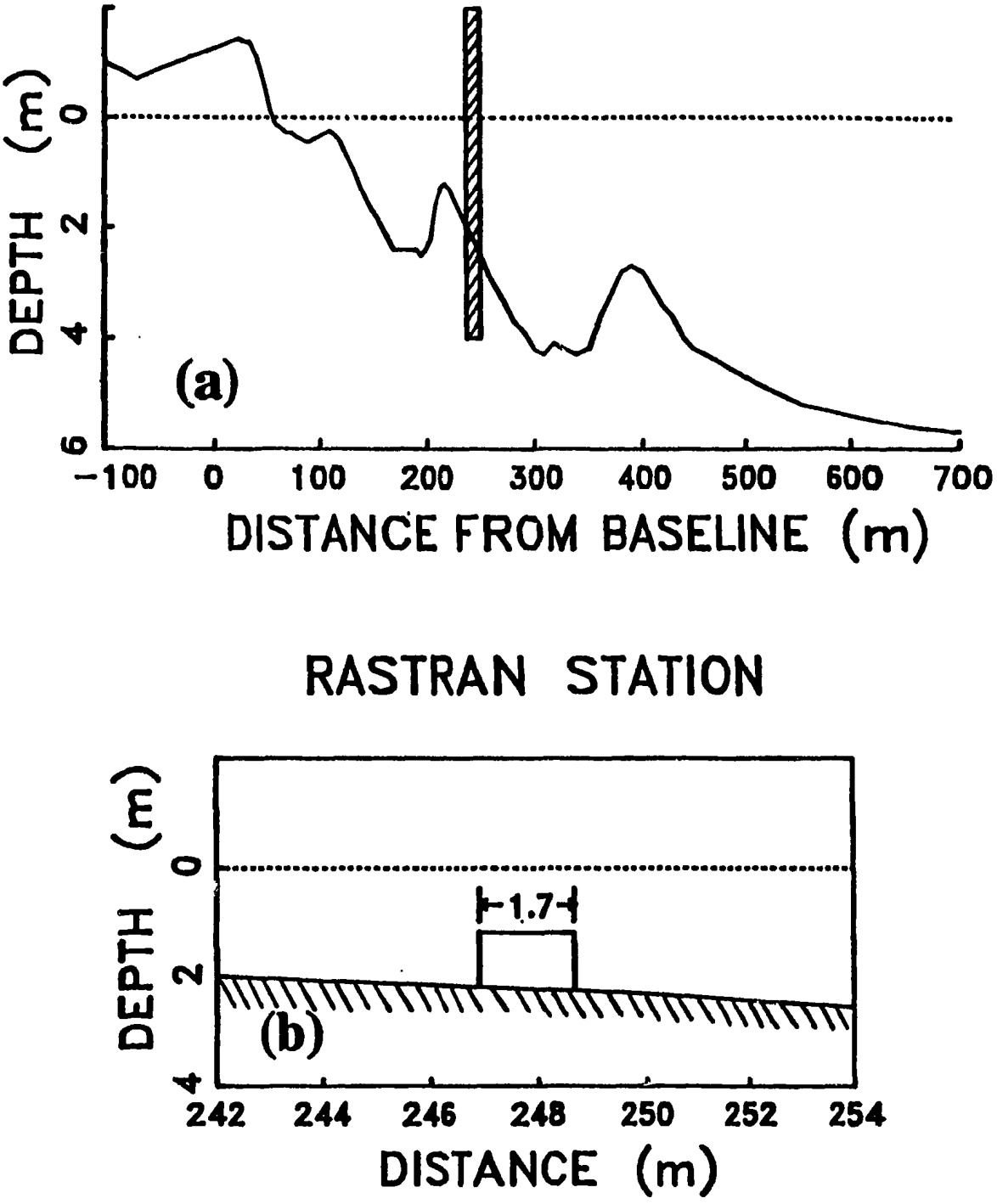

Figure 2.5. (a) Beach profile at Stanhope Lane, Prince Edward Island. Box inset of RASTRAN site is shown in (b). (b) The deployment location of the RASTRAN system, showing RASTRAN frame, with no vertical exaggeration.

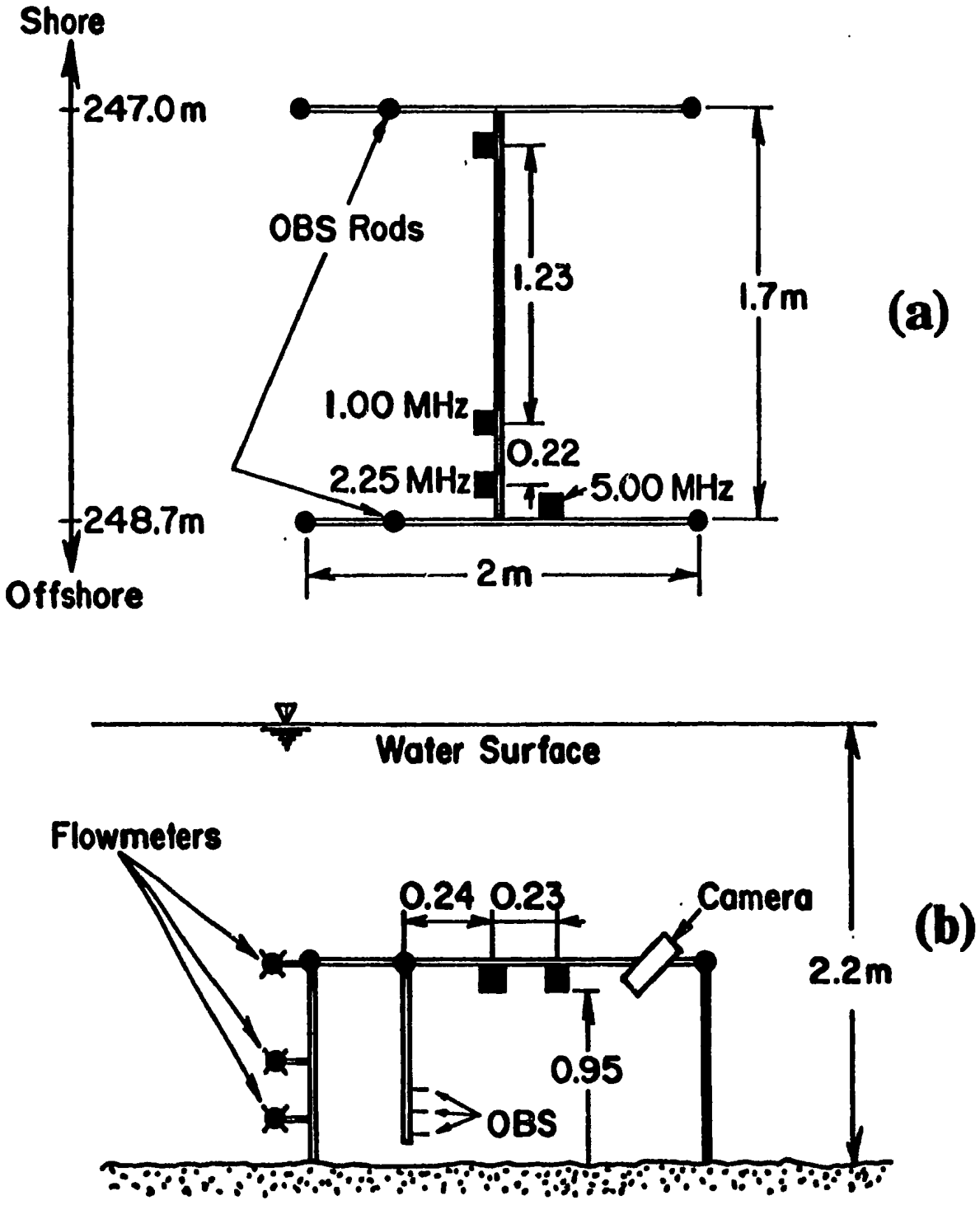

Figure 2.6. The configuration of the RASTRAN system in the 1989 field experiment. (a) Plan view. (b) End view, looking shoreward. Distances are in m.

2.4 Preparation of Uniform Sand Particles

Natural sand from three different locations: Queensland Beach, Nova Scotia; Bluewater Beach, Georgian Bay, Ontario; and Stanhope Beach, Prince Edward Isla[illegible] was washed several times in tap water to remove soluble salts, then dried at room temperature. For the uniform sand experiments, the dried sand was sieved into narrow size fractions by using 20.3 cm diameter wire-mesh sieves on the Ro-Tap mechanical shaker and following the methodology outlined by Carver [1971]. The size range of sand particles is from 88 μm to 500 μm in diameter, sieved at the quarter-phi intervals, where phi$=-log_2 d$, and d is the particle diameter in units of mm. Sand particles in each fraction are assumed to be uniform and can be represented by the midpoint of the corresponding sieve interval with the same grain density as quartz, 2700 kg/m^3.

CHAPTER 3 SCATTERING THEORY

To determine the properties of suspended particles from acoustic signals, such as the concentration and the size, we need to know the scattering cross sections of sand grains and the system sensitivity. In this chapter, we discuss first the dependence of the acoustic output on the characteristics of the water-sediment mixture, then the directivity pattern of the sounder. Because straight wires are used as standard targets to determine the system sensitivity, acoustic scattering from finite-length cylinders is explored in Section 3.3.

3.1 Scattering from a Cloud of Particles

The RASTRAN system, and most other existing acoustic techniques as well, are pulsed monostatic systems. By "monostatic" we mean that the same transducer is used both to transmit and receive. Consider a pulsed monostatic system, as shown in Figure 3.1, with a narrow beamwidth $2\beta_e$ and the pulse duration τ. The range width of the detected volume is $c\,\tau/2$ [Clay and Medwin, 1977, p. 231], where c is the sound speed in water, and the detected volume is assumed to be located in the farfield of the transducer. Typically, τ is 20 μs in the present application, and the sound speed in water is 1482 m/s for T = 20° C and zero salinity. Hence, the thickness of the detected volume is about 1.5 cm. It is assumed that the size distribution and the concentration are homogeneous inside the detected volume. The physical quantities at different positions, however,

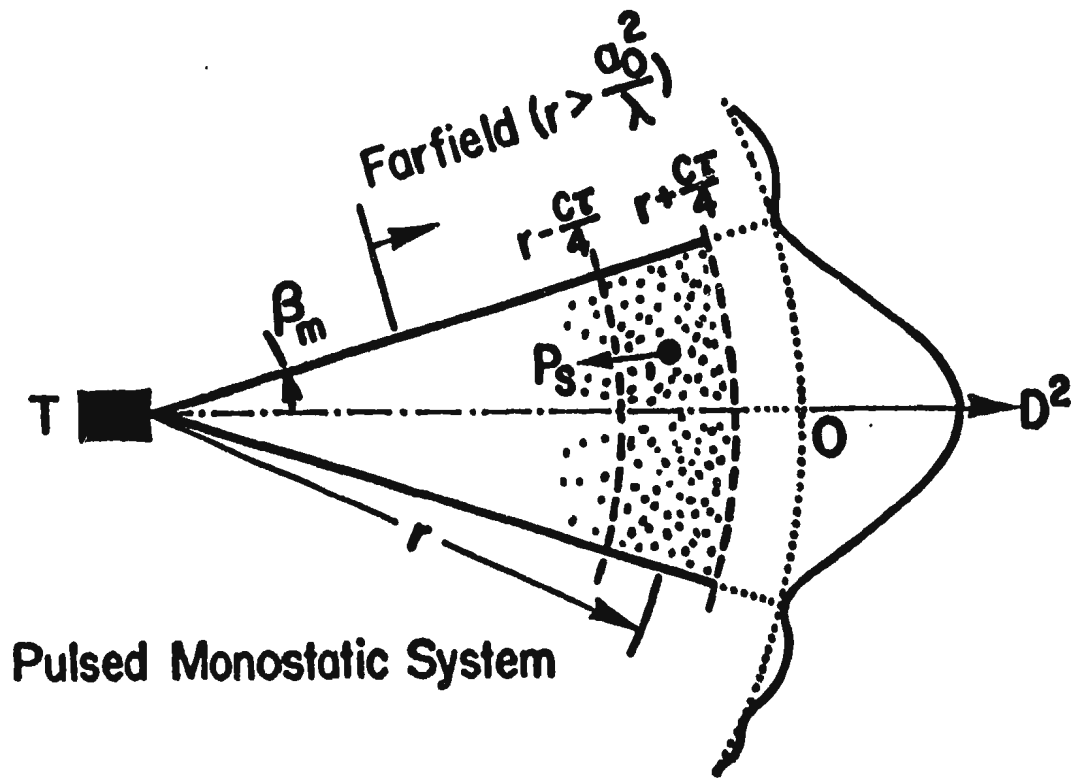

Figure 3.1. The geometry for a pulsed monostatic system. T is the transducer, a_0 the radius of a circular transducer, and D the transducer directivity. The remaining symbols are defined in the text.

could be different. The motion of suspended particles in water can also be ignored compared with the sound speed in water. Consequently, the suspended sand particles can be considered stationary during the passage of the transmitted pulse. Finally we assume that concentration is low enough that multiple scattering can be ignored. It should be emphasized that the last assumption could be violated if the volume concentration of the suspended particles is greater than 1% [Varadan *et al.*, 1983].

The pressure amplitude of incident spherical sound waves in the detected volume can be written as

$$p_i = p_* r_* \frac{D}{r} \exp\left[-\alpha_0 r - \int_*^r \bar{\alpha}_s \, dr\right], \tag{3.1}$$

where p_* is the on-axis pressure amplitude at the reference distance r_* when the fluid has no suspended particles, r is the distance from the transducer to the detected volume with $r \gg r_*$ and α_0 is the attenuation coefficient in water, which depends on the sound frequency and properties of the fluid, such as viscosity [Clay and Medwin, 1977, p.418]. It is assumed that r_* is small enough that $\alpha_0 r_* \ll 1$. For most cases fluid properties are uniform over the whole detected range, so that α_0 can be assumed to be a constant. In Eq. (3.1) α_s is the attenuation due to the suspended particles, and is a function of frequency, the concentration and size of the suspended sediment. The overbar denotes the average over the size distribution. D is the transducer directivity.

Let us represent a sand particle by a solid sphere with equivalent size. The backscattered pressure amplitude from each particle can then be written as

$$p_s = p_i \frac{a \,|\, f_\infty(x) \,|\, D}{2r} \exp\left[-\alpha_0 r - \int_*^r \bar{\alpha}_s \, dr\right], \tag{3.2}$$

where a is the radius of the particle, and x is the non-dimensional radius or frequency, given by $x = k_c a = \frac{2\pi a}{\lambda}$, where k_c and λ are respectively the wavenumber and wavelength of the sound wave in the fluid. Since $2\pi a$ is the circumference of the particle, x can be considered as the ratio of the circumference to the wavelength. In Eq. (3.2), $f_\infty(x)$ is the form factor at the scattering angle

$\theta = 180°$.

The mean square scattered pressure from a cloud of suspended particles can be expressed by [Hay, 1983]

$$\hat{p}_s^2 = \iiint_v \left[\int_0^\infty N p_s^2 n(a) da \right] dv, \tag{3.3}$$

where $n(a)$ is the normalized size distribution, and v is the detected volume. N is the number of particles per unit volume, and takes the form of

$$N = \frac{3M}{4\pi \rho_o' \int_0^\infty a^3 n(a) da}, \tag{3.4}$$

in which M is the mass concentration, and ρ_s' is the grain density of the particles, which is assumed to be independent of the size distribution. Assuming the transmitted pulse shape is rectangular, the detected volume v at any range can be written as

$$v = 2\pi \int_{r-c\tau/4}^{r+c\tau/4} \int_0^{\beta_m} r'^2 \sin\beta d\beta dr', \tag{3.5}$$

where $r - \frac{c\tau}{4}$ and $r + \frac{c\tau}{4}$ are the near and the far boundaries of the detected volume respectively (see Figure 3.1), β is the angle with respect to the acoustic axis, and β_m is the angle beyond which the contribution of scatterers to the total scattered pressure at the receiver is negligible. β_m is discussed further in Section 3.2.

By substituting Eqs. (3.1)-(3.5) into (3.3), assuming that M, N, and $n(a)$

are homogeneous in the detected volume, we get

$$\hat{p}_o^2=\frac{3p_o^2r_o^2\kappa\epsilon}{8}\frac{\int_o^\infty a^2\,|\,f_\infty(k_c\,a)\,|^2n(a)da}{\int_o^\infty a^3n(a)da}\int_{r-c\,\tau/4}^{r+c\,\tau/4}\frac{\exp\left[-4\alpha_o\,r'-4\int_o^{r'}\bar{\alpha}_o\,dr''\right]}{r'^2}dr' \quad (3.6)$$

where κ is given by

$$\kappa=\int_o^{\beta_m}D^4\sin\beta d\,\beta. \quad (3.7)$$

and ϵ is the volume concentration, which is related to M through

$$\epsilon=\frac{M}{\rho_o'}. \quad (3.8)$$

The integral with respect to r' in Eq. (3.6) needs further discussion. By substituting $\eta=r'-r$, we have

$$\int_{r-c\,\tau/4}^{r+c\,\tau/4}\frac{\exp\left[-4\alpha_o\,r'-4\int_o^{r'}\bar{\alpha}_o\,dr''\right]}{r'^2}dr'=$$

$$=\exp\left[-4\alpha_o\,r-4\int_o^{r}\bar{\alpha}_o\,dr''\right]\int_{-c\,\tau/4}^{c\,\tau/4}\frac{\exp\left[-4(\alpha_o+\bar{\alpha}_o)\eta\right]}{(r+\eta)^2}\,d\,\eta. \quad (3.9)$$

The range between the detected volume and the transducer r is much greater than $\frac{c\,\tau}{4}$, that is, the denominator of Eq. (3.9) $(r+\eta)$ can be approximated by r without substantially reducing accuracy. Then, Equation (3.6) becomes

$$\hat{p}_o^2=\frac{3p_o^2r_o^2\omega\kappa\tau\epsilon}{16}\frac{\int_o^\infty x^2\,|\,f_\infty(x)\,|^2n(x)dx}{\int_o^\infty x^3n(x)dx}\frac{\sinh\zeta}{\zeta}\frac{\exp[-4\alpha_o\,r-4\int_o^{r}\bar{\alpha}_o\,dr'']}{r^2}, \quad (3.10)$$

with

$$\zeta = c\tau \left[\alpha_e + \bar{\alpha}_e\right]. \tag{3.11}$$

The detected voltage V_e is proportional to $\hat{p}_e$, so the rms detected voltage can be written as

$$\bar{V}_e = S\sqrt{\epsilon}F\left(n(a), |f_\infty(x)|\right)\left[\frac{\sinh\zeta}{\zeta}\right]^{\frac{1}{2}}\frac{\exp[-2\alpha_e r]}{r}\exp\left[-2\int_e^r \bar{\alpha}_e\, dr''\right], \tag{3.12}$$

where S is a system sensitivity constant, and takes the form

$$S = Ap_e r_e \sqrt{\frac{3}{16}\omega\kappa\tau}, \tag{3.13}$$

with A, a constant. $F\left(n(a), |f_\infty(x)|\right)$ is given by

$$F\left(n(a), |f_\infty(x)|\right) = k_c^{-\frac{1}{x}}\left[\frac{\int_e^\infty a^2 |f_\infty(x)|^2 n(a)da}{\int_e^\infty a^3 n(a)da}\right]^{1/2}$$

$$\equiv \left[\frac{\int_e^\infty x^2 |f_\infty(x)|^2 n(x)dx}{\int_e^\infty x^3 n(x)dx}\right]^{1/2}, \tag{3.14}$$

The receiver circuitry of the Mesotech 810 sounder uses Time Variable Gain (TVG), to compensate for the signal level losses due to the term $\frac{\exp[-2\alpha_e r]}{r}$. Let $\bar{V}_{TVG}$ represent the RASTRAN output corrected with TVG, then we have

$$\overline{V}_{TVG} = S\sqrt{\epsilon}F\left(n(a), |f_{\infty}(x)|\right)\left[\frac{\sinh\zeta}{\zeta}\right]^{\frac{1}{2}} \exp\left[-2\int_{o}^{r}\overline{\alpha}_{e}\,dr''\right]. \quad (3.15)$$

We will only deal with $\overline{V}_{TVG}$ in the following discussion, so later the subscript *TVG* will be suppressed for simplicity.

Eq. (3.15) is the basis for discussion in the rest of this thesis, and it can be divided into four elements, each of which has a different physical meaning.

1. The first element is S, which is a constant depending only on the acoustic system itself, including the sound frequency, the directivity pattern, pulse duration and the beamwidth. An accurate value of S for each sounder is critical for obtaining the actual concentration from the detected voltage.

2. The second element is $\sqrt{\epsilon}$, which is the square root of the volume concentration. It indicates that $\overline{V}^2$ is linearly dependent on the concentration M if the attenuation due to scattering is negligible.

3. The third element is $F\left(n(a), |f_{\infty}(x)|\right)$, which is determined by the size distribution and backscatter form factor of the suspended sand particles. If the scattering characteristics are known, then size distribution parameters can be estimated through this element.

4. The fourth element is $\left[\frac{\sinh\zeta}{\zeta}\right]^{\frac{1}{2}}\exp[-2\int_{o}^{r}\overline{\alpha}_{e}\,dr'']$, which represents the correction for attenuation due to particles in suspension. The term $\left[\frac{\sinh\zeta}{\zeta}\right]^{\frac{1}{2}}$ corrects for attenuation across the detected volume [Hay, 1991].

It is useful at this stage to discuss the characteristics of $F(n(a), |f_\infty(x)|)$. For the simplest attempt, let us consider a case in which all particles are spheres of uniform size. In this special case, Eq. (3.14) becomes

$$F(n(a), |f_\infty(x)|) = \frac{|f_\infty(x)|}{\sqrt{x}}. \tag{3.16}$$

it can be seen that $F(n(a), |f_\infty(x)|)$ is linearly proportional to the form factor $|f_\infty|$ of the particle.

The results of theoretical calculations of $\frac{a\alpha_s}{\epsilon}$, $|f_\infty(x)|$, $|f_\infty(x)/\sqrt{x}$ are shown in Figure 3.2 on the basis of a resonance-free (rigid) spherical scatterer. It was found that the theoretical results for a non-resonant (rigid) sphere with the density of quartz yields better estimates of α_s for suspended natural sands than those obtained from other spherical scatterer models [e.g., Sheng and Hay, 1988; Hay and Schaafsma, 1989]. It has also now been shown that the same is true for the backscatter form factor [Hay, 1991]. The range of x chosen for the computations was 0.01 to 30.0 at intervals of 0.01 in x. This spans most of the operating frequency range of interest (0.1 to 10.0 MHz) for the sand size range (30 μm to 1 mm radius). The physical properties used for quartz and water are listed in Table 3.1.

It can be seen from Figure 3.2 that for $x < 1$ both $|f_\infty|$ and $\frac{a\alpha_s}{\epsilon}$ increase with x. For $x \gg 1$, however, $|f_\infty|$ and $\frac{a\alpha_s}{\epsilon}$ approach to 1 and $\frac{3}{4}$, respectively. It can also be seen, from Figure 3.2, that for a given acoustic frequency, $|f_\infty(x)|/\sqrt{x}$ increases with scatterer radius for $x<1$, and is

inversely proportional to the radius for larger x. The maximum value of $|f_{\infty}(x)|/\sqrt{x}$ occurs when the particle circumference is approximately equal to the sound wavelength.

Table 3.1. Physical properties used in calculation*

Quartz		
Density	ρ_0'	2.65×10^3 kgm^{-3}
Stainless Steel		
Density	ρ_{0_s}'	7.70×10^3 kgm^{-3}
Compressional wave speed	c_{p_s}	5762 ms^{-1}
Shear wave speed	c_s'	3185 ms^{-1}
Water**		
Density	ρ_0	0.998×10^3 kgm^{-3}
Speed of sound	c	1482 ms^{-1}

* All the data come from *Handbook of Physical Constants* [Clarke, 1966], and we use the average value if there are several values available for the same material.

** The sound speed in the water is calculated using the formula given by Clay and Medwin [1977, p. 88] with T = 20° C and zero salinity.

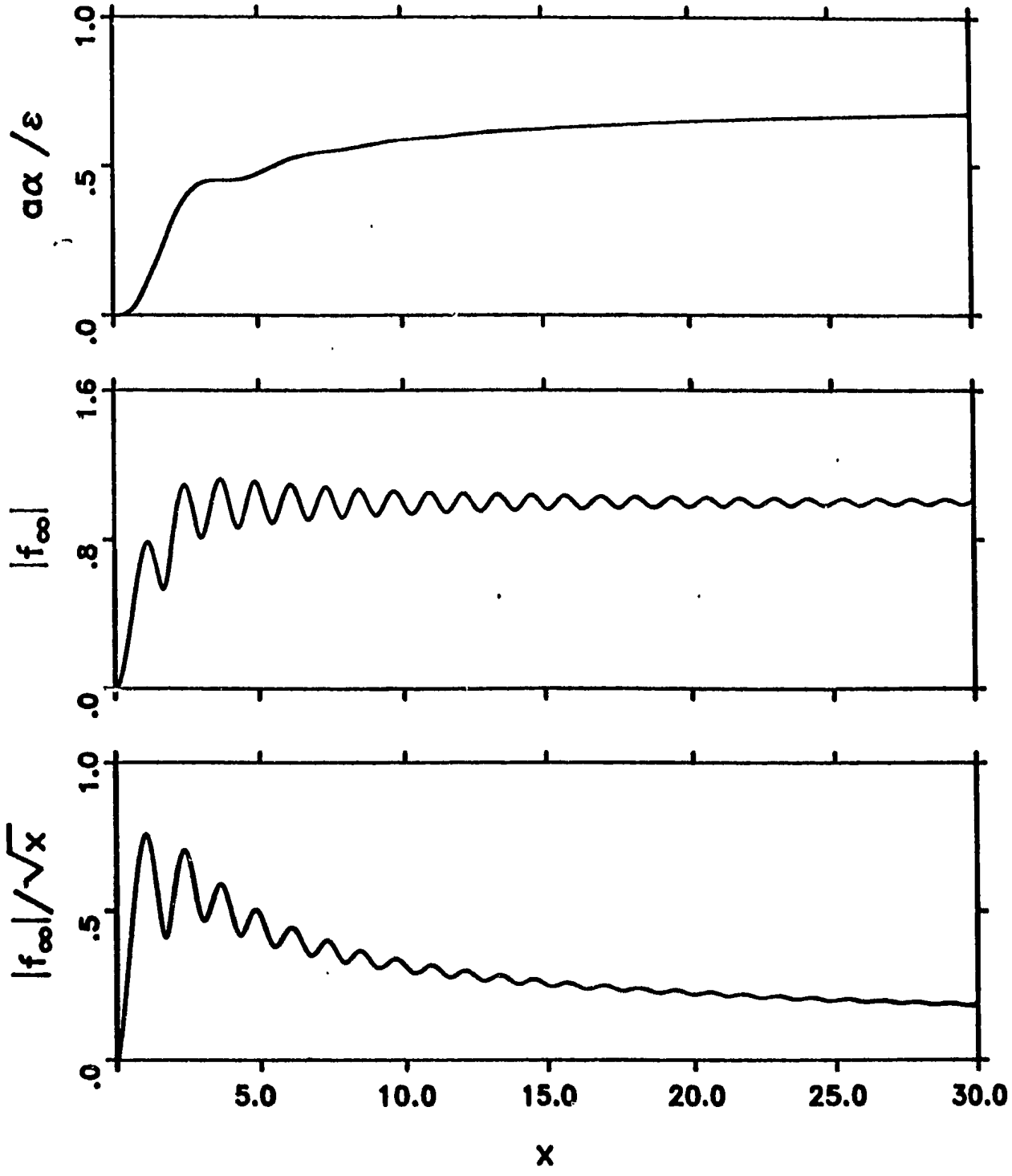

Figure 3.2. Theoretical results of $a\alpha_e/\epsilon$, $|f_\infty|$, and $|f_\infty|/\sqrt{x}$ for a non-resonant (rigid) spherical scatterer.

3.2 Directivity Pattern

The directivity pattern of a transducer is a measure of its relative response as a function of orientation in a given plane [Albers, 1965, p.290]. For a circular transducer of radius a_o uniformly sensitive over its surface, the farfield theoretical directivity pattern can be expressed by [Clay and Medwin, 1977, p.144]

$$D = \frac{2J_1(k_c\, a_o \sin\beta)}{k_c\, a_o \sin\beta}. \tag{3.17}$$

where β is the angle with respect to the acoustic axis i.e. the same as in Eq. (3.7). Conventionally, the half beamwidth β_o is chosen at the - 3 dB points of the main lobe of the beam pattern, that is [Abramowitz and Stegun, 1968, p.370]

$$\sin\beta_o = \frac{1.616}{k_c\, a_o}. \tag{3.18}$$

In Section 3.1 the angle β_m was used, which will be defined here as the angle corresponding to the first zero of D (Figure 3.1). The main reason for introducing β_m is that the contribution of the scattered pressure to the total pressure between the angle β_o and the angle β_m is not too small to be ignored. An example to support this argument will be given later. First let us find the explicit form for β_m based on the theoretical directivity pattern given by Eq. (3.17). The first zero of D in Eq. (3.17) occurs at [Abramowitz and Stegun, 1968, p.370]

$$\sin\beta_m = \frac{3.8317}{k_c\, a_o}. \tag{3.19}$$

From Eqs. (3.18) and (3.19), we obtain

$$\beta_m = \arcsin\left[2.371\sin\beta_o\right], \tag{3.20}$$

which relates β_o and β_m.

The measured directivity pattern is plotted in Figure 3.3 for three units with frequencies 1, 2.25 and 5 MHz. The solid line in Figure 3.3 is the farfield theoretical directivity pattern by using the effective radius of each sounder listed in Table 3.2. It can be seen, from Table 3.2, that the effective radius is smaller than the actual radius by about 14% for the 1 MHz unit, 27% for the 2.25 MHz unit, and 25% for the 5 MHz unit smaller, which is presumably caused by the way the transducer is mounted. Figure 3.3 shows that the theoretical results given by Eq. (3.17) with the effective radius fit the measured data quite well in the main lobe of the beam pattern. The theoretical results, however, do not predict both the magnitude and the position of the side lobes. Since the maximum values of the side lobes are less than -12 db, therefore, the relative contribution from those side lobes are small and can be ignored.

The assumption about the farfield region made at the beginning of this chapter also needs to be checked. Following Clay and Medwin [1977, p.155], the critical range R_c for the farfield can be written as

$$R_c = \frac{\pi a_o^2}{\lambda} \tag{3.21}$$

in which a_o is the effective radius. The estimated values of R_c with β_o, and β_m for three units are listed Table 3.2. It is clear that the assumption of the farfield holds only when the range is greater than the maximum value of R_c for the three sounders listed in Table 3.2, which is about 25 cm.

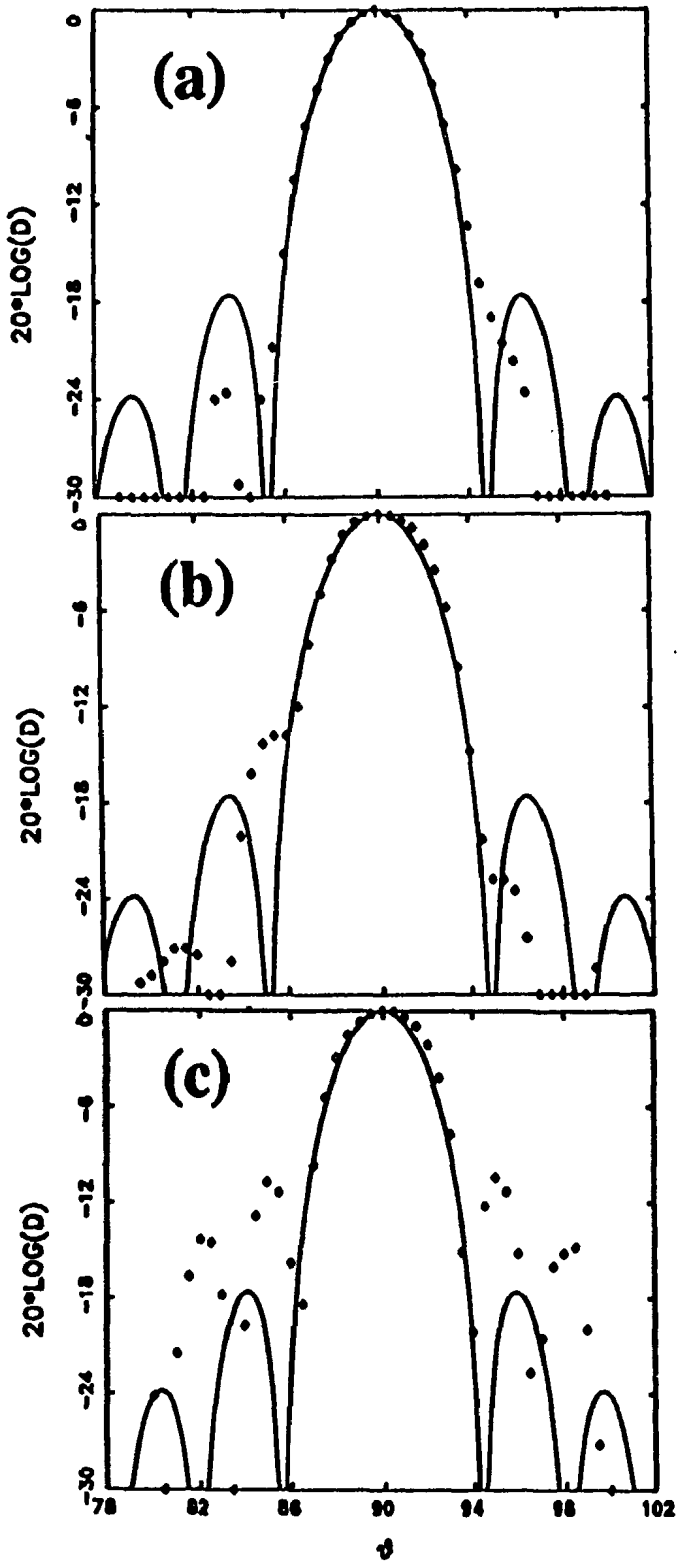

Figure 3.3. Comparison between measured and theoretical directivity pattern at: (a) 1 MHz; (b) 2.25 MHz; and (c) 5 MHz. The symbols represent the amplitude of the spectral peak made with the probe hydrophone at the fundamental frequency. Solid lines denote the farfield theoretical directivity pattern by using the effective radius listed in Table 3.2.

Table 3.2. Specifications of three sounders with frequencies of 1, 2.25, and 5 MHz. a_o^* is the actual radius of the transducer, and a_o is its effective radius, for which Eq. (3.17) provides the best fit to the measurements in the main lobe, and R_c is the critical range for the farfield. The sound speed in water is chosen to be 1482 m/s (for T = 20°, and zero salinity).

f (MHz)	β_o (degree)	β_m (degree)	a_o^* (cm)	a_o (cm)	R_c (cm)
1.00	2.00	4.75	1.27	1.09	25.2
2.25	2.05	4.87	0.64	0.47	10.6
5.00	1.85	4.39	0.32	0.24	6.1

Returning now to the argument about the exceeding contribution from scatterers beyond β_o. For an quantitative discussion, define $\delta(\beta^*)$ as the ratio of the contribution from scatterers in $\beta \leq \beta^*$ to the contribution from scatterers in $\beta \leq \beta_o$. Mathematically $\delta(\beta^*)$ can be expressed by

$$\delta(\beta^*) = \frac{\int_o^{\beta^*} D^4 \sin\beta d\beta}{\int_o^{\beta_o} D^4 \sin\beta d\beta}. \tag{3.22}$$

Let us consider an acoustic transducer with typical half power beamwidth $\beta_o = 2°$ ($\beta_m = 4.75°$). Variations of $\delta(\beta^*)$ are shown in Figure 3.4, in which the theoretical results of D^2 given by Eq. (3.17) are also plotted. It can be seen, from Figure 3.4, that $\delta(\beta^*)$ increases with β^* in the main lobe of the beam pattern ($\beta^* \leq \beta_m$), $\delta(\beta^*)=1$ at $\beta^*=\beta_o$, and $\delta(\beta^*)$ approaches to 1.28 for $\beta^* \geq \beta_m$. The difference in the value of $\delta(\beta^*)$ between $\beta^*=\beta_m$ and $\beta^*=\beta_o$ is as large as 28%.

The fact that $\delta(\beta^\circ)$ approaches a constant for $\beta^\circ \geq \beta_m$ (see Figure 3.4), on the other hand, indicates that the contribution from scatterers beyond β_m is small and can be ignored. It should be noted that the contribution for $\beta^\circ > \beta_m$ comes from the side lobes of the directivity pattern.

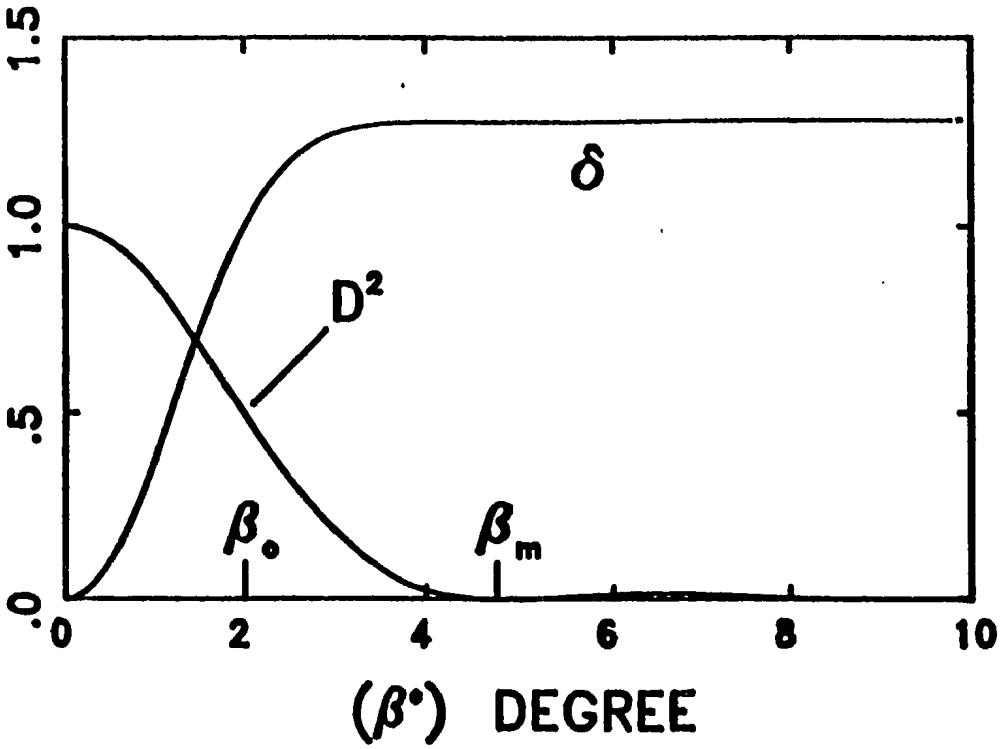

Figure 3.4. Variations of $\delta(\beta^\circ)$ as a function of β° for an acoustic transducer with typical half power beamwidth $\beta_0 = 2^\circ$. Computed results of D^2 are also included.

3.3 Scattering From a Cylinder of Finite Length

The purpose of this section is to obtain analytical results for the scattered pressure from a finite cylinder in the farfield of a monostatic system, such as the RASTRAN system.

Acoustic scattering from a solid cylinder of arbitrary length in water is a very complicated problem to describe analytically. The boundary conditions for the cylinder have cylindrical symmetry, but the scattered solution at large distances spreads spherically if the cylinder is not infinitely long. It has been shown [Andreeva and Samovol'kin, 1977, Stanton, 1988a, 1988b] that the scattering characteristics of the cylinder depend on its length L, and the radius of the first Fresnel zone of the receiver, which for the half period zone is given by $\sqrt{r\lambda/2}$ [Clay and Medwin, 1977, p.50]. By letting

$$\psi = \frac{L/2}{\sqrt{r\lambda/2}} = \frac{L}{\sqrt{2r\lambda}}, \tag{3.23}$$

There are two limiting cases: the case of $\psi \to \infty$, which physically means that the length of the cylinder is much longer than the diameter of the first Fresnel zone and is called an infinite cylinder [e.g. Faran, 1951]; and the case of $\psi \to 0$, which means that the length of the cylinder is much shorter than the diameter of the first Fresnel zone, and is called a short cylinder [e.g. Andreeva and Samovol'kin, 1977; Stanton, 1988a, 1988b]. It should be pointed out that quite different expressions for the radius of the first Fresnel zone have been used in the past, such as $\sqrt{r\lambda/2}$ chosen by Andreeva and Samovol'kin [1977], and $\sqrt{r\lambda}$ chosen by Stanton [1988a, 1988b]. The expression we used was based on the fact that the maximum

phase difference in the same zone is not greater than π for the monostatic system (for which the incident wave is spherical).

The scattering problem of a spherical wave incident on an infinite cylinder has studied lately by Li and Ueda [1990]. The analytical results for a spherical wave incident on a finite cylinder, especially for the case in which $\psi \to 1$, have not been fully explored yet. The existing results of acoustic scattering from a finite cylinder only dealt with the case of a plane incident wave rather than a spherical one, and the directivity pattern was also totally ignored. In the following discussion, we first follow the approach used by Stanton [1988a, 1988b] to find theoretical results for the scattered pressure from a cylinder with $\psi \to 1$ by using the concept of volume flow. The assumption of $\frac{L}{2a_w} > 1$ made by Stanton [1988a] is also used here to ignore the end effects of the finite cylinder, where a_w is the radius of the cylinder, so that the volume flow per unit length of a finite cylinder can be assumed to be same as that for an infinite cylinder. Consequently, the problem of finding the volume flow for a finite cylinder becomes that of finding the volume flow for an infinite cylinder, which can be easily obtained by using existing results for the scattered pressure from an infinite cylinder discussed by Faran [1951].

The concept of volume flow was first introduced by Skudrzyk [1971, Chapter 18] to find the analytical solution for scattering from an infinite cylinder. The basic idea is that the sound pressure of a small spherical source is determined by its volume flow, that is

$$p = -\frac{ik_c \rho_w' c Q}{4\pi r_s} \exp\left[ik_c r_s\right], \tag{3.24}$$

in which the time dependence has been suppressed. In Eq. (3.24) Q is the volume

flow rate, r_s is the distance from the spherical source to any field point, and ρ'_w is the mass density of the cylinder. It has been shown [Skudrzyk, 1971, p.348] that if the field point is sufficiently far away from the source and the diameter of the sound source is smaller than one third of the wave length, the sound pressure p is determined only by its volume flow and is not influenced by the shape of the source. If two sources produce equal volume flow, then they will generate the same sound pressure and the same sound energy.

Let us consider a case in which acoustic plane waves are incident on an infinite cylinder and the acoustic axis is orthogonal to the longitudinal axis of the cylinder, taken to coincide with the z-axis. The scattered pressure from this cylinder can be represented by a linear distribution of point sources (with very small diameter) of constant intensity along the z-axis, so that the contribution of an infinitesimal segment of length dz to the total scattered pressure is is

$$dp = -\frac{ik_c \rho'_w cq}{4\pi r_s}\exp[ik_c r_s]dz, \tag{3.25}$$

in which q is the volume flow per unit length, and is assumed to be invariant regardless the length of the cylinder, based on the assumption made at the beginning of this Section.

The total pressure is given as the integral of dp along the line

$$p = -\frac{ik_c \rho'_w cq}{4\pi}\int_{-L/2}^{L/2}\frac{\exp[ik_c r_s]}{r_s}dz. \tag{3.26}$$

It has been shown [Skudrzyk, 1971, p.427] that for L infinite

$$\int_{-\infty}^{\infty}\frac{\exp[ik_c r_s]}{r_s}dz = -i\pi H_o^{(1)}(k_c r) \tag{3.27}$$

in which r is the perpendicular distance from the cylinder to the field point, and $H_o^{(1)}$ the cylindrical Hankel function of the first kind of zero order. For large distances from the cylinder the asymptotic expression for the $H_o^{(1)}(k_c\, r)$ term can be used, and we have

$$\int_{-\infty}^{\infty} \frac{\exp[ik_c\, r_o]}{r_o} dz = \sqrt{\frac{2\pi}{k_c\, r}} \exp\left[i\left(k_c\, r - \frac{\pi}{4}\right)\right]. \tag{3.28}$$

By substituting Eq (3.28) into Eq. (3.26), the total scattered pressure in the farfield in terms of volume flux can be written as

$$p = \frac{k_c\, \rho_w'\, cq}{\sqrt{8\pi k_c\, r}} \exp\left[i\left(k_c\, r - \frac{\pi}{4}\right)\right]. \tag{3.29}$$

At the same time, the scattered pressure at large distances from an infinite cylinder can also be obtained by using the partial wave phase shift formalism [e.g. Faran, 1951], and it takes the form

$$p = p_o \sqrt{\frac{x_w}{2k_c\, r}}\, f_w(x_w) \exp\left[i\left(k_c\, r - \frac{\pi}{4}\right)\right], \tag{3.30}$$

where $x_w = k_c\, a_w$, and f_w is the form factor for an infinite cylinder, which can be expressed by

$$f_w(x_w) = \frac{2}{\sqrt{\pi x_w}} \sum_{n=o}^{\infty} (-1)^n\, \epsilon_n\, A_n, \tag{3.31}$$

in which

$$\epsilon_n = \begin{cases} 1 & n = 0 \\ 2 & n \geq 0 \end{cases} \tag{3.32}$$

and

$$A_n = -i \sin\eta_n \exp[-i\,\eta_n]. \tag{3.33}$$

In Eq. (3.33) η_n is the phase shift of the nth partial wave [Faran, 1951], and is

given by

$$\tan\eta_n = \tan\delta_n(x_w)\frac{\tan\alpha_n(x_w)+\tan\Phi_n}{\tan\beta_n(x_w)+\tan\Phi_n}, \tag{3.34}$$

where

$$\begin{cases} \tan\alpha_n(z) = -\dfrac{zJ_n'(z)}{J_n(z)} \\ \tan\beta_n(z) = -\dfrac{zN_n'(z)}{N_n(z)} \\ \tan\delta_n(z) = -\dfrac{J_n(z)}{N_n(z)} \end{cases} \tag{3.35}$$

and

$$\tan\Phi_n = \frac{\rho_o s_w'^2}{\rho_w'} \frac{\dfrac{\tan\alpha_n(x'_w)}{1+\tan\alpha_n(x'_w)} - \dfrac{n^2}{\tan\alpha_n(s'_w)+n^2-s'^2_w/2}}{\dfrac{\tan\alpha_n(x'_w)+n^2-s'^2_w/2}{1+\tan\alpha_n(x'_w)} - \dfrac{n^2(\tan\alpha_n(s'_w)+1)}{\tan\alpha_n(s'_w)+n^2-s'^2_w/2}}, \tag{3.36}$$

in which J_n and N_n are respectively cylindrical Bessel functions of the first and the second kind, the prime on the Bessel function denotes the derivation with respect to the argument, and $x'_w = k_c' a_w$ and $s'_w = k_s' a_w$. Here k_c' and k_s' are, respectively, the wavenumbers of the compression and shear waves in the cylinder.

Comparing Eq. (3.30) and Eq. (3.29), the volume flow per unit length of an infinite cylinder is

$$q = \frac{p_o\sqrt{4\pi x_w} f_w(x_w)}{k_c \rho_w' c}. \tag{3.37}$$

Based on the assumption made at the beginning of this Section, the expression in Eq. (3.37) is also taken to be the volume flow per unit length of a finite cylinder.

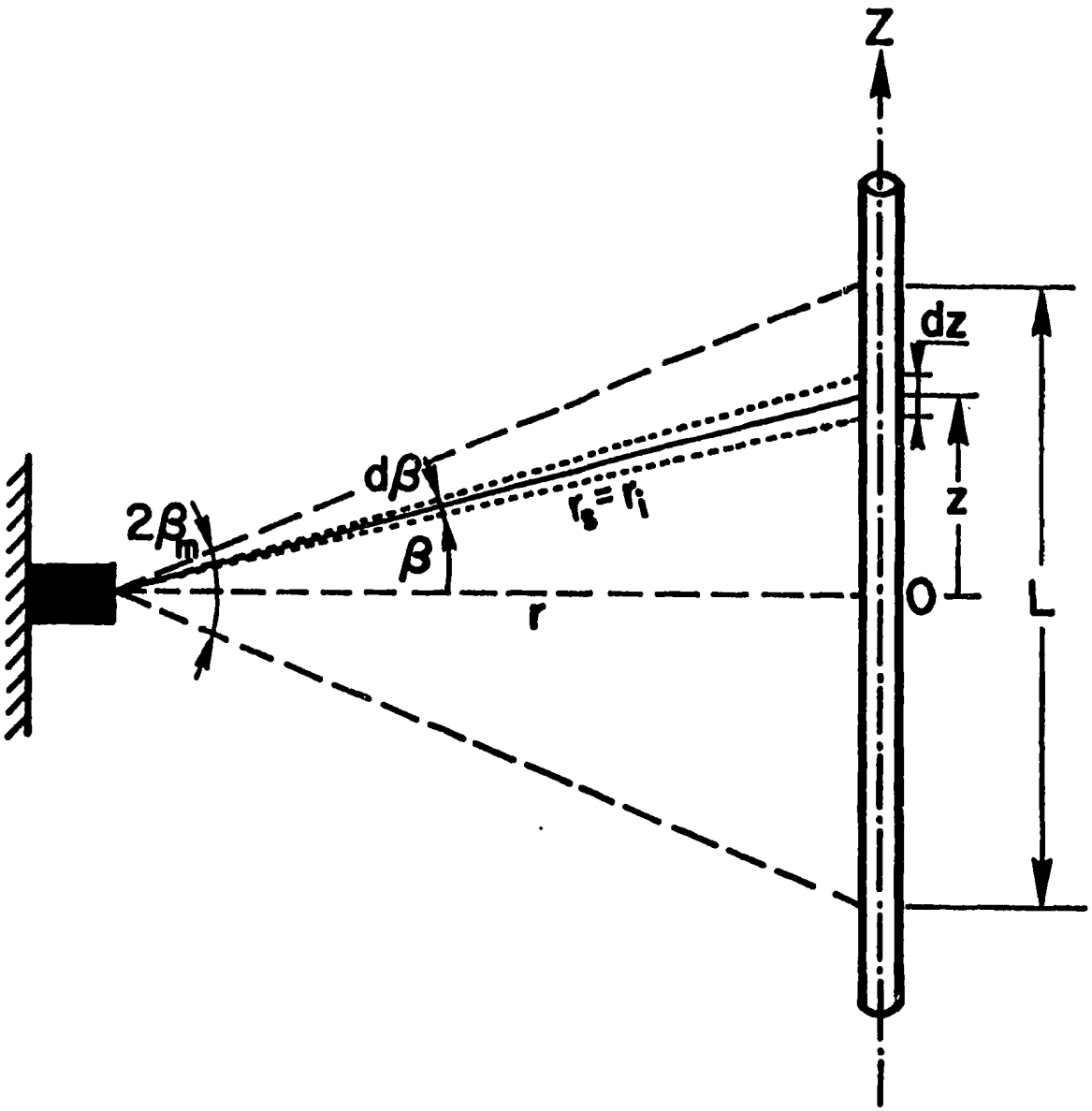

Figure 3.5. Choice of the coordinate system for acoustic scattering from a normal oriented cylinder of finite length, in which β is the angle with respect to the acoustic axis, L is the effective length of the cylinders given by $2r\sin\beta_m$, and β_m was defined in Eq. (3.19).

Let us consider the total scattered pressure from a finite cylinder with effective length L. Substituting Eq. (3.37) into Eq. (3.25), the contribution of an infinitesimal segment of length dz to the total pressure at large distances becomes

$$dp_w = -\frac{ip_o\sqrt{x_w}f_w(x_w)}{\sqrt{4\pi}}\frac{\exp[ik_c r_o]}{r_o}dz. \tag{3.38}$$

The total pressure can be obtained simply by integrating dp_w from $-\frac{L}{2}$ to $\frac{L}{2}$,

$$p_w = -\frac{ip_o\sqrt{x_w}f_w(x_w)}{\sqrt{4\pi}}\int_{-L/2}^{L/2}\frac{\exp[ik_c r_o]}{r_o}dz. \tag{3.39}$$

Up to here the results are similar to those given by Stanton [1988a, 1988b], which are for the case of a normally incident plane wave. Now let us consider the case in which the incident wave is spherical, with narrow beamwidth.

The scattering problem of a spherical wave incident on a finite cylinder is difficult to solve analytically. The difficulty, however, can be overcome for the narrow beam system, in which the incident waves are not too far off the normal direction.

We first turn our attention to the case in which the incident wave is continuous. By using the coordinate system shown in Figure 3.5, a spherical incident wave can be expressed by

$$p_i = p_o r_o D \frac{\exp[-\alpha_o r_s]}{r_s} \exp\left[ik_c (r_o - r)\right], \tag{3.40}$$

in which the attenuation due to water α_o, and the directivity of the transducer D have been included. Variations in incident wave intensity perpendicular to the z-axis will be ignored, since only narrow cylinders are considered. In Eq. (3.40), p_o and r_o have the same meaning as in Section 3.1. It should be pointed out that the term $\exp[ik_c (r_s - r)]$ in the above expression is to account the phase difference of a spherical incident wave at different positions of the cylinder with respect to the origin of the z-axis (see Figure 3.5). The contribution of an infinitesimal segment of length dz to the total pressure can be written as

$$dp_w = -ip_i D \frac{\exp[-\alpha_o r_s]}{r_s} \sqrt{\frac{x_w}{4\pi}} f_w(x_w) \exp[ik_c r_s] dz. \tag{3.41}$$

The total scattered pressure can be obtained by integrating Eq. (3.41) from $-\frac{L}{2}$ to $\frac{L}{2}$, where L is the effective length determined by the main lobe of the directivity pattern, that is,

$$L = 2r \tan\beta_m, \tag{3.42}$$

therefore,

$$p_w = -ip_o r_o \sqrt{\frac{x_w}{4\pi}} f_w(x_w) \int_{-L/2}^{L/2} D^2 \frac{\exp\left[ik_c (2r_s - r) - 2\alpha_o r_s\right]}{r_s^2} dz, \tag{3.43}$$

in which the expression for p_i given by Eq. (3.40) has been used.

Before we proceed Eq. (3.43) further by employing the geometry shown in Figure 3.5, let us consider the case in which the spherical incident wave is a pulsed one. The incident wave in this case can be expressed by

$$p_i = \begin{cases} p_o r_o D \dfrac{\exp[-\alpha_o r_o]}{r_o} \exp\left[ik_c (r_o - r)\right] & \dfrac{r_o}{c} < t < \dfrac{r_o}{c} + \tau \\ 0 & \text{otherwise} \end{cases} \tag{3.44}$$

where $t = 0$ corresponds to the time of the beginning of pulse transmission. Clearly the nonzero scattered pressure takes place only in the time interval of $\frac{2r_o}{c} < t < \frac{2r_o}{c} + \tau$. For practical reasons, we are only interested in the maximum scattered pressure from the cylinder in the aforementioned time interval. The determination of the exact time at which the scattered pressure reaches its maximum is a nontrivial problem, which is dependent on r, β_m, τ, and the dimension of the first Fresnel zone. For simplicity, it is assumed that the maximum scattered pressure occurs at time $t = \frac{2r}{c} + \frac{\tau}{2}$.

$$p_{w,max} = -ip_o r_o \sqrt{\frac{x_w}{4\pi}} f_w(x_w) \int_{-L_p/2}^{L_p/2} D^2 \frac{\exp\left[ik_c (2r_o - r) - 2\alpha_o r_o\right]}{r_o^2} dz, \tag{3.45}$$

where L_p is the effective length of the cylinder at $t = \frac{2r}{c} + \frac{\tau}{2}$ in a pulsed system. It must be pointed out that, unlike L in the continuous wave case, L_p is determined not only by the main lobe of the directivity pattern, but also by the pulse width. Figure 3.6 schematically sketches the geometry of the problem, where L is mainly determined by the main lobe, and Z_{max}, which is the perpendicular distance from the acoustic axis to the intersection of the cylinder and the pulse front at $t = \frac{2r}{c} + \frac{\tau}{2}$ (see Figure 3.6), on the other hand, is mainly determined by the pulse width. From Figure 3.6, we have for $c\tau \ll r$

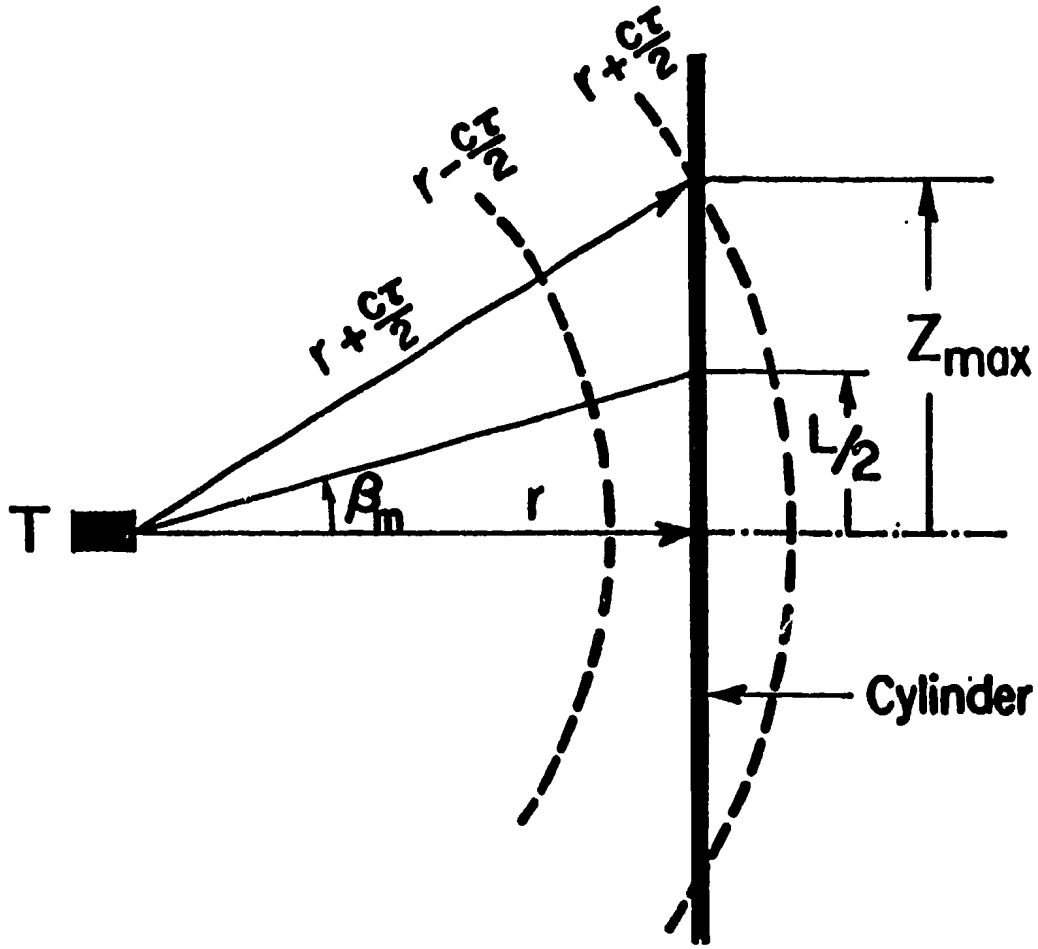

Figure 3.6. Schematic sketch of the pulsed wave case. T is the transducer, τ is the pulse duration, and remaining symbols are defined in the text.

$$Z_{max} = \sqrt{rc\,\tau + \frac{(c\,\tau)^2}{4}} \approx \sqrt{rc\,\tau} \tag{3.46}$$

The effective length L_p then is determined by the minimum value among L and $2Z$ max, that is

$$L_p = \min\left(L, 2Z_{max}\right), \tag{3.47}$$

For determining quantitatively the minimum of L and $2Z_{max}$, consider the ratio of L to $2Z_{max}$, that is

$$\frac{L}{2Z_{max}} = \frac{2r\tan\beta_m}{2\sqrt{rc\,\tau}} = \sqrt{\frac{r}{c\,\tau}}\tan\beta_m . \tag{3.48}$$

For given β_m and τ, the above ratio increases with increasing separation between sounder and wire. The value of $c\,\tau$ in our work is about 3 cm (see Section 3.1), β_m is about 5°, and the maximum value of r, which we used, is about 90 cm. It indicates that $L/2Z_{max}$ is always less than 0.5 for the situation in which we are interested. Therefore we will take

$$L_p = L = 2r\tan\beta_m . \tag{3.49}$$

By using Eq. (3.49) in Eq. (3.45), it can be seen that the maximum scattered pressure for pulses of this duration takes the same form as the scattered pressure in the continuous wave case.

From the geometry shown in Figure 3.5, we have

$$dz = \frac{r}{\cos^2\beta}\,d\beta; \qquad r_s = \frac{r}{\cos\beta} \tag{3.50}$$

The substitution of Eq. (3.50) into Eq. (3.45) gives us

$$p_{w,max} = -ip_o r_o \sqrt{\frac{x_w}{\pi}} f_w(x_w) \frac{\exp\left[ik_c r - 2\alpha_o r\right]}{r}$$
$$\times \int_0^{\beta_m} D^2 \exp\left[2r\left(ik_c - \alpha_o\right)\left(\csc\beta - 1\right)\right] d\beta. \tag{3.51}$$

It should be noted that since $\alpha_o \ll k_c$ for sounders operating in the MHz range, variations of $\exp[-2\alpha_o r(\csc\beta - 1)]$ in the main lobe of the directivity pattern for a narrow beam system are small and can be replaced by unity. By using Eq. (3.49) in Eq. (3.23), we have

$$\psi = \sqrt{\frac{k_c r}{\pi}} \tan\beta_m . \tag{3.52}$$

which indicates that for a given transducer with fixed values of β_m and k_c, ψ is only dependent on the distance between the transducer and the cylinder. Solving for $k_c r$ in the above equation, we have

$$k_c r = \frac{\pi\psi^2}{\tan^2\beta_m}. \tag{3.53}$$

By substituting Eq. (3.53) into Eq. (3.51), the maximum scattered pressure at large distances from a finite cylinder can finally be written as

$$p_{w,max} = p_o r_o \Gamma \sqrt{\frac{x_w}{2k_c r}} f_w(x_w) \frac{\exp[-2\alpha_o r]}{r} \exp\left[i\left(k_c r - \frac{\pi}{4}\right)\right] \tag{3.54}$$

in which Γ is given by

$$\Gamma = \frac{\sqrt{2}\psi}{\tan\beta_m} e^{-i\frac{\pi}{4}} \int_0^{\beta_m} D^2 \exp\left[\frac{2i\pi\psi^2(\csc\beta - 1)}{\tan^2\beta_m}\right] d\beta, \tag{3.55}$$

and D can be written as

$$D = \frac{0.5220\sin\beta_m}{\sin\beta} J_1\left[\frac{3.8317\sin\beta}{\sin\beta_m}\right] \tag{3.56}$$

by substituting $k_c\, a_0$ in Eq. (3.19) into Eq. (3.17).

Writing $\Gamma = |\Gamma| \exp(i\Theta)$, the numerical results for $|\Gamma|$ and Θ are shown in Figure 3.7 for $\beta_0 = 2^\circ$ ($\beta_m = 4.75^\circ$), which is the typical half power beamwidth of the RASTRAN system. It can be seen, from Figure 3.7, that $|\Gamma|$ increases linearly with ψ up to $\psi = 0.5$, and tends to 0.7 for very large ψ. Θ increases with ψ from -45° at $\psi = 0$ to 0° at very large ψ.

The above features of Γ in the cases of $\psi \ll 1$ and $\psi \gg 1$ can also be obtained analytically for a very narrow beam system, for which the rigorous derivation is given in Appendix A. It is shown that (see Appendix A)

$$\Gamma = \begin{cases} 0.636\psi e^{-i\frac{\pi}{4}} & \text{for } \psi \to 0 \\ \dfrac{1}{\sqrt{2}} & \text{for } \psi \to \infty \end{cases} \tag{3.57}$$

which indicates that $|\Gamma|$ is a linear function of ψ and Θ is equal to 45° for very small ψ, while $|\Gamma|$ approaches to a constant and Θ is equal to zero for very large ψ, which are consistent with numerical results shown in Figure 3.7.

Results in Eq. (3.57) can also be obtained simply if we compare the complex variation of the exponential term in Eq. (3.55) with the variation of D^2 in the main lobe of the directivity pattern. For simplicity, we consider a very narrow beamwidth, for which $2i\pi\psi^2(\csc\beta - 1)/\tan^2\beta_m$ can be approximated by $\approx i\pi\psi^2\beta^2/\beta_m^2$ $(= ik_c\, r\, \beta^2)$.

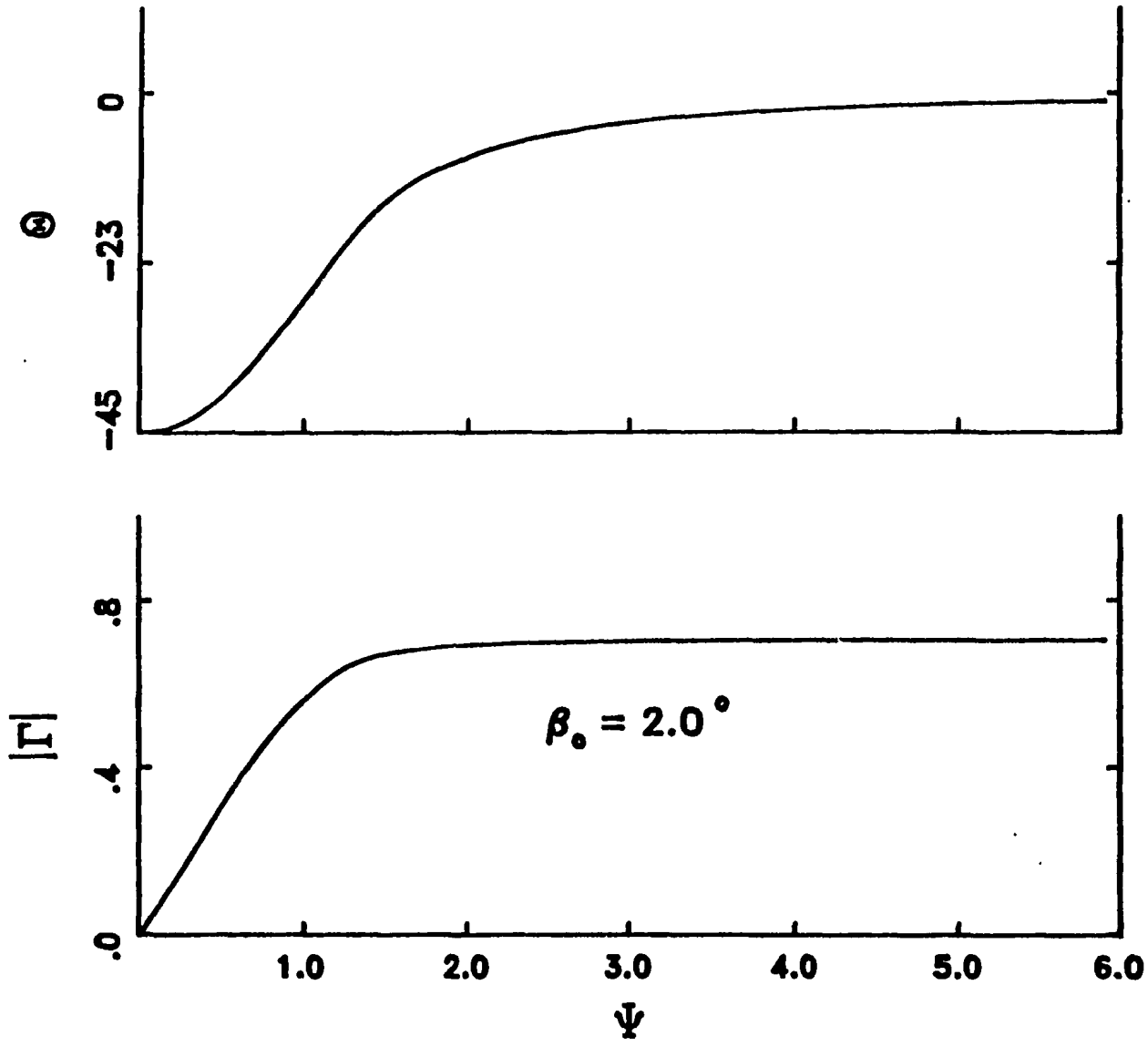

Figure 3.7. Calculated values of Θ and $|\Gamma|$ as a function of ψ for a transducer with half power beamwidth $\beta_o = 2°$ ($\beta_m = 4.75°$).

Consider now the case of $\psi \ll 1$, where the effective length of the cylinder is much smaller than the diameter of the first Fresnel zone, caused by small values of $k_e r$ for given β_m (but the cylinder is still in the farfield of the transducer and the receiver is at large distances from the cylinder). This case can be considered as a short cylinder, in which variations of $\exp[2i\pi\psi^2\beta^2/\beta_m^2]$ in the main lobe of the directivity pattern are small and can be replaced by unity. We have

$$\Gamma = \frac{\sqrt{2}\psi}{\beta_m} e^{-i\frac{\pi}{4}} \int_0^{\beta_m} D^2 d\beta \qquad (\text{for } \psi \to 0). \tag{3.58}$$

The integral $\int_0^{\beta_m} D^2 d\beta$ in the above expression is constant, and is equal to $0.450\beta_m$ for a very narrow beam system (see Appendix A). By using this result in Eq. (3.58), it can be seen that Eq. (3.58) is identical to Eq. (3.57) for $\psi \to 0$. The maximum scattered pressure in this case can be written as

$$p_{w,max} = -ip_o r_o \frac{0.450L}{r} \frac{\sqrt{x_w}}{2\sqrt{\pi}} f_w \frac{\exp[-2\alpha_o r]}{r} \exp[ik_e r] \qquad (\psi \to 0) \tag{3.59}$$

which implies that the scattered pressure from a short cylinder linearly increases with the effective length of the cylinder for small ψ. Similar results were obtained by Stanton [1988a] for the case of a plane wave incident on a short cylinder.

For the case of $\psi \gg 1$, in which the effective length of the cylinder is much greater than the diameter of the first Fresnel zone, is equivalent to very large values of $k_e r$ for a given β_m. This case can be considered as an infinite cylinder, in which the variation due to $\exp[-i\pi\psi^2\beta^2/\beta_m^2]$ in the main lobe is rapid, and its wave cycle becomes shorter for larger β. It can be expected that the main

contribution to $|\Gamma|$ comes from the first several cycles of $\exp[i\pi\psi^2\beta^2/\beta_m^2]$ $(=\exp[ik_e r\beta^2])$. Hence we have, by the method of stationary phase,

$$\psi\int_0^{\beta_m} D^2\exp\left[i\pi\psi^2\beta^2/\beta_m^2\right]d\beta=\psi D_*^2\int_0^{\beta_m}\exp\left[i\pi\psi^2\beta^2/\beta_m^2\right]d\beta$$

$$\leq\psi\int_0^{\beta_m}\exp\left[i\pi\psi^2\beta^2/\beta_m^2\right]d\beta \quad (\text{for } \psi\gg 1), \tag{3.60}$$

in which D_* is the value at some β located in the first several cycles of $\exp[i\pi\psi^2\beta^2/\beta_m^2]$. The value of D_* is set to be $D_{|\beta=0}=1$ in the last expression in Eq. (3.60).It can be expected that the inequality in Eq. (3.60) becomes an identity for $\psi\to\infty$. From Gradshteyn and Ryzhik [1980, p.395], we have

$$\lim_{\psi\to\infty}\left\{\psi\int_0^{\beta_m}\exp\left[i\pi\psi^2\beta^2/\beta_m^2\right]d\beta\right\}=\frac{\beta_m}{2}e^{i\frac{\pi}{4}}. \tag{3.61}$$

Substituting the above expression into Eq. (3.55), we get

$$\Gamma=\frac{1}{\sqrt{2}} \qquad (\text{for} \quad \psi\to\infty), \tag{3.62}$$

which is identical to Eq. (3.57) for $\psi\to\infty$. The maximum scattered pressure in this case is given by

$$p_{w,max}=p_* r_*\sqrt{\frac{\pi_w}{4k_e r}}f_w\frac{\exp[-2\alpha_* r]}{r}\exp\left[i(k_e r-\frac{\pi}{4})\right] \quad (\psi\to\infty) \tag{3.63}$$

which indicates that the scattered pressure from an infinite cylinder is independent of the length of the cylinder and decreases as $\exp[-2\alpha_* r]r^{-2/3}$. Similar results were obtained by Faran [1951] for the case of a plane wave incident on an

infinite cylinder.

Returning now to Eq. (3.54), the detected voltage from the cylinder is given by

$$\bar{V}_w = A\left[p_{w,max}\, p^{*}_{w,max}\right]^{\frac{1}{2}} = S_w \mid \Gamma \mid \frac{\sqrt{x_w} \mid f_w(x_w) \mid}{\sqrt{2k_c r}} \frac{\exp[-\alpha_0 r]}{r} \tag{3.64}$$

with

$$S_w = A p_e r_e . \tag{3.65}$$

where A is a proportionality factor, and has the same meaning as that in Eq. (3.13). After using the concept of TVG, we have

$$\bar{V}_w = S_w \mid \Gamma \mid \frac{\sqrt{x_w} \mid f_w(x_w) \mid}{\sqrt{2k_c r}} \tag{3.66}$$

Comparing with Eq. (3.15), it can be found that the structure of Eq. (3.66) is very similar to that of Eq. (3.15). The term $\sqrt{x_w} \mid f_w(x_w) \mid$ is similar to the term $F(X)$ in Eq. (3.15), and represents acoustic scattering characteristics of a cylinder. $\mid \Gamma \mid$ is a special function describing the effects of cylinder length on the scattered pressure. S_w is a system constant for scattering from a stationary cylinder, and is related to S through the term $A p_e r_e$, where S is the system constant for scattering from a cloud of suspended particles. The relation between S and S_w can be written as

$$S = S_w \sqrt{\frac{3}{16}\omega\kappa\tau} \tag{3.67}$$

CHAPTER 4 STANDARD TARGET MEASUREMENTS

The system sensitivity factor S is required to obtain the actual concentration from the detected voltage. The determination of the sensitivity factor S by using standard targets is used in this thesis. It should be emphasized that the standard targets are not only useful for obtaining the sensitivity factor S for each transducer in the laboratory, but also for determining S in the field.

The standard targets used in this thesis are straight stainless steel wires, which were mounted on a frame so that they can be adjusted vertically and rotated about a vertical axis to get the maximum acoustic output. The maximum signal is assumed to occur when the acoustic axis and the wire axis are orthogonal, and hence the theoretical results for a finite cylinder discussed in Section 3.3 can be immediately applied to this chapter. Four different wire radii were used, which are listed in Table 4.1, with the values of x_w at the three different frequencies. Although the wire used in the laboratory was 45 cm long, only a small segment of the wire was detected by the acoustic system because of its very narrow beamwidth. The effective detected length of the wire is expressed by Eq. (3.42), that is $L = 2r\tan\beta_m$. Typical values of ψ given by Eq. (3.52) are listed in Table 4.2.

The mathematical expression in Eq. (3.66) for the detected voltage scattered from a finite cylinder is rewritten in the following, since it forms the basis for discussion in the rest of this chapter.

Table 4.1. The radii of four stainless-steel wires used in the laboratory with the corresponding values of x_w at the three frequencies. The sound speed c is chosen to be 1482 m/s (T = 20° and zero salinity).

Radius	Value of x_w $\left(=\frac{2\pi a_w}{\lambda}\right)$		
μm	1.00 MHz	2.25 MHz	5.00 MHz
63.5	0.27	0.61	1.35
76.2	0.32	0.73	1.62
101.6	0.43	0.97	2.15
127.0	0.54	1.21	2.69

Table 4.2. Numerical values of ψ for three frequencies at different range r (T = 20° and zero salinity).

Freq.	Beamwidth		ψ $(= 2r\tan\beta_m/\sqrt{2r\lambda})$					
(MHz)	β_0	β_m	r=30 cm	40 cm	50 cm	60 cm	70 cm	80 cm
1.00	2.00	4.75	1.67	1.93	2.16	2.36	2.55	2.73
2.25	2.05	4.87	2.57	2.97	3.32	3.64	3.93	4.20
5.00	1.85	4.39	3.45	3.99	4.46	4.88	5.28	5.64

$$\bar{V}_w = S_w \frac{|\Gamma|}{\sqrt{2k_c r}} \sqrt{x_w}\, |f_w(x_w)| \tag{4.1}$$

It is obvious, from Eq. (4.1), that the sensitivity S_w can not be obtained without *a priori* knowing both $|\Gamma|$ and $|f_w(x_w)|$. Although the theoretical results for both are available based on the discussion in Section 3.3, these need to be carefully checked before using them to estimate S_w.

The form factor $|f_w(x_w)|$ in Eq. (3.31) depends on the non-dimensional radius x_w only. Therefore, measured values $|f_m(x_w)|$ can be obtained by placing wires with different radii at the same position. By doing so, the term $S_w |\Gamma| / \sqrt{2k_c r}$ in Eq. (4.1) is constant. Since x_w is known and $\bar{V}_w$ is the measured quantity, then a measured value of $|f_w(x_w)|$ can be determined for each wire from

$$|f_m(x_w)| = K_f(r) \frac{\bar{V}_w}{\sqrt{x_w}}. \tag{4.2}$$

where $K_f(r)$ a proportionality constant, which can be estimated by minimizing the difference between the measured values $|f_m(x_w)|$ and calculated values $|f_w(x_w)|$ for several different wire radii by least squares. That is, for the four wire sizes used here,

$$K_f(r) = \frac{\sum_{i=1}^{4} \sqrt{x_{w,i}}\, |f_{w,i}(x_w)|\, \bar{V}_{w,i}}{\sum_{i=1}^{4} \left[\bar{V}_{w,i}\right]^2}. \tag{4.3}$$

in which the index i denotes the different wire radii. Using this estimate of $K_f(r)$, the measured values of $|f_m(x_w)|$ can be obtained from $\bar{V}_w$ through Eq. (4.2), and are shown in Figure 4.1a at the selected range $r \approx 85.6$ cm, with calculated values of $|f_w|$ denoted by the solid line. The agreement between

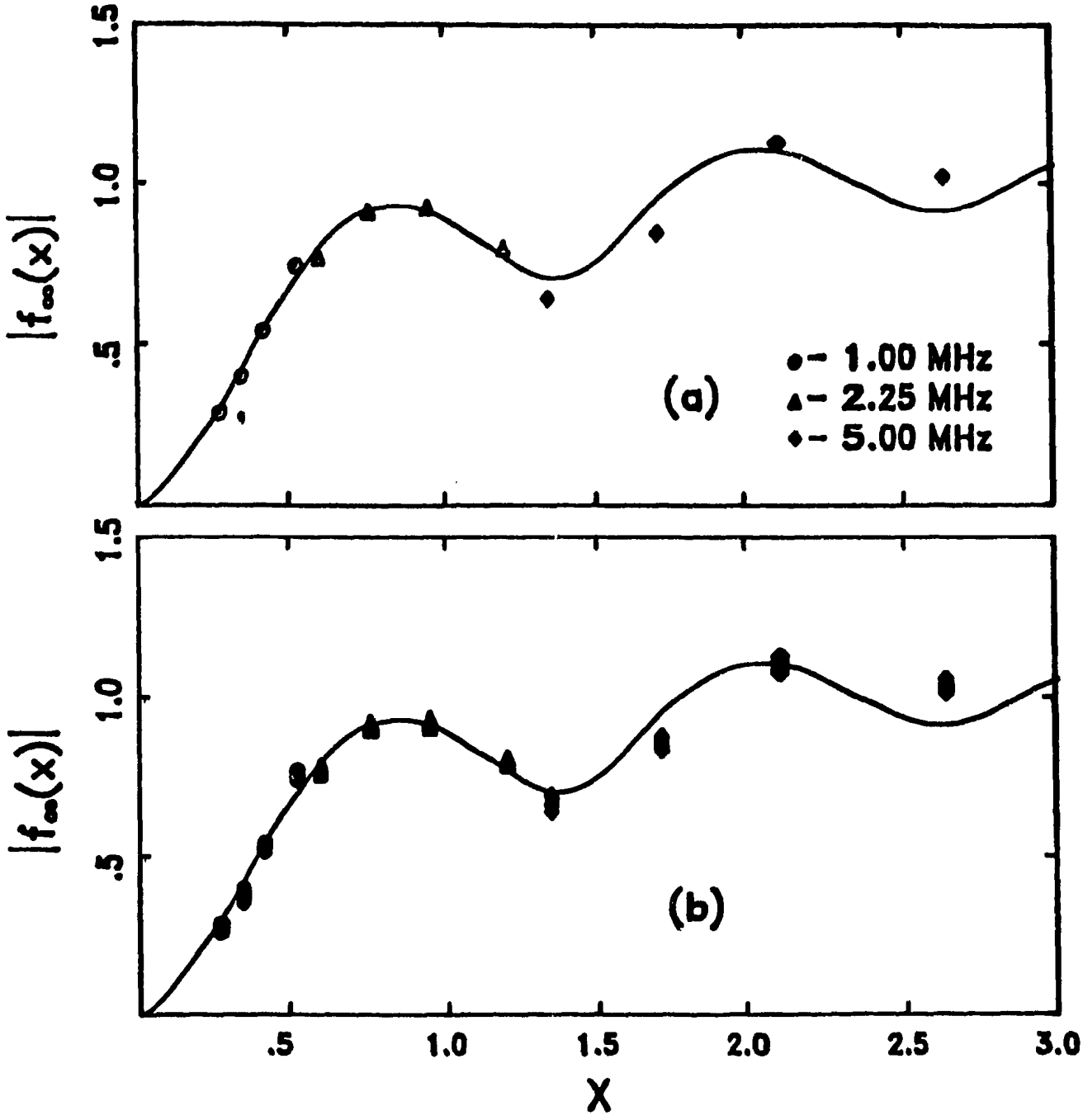

Figure 4.1. Comparison between calculated and measured values of the form factor $|f_{\infty}(x)|$ at: (a) the selected range $r \approx 86$ cm, (b) all seven positions $r \approx$ 38, 46, 54, 62, 70, 78, and 86 cm. The calculated values are denoted by the solid line.

the measured and the calculated values is quite good at all three frequencies. Some discrepancies between measured and calculated values of the form factor may be due to the difficulty of placing different wires at the exactly same position.

Table 4.3. The values of $K_f(r)$ and values of $K_f(r)/\sqrt{r}$ at seven different positions for three transducers with frequencies of 1, 2.25 and 5 MHz.

Range	$K_f(r)$ (Volts^{-1})			$K_f(r)/\sqrt{r}$ (cm$^{-1/2}$Volts^{-1})		
cm	1.00 MHz	2.25 MHz	5.00 MHz	1.00 MHz	2.25 MHz	5.00 MHz
38	0.669	1.92	7.26	1.09	3.12	11.8
46	0.692	1.97	7.81	1.02	2.91	11.5
54	0.729	2.10	8.46	0.992	2.86	11.5
62	0.753	2.16	8.82	0.956	2.74	11.2
70	0.792	2.26	9.08	0.947	2.70	10.9
78	0.830	2.39	8.48	0.940	2.70	9.62
86	0.877	2.46	9.75	0.946	2.65	10.5

It should be noted that the constant $K_f(r)$ is a function of r. Therefore, different values of $K_f(r)$ are obtained if different positions are chosen to measure the form factor by using four wires. $K_f(r)$ at seven different positions were estimated using Eq. (4.3), and are listed in Table 4.3. It can be seen, from Table 4.3, that $K_f(r)$ increases with the distance between the transducer and the position of the four wires. The values of $K_f(r)/\sqrt{r}$ at each frequency listed in Table 4.3, on the other hand, are almost constant. The measured values of the form factor made at seven positions are shown in Figure 4.1b, with the calculated results for $|f_w(a_w)|$, obtained using the elastic properties of stainless steel in Table 3.1, denoted by a solid line. Figure 4.1b shows that theoretical results for

the form factor provide a good fit to data measured at all seven positions, especially for 1 and 2.25 MHz transducers. There is some degree of scatter for the 5 MHz transducer, which may be because the 5 MHz transducer has the smallest wavelength, so that it is very sensitive to the orientation of the wires.

$K_f(r)$ is also related to the system sensitivity constant. From Eqs. (4.2) and (4.1), we have

$$S_w = \frac{\sqrt{2k_c r}}{K_f(r)\,|\Gamma|}, \tag{4.4}$$

which indicates that the variation of $K_f(r)/\sqrt{r}$ with respect to r should represent the variation of $|\Gamma|^{-1}$. It can be seen, from Table 4.3, that the maximum variation of $K_f(r)/\sqrt{r}$ in the range of 38 cm to 86 cm from the transducer is about 14%, 16% and 20% for the 1, 2.25, and 5 MHz transducers, respectively, which implies that Γ must be nearly independent of r.

The next consideration is the comparison between measured and calculated values of $|\Gamma|$. Since $|\Gamma|$ depends only on ψ, for a specific transducer different values of ψ can be achieved by changing the distance between the transducer and the wire. By placing the same wire at different ranges, since $S_w\sqrt{x_w}\,|f_w(x_w)|$ is constant now, the measured value $|\Gamma_m|$ can be written as

$$|\Gamma_m| = K_\Gamma(a_w)\sqrt{2k_c r}\,\overline{V}_w. \tag{4.5}$$

in which $K_\Gamma(a_w)$ is a proportionality constant, representing the term $1/\left[S\sqrt{x_w}\,|f_w(x_w)|\right]$ in Eq. (4.1). K_Γ can also be estimated by using the least square method, that is

$$K_\Gamma(a_w) = \frac{\sum_{j=1}^{7} |\Gamma_j\sqrt{2k_c r_j}|\,\overline{V}_{w,j}}{\sum_{j=1}^{7}\left[\sqrt{2k_c r_j}\,\overline{V}_{w,j}\right]^2}. \tag{4.6}$$

in which the index j represents the different ranges at which the wire was located from the transducer. The comparison between the measured and calculated values of $|\Gamma|$ is shown in Figure 4.2a for the selected radius $a_w = 127$ μm, in which the solid line represents the calculated results. Two conclusions can be drawn from Figure 4.2a. First, the agreement between the two is good. Secondly the value of $|\Gamma|$ approaches a constant value in the range we are interested in, which means the expression for scattered pressure tends to that for an infinite cylinder.

Table 4.4. The values of $K_\Gamma(a_w)$ calculated by Eq. (4.6) for four radii and for three transducers with frequencies of 1, 2.25 and 5 MHz.

Radius	Value of $K_\Gamma(a_w)$ (Volts^{-1})		
μm	1.00 MHz	2.25 MHz	5.00 MHz
63.5	0.0521	0.0239	0.0495
76.2	0.0333	0.0179	0.0343
101.6	0.0217	0.0160	0.0241
127.0	0.0135	0.0165	0.0229

The measured values of $|\Gamma_m|$ for all four wires are plotted in Figure 4.2b, in which $K_\Gamma(a_w)$ was obtained for each wire by using Eq. (4.6), and is listed in Table 4.4 for three transducers with frequencies of 1, 2.25 and 5 MHz. The solid line in Figure 4.2b denotes the theoretical results of $|\Gamma|$, the same as those in Figure 4.2a. It can be seen, from Figure 4.2b, that the theoretical results of $|\Gamma|$ provide a reasonable fit to the data for all four wires.

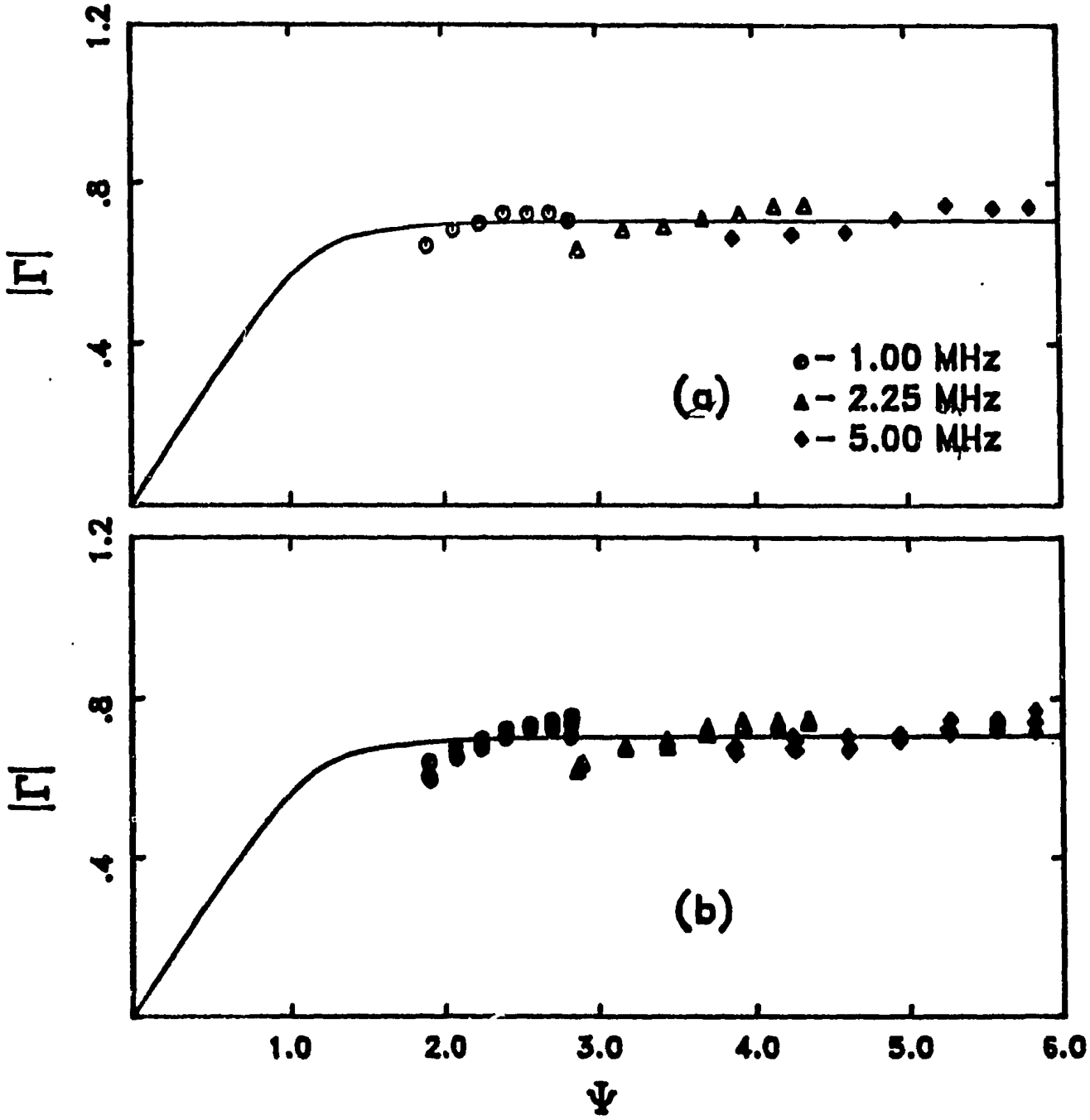

Figure 4.2. Comparison between calculated and measured $|\Gamma|$ for: (a) the wire with $a = 127$ μm, (b) all four wires with 63.5, 76.2 101.6 and 127.0 μm in radius. The calculated values of $|\Gamma|$ are denoted by the solid line.

From the above two comparisons it is clear that the calculated values of $|f_w|$ and Γ can be used for the further analysis. By using numerical values of $|f_w|$ and $|\Gamma|$, S_w for each model 810 transducer can be estimated by least squares. That is

$$S_w = \frac{\sum_{j=1}^{7}\sum_{i=1}^{4}\left[V_{ij}\,|\Gamma_j|\,\frac{\sqrt{x_i}\,|f_w(x_i)|}{\sqrt{2k_c r_j}}\right]}{\sum_{j=1}^{7}\sum_{i=1}^{4}\left[|\Gamma_j|^2\,\frac{x_i\,|f_w(x_i)|^2}{2k_c r_j}\right]}, \tag{4.7}$$

in which the indexes i and j have the same meanings as above. The estimated values of S_w are listed in Table 4.5. The sensitivity factor S for a cloud of suspended particles in water is also given, calculated from S_w using Eq. (3.71).

Table 4.5. Estimated values of S_w and S for three frequencies. The pulse duration is 20 μs, the sound speed is 1482 m/s (for T = 20° and zero salinity). The values of S from the glass bead measurements are made available from Hay [1991].

f	β_e	β_m	Wires		Glass Beads	$\frac{S(\text{wires})}{\sqrt{2}}$
(MHz)	(degree)	(degree)	S_w (Volts)	S (Volts)	S (Volts)	
1.00	2.00	4.75	128.96	12.95	9.76	9.16
2.25	2.05	4.87	69.81	10.78	7.68	7.62
5.00	1.85	4.39	26.03	5.41	4.12	3.83

Accurate error analysis for S is difficult. The value of S determined from wire measurements, however, can be validated by an independent estimate of S

using different standard targets, such as uniform lead-glass beads, which was suggested by Hay [1991], since the form factor for glass beads can be theoretically calculated due to its spherical shape [Hay and Schaafsma, 1989]. By using uniform glass beads with nine different size fractions in the laboratory, and controlling the concentration so as to be low enough (around 1 g/l at the center of the jet), the sensitivity factor S can be estimated from the siphoned concentration, the detected voltage and the calculated form factor in Eq. (3.15). The results are also listed in Table 4.5. It can be seen, from Table 4.5, that the sensitivity factors obtained from glass bead measurements are smaller than those from wire measurements for three frequencies by factor of 0.70 to 0.76, or roughly $1/\sqrt{2}$. The exact cause for this difference is unclear, although it is interesting to note that the scattered signals from wires are coherent, while signals from a cloud of particles are incoherent, and the factor $1/\sqrt{2}$ is equivalent to converting the wire signals from peak amplitudes to rms amplitudes. If dividing the sensitivity factor obtained from wire measurements by a constant $\sqrt{2}$, then S is respectively equal to 9.16, 7.62 and 3.83 for 1, 2.25 and 5 MHz, which agrees well with the sensitivity factor obtained from glass bead measurements with a relative difference less than 7%. Therefore, the sensitivity factor to be used in the rest of the thesis is that obtained from glass bead measurements or that obtained from wire measurements dividing by $\sqrt{2}$.

Backscatter measurements from wires were also made at the field site. An adjustable frame was mounted in a barrel 60 cm in diameter and 85 cm deep, which was filled with natural seawater. Wires with three different radii 63.5, 76.2, 127.0 μm were respectively mounted at the lower portion of the frame, while the acoustic transducer was located at the top of barrel and was submerged in

seawater. The distance between the transducer and the wire was about 64 cm. The water temperature in the barrel was recorded twice per day, which varied in the range of 5.8° to 12.4° C during the period of field calibration. The salinity of the seawater was 28.97 ppt. The sensitivity factor for each transducer is obtained from detected backscattered voltages by using calculated values of both $|f_w(x_w)|$ and $|\Gamma|$, and is listed in Table 4.6, in which the estimated value S_w obtained in the laboratory (see Table 4.5) is also tabulated for purpose of comparison. The differences between the values of S_w obtained in the laboratory and the averaged values obtained in the field is about 15%, 14% and 21% for 1, 2.25, and 5 MHz, respectively. This is not too large, and the sensitivity factor S_w for each transducer, therefore, can be considered invariant.

No comparison is made between measured and calculated values of $|\Gamma|$ due to the fact that backscatter measurements from wires in the field were made only at a single range. Measured values of the form factor $|f_w(x_w)|$ for all field calibration data are shown in Figure 4.3a by using the estimated value of sensitivity factor obtained in the field site and calculated values of $|\Gamma|$. The solid line in Figure 4.3a denotes calculated results of $|f_w(x_w)|$, as in Figure 4.1. It can be seen, from Figure 4.3a, that the agreement between measured and calculated values is reasonably good for $x_w \leq 1$. For $x_w > 1$, however, differences between measured and theoretical values are greater for larger value of x with the maximum difference of 45% at $x = 2.69$. These large differences could be attributed to temperature variations during the experiment, or to bubble formation on the wire or on the transducer. The latter is thought to be the most likely possibility, since bubble formation was a problem.

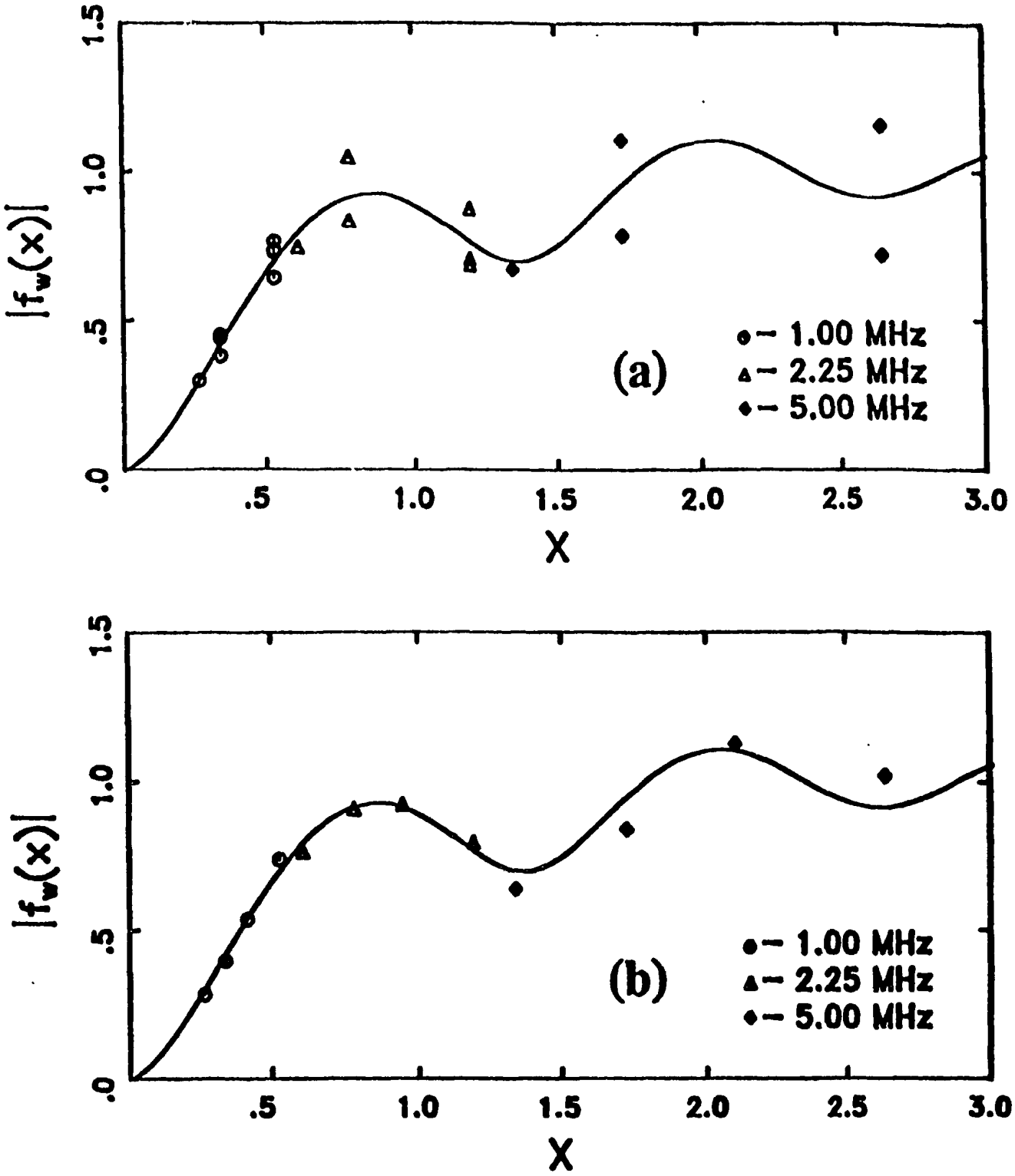

Figure 4.3. Comparison between calculated and measured values of the form factor $|f_w(x_w)|$ for: (a) all field calibration data, water temperature varied from 5.8 to 12.4° C; (b) selected field calibration data collected on the same day with roughly constant water temperature of 5.8° C. The solid line denotes the calculated values of $|f_w(x_w)|$.

Table 4.6. Estimated values of S_w from all field calibration data, in which the seawater temperature varied from 5.8° C to 12.4°, and the salinity is about 28.97 ppt. The values in the parentheses are those from selected field calibration data collected in the same day with water temperature of 5.8° C.

f	β_o	β_m	Values of S_w (Volts)			Variation	
(MHz)	(degree)	(degree)	Laboratory	Field Site		(%)	
1.00	2.00	4.75	128.96	148.81	(153.08)	15	(19)
2.25	2.05	4.87	69.81	59.93	(65.53)	14	(6)
5.00	1.85	4.39	26.03	31.44	(36.75)	21	(41)

Figure 4.3b shows the comparison between selected measured values and calculated results of the form factor, in which the measured data were those collected on the same day with the roughly constant water temperature of about 5.8° C. The sensitivity factors obtained from these data points are also listed in Table 4.6. It can be seen, from Figure 4.3b, that measured data fit reasonably well to calculated results for all x. The variation of S_w by using these selected data comparing with S_w estimated in the laboratory, however, is 40% for 5 MHz (Table 4.6), which is very large, although the variation is 19% and 6% for 1 and 2.25 MHz transducers, respectively, is comparable to those in Figure 4.3a. As has been mentioned, this large variation for the 5 MHz transducer could result from bubbles.

CHAPTER 5 SCATTERING CHARACTERISTICS OF NATURAL SAND PARTICLES

Natural sediment particles are irregular in shape. This makes it difficult to obtain theoretical values of $|f_\infty(x)|$, which are, however, required in order to extract both the suspended particle concentration and the size from multi-frequency acoustic signals through Eq. (3.15). This means that $|f_\infty(x)|$ must be based upon measurements. If the size distribution of sediments conforms to some standard distribution, then $F(n(a), |f_\infty(x)|)$ for natural sand particles can be constructed by using a semi-empirical expression for the form factor. In this chapter we obtain a semi-empirical form for $|f_\infty(x)|$ for suspended sand particles. The Chapter begins with a review of the analytical representation for the size distribution of sand particles.

5.1 Log-Normal Size Distribution of Sediment Particles

It is generally found that most natural sediments conform to a log-normal size distribution [e.g., Hatch and Choate, 1929; Einstein, 1944; Chow, 1954; Flammer, 1962]. Accordingly, the size distribution of the natural sediment particles will be expressed by

$$n(a)da = \frac{1}{\sqrt{2\pi}\ln\sigma_g}\exp\left[-\frac{(\ln a - \ln a_g)^2}{2\ln^2\sigma_g}\right]d(\ln a), \tag{5.1}$$

where a_g and σ_g are, respectively, the geometric mean radius and the geometric standard deviation.

The sand from Stanhope Lane Beach was sieved into different size classes,

and the sand in each class was weighed to obtain the fraction of total sample weight, which represents $n(a)da \approx n(a)\Delta a$. The measured values of the size spectral density function, then, can be found by dividing the fraction in each class by Δa, and they are plotted in Figure 5.1, in which solid lines represent the log-normal distributions with $a_g = 79$ μm and $\sigma_g = 1.1, 1.25, 1.5$. The probability function in Figure 5.1 is defined as

$$\text{Probability } (a' < a) = \int_{\bullet}^{a} n(a')da' \tag{5.2}$$

It can be seen, from Figure 5.1, that the log-normal distribution with $a_g = 79$ μm and $\sigma_g = 1.25$ provides a reasonably good fit to the data for both the density function $n(a)$ and the probability function, and the asymmetrical property of the natural sand particles is well represented by the analytical distribution. The curves with $\sigma_g = 1.1$ and 1.5 in Figure 5.1, which fit the data the least well, on the other hand, are used to demonstrate the effect of the geometric standard deviation σ_g on the fit. The appropriateness of the log-normal distribution to natural sediments is also validated by testing the two other beach sands used in the laboratory experiments, and included in Table 5.1, in which the values of a_g and σ_g are again those used to obtain the best visual fit.

Table 5.1. Values of a_g and σ_g, which are used to obtain the best visual fit to three different beach sands by the log-normal distribution. The bandwidth was calculated by $a_{84}-a_{16}$, where a_{16} and a_{84} represent the radius of the 16th and 84th of cumulative percentile of the log-normal distribution, respectively.

Source of Sand		a_g (μm)	σ_g	Bandwidth (μm)
Bluewater Beach, Ont.	(BWB)	68	1.30	36
Stanhope Beach, PEI	(SHB)	79	1.25	35
Queensland Beach, N.S.	(QLB)	175	1.35	42

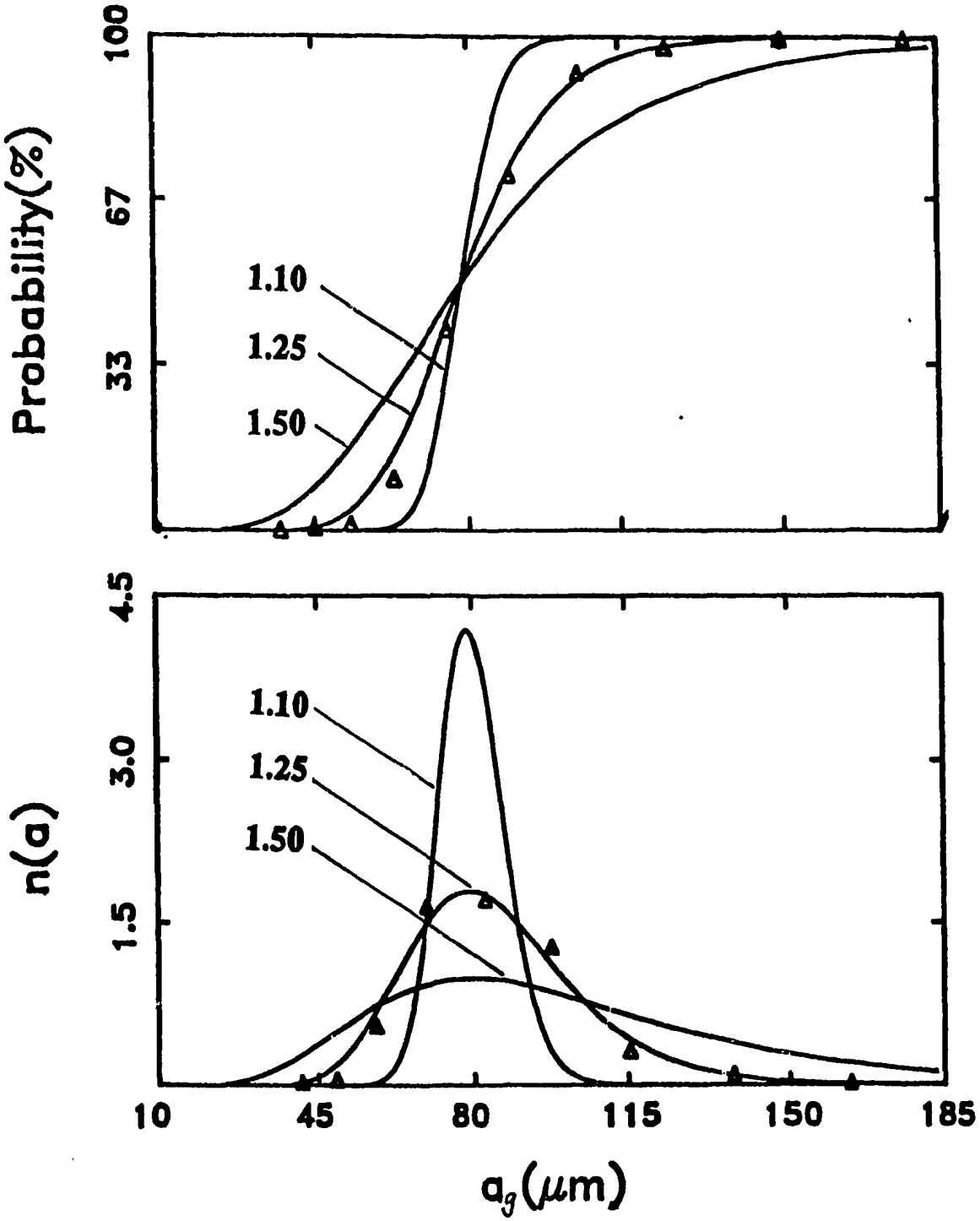

Figure 5.1. Comparison between the sieved size distribution and the log-normal distribution for Stanhope Beach sand. The symbols are measurements made by wire-mesh sieves. Solid lines represent the log-normal distributions with $a_g = 79$ μm and $\sigma_g = 1.1, 1.25, 1.5$, as indicated.

Table 5.2. Sieved size fractions and corresponding values of x. d is the mean grain size in diameter. The sound speed c = 1482 m/s (for T = 20° and zero salinity).

Size fraction	d	$x \left(=\frac{\pi d}{\lambda}\right)$		
μm	μm	1.00 MHz	2.25 MHz	5.00 MHz
90.0 - 106.0	98.0	0.21	0.47	1.04
106.0 - 125.0	115.5	0.24	0.55	1.22
125.0 - 150.0	137.5	0.29	0.66	1.46
150.0 - 180.0	165.0	0.35	0.79	1.75
180.0 - 212.0	196.0	0.42	0.94	2.08
212.0 - 250.0	231.0	0.49	1.10	2.45
250.0 - 300.0	275.0	0.58	1.31	2.92
300.0 - 355.0	327.5	0.69	1.56	3.47
355.0 - 425.0	390.0	0.83	1.86	4.13
425.0 - 500.0	462.5	0.98	2.21	4.90

The measured form factor for uniformly-sized sand particles ($|f_\infty(x)|$), which was estimated from detected voltages, centerline concentrations, and the sensitivity factor for each transducer (Table 4.2) through Eq. (5.4), are plotted in Figure 5.2, where the error bars are ± standard error. Theoretical results of the form factor for a rigid spherical scatterer are also shown in Figure 5.2, in which the solid line is the results for a rigid sphere with the same grain density as quartz and the dashed line is the results for a rigid sphere of infinite density. Figure 5.2 indicates that results given by theory for a rigid movable (finite density) sphere compare well with the measured form factor for sand particles $|f_\infty(x)|$ in the range $x \sim 1$, while the results for a rigid immovable (infinitely dense) sphere fits the data the least well in the same region ($x \sim 1$). In the region of

5.2 Backscatter Measurements from Uniform Sand

Backscatter measurements as a function of particle size were made for natural sand in the water tank (Figure 2.3) at one particle concentration for each size fraction. A total of ten size fractions were used, and the size of particles in each fraction is assumed to be uniform and represented by the midpoint of the corresponding sieve interval. The ten size fractions are listed in Table 5.2 with the corresponding values of $x = k_c a$ for all three frequencies. Based on Eq. (3.15), the detected voltage at the centerline of the jet can be expressed by

$$\overline{V}_o = S \sqrt{\frac{M_o}{\rho_o'}} \frac{|f_\infty(x)|}{\sqrt{x}} \sqrt{\frac{\sinh\zeta}{\zeta}} \exp\left[-2\int_o^{r_o} \alpha_s \, dr\right], \tag{5.3}$$

in which $\overline{V}_o$ and M_o denote values at the centerline of the jet, and $F\left(n(a), |f_\infty(x)|\right)$ has been replaced by $\dfrac{|f_\infty(x)|}{\sqrt{x}}$ due to the unform size distribution (see Eq. (3.16)), where $|f_\infty(x)|$ is the form factor for uniformly-sized sand particles.

Since centerline concentrations were kept small, the corrections for both α_s and $\sqrt{\dfrac{\sinh\zeta}{\zeta}}$ can be neglected. Eq. (5.2) becomes

$$\overline{V}_o = S \sqrt{\frac{M_o}{\rho_o'}} \frac{|f_\infty(x)|}{\sqrt{x}}. \tag{5.4}$$

The measured form factor for the sand particles can be written as

$$|f_\infty(x)| = \frac{\sqrt{x}\,\overline{V}_o}{S\sqrt{M_o/\rho_o'}}. \tag{5.5}$$

$x \leq 1$ the shape irregularities of sand particles do not have significant effects on the scattering cross section, but the grain density of sand particles could be important, which is consistent with our previous finding [Sheng and Hay, 1988] for attenuation cross sections. For the region of $x > 2$, theoretical results both for a rigid movable sphere and for a rigid immovable sphere fit data badly, and a rigid immovable sphere once again provides the worst fit to measured values. It also appears that for $x > 2$ the measured form factor of uniformly-sized sand particles is smoother and greater than those given by theory (Figure 5.2), both of which may be due to grain shape irregularities [Sheng and Hay, 1988; Hay, 1991].

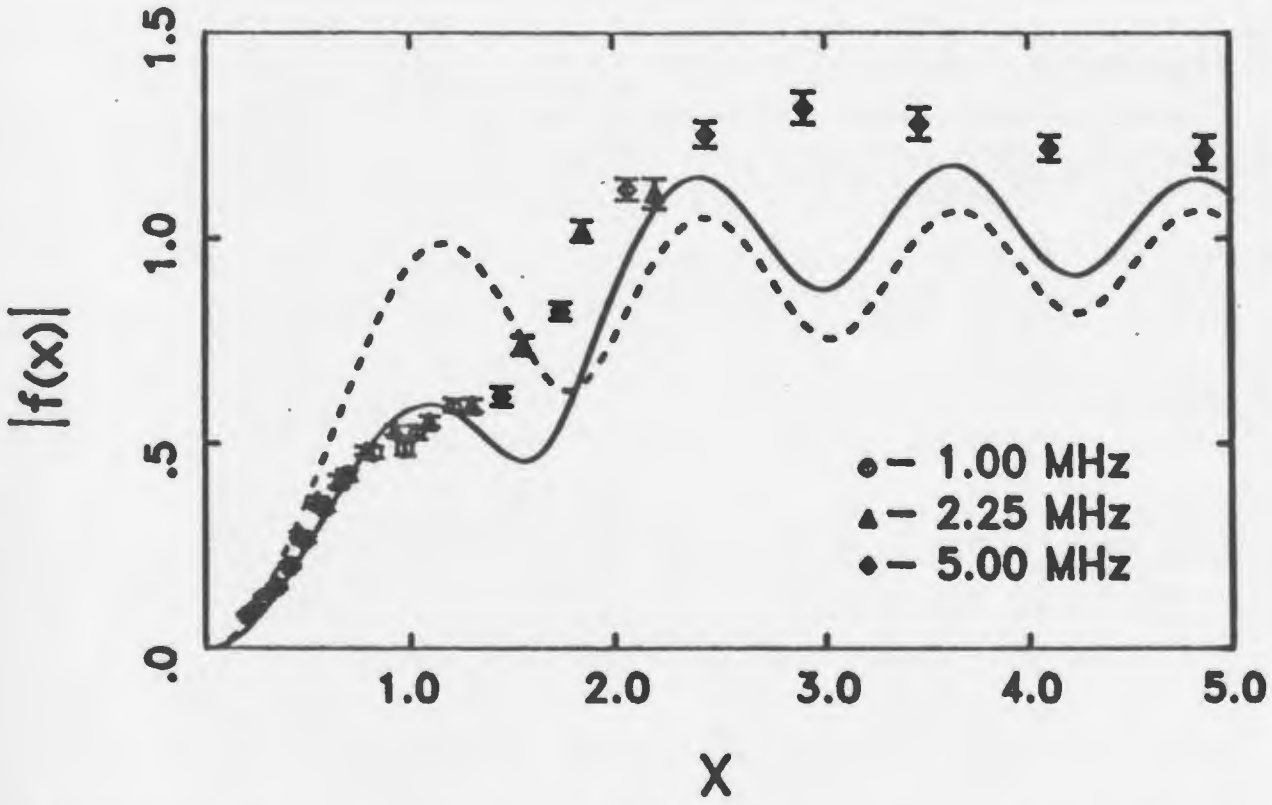

Figure 5.2. The measured values of $|f_{\infty}(x)|$ for uniformly-sized sand particles in water. The solid line is the theoretical results for a rigid sphere with the same density as quartz, and the dashed line is the theoretical results for a rigid sphere of infinite density.

5.3 Semi-Empirical Expression for $|f_{\infty}(x)|$

In order to designate a semi-empirical expression for the form factor of sand particles from theoretical results for a rigid movable sphere, it is desirable to smooth out the oscillations appearing on the theoretical results shown in Figure 5.2, and to remove the difference between measured values and smoothed theoretical results in the region of $x > 2$. The above two tasks are accomplished by the expression

$$|f_{\infty}(x)| = \frac{1+1.25x^4}{1+x^4}\left[\frac{a\int_0^{\infty} a'^2 |f_{\infty,\text{rigid}}|^2 n(a',\sigma_g=1.2)da'}{\int_0^{\infty} a'^3 n(a',\sigma_g=1.2]da')}\right]_{a_r=a}^{1/2}, \quad (5.6)$$

where $n(a',\sigma_g=1.2)$ is the log-normal distribution with $\sigma_g=1.2$, and $|f_{\infty,\text{rigid}}|$ is the form factor for a non-resonant spherical scatterer, of which the calculated values were shown in Figure 3.2. Eq. (5.6) physically means that the acoustic scattering characteristics of uniform natural sand particles are approximated by those for nonuniform rigid movable spheres with $\sigma_g = 1.2$ in the region of $x < 1$. For $x > 1$, the form factor of uniform sand particles, however, is 1.25 times larger than that for the nonuniform movable spheres with $\sigma_g = 1.2$.

An alternative way to explain the expression given by Eq. (5.6) is to separate the term on its right hand side into two parts, the first part is the multiplication factor $(1+1.25x^4)/(1+x^4)$, and the second part is inside the square brackets. The computing results of the second part are shown in Figure 5.3a by a solid line,

from which it can be seen that the oscillations appearing on theoretical results have been completely smeared out. The smoothed results fit data quite well for $x<1$ and even in the vicinity of $x=1$, but they are smaller than measured values for $x>1$ by a nearly constant multiplication factor 1.25. It is clear, therefore, that the first part of Eq. (5.6) is designed to remove this nearly constant multiplication factor in the region of $x>1$, but not to substantially affect the smoothed results in the region of $x \leq 1$, which is the reason why the fourth power is used in the first part. The computing results of the whole expression of Eq. (5.6) are shown in Figure 5.3b by the solid line. It can be seen that the expression given by Eq. (5.6) gives a reasonable fit to data in the whole region $0<x \leq 5$, although it slightly overestimates measured values around $x=1$.

It can now be concluded that the explicit form of $|f_\infty(x)|$ given in Eq. (5.5) and the log-normal size distribution given by Eq. (5.1), therefore, can be employed to calculate $F(n(a), |f_\infty(x)|)$ for natural sand with various size distributions.

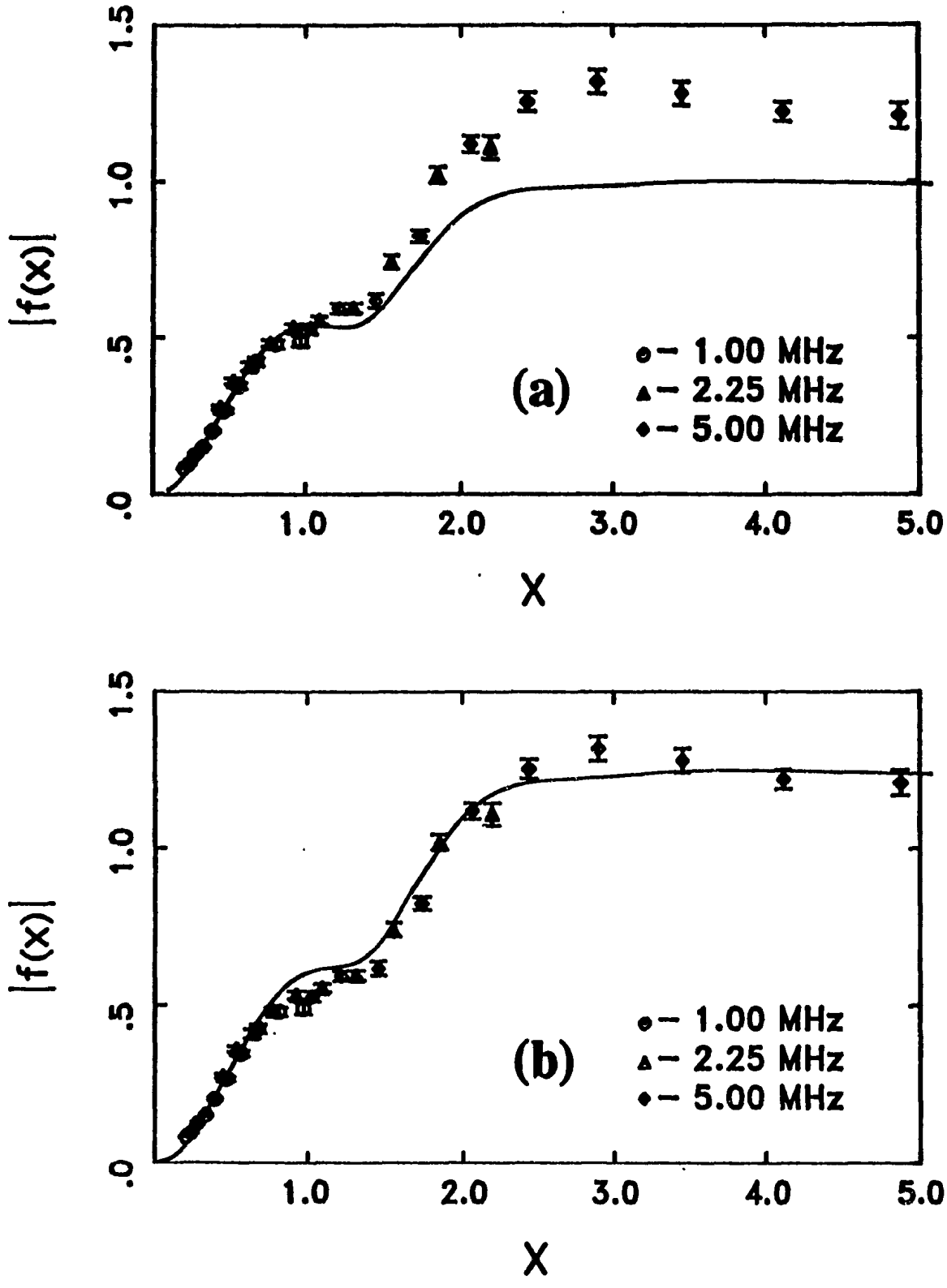

Figure 5.3. The measured form factor of uniform sand particles in water with the fitting function of: (a) the term inside the square brackets in Eq. (5.6); (b) the complete expression in Eq. (5.6).

CHAPTER 6 INVERSION METHODS FOR DATA ANALYSIS

After knowing the sensitivity factor S and the semi-empirical form of the form factor for the sand particles, both the suspension concentration and the particle size can, in principle, be extracted from multi-frequency acoustic signals through Eq. (3.15). In this chapter, we present the inversion methods in detail which will be used for the RASTRAN data analysis. In this chapter the procedure used to correct the scattering attenuation is also considered.

6.1 Estimating Size and Concentration

For the moment, assuming the scattering attenuation has been completely corrected for, or is small, the scattered signal for the three modules in the same range bin, based on Eq. (3.15), can be expressed by

$$\begin{cases} \overline{V}_1 = S_1 \sqrt{\dfrac{M}{\rho_s}} F\left(n(a), |f_\infty(x_1)|\right) \\ \overline{V}_2 = S_2 \sqrt{\dfrac{M}{\rho_s}} F\left(n(a), |f_\infty(x_2)|\right) \\ \overline{V}_5 = S_5 \sqrt{\dfrac{M}{\rho_s}} F\left(n(a), |f_\infty(x_5)|\right) \end{cases}, \tag{6.1}$$

where the subscripts 1, 2 and 5 represent the frequency of each sounder (1, 2.25 or 5 MHz). For a log-normal particle size distribution, the function $F\left(n(a), |f_\infty(x_i)|\right)$ is a function of a_g, σ_g and $k_{c,i}$, where $i=1,2,5$. Let $X_i = k_{c,i}\, a_g$, then

$$F(X_i,\sigma_g) \equiv F\left(n(a), |f_\infty(z_i)|\right) =$$

$$= k_{c,i}^{-1/2}\left[\frac{\int_0^\infty a^2 |f_\infty(z_i)|^2 \exp\left[-\frac{(\ln a-\ln a_g)^2}{2\ln^2\sigma_g}\right] d\ln a}{\int_0^\infty a^3 \exp\left[-\frac{(\ln a-\ln a_g)^2}{2\ln^2\sigma_g}\right] d\ln a}\right]^{1/2} \tag{6.2}$$

by using Eqs. (3.14) and (5.1). Based on the assumption of homogeneity in the detected volume made in Chapter 3, both M and a_g in Eq. (6.1) are constant in each range bin. By forming the three ratios from Eq. (6.1)

$$\begin{cases} \dfrac{F(X_2,\sigma_g)}{F(X_1,\sigma_g)} = \dfrac{S_1}{S_2}\dfrac{\bar{V}_2}{\bar{V}_1} \\ \dfrac{F(X_5,\sigma_g)}{F(X_1,\sigma_g)} = \dfrac{S_1}{S_5}\dfrac{\bar{V}_5}{\bar{V}_1} \\ \dfrac{F(X_5,\sigma_g)}{F(X_2,\sigma_g)} = \dfrac{S_2}{S_5}\dfrac{\bar{V}_5}{\bar{V}_2} \end{cases}, \tag{6.3}$$

we eliminate M. Eq. (6.3) can be used to estimate the size distribution parameters a_g and σ_g of suspended sediment, as we shall now explain. The measured F-ratios in each range bin can be enumerated from the detected voltages through Eq. (6.3). At the same time, the theoretical ratios can be calculated by using the semi-empirical expression for $|f_\infty(z)|$ and the log-normal distribution. From Eq. (6.2), we have

$$\frac{F(X_i,\sigma_g)}{F(X_j,\sigma_g)} = \frac{k_{c,j}^{1/2}}{k_{c,i}^{1/2}}\left[\frac{\int_0^\infty a^2 |f_\infty(z_i)|^2 \exp\left[-\frac{(\ln a-\ln a_g)^2}{2\ln^2\sigma_g}\right] d\ln a}{\int_0^\infty a^2 |f_\infty(z_j)|^2 \exp\left[-\frac{(\ln a-\ln a_g)^2}{2\ln^2\sigma_g}\right] d\ln a}\right]^{1/2} \quad (i \neq j). \tag{6.4}$$

The theoretical values of the three ratios with different σ_g are plotted in Figure

6.1 as a function of a_g. The range of a_g chosen for the computations was 5 to 180 μm, the corresponding range of x is: 0.02 to 0.76 for 1 MHz; 0.04 to 1.72 for 2.25 MHz; and 0.08 to 3.82 for 5 MHz. Figure 6.1 exhibits the tendency for the theoretical ratios with different σ_g to converge to a limiting value when $a_g \to 0$ and an asymptotic value for $a_g \to \infty$. These values can be estimated analytically using the asymptotic values of the form factor for $x \to 0$ and $x \to \infty$.

For $x \ll 1$, the Rayleigh or long wavelength range, $| f_\infty(x) |$ can be written as [Rayleigh 1945, p.283]

$$| f_\infty(x) | \approx Gx^2 \equiv Gk_c^2 a^2 \qquad (\text{for } x \ll 1), \tag{6.5}$$

where G is a constant, independent of x and independent of grain shape. By substituting Eq. (6.5) into Eq. (6.4), we have

$$\frac{F(X_i,\sigma_g)}{F(X_j,\sigma_g)} = \left(\frac{k_{c,i}}{k_{c,j}}\right)^{3/2} \qquad (\text{for } a_g \ll k_{c,i}^{-1} \text{ and } i \neq j), \tag{6.6}$$

which indicates that the F-ratio is only a function of k_c and independent of a_g and σ_g in the case of $a_g \ll k_{c,i}$ (or $x \ll 1$). To check the numerical results of $F(X,\sigma_g)$ for $x \ll 1$ depicted in Figure 6.1, let us estimate three F-ratios through Eq. (6.6). It follows that

$$\begin{cases} \dfrac{F(X_2,\sigma_g)}{F(X_1,\sigma_g)} \approx \left(\dfrac{k_{c,2}}{k_{c,1}}\right)^{3/2} = \left(\dfrac{2.25}{1.0}\right)^{3/2} = 3.38 \\ \dfrac{F(X_5,\sigma_g)}{F(X_1,\sigma_g)} \approx \left(\dfrac{k_{c,5}}{k_{c,1}}\right)^{3/2} = \left(\dfrac{5.0}{1.0}\right)^{3/2} = 11.18 \qquad (\text{for } a_g \ll k_c^{-1}). \\ \dfrac{F(X_5,\sigma_g)}{F(X_2,\sigma_g)} \approx \left(\dfrac{k_{c,5}}{k_{c,2}}\right)^{3/2} = \left(\dfrac{5.0}{2.25}\right)^{3/2} = 3.31 \end{cases} \tag{6.7}$$

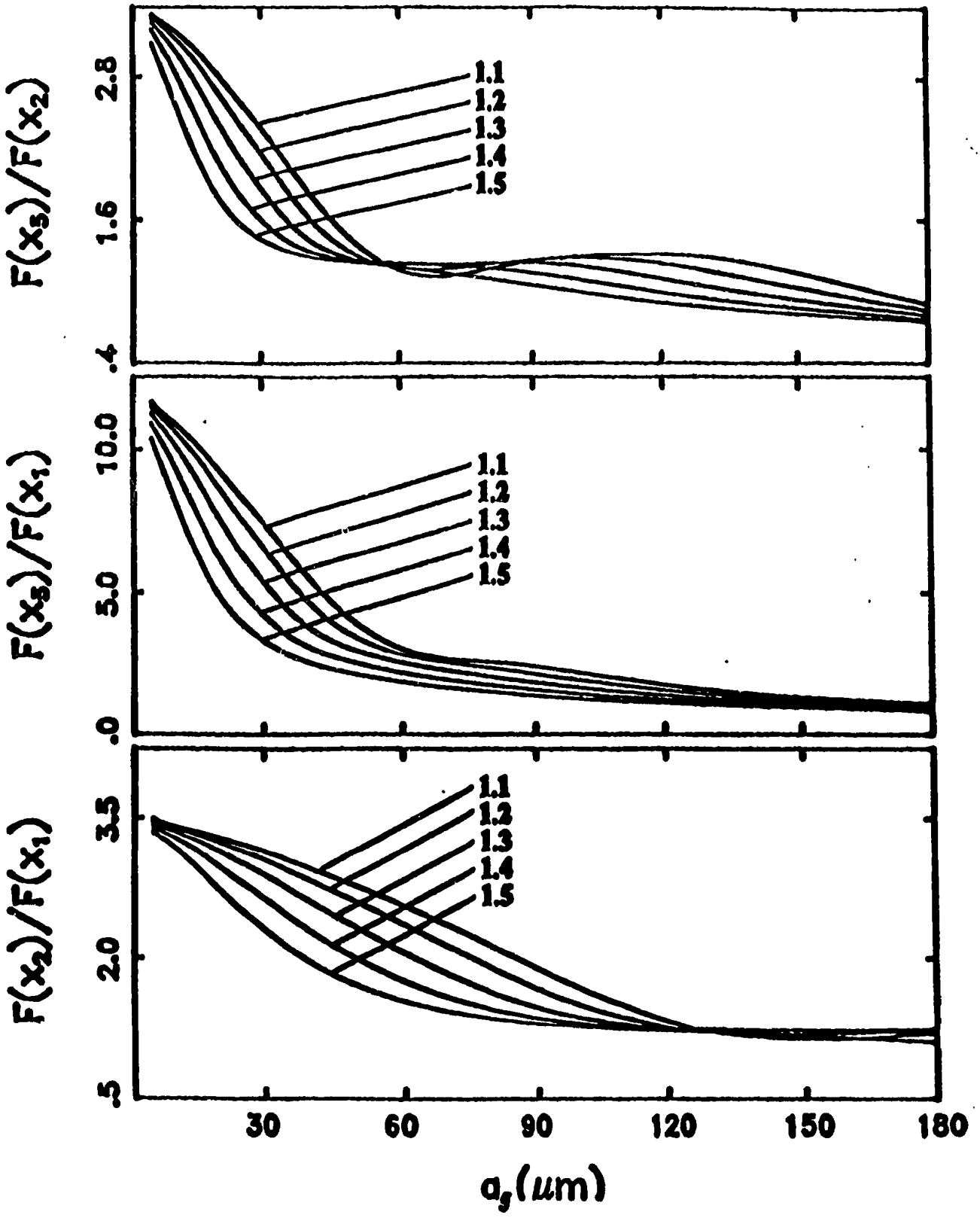

Figure 6.1. The theoretical ratios of $F(X_5,\sigma_g)/F(X_2,\sigma_g)$, $F(X_5,\sigma_g)/F(X_1,\sigma_g)$ and $F(X_2,\sigma_g)/F(X_1,\sigma_g)$, for $\sigma_g = 1.1$, 1.2, 1.3, 1.4, and 1.5, as indicated.

It is difficult to estimate accurately the limiting value for $a_g \to 0$ from Figure 6.1, due to large variations of the calculated ratios at the smallest a_g ($\sim 4\mu$m), specifically for $F(X_5,\sigma_g)/F(X_1,\sigma_g)$ and $F(X_5,\sigma_g)/F(X_2,\sigma_g)$. However, by choosing the mean value of the ratios with different σ_g at $a_g \sim 4$ μm, the limiting values estimated from the diagram are about 3.4 for $F(X_2,\sigma_g)/F(X_1,\sigma_g)$, 11.0 for $F(X_5,\sigma_g)/F(X_1,\sigma_g)$, and 3.2 for $F(X_5,\sigma_g)/F(X_2,\sigma_g)$, which, it can be seen, agree well with the numerical values (relative error less than 3%).

On the other hand, the asymptotic values of the ratios can also be obtained by using the approximation for the form factor for $x \to \infty$. From experimental results shown in Figure 5.3, it can be seen

$$|f_\infty(x)| \approx 1.25 \qquad (\text{for } x \gg 1), \tag{6.8}$$

By substituting Eq. (6.8) into Eq. (6.4), we have

$$\frac{F(X_i,\sigma_g)}{F(X_j,\sigma_g)} = \left(\frac{k_{c,j}}{k_{c,i}}\right)^{1/2} \qquad (\text{for } a_g \gg k_{c,i}^{-1} \text{ and } i \neq j), \tag{6.9}$$

which indicates that the F-ratio is independent of a_g and σ_g in the case of $a_g \gg k_c^{-1}$ (or $x \gg 1$). The three F-ratios for $x \gg 1$ can be approximated through Eq. (6.9) by

$$\begin{cases} \dfrac{F(X_2,\sigma_g)}{F(X_1,\sigma_g)} \approx \left(\dfrac{k_{c,1}}{k_{c,2}}\right)^{1/2} = \sqrt{\dfrac{1.0}{2.25}} = 0.67 \\ \dfrac{F(X_5,\sigma_g)}{F(X_1,\sigma_g)} \approx \left(\dfrac{k_{c,1}}{k_{c,5}}\right)^{1/2} = \sqrt{\dfrac{1.0}{5.0}} = 0.45 \quad (\text{for } a_g \gg k_c^{-1}). \\ \dfrac{F(X_5,\sigma_g)}{F(X_2,\sigma_g)} \approx \left(\dfrac{k_{c,2}}{k_{c,5}}\right)^{1/2} = \sqrt{\dfrac{2.25}{5.0}} = 0.67 \end{cases} \tag{6.10}$$

Figure 6.1 illustrates the tendency toward these calculated ratios as $a_g \rightarrow \infty$.

In this thesis we do not consider very fine sand with $a_g < 40$ μm, therefore, the theoretical ratios in Figure 6.1 are replotted in Figure 6.2 in the new range of a_g: 40 μm $\leq a_g \leq$ 180 μm. Conceptually, by matching the measured ratios with the calculated ratios given in Figure 6.2, a_g and σ_g in each range bin can be resolved.

Before presenting the detailed numerical procedure for the data inversion, the diagram in Figure 6.2 needs more careful examination. For $a_g > 100$ μm, the slope of $F(X_2,\sigma_g)/F(X_1,\sigma_g)$ tends to zero, and as a result, any small errors associated with the measured values of $F(X_2,\sigma_g)/F(X_1,\sigma_g)$ can bring about larger errors for the estimated values of a_g and σ_g. For $a_g < 100$ μm, on the other hand, a_g is a multi-valued function of $F(X_5,\sigma_g)/F(X_2,\sigma_g)$, which makes the numerical procedure more complicated.

It is clear that there are two linearly-independent ratios, which can be used to estimate parameters of the size distribution. Depending on the mean size and the standard deviation, they are: $F(X_2,\sigma_g)/F(X_1,\sigma_g)$ and $F(X_5,\sigma_g)/F(X_1,\sigma_g)$ for $a_g \leq 100$ μm, and $F(X_5,\sigma_g)/F(X_1,\sigma_g)$ and $F(X_5,\sigma_g)/F(X_2,\sigma_g)$ for $a_g > 100$ μm. A procedure for estimating a_g and σ_g from the measured and calculated values of F-ratios was tried as follows. In each range bin, five different values of a_g corresponding to five different σ_g curves in Figure 6.2 were obtained using the measured value of $F(X_5,\sigma_g)/F(X_1,\sigma_g)$. Similarly, a second set of five values of a_g with corresponding σ_g were obtained from Figure 6.2 by using $F(X_2,\sigma_g)/F(X_1,\sigma_g)$ if $\bar{a}_g < 100$ μm, or using $F(X_5,\sigma_g)/F(X_2,\sigma_g)$ if $\bar{a}_g > 100$ μm where $\bar{a}_g$ is the mean of five values of a_g obtained from the

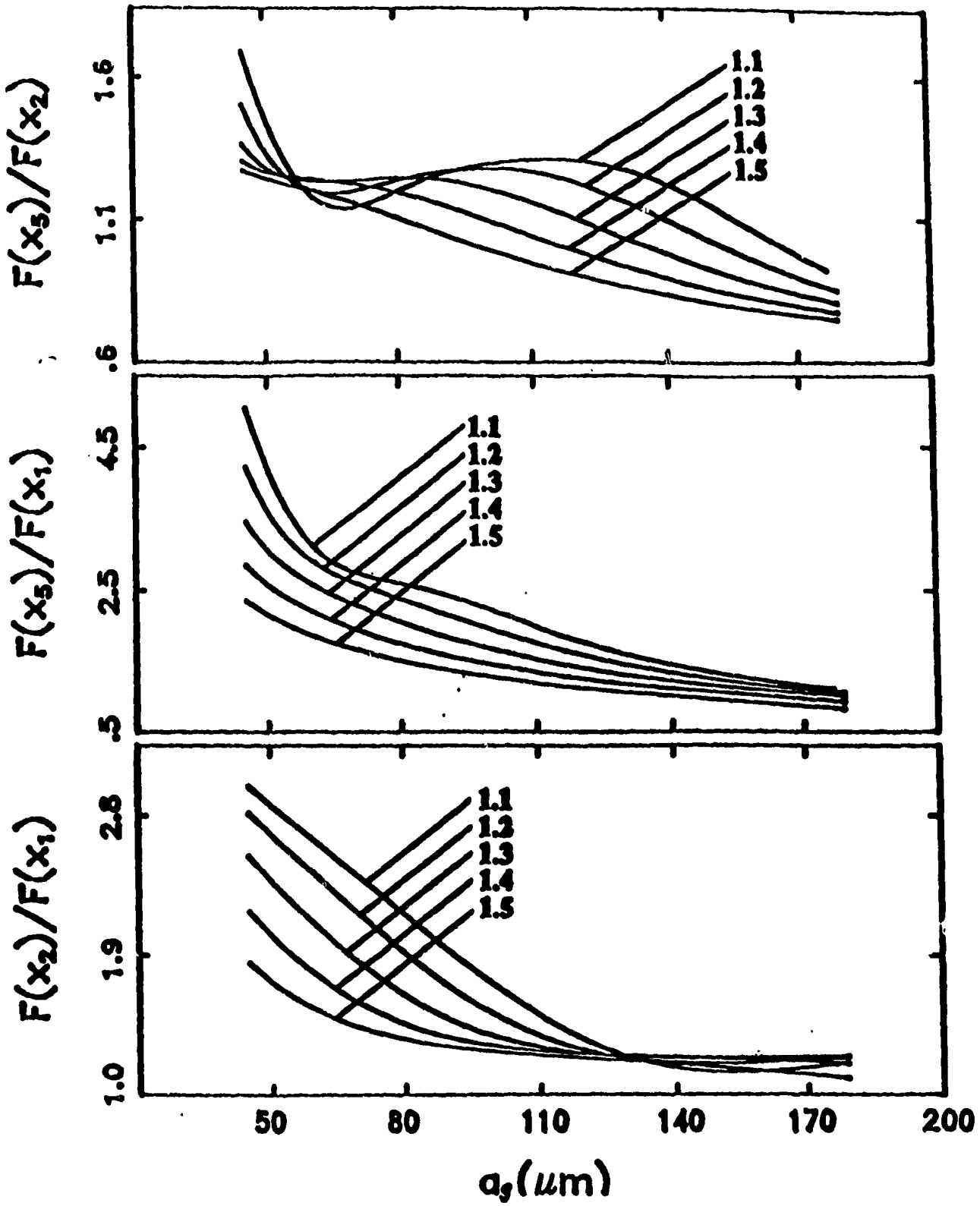

Figure 6.2. The theoretical ratios of $F(X_3,\sigma_g)/F(X_2,\sigma_g)$, $F(X_3,\sigma_g)/F(X_1,\sigma_g)$, and $F(X_2,\sigma_g)/F(X_1,\sigma_g)$ for $\sigma_g = 1.1$, 1.2, 1.3, 1.4, and 1.5, as indicated. Data are same as those in Figure 6.1 but with 40 μm $\leq a_g \leq$ 180 μm.

$F(X_5,\sigma_g)/F(X_1,\sigma_g)$ case. By plotting these two sets of values on the same a_g versus σ_g diagram, the estimated values of a_g and σ_g were taken to be those at the intersection point of the two curves. It was found, however, that there was no intersection point in some range bins, or there was an intersection point, but estimated values of a_g and σ_g from the intersection point were not reasonable. Consequently, the value of σ_g in our numerical algorithm is assumed to be given, which is the biggest disadvantage in the present inversion method.

According to the above discussion, we have the following procedure to estimate a_g:

1. For a given value of σ_g, a rough estimate of $a_g^{'}$ can be obtained from matching the measured value of $F(X_5,\sigma_g)/F(X_1,\sigma_g)$ to its calculated value;
2. If $a_g^{'} \leq 100\ \mu$m, another estimate of radius $a_g^{''}$ can be obtained by matching the measured value of $F(X_2,\sigma_g)/F(X_1,\sigma_g)$ to its calculated value;
3. If $a_g^{'} > 100\ \mu$m, $a_g^{''}$ can be estimated by matching the measured value of $F(X_5,\sigma_g)/F(X_2,\sigma_g)$ to its calculated value;
4. The final estimate of a_g is obtained by averaging $a_g^{'}$ and $a_g^{''}$.

After evaluating a_g, the next step is to find the particle concentration M in the same range bin through Eq. (6.1). The particle concentration M, based on Eq. (6.1), can be expressed in terms of the detected voltage and $F(X,\sigma_g)$; that is

$$M = \rho_w' \left[\frac{V}{SF(X,\sigma_g)}\right]^2, \tag{6.11}$$

in which $F(X,\sigma_g)$ is the calculated value using Eq. (6.2). Based on the characteristics of $F(X,\sigma_g)$ in Figure 6.2, the particle concentration in each range bin

can be estimated by

$$M = \begin{cases} \dfrac{\rho_o'}{2}\left[\dfrac{\bar{V}_1^2}{S_1^2 F(X_1,\sigma_g)} + \dfrac{\bar{V}_2^2}{S_2^2 F(X_2,\sigma_g)}\right] & (\text{for } a_g \leq 100\mu\text{m}) \\ \dfrac{\rho_o'}{2}\left[\dfrac{\bar{V}_2^2}{S_2^2 F(X_2,\sigma_g)} + \dfrac{\bar{V}_5^2}{S_5^2 F(X_5,\sigma_g)}\right] & (\text{for } a_g > 100\mu\text{m}) \end{cases} \tag{6.12}$$

6.2 Corrections for Attenuation due to Scattering

The terms $\exp[-4\int_o^r \bar{\alpha}_s\, dr]$ and $\sinh\varsigma/\varsigma$ have been ignored in the presentation of the inversion method in the last section. These terms, however, also depend on the particle concentration and size. It was assumed that if the particle concentrations are low, of order 1% by volume (or 30 g/l), multiple scattering is negligible [Varadan *et al.*, 1983], then the scattering attenuation $\bar{\alpha}_s$ is a linear function of M. The recent experiments by Hay [1991] indicated that the attenuation $\bar{\alpha}_s$ of natural sand indeed increases linearly with M in the range of $M \leq 24$ g/l. It may be possible, however, that the upper limit for the linear region of α_s to hold can be much higher than 1%. This kind of speculation comes from the fact that the linear region of the scattering attenuation for kaolin can be up to 10% [Urick, 1948]. New experiments are needed to clarify the maximum concentration, up to which that the linear relationship holds, for natural sand particles. In the following discussion, it is assumed, in general, that the particle concentrations are low enough to ignore multiple scattering. Then we have

$$\bar{\alpha}_s = \frac{k_c \xi}{\rho_o'} M, \tag{6.13}$$

in which $\xi = \bar{\alpha}_s / k_c \epsilon$, and $\bar{\alpha}_s = \int_o^\infty \alpha_s n(a) da$. Here α_s is scattering attenuation for a non-resonant spherical scatterer (see Figure 3.2). Figure 6.3 shows the theoretical values of ξ with different σ_g as a function of a_g assuming the size distribution is log-normal. The exponent in Eq. (3.15) can be written as

$$\int_o^{r_i} \bar{\alpha}_s \, dr'' = \frac{k_c \delta r}{\rho_o'} \left[\sum_{k=1}^{i-1} \xi_k M_k + \frac{1}{2} \xi_i M_i \right]. \tag{6.14}$$

where the index k denotes the kth range bin, r_i is the upper limit of the integration, which is given by $(i-0.5)\delta r$, and δr is the bin width. It can be seen, from Eq. (6.14), that we need to know the value of M_i before correcting the attenuation loss. However, in the last section, we assumed that the scattering attenuation has been completely corrected before we can estimate concentration M_i. In other words, these two problems are coupled together.

It has been shown in the laboratory [Hay, 1991, see also Figure 7.1] that the scattering attenuation at 1.00 MHz is very small for $M < 30 g/l$ and for $a_g < 200\ \mu$m. By assuming that the size distribution at the range r_i is the same as that at the range r_{i-1}, that is $F_i(X_1, \sigma_g) = F_{i-1}(X_1, \sigma_g)$, then an approximate estimate for M_i in the ith range bin can be obtained from

$$M_i^* = \rho_o' \left[\frac{V_i}{S_1 F_{i-1}(X_1, \sigma_g)} \right]^2. \tag{6.15}$$

It should be noted that M_i^* given by Eq. (6.15) is only a rough estimate to correct for scattering attenuation. The final estimate of M_i is made using the method

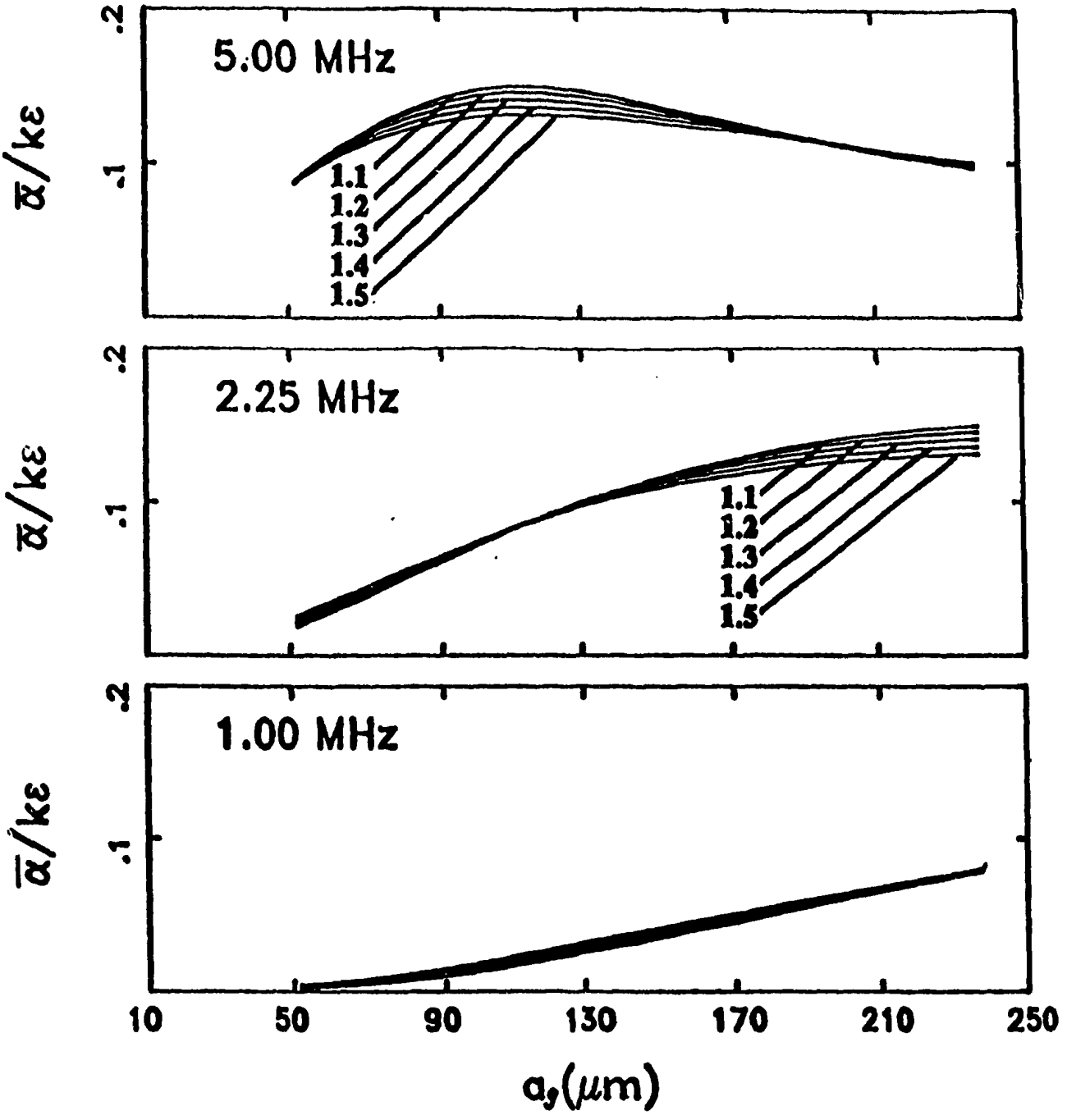

Figure 6.3. The theoretical values of $\xi = \bar{\alpha}_e / k_c \epsilon$ for three frequencies with $\sigma_g = 1.1$, 1.2, 1.3, 1.4, and 1.5, as indicated.

presented in the last section. Eq. (6.14) can now be expressed by

$$\int_0^r \bar{\alpha}_e \, dr'' = \frac{k_c \, \delta r}{\rho_o'} \left[\sum_{k=1}^{i-1} \xi_k M_k + \frac{\rho_o' \xi_{i-1}}{2} \left(\frac{V_i}{S_1 F_{i-1}(X_1, \sigma_g)} \right)^2 \right]. \qquad (6.16)$$

Similarly, ς in Eq. (3.11) can be approximated by

$$\varsigma = c \, \tau \left[\alpha_o + k_c \, \xi_{i-1} \left(\frac{V_i}{S_1 F_{i-1}(X_1, \sigma_g)} \right)^2 \right]. \qquad (6.17)$$

It becomes clear, therefore, that the effects of α_c and $\sinh\varsigma/\varsigma$ at 22.25 and 5 MHz are corrected for in each range bin by using $F(X_1, \sigma_g)$ and $\bar{V}_1$ in the previous range bin. These corrected voltages are then used to obtain M and a_g by applying the procedure discussed in the last section. The value $F(X_1, \sigma_g)$ at this range can be used to correct $\bar{\alpha}_e$ and $\sinh\varsigma/\varsigma$ for the next range bin, and so on.

CHAPTER 7 LABORATORY RESULTS

In this chapter, data from laboratory sediment jet measurements are presented and discussed, and are used to evaluate the validity and the limitations of the inversion method in estimating particle concentration and size from multi-frequency acoustic signals.

The conventional calibration curves were obtained by plotting the measured concentration sampled at the centerline of the jet on the horizontal axis, and the squared mean acoustic backscattered voltage at the same position in the jet, on the vertical axis. It has been discussed in Chapter 3 that $\overline{V}^2$ is linearly proportional to the concentration only if the concentration is low enough that the effect of the correction term $\left[\sinh\varsigma/\varsigma\right]^{1/2} \exp[-2\int_0^r \bar{\alpha}_e\, dr']$ can be ignored. Typical calibration curves for Stanhope Beach (SHB) sand (See Table 5.1) are depicted in Figure 7.1. The solid line represents the linear relation between M and $\overline{V}^2$, of which the slope was calculated by linear least squares fit to data points in the low concentration region: that is, all points for 1 MHz, the first 7 points for 2.25 MHz, and the first 5 points for 5 MHz. It can be seen from Figure 7.1 that the linear region of the calibration curve can be up to at least 25 g/l for 1 MHz, 12 g/l for 2.25 MHz and only 4 g/l for 5 MHz. After this concentration, especially for 2.25 and 5 MHz, the data points are departure from the straight line, which indicates that the above mentioned correction term plays an important role in the calibration relation, and its effect is larger for higher frequencies.

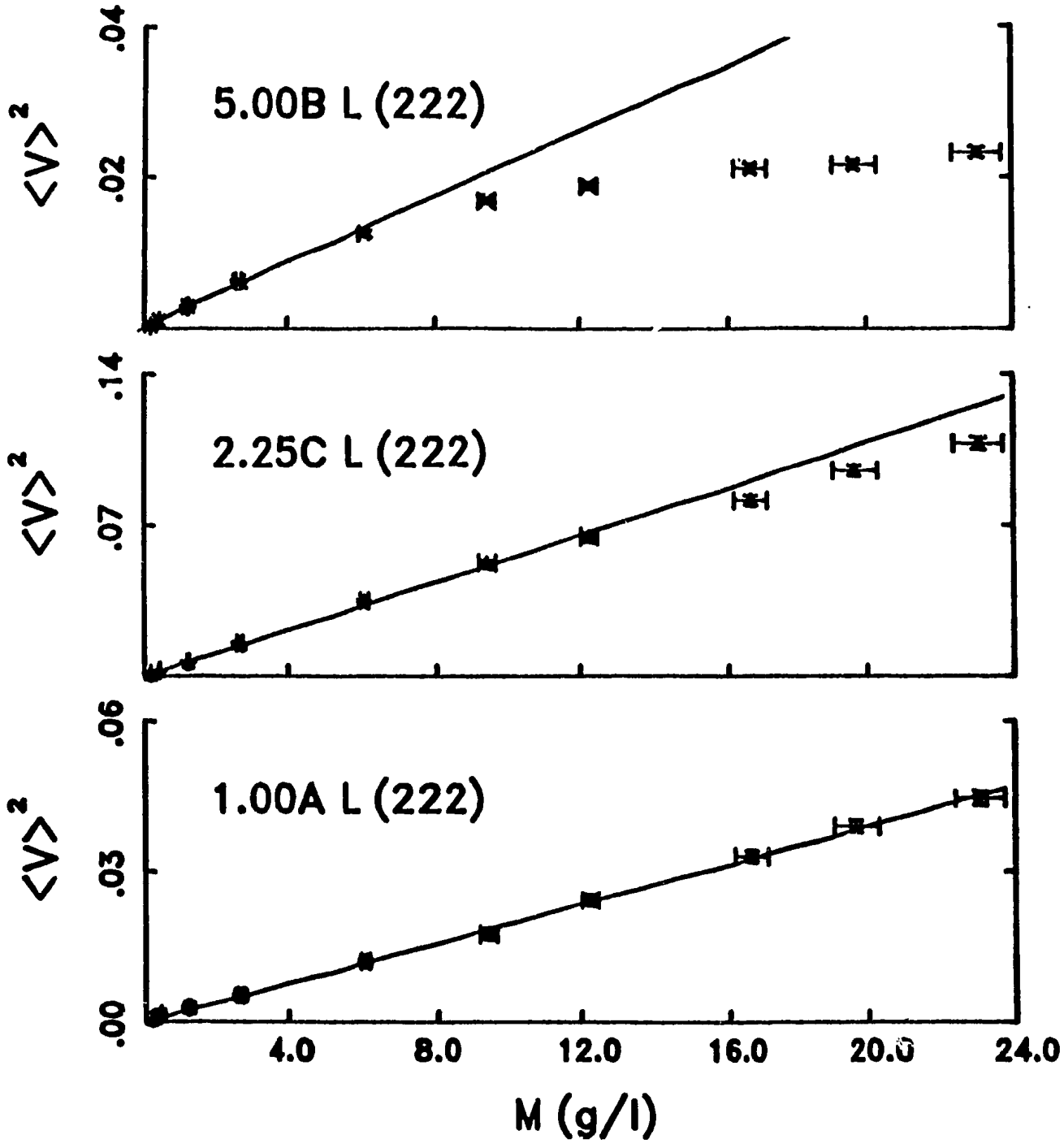

Figure 7.1. Calibration curves for three transducers with frequencies of 5 (top), 2.25 (middle), 1 (bottom) MHz using Stanhope Beach sand, of which the geometric radius is 79 μm, and the geometric standard deviation σ_g is 1.25. Solid lines represent linear least squares fits using data points in the linear region, that is, all points for 1 MHz, the first 7 points for 2.25 MHz, and the first 5 points for 5 MHz.

It should be emphasized that such calibration curves are always required to convert acoustic data to actual concentrations for single frequency acoustic techniques, such as those mentioned in Section 1.2. The present inversion method, on the other hand, no longer requires the conventional calibration relation. Hence, the invariant presupposition about the sediment size is not demanded. In fact, to obtain the variation of size with time and height is one of the objectives of both the RASTRAN system and the inversion method. What we need, instead, is the sensitivity factor of each sounder, and the standard deviation σ_g of suspended sediments. The concentration M and the geometric mean radius a_g can then be directly extracted from the multi-frequency acoustic signals.

Measurements were made with the sediment jet in the laboratory test tank (Figure 2.3) using uniform sand with ten size fractions (Table 5.2), and three natural size distributions (Table 5.1). The concentrations at the centerline of the jet were in the range $0.2\ \text{g/l} \leq M_o \leq 30\ \text{g/l}$ (see Appendix B). The compositions of different sizes with different concentrations make it possible to evaluate the accuracy of the inversion method presented in Chapter 6.

In each run of laboratory jet experiments, 200 sets of acoustic jet profiling data at the frequencies of 1, 2.25, and 5 MHz were collected with 1.11 cm spatial resolution. Four suction samples at the jet centerline were taken with the J-tube (section 2.2) immediately after the acoustic data were collected. The time-mean acoustic jet profile at each frequency was obtained by averaging the acoustic profile data over 200 sets. Considering that the effective range resolution of the system cannot be better than $c\,\tau/2$=1.5 cm, the rectangular running average 2 bins in width was further applied on the time-mean acoustic jet profile. Spatial

shifting with 1 range bin for 1 and 5 MHz sounders was also made, since these two sounders were tilted (see Figure 2.3). The comparisons between measured values and computed values of M_e and a_g for 55 different sediment jet measurements are shown in Figures 7.2a and 7.3a in the form of scatter diagrams, in which the measured concentrations are the average of four suction measurements, and the measured radius is from the midpoint of each sieved interval for the uniform sand particles (Table 5.2), or the geometric mean radius for the three natural sands (Table 5.1). It should be pointed out that the theoretical F-ratios with $\sigma_g = 1$ were calculated as well in order to process the uniform size data. The inverted and measured values of centerline concentration and size are also listed in Appendix B.

The solid lines in Figures 7.2a and 7.3a represent perfect agreement between inverted and measured data, while the dashed lines were obtained by linear regression. R_{yz} in Figures 7.2 and 7.3 is the correlation coefficient, which is given by

$$R_{yz} = \frac{\sum_{i=1}^{I} (y_i - \bar{y})(z_i - \bar{z})}{\left[\sum_{i=1}^{I} (y_i - \bar{y})^2 \sum_{i=1}^{I} (z_i - \bar{z})^2 \right]^{1/2}}, \tag{7.1}$$

where I is the total number of data points in the plot, and y_i represents the measured value, and z_i the calculated value. D_{zy} is an estimate of the mean relative systematic error, which is given by

$$D_{yz} = \sum_{i=1}^{I} \frac{| y_i - z_i |}{y_i}, \tag{7.2}$$

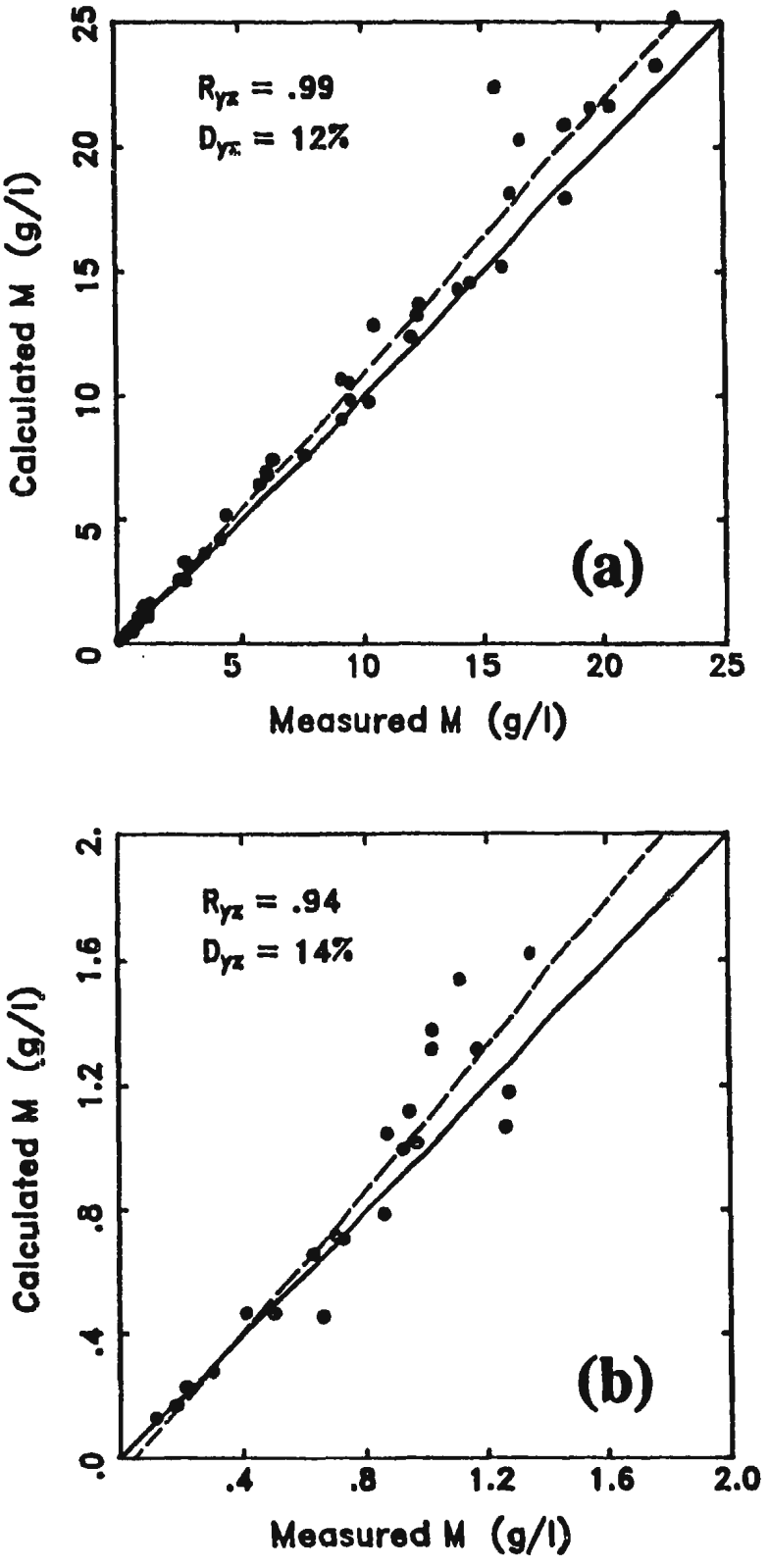

Figure 7.2. Scatter plot of inverted and measured centerline concentrations for: (a) all sediment jet measurements; (b) selected jet measurements with centerline concentrations of less than 1.6 g/l.

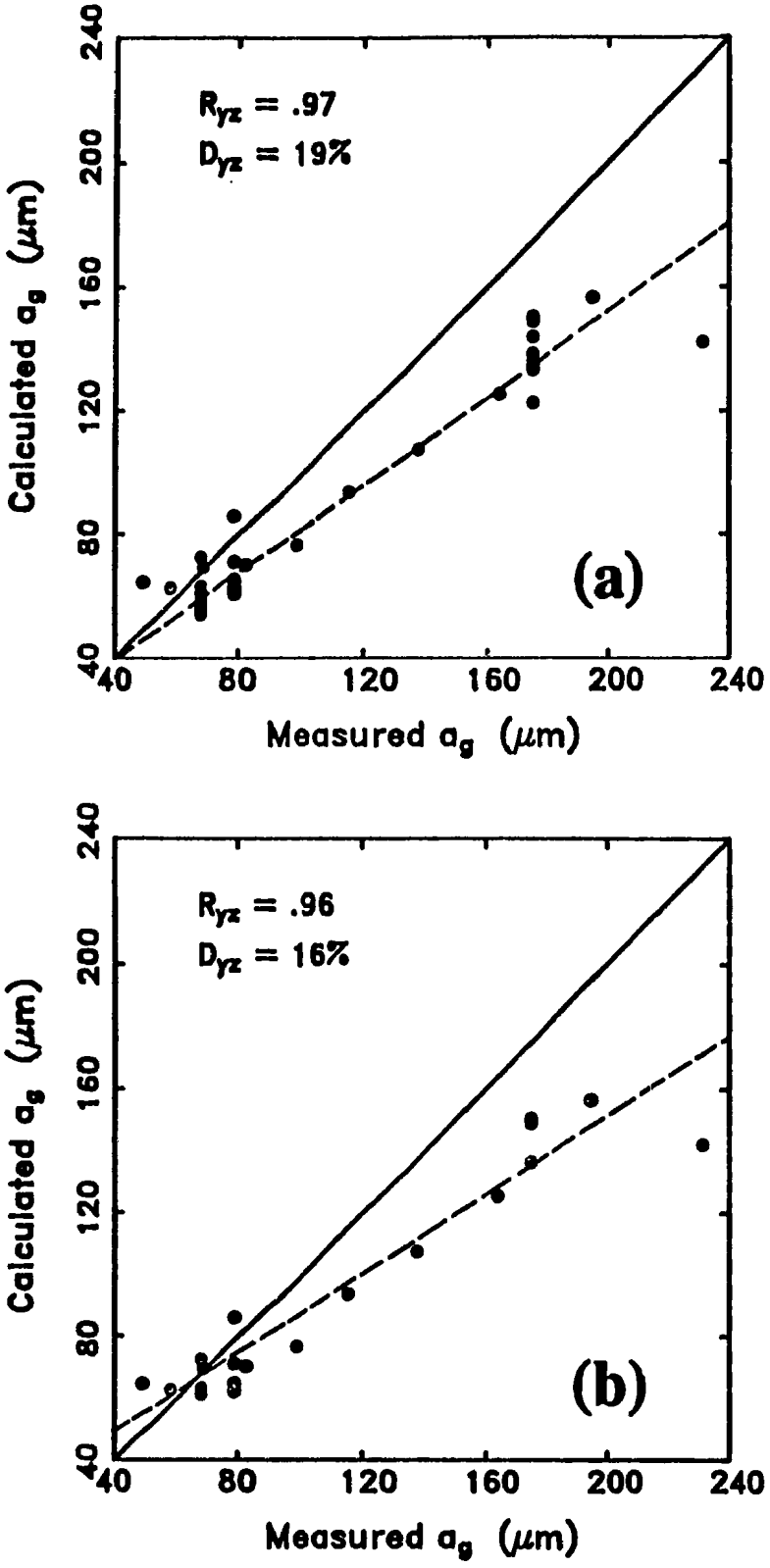

Figure 7.3. Scatter plot of inverted and measured centerline particle sizes in radius for: (a) all sediment jet measurements; (b) selected jet measurements with centerline concentrations of less than 1.6 g/l.

By examining Figure 7.2a, it can be seen that the correlation coefficient R_{yx} is as high as 0.99, which means that the particle concentrations obtained from multi-frequency acoustic data are highly correlated linearly with the measured concentrations. The linear regression line (the dashed line) in Figure 7.2a is slightly above the perfect agreement line (the solid line), which indicates that inversion methods slightly overestimates concentrations at the centerline of the jet. The systematic error in Figure 7.2a is about 12%, which is not very large. From the above statistics, therefore, it can be concluded that the centerline concentration was well represented by the inversion procedure presented in Chapter 6 from the RASTRAN data in the range of $0.2 \leq M_o \leq 30$ g/l. The discrepancy between the inverted and the measured values may result partially from the different propagation paths at the different frequencies (see Figure 2.3), partially from errors in measuring the concentration by the siphon method, and partially from the errors in correcting TVG by using the computed attenuation coefficient α_o.

Comparisons between the inverted and known values of centerline particle size in Figure 7.3a, however, exhibit a greater degree of scatter. Although the linear correlation coefficient is 0.97, which is also high, the linear regression line is well below the perfect agreement line, which may indicate that the inversion method underestimates particle sizes in the jet experiments. The systematic error is 19%, which is larger than that for particle concentrations. It also appears that the inversion method is less sensitive to sand particles with finer size fractions than those with coarser size fractions, and that there are large variations in inverted particle sizes for the same sand type at different concentrations. Besides the three error sources mentioned above which also affect the comparison in

Figure 7.3a, there are a number of other potential contributing factors. One factor is the mathematical procedure presented in Chapter 6, in which the ratio of the detected voltages of pairs of units was used to determine the size of the suspended sediments. A second factor is the sorting characteristics of the sediment jet. It was found visually that for the finer size fractions, particles remained suspended at higher levels in the cone (Figure 2.3), which might cause a shift toward coarser particle sizes at the jet centerline. For coarser size fractions, however, the size of suspended sediment at the center of the jet may be somewhat finer than the injected material, due to deposition of the largest particles in horizontal segments of the circuit (Figure 2.3).

In order to determine whether the large discrepancy in Figure 7.3a may result from the procedure of correcting for the scattering attenuation, the same data in Figures 7.2a and 7.3a but with the centerline concentration of less than 1.6 g/l are replotted in Figure 7.2b for particle concentrations and Figure 7.3b for particle sizes. It was mentioned before that the effect of the attenuation due to scattering is negligible for such low concentrations. The linear correlation coefficient R_{yz} in Figure 7.2b is 0.94, slightly smaller than that in Figure 7.2a, while the linear regression line for $M_o > 0.4$ g/l in Figure 7.2b is above the perfect agreement line, and the systematic error is about 14%, also very similar to Figure 7.2a. The same tendency as in Figure 7.3a can be also seen in Figure 7.3b, except that the systematic error is slightly smaller in Figure 7.3b. It can be deduced, hence, that the large discrepancy between inverted and measured values of particle size does not come from the correction procedure discussed in Section 6.2.

The centerline concentration is as low as 0.12 g/l (Appendix B, see also Figure 7.2), which is so low that the signal amplitude is small, especially at 1 MHz, and especially for the smallest particles at 1 MHz. The lower accuracy in the data with the centerline concentration of less than 0.5 g/l could be one of main reasons why there are large variations in the inverted particle sizes for the same sands (see Figure 7.3, also Appendix B). The data plotted in Figure 7.4 are those in Figure 7.3b but excluding data with the centerline concentration of less than 0.5 g/l. It can be seen, from Figure 7.4, that inverted particle sizes for the natural sand distribution are now more consistent with the uniform size estimates, which supports our speculation. It can be also found, from Figure 7.4, that the data points for the two smallest sieved sizes are well above the perfect agreement line, and the data point with the largest sieved size is far below the perfect agreement line, both of which could well be explained by the sorting characteristics of the sediment jet mentioned above. The linear regression line in Figure 7.4 is computed from all points except these three. It can be seen that data points except these three can be fitted reasonably well by the linear regression line.

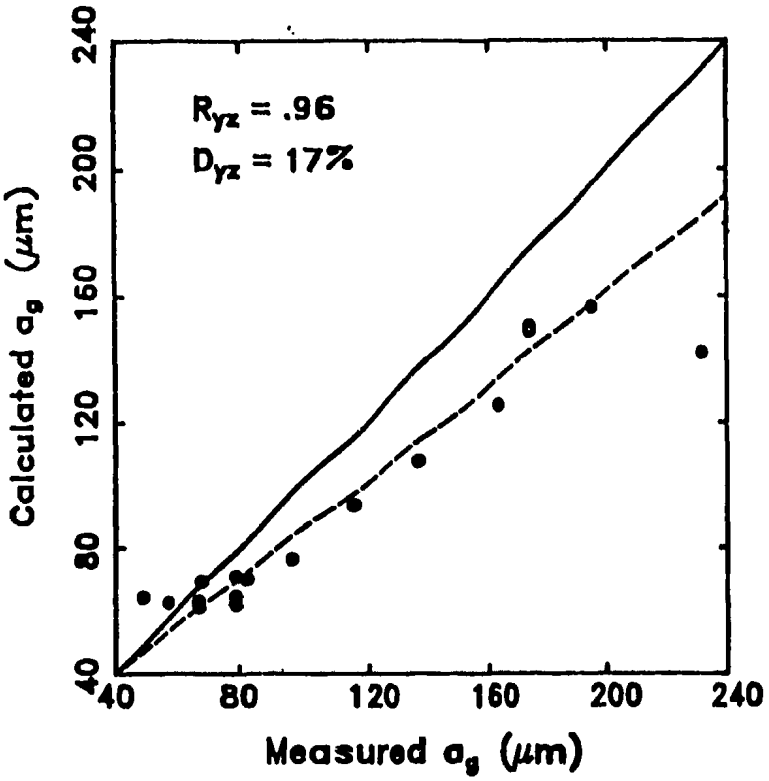

Figure 7.4. Scatter plot of inverted and measured centerline particle sizes in radius for selected jet measurements with centerline concentrations between 0.5 g/l and 1.6 g/l.

CHAPTER 8 FIELD RESULTS

The inversion method is used in this chapter to convert RASTRAN data collected at Stanhope Beach in October-November 1989 under natural dynamic conditions, in which surface waves, tides, and longshore currents all make contributions to the sediment transport, and to particle concentrations and size. The field data are employed to demonstrate the potential of the RASTRAN system and the appropriateness of the mathematical procedure presented in Chapter 6 in measuring the suspended sediment transport for three cases of different surface wave energy.

In section 8.1 we describe the surface wave conditions in four selected segments of field data, one corresponding to low surface wave energy, one to intermediate, and two to high surface wave energy conditions. Section 8.2 illustrates the color-coded acoustic images. In section 8.3 we present acoustic images of concentration and size converted from the multi-frequency acoustic signals. Section 8.4 compares particle concentrations at the same depth measured by Optical Backscatter sensors (OBS) and RASTRAN, since the OBS data provide the only available independent check on the accuracy of the inversion method for the field data. In section 8.5 we discuss time mean vertical profiles of particle concentration and size, averaged over three different time intervals, which are all longer than several surface wave cycles. Section 8.6 obtains the sediment eddy diffusivity from time-averaged vertical profiles of concentration and size by assuming a balance between vertical diffusion and settling. In section 8.7 we calculate the sediment flux profiles and sediment transport rates from the cross-shore current and

inverted particle concentrations. Section 8.8 estimates the eddy diffusivity due to turbulence only.

8.1 Wave Conditions

Four RASTRAN data files chosen from periods of different wave conditions when both the OBS and flowmeter signals were available from UDATS. The four selected data files are: SHB89300.030, SHB89301.015, SHB89308.046 and SHB89308.047, in which "SHB" indicates the location of the field experiment (Stanhope Beach), the following five characters denote the year and Julian Day when the file was collected, and the extension of the file name is the sequential run number. For example: "SHB89300.030" indicates that this file was run 030 collected at the Stanhope Beach on Julian Day 300 (Oct. 27), 1989. The selected runs with the start time are listed in Table 8.1, with the measured values of temperature and salinity (obtained from bucket samples at the shoreline), which were used to calculate both the sound speed and the attenuation due to sea water.

Table 8.1. Four field data files from periods of three wave conditions, and the maximum magnitude of the power spectral density (PSD) in $cm^2s^{-2}Hz^{-1}$ at the frequency f_{max}. The measured value of salinity is near constant, about 28.96 ppt.

Energy	File	Start Time	T (° C)	PSD	f_{max} (Hz)
Low	SHB89300.030	27-OCT-89:07:37	9.0	22.6	0.18
Medium	SHB89301.015	28-OCT-89:22:14	9.0	52.5	0.25
High	SHB89308.046	4-NOV-89:13:47	8.3	282.5	0.17
	SHB89308.047	4-NOV-89:13:54	8.3	256.2	0.17

The power spectral density was calculated from the records of cross-shore currents at a height of about 20 cm from the bed. The computations were performed by using code from Press *et al.* [1986, Chapter 12], in which some errors in their subroutine SPCTRM were corrected. The velocity records with 2560 points were first divided into eight segments. By overlapping segments with one half of their length, each segment contained 512 points. The discrete Fast Fourier Transform in each segment was computed after applying the Welch window [Welch, 1978] in the time domain. The mean power spectral density was finally obtained by averaging the spectral densities from all segments. The degrees of freedom of the approximating chi-square distribution is 1.63 multiplying by the number of segments [Welch, 1978], in the case here, the number of degrees of freedom is roughly 13. The 90% confidence interval for the power spectral density estimate is between 0.58 and 2.20 multiplying by the estimated value itself. The Welch window was chosen because it has a narrower central peak and smaller sidelobes, compared with other windows [Press *et al.*, 1986, p.425].

The calculated power spectral densities are shown in Figure 8.1 for the low energy, in Figure 8.2 for the medium energy, and in Figure 8.3 for the high energy records. The Nyquist frequency for these data sets in Figures 8.1-8.3 is about 3.3 Hz. The peak value of power spectral density in each energy case is also listed in Table 8.1, with the corresponding frequency f_{max}. It can be seen that the peak magnitude of power spectral density in the high energy case is 12 times larger than that in the low energy case, and 5 times larger than that in the medium energy case. The corresponding frequency at maximum energy f_{max} in the low and high energy cases is similar, and in the medium energy is about 40% larger, indicating the presence of shorter period waves.

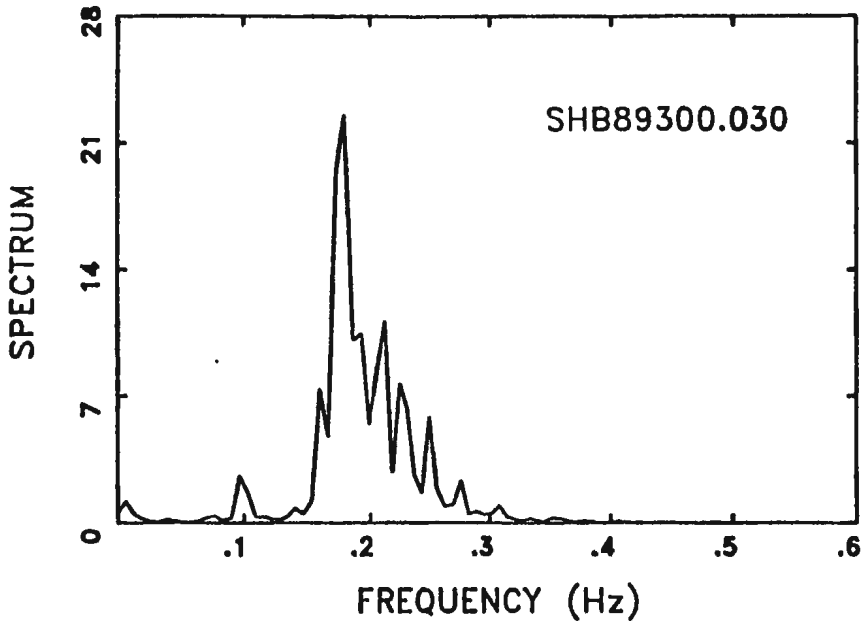

Figure 8.1. The power spectral density in the low energy case in units of $cm^2s^{-2}Hz^{-1}$.

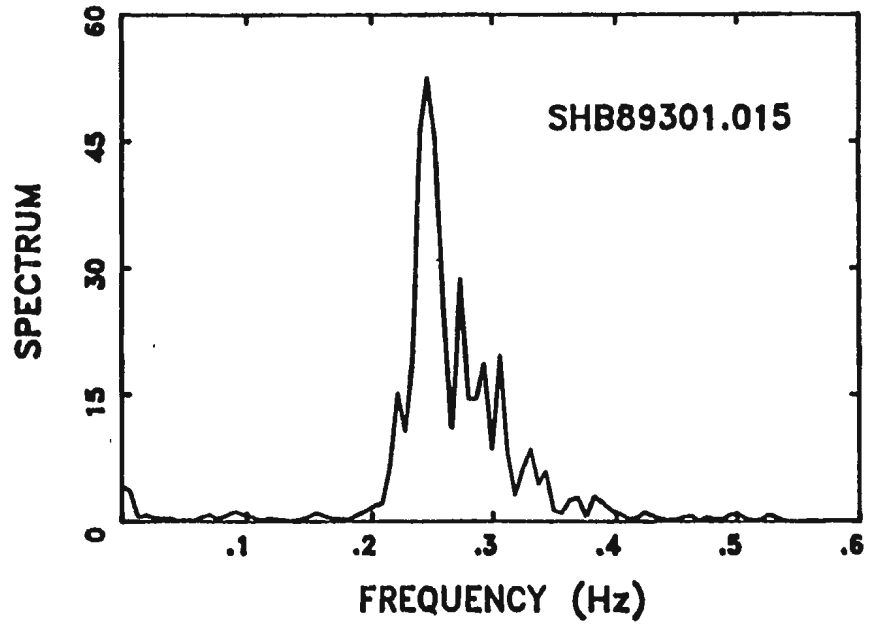

Figure 8.2. The power spectral density in the medium energy case in units of $cm^2s^{-2}Hz^{-1}$.

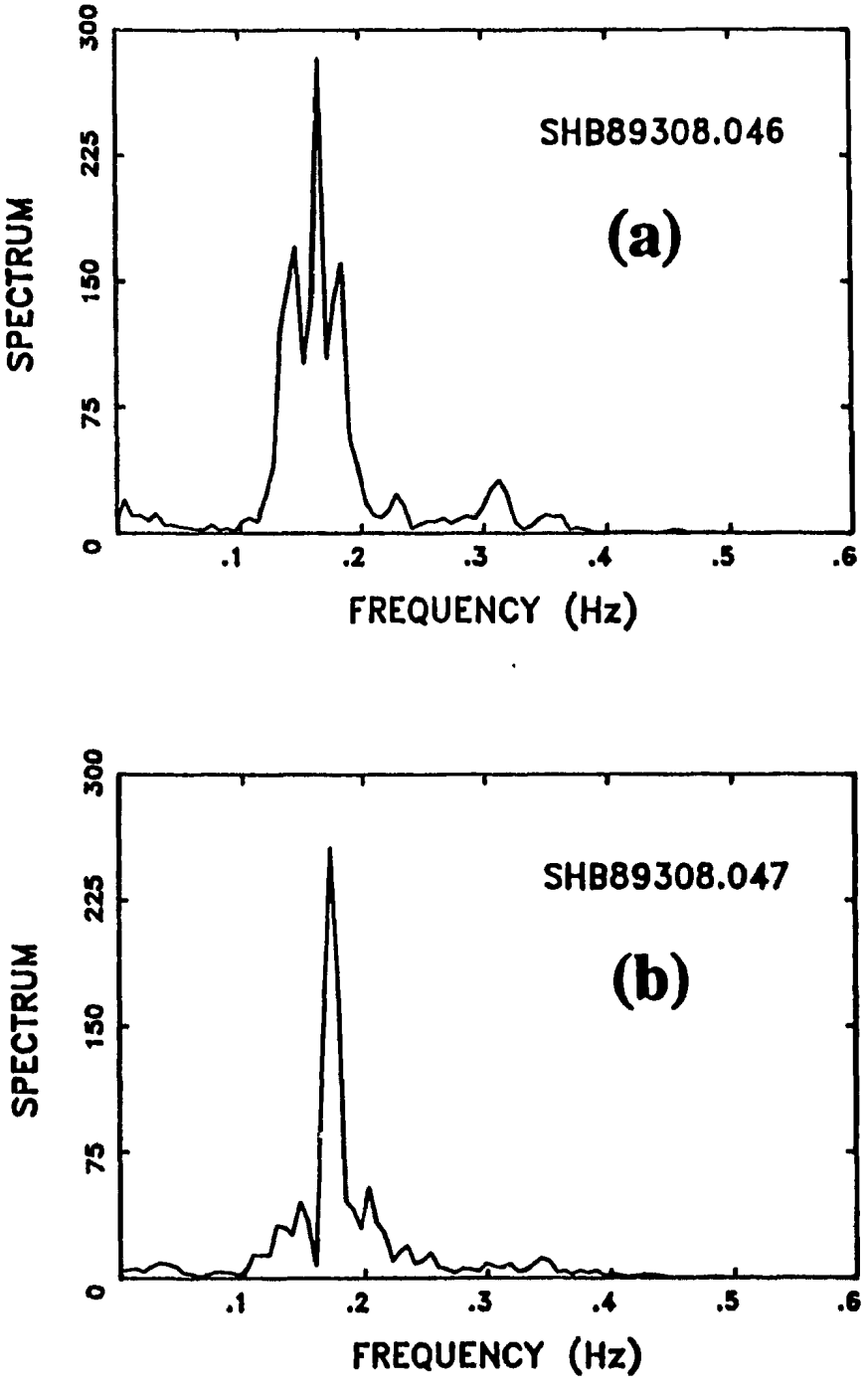

Figure 8.3. The power spectral density in units of $cm^2s^{-2}Hz^{-1}$ for the two consecutive runs in the high energy case.

8.2 Acoustic Images of Sediment Suspension

During the field experiment, 2600 4-ping ensemble averaged sets were collected in each RASTRAN run at a acquisition rate of about 6.6 Hz. Each set consisted of four profiles at three different frequencies, and each profile included 53 range bins with a bin width of 1.8 cm. Consequently, the size of each RASTRAN data file is 1.17 Mbytes, which can be stored on one 1.2 Mbyte floppy disk. Recognizing that an enormous quantity of acoustic data exists, it is desirable to create a computer graphics color-coded plot of the data. This was done using the Halo'88 graphics package.

Figures 8.4-8.6 show typical color-coded acoustic images of RASTRAN data produced with a 640×480 resolution display on a Compaq Deskpro 385/25 personal computer, and printed on a Hewlett Packard Paint Jet printer. The number of displayed channels is user-selectable with the maximum number of 8 (only five channels are chosen in Figures 8.4-8.6). Display channels 1 to 4 were assigned to the RASTRAN data, while channels 5 to 8 were used for channels from an A/D board in the computer, which were assigned to selected OBS's and current meters signals from the D/A outputs of UDATS.

The horizontal axis in Figures 8.4-8.6 is the time scale in units of minutes, reading from left to right. Channel 8, appearing on the top of the plot, is the cross-shore velocity component from an electromagnetic current meter at about 20 cm from the bed. The vertical scale of that channel is voltage: 1.0 volt represents 0.6 m/s. The positive value denotes onshore direction of the current. Channel 7 is the record of an optical backscatter sensor (OBS) mounted at about

5 cm from the bed. The unit of vertical scale for Channel 7 is also voltage. The calibration relation is 1.0 volt $\approx$ 10 g/l. Beneath channels 7 and 8 are the acoustic images of the RASTRAN data for the cluster of sounders operating at 1, 2.25 and 5 MHz (Figure 2.6). The vertical axis in these three channels is the distance of the range bin from the transducer in units of cm. The color of each range bin varies with the amplitude of the acoustic data, which may be the detected voltage, or the concentration, or the size. This scale is defined in the palette at the bottom of the plot with 8 different colors. If the amplitude of the acoustic data is less than the minimum value given in the color palette, the color white (or blank) is used. If the value is greater than the maximum value given by the color palette, on the other hand, the color black will be used. There are only 600 horizontal pixels available which can be used to display the data, therefore, a complete RASTRAN data set with 2600 sets can only be plotted either by averaging it over 4 (or 5) sets, or by separating it into several portions. In Figures 8.4-8.6 the results are averaged over 4 sets.

Other features of the imaging program include: (a) TVG was recorrected using the bucket measurements of temperature and salinity; (b) both the width of the averaging window in the time domain and the initial set number to be displayed are user-selectable, which allows the imaging program to be more useful; (c) the vertical scales and the minimum and the maximum values of the color palette can be easily reset by users; (d) time series of RASTRAN data at a user-selected range can be plotted; (f) almost all parameters to be used in the imaging program can be displayed on the screen in a convenient menu.

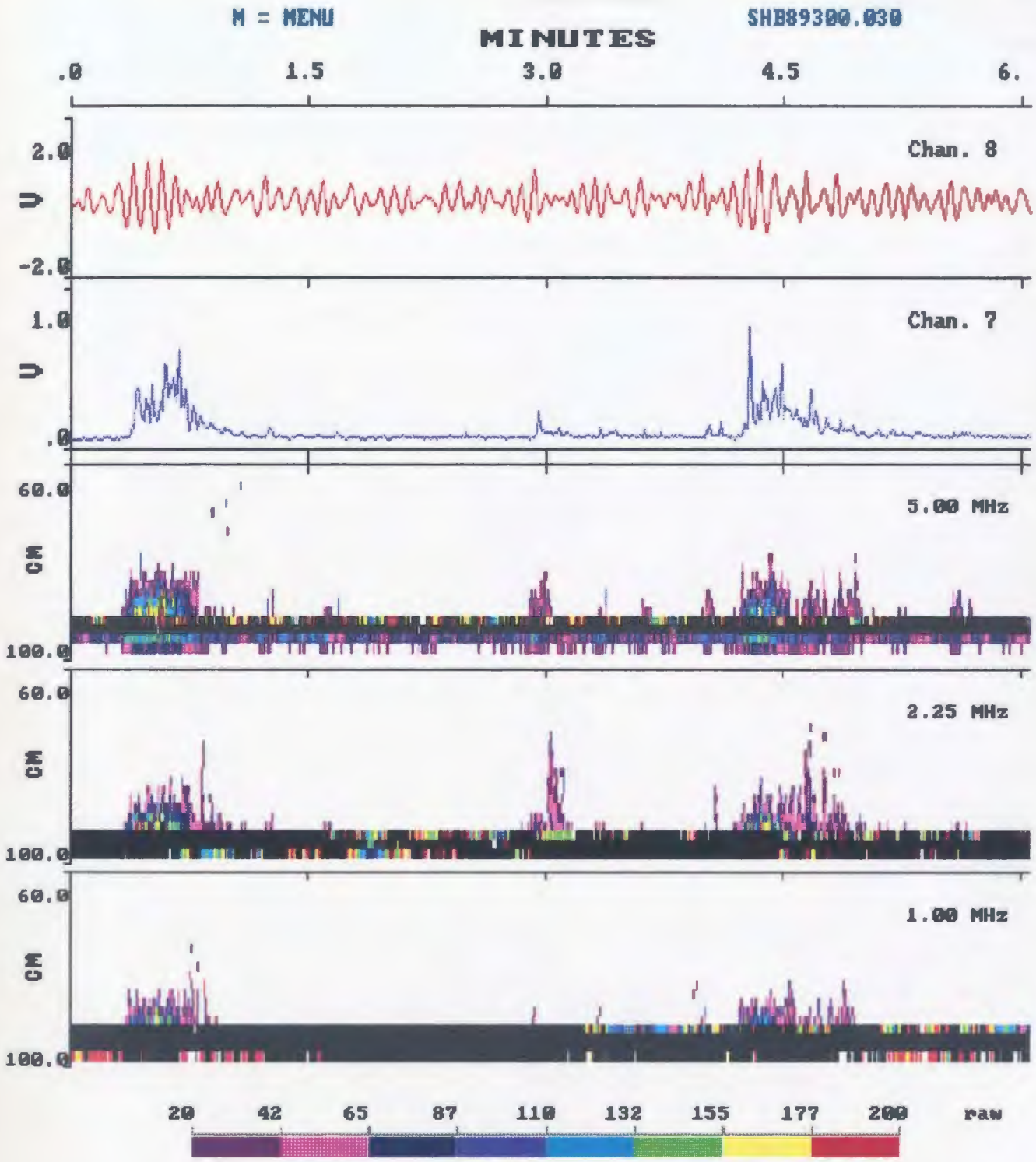

Figure 8.4. Color images of the raw acoustic data with records of the OBS and the flowmeter in the low energy case. The curve appearing on the top of the plot is the record of cross-shore currents in units of volts: 1 V = 0.6 cm/s; the second one is the record of the OBS also in units of volts: 1 V = 10 g/l. Beneath them is the color images of the RASTRAN data for the cluster of three sounders at 5, 2.25 and 1 MHz, respectively. Values in the color palette are in millivolts.

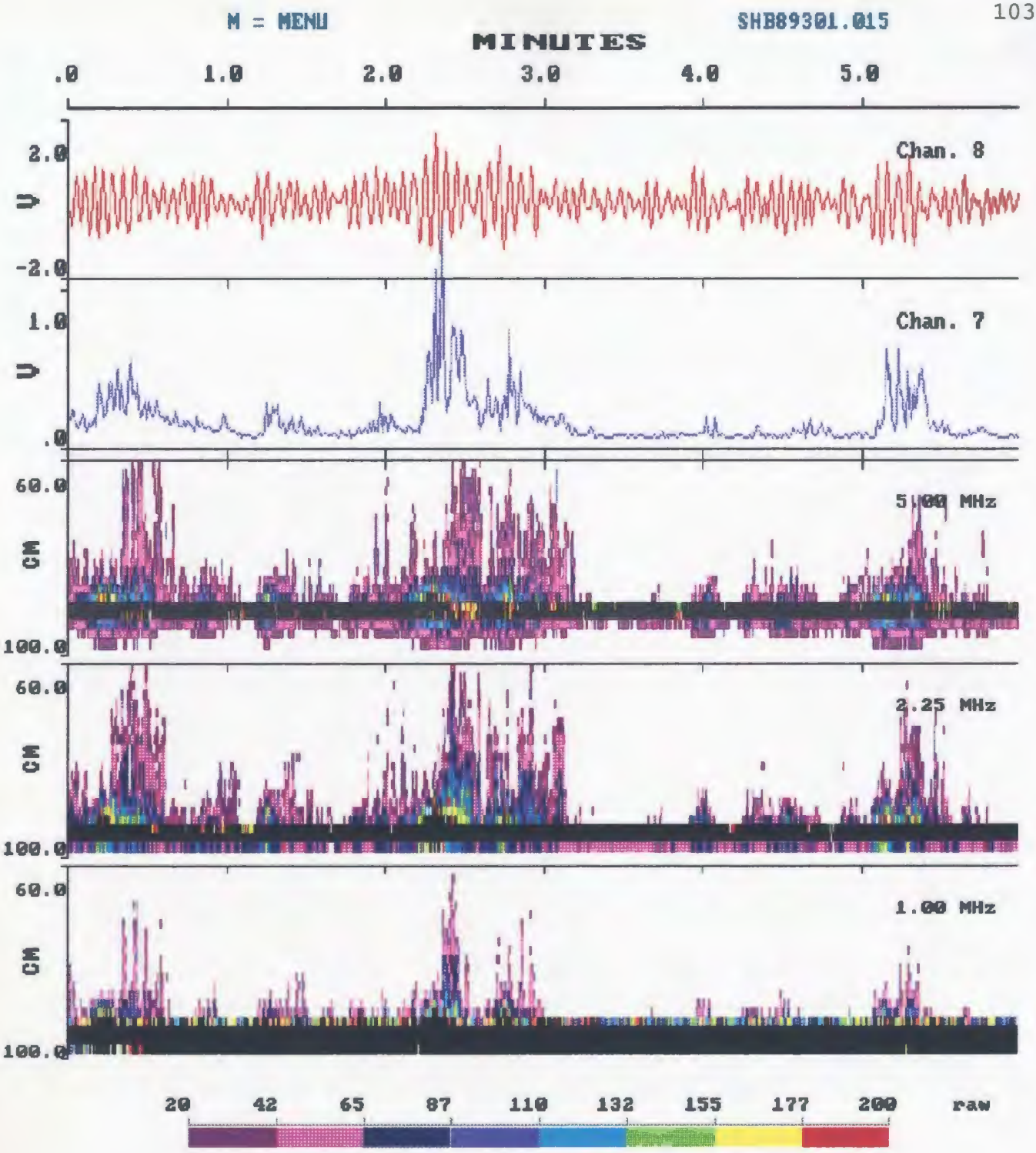

Figure 8.5. Color images of the raw acoustic data with records of the OBS and the flowmeter in the medium energy case. Otherwise as in Figure 8.4.

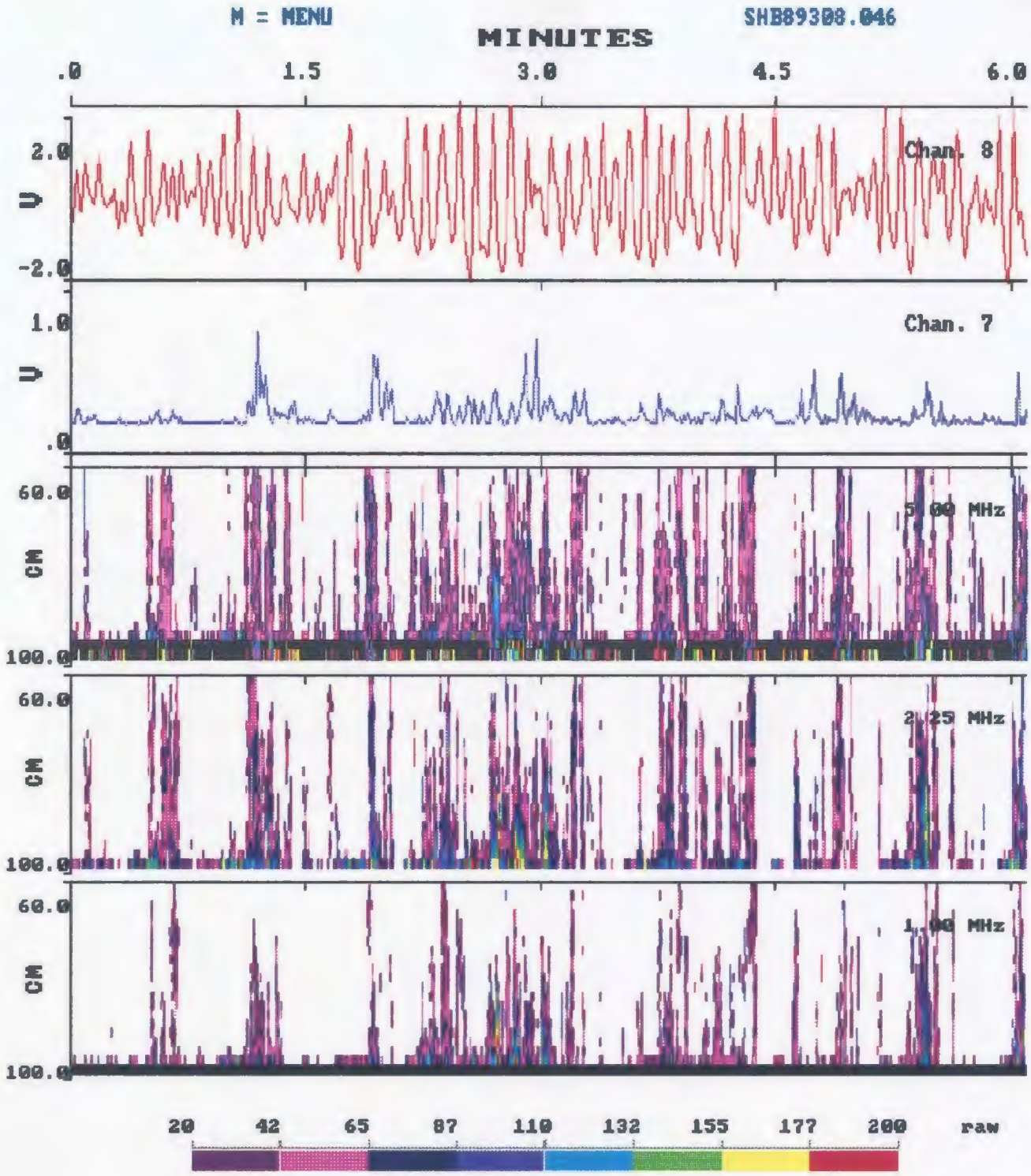

(a)

Figure 8.6. Color images of the raw acoustic data with records of the OBS and the flowmeter in the high energy case for two consecutive runs: (a)SHB89308.046, (b)SHB89308.047. Otherwise as in Figure 8.4.

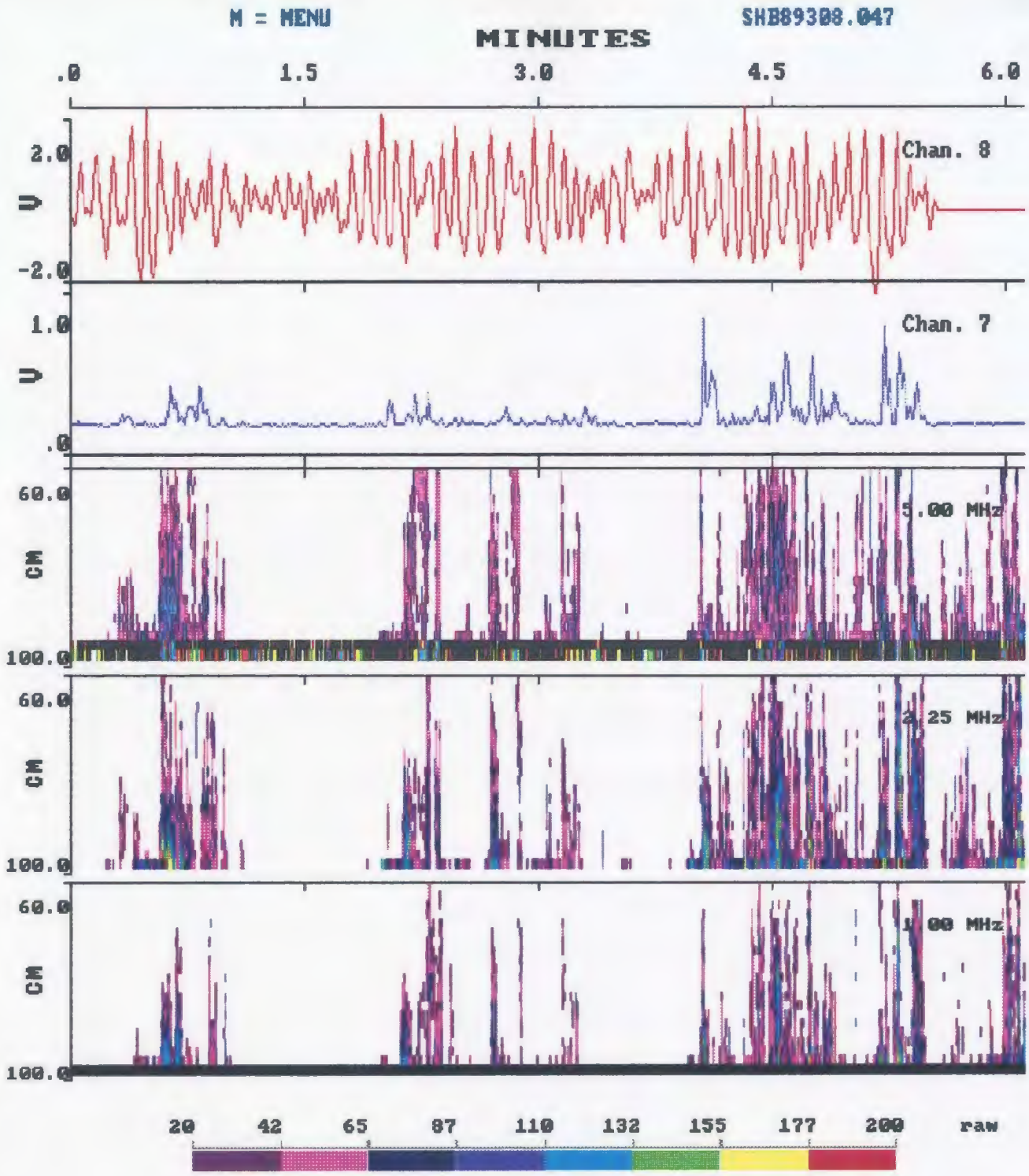

(b)

Figure 8.6. (continued)

The color images in Figures 8.4-8.6 clearly document the ability of the RASTRAN system to "see" scatterers over the 1 m range, and the great opportunity provided by such a system in observing the time evolution of sediments in suspension. The intermittent nature of the suspended sediment profile is also evident in the color images. The strong scattered signal at about 95 cm is that scattered from the "solid" sea-bed. The bottom echo (Figures 8.4 and 8.5, 5 MHz) may represent rescattering from the bottom reflected pulse.

It can also be seen, from Figures 8.4-8.6, that bottom sediment is lifted into suspension primarily by a group of large waves instead of an individual wave, which is consistent with previous studies [Hanes and Huntley, 1986; Hay *et al.*, 1988; Vincent and Green, 1990]; and the relative changes in the OBS data are comparable to those for RASTRAN at the same depth. Quantitative comparisons of particle concentration between OBS and RASTRAN data are made in Section 8.3.

Images in Figures 8.4-8.6, however, are burdensome to some degree due to the attempt to display the complete RASTRAN run in one screen. For detailed description, therefore, two or three windows, corresponding to periods of intense resuspension, were selected. Each window consists of 600 sets. The data in each window, then, can all be visualized in the one screen without set averaging. The number of windows in each run is tabulated in Table 8.2, with some characteristics of surface waves in each window, calculated from the on-offshore component of velocity measured at about 20 cm from the bed. The significant cross-shore wave velocity near the bed $U_{1/3}$ listed in Table 8.2 is defined in a similar way to the significant wave height, as the average of the first one third largest peak

values of the cross-shore velocities [LeBlond and Mysak, 1978, p.485]. U_{max} in Table 8.2 is the maximum magnitude of the cross-shore wave velocity in the given window. It can be seen, from Table 8.23, that $U_{1/3}$ in the high energy case is more than 30% larger than $U_{1/3}$ in the medium energy, and about 60% larger than $U_{1/3}$ in the low energy case. It should be noted that the left boundary of each window listed in Table 8.2 was chosen by centering the larger event in the window, therefore, this choice is rather arbitrary.

Besides the aforementioned two time segments, there is also another time segment which will be used in the later discussions of this Chapter. That is a single event, which is defined by a single group of waves. The left and right boundaries of a single event are determined at both points where the cross-shore currents are maxima (or both are minima) with clear water beyond the boundaries. The time duration of an event varies and depends on the apparent duration of the group of waves. Only one noteworthy event was chosen in each window, and no events were selected in the high energy case due to the difficulty in determining the positions of the left and right boundaries, since the sediment suspension events in this case were not clearly isolated from each other. The selected events in the low and medium energy cases are also listed in Table 8.2.

The high frequency fluctuations in the backscatter signals are large. In order to apply the inversion method presented in Chapter 6, it is desirable to smooth them out by using a low-pass filter. A rectangular running average 8 sets in width (about 1.2 sec) in the time domain was applied. The window width of 8 sets was chosen since it was wide enough to smooth out the high frequency fluctuations in the signals, but still short compared with the typical surface wave period (4-5

to the vertical extent and strength of the signal.

It has been recognized [e.g. Vincent *et al.*, 1986] that in the surf zone particularly, small concentrations of air bubbles in the path of the acoustic beam can significantly alter the acoustic backscattered signal. Besides air bubbles, high concentration eddies and other acoustic scatterers, such as algae, seaweed, fish, rotten wood, and other biological objects in water, could also affect the acoustic data to some degree. The contamination by bubbles in the water column was carefully examined. The RASTRAN data collected during calm conditions (called acoustic zero run) were used to establish minimum background levels. The presence of bubbles injected into the water by breaking waves, on the other hand, were determined by examining the acoustic data at the range bins close to the transducer. Normally the sizes and concentration of bubbles in water generated by breaking waves decrease with depth [Wu, 1981]. Therefore, if these bubbles appeared in the path of the acoustic beam, the scattered signal from bubbles would be stronger closer to the transducer. It was found that the magnitudes of backscattered signals in the range bins closer to the transducer for the four selected field data listed in Table 8.1 were small, and of the same order as those of data collected during calm conditions, which indicates little contamination by bubbles. It is still not eliminated, however, the possibility that the selected acoustic data could be altered by acoustic interference other than air bubbles. A typical example can be found from the acoustic data shown in Figure 8.9d, from which it can be seen that there were strong backscattered signals at mid-heights in suspension at the time of 4.46 minutes, and 5.36 minutes, respectively, and lasting for about 3 seconds, which could be evidence for the appearance of eddies or the aforementioned acoustic interference in the path of the sound beam.

Table 8.2. Characteristics of surface waves calculated from the current measurement at 20 cm above bed. $U_{1/3}$ and U_{max} are respectively the significant wave velocity and the maximum wave velocity near the bed in the cross-shore direction, t_w is the averaged wave period in the given window. Time duration of a single event selected in each window in the low and medium energy cases is also included.

File	Window				Event		
	No.	t_w (sec)	$U_{1/3}$ (m/s)	U_{max} (m/s)	No.	Period (min)	Duration (sec)
SHB89300.030	A	5.4	0.43	0.60	1	0.23-0.81	34.8
	B	5.1	0.42	0.56	2	4.12-4.58	27.6
SHB89301.015	A	3.6	0.53	0.64	1	0.07-0.67	36.0
	B	3.8	0.71	0.98	2	2.12-2.60	28.8
	C	3.5	0.51	0.72	3	4.95-5.46	30.6
SHB89308.046	A	4.8	1.24	1.38			
	B	5.1	1.18	1.37			
SHB89308.047	A	4.8	0.88	1.37			
	B	5.4	0.99	1.27			

seconds, see Table 8.2). The filtered data in the selected windows are plotted in Figures 8.7-8.9 for the three different wave energy cases. The overall similarity of the filtered return signals for the three different transducers in the above figures clearly demonstrates that the data at the different frequencies are correlated, and it is appropriate, therefore, to use the procedure in Chapter 6 to extract concentration and size. It should be mentioned that, since each sounder has a different sensitivity factor, and different characteristics of $F(X,\sigma_g)$ and scattering attenuation, the false color images of the same sediment suspension event for different channels using the same color palette may give different impressions as

Since three individual transducers were mounted separately on the frame, the same range bin for different units may not represent the same height above bottom. Height offsets for the three units, therefore, are required. *In situ* measurements of the transducer heights were made by divers on three different dates during the period of the RASTRAN deployment (2 weeks). Taking an average of these three measurements, the 1 MHz transducer was 1 cm above the 5 MHz transducer, and the 2.25 MHz transducer was 2 cm above the 5 MHz. It should be noted that the accuracy of diver measurements, which were made with a tape measure, is not really known. The relative height offsets can also be obtained by calculating the mean value of the depth difference of each pair of transducers, which were measured using a LeCroy model 9400 120 MHz digital oscilloscope to a resolution of 0.1 cm. The depth differences for each pair of transducers, again choosing the 5 MHz transducer as the reference, are plotted in Figure 8.10. The data in Figure 8.10 display a high degree of scatter, with a typical amplitude of 2-3 cm, which could well be due to the migration of sand ripples. It is the time-mean value that has special meaning to us, since this represents the relative spatial offset of these two transducers. The spatial offset is 1.8 cm between units of 1 MHz and 5 MHz transducers, and 3.1 cm between units of 2.25 MHz and 5 MHz transducers. These values are comparable with the diver measurements, and have been used in generating Figures 8.7-8.9.

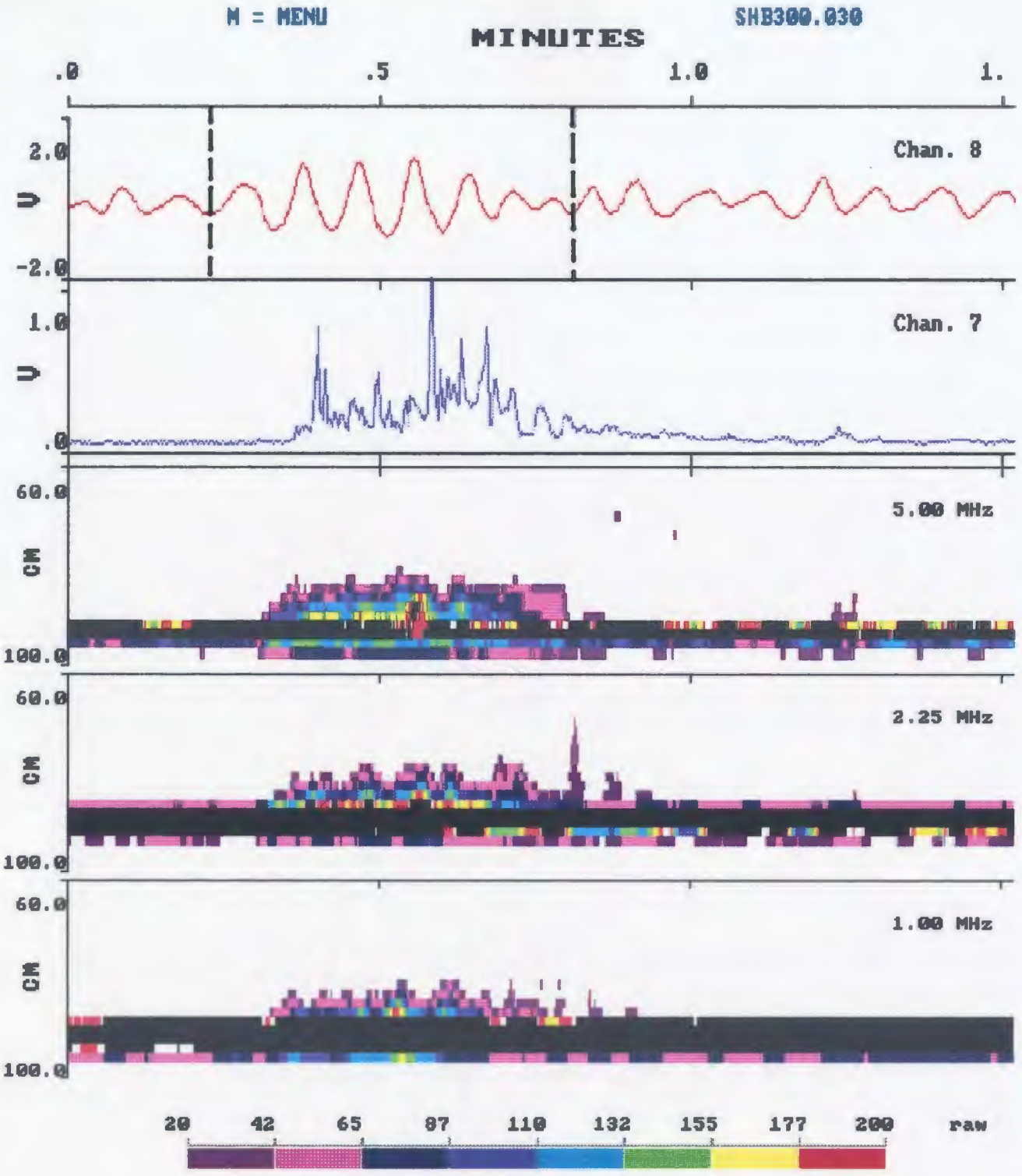

(a)

Figure 8.7. Color images of the filtered acoustic data in the low energy case for: (a) Window A, dashed lines represent boundaries of Event 1; (b) Window B, dashed lines represent boundaries of Event 2. Otherwise as in Figure 8.4.

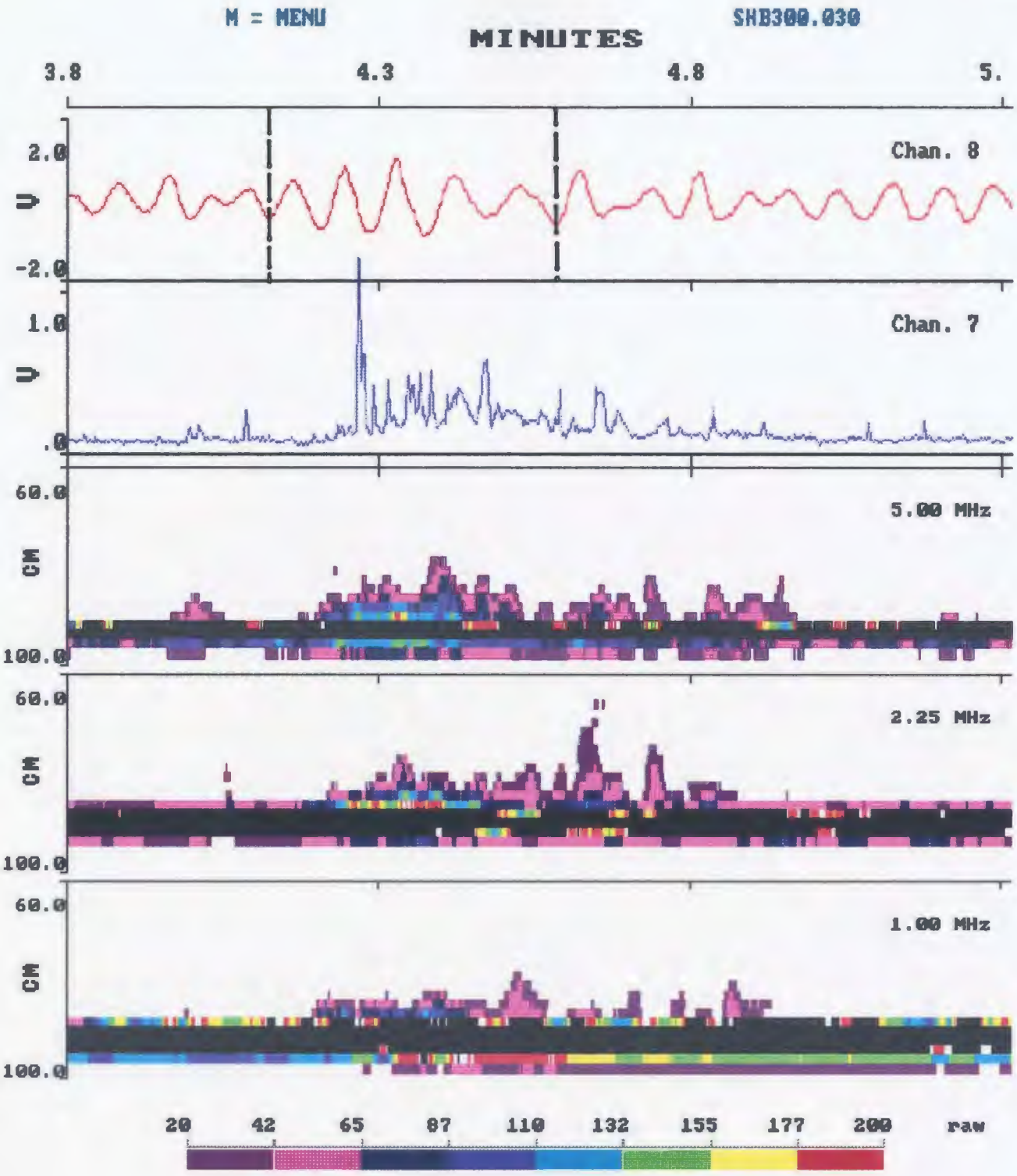

(b)

Figure 8.7. (continued)

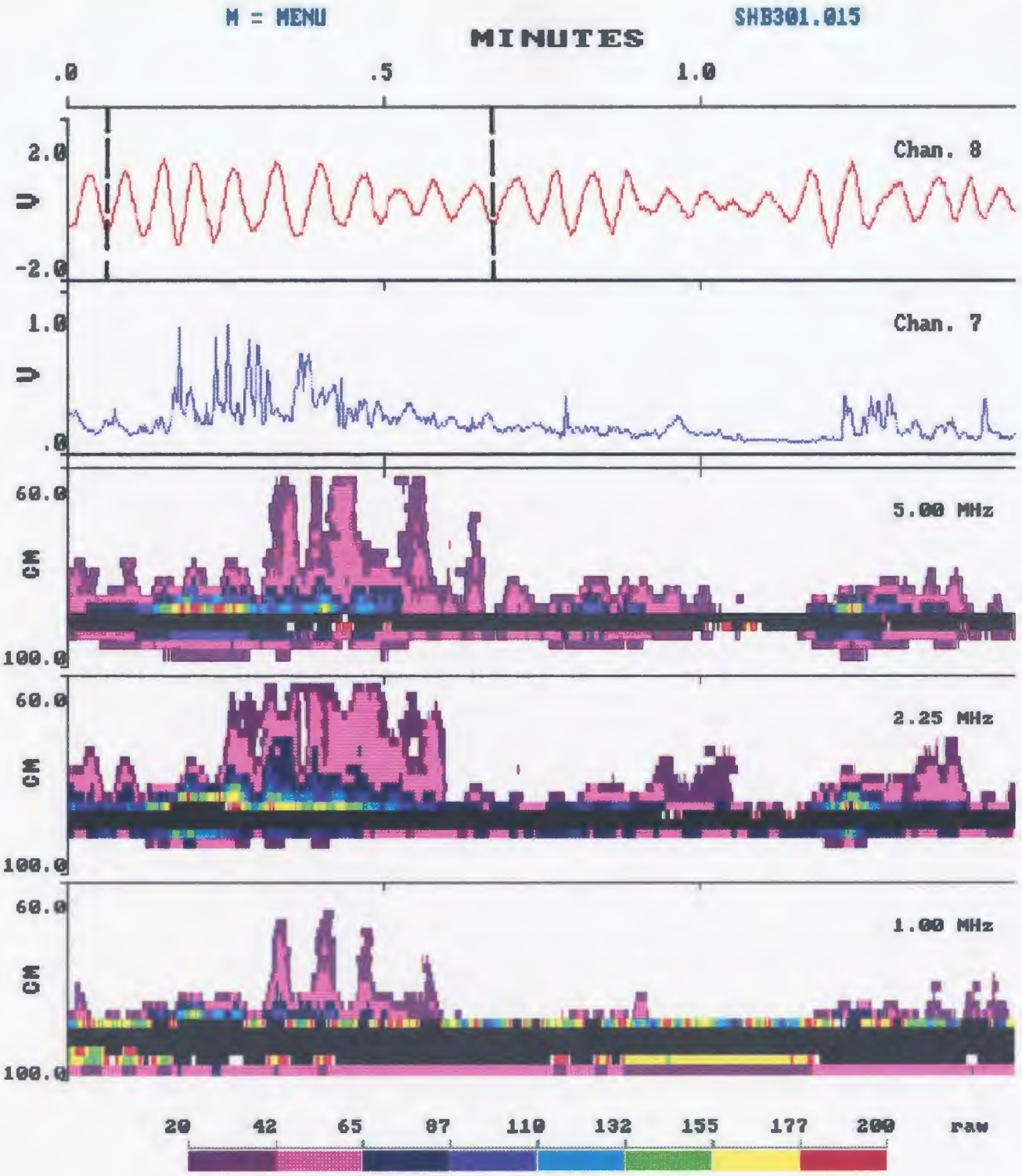

(a)

Figure 8.8. Color images of the filtered acoustic data in the medium energy case for: (a) Window A dashed lines are boundaries of Event 1; (b) Window B, dashed lines are boundaries of Event 2; (c) Window C, dashed lines are boundaries of Event 3. Otherwise as in Figure 8.4.

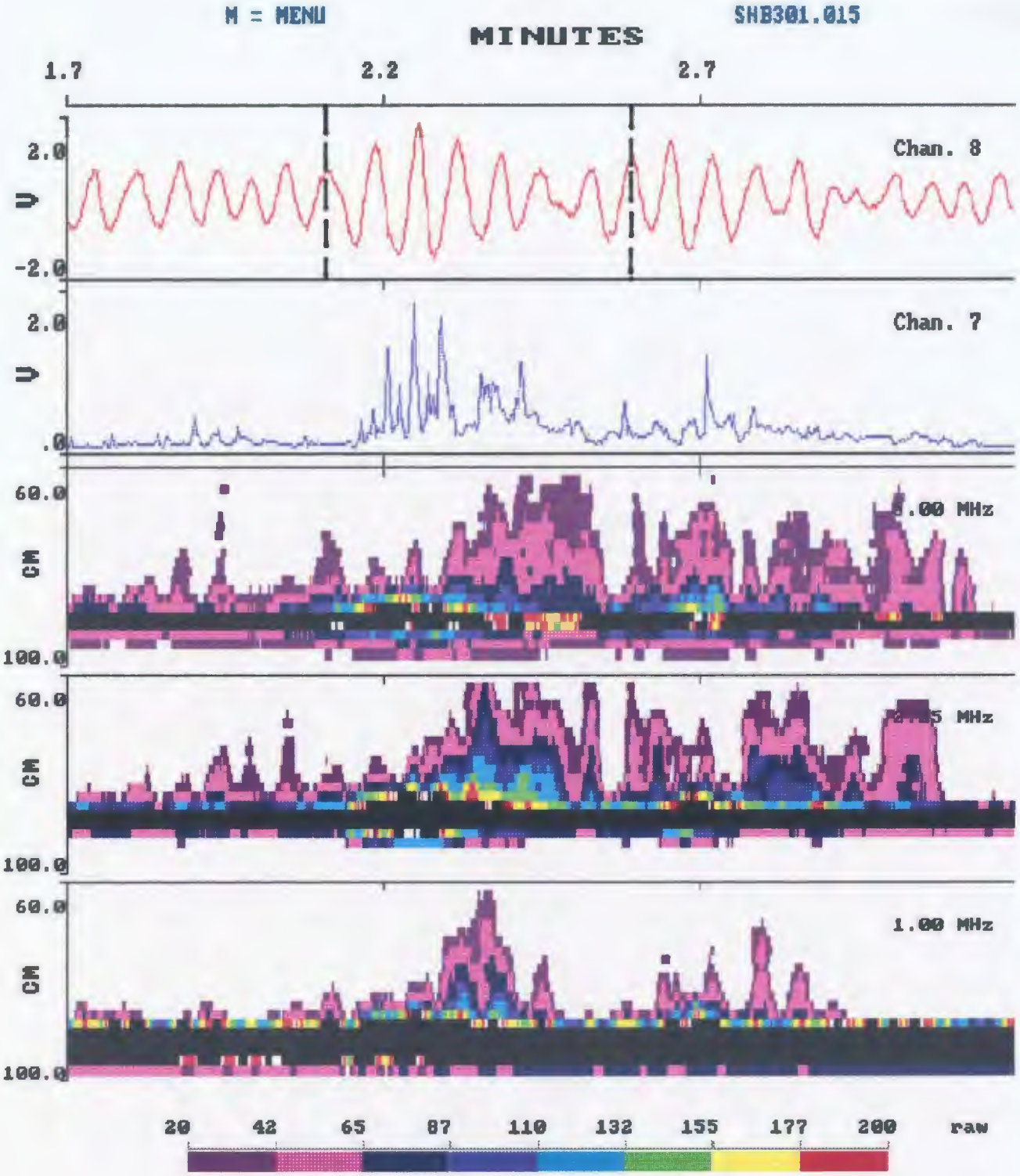

(b)

Figure 8.8. (continued)

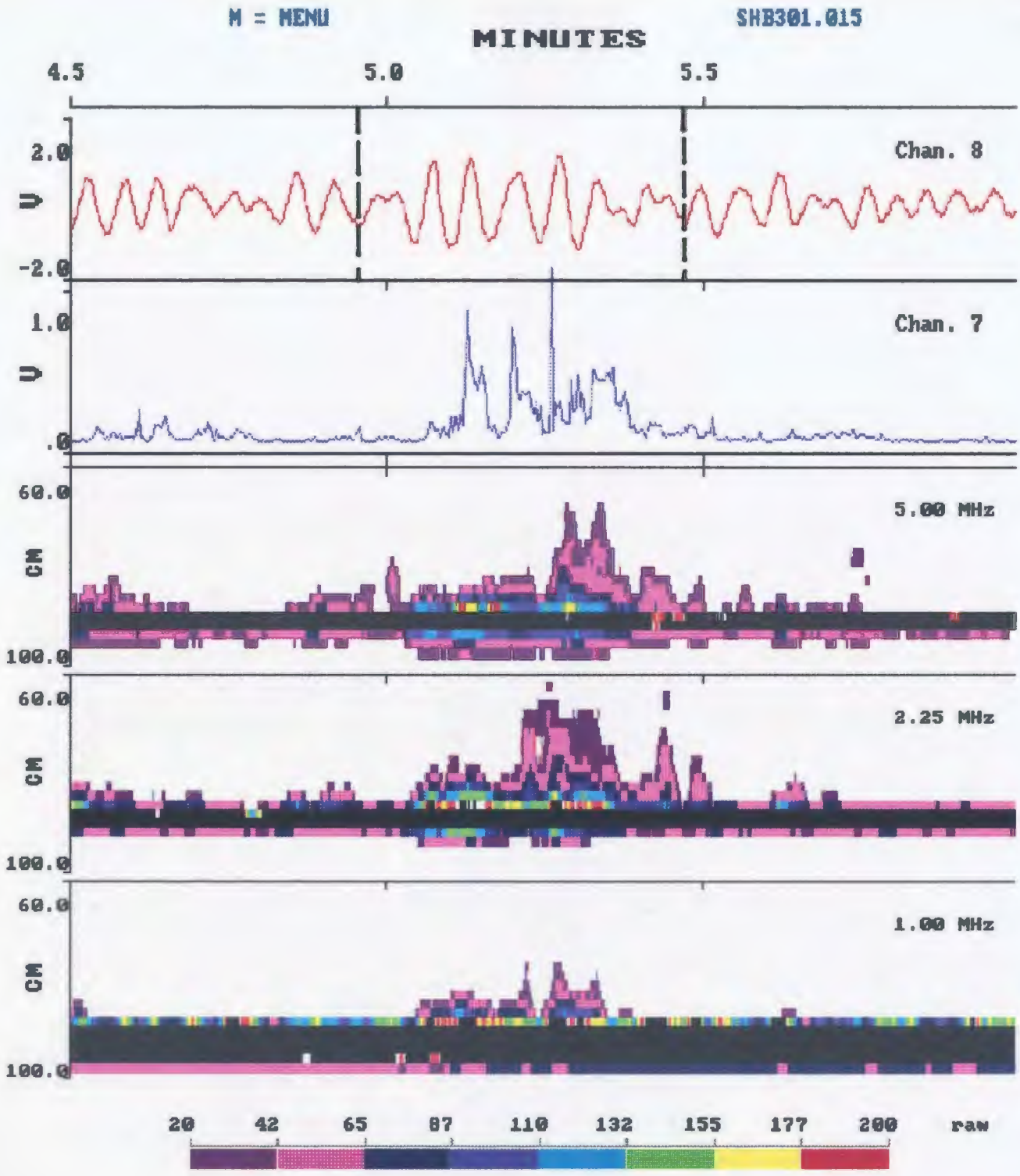

(c)

Figure 8.8. (continued)

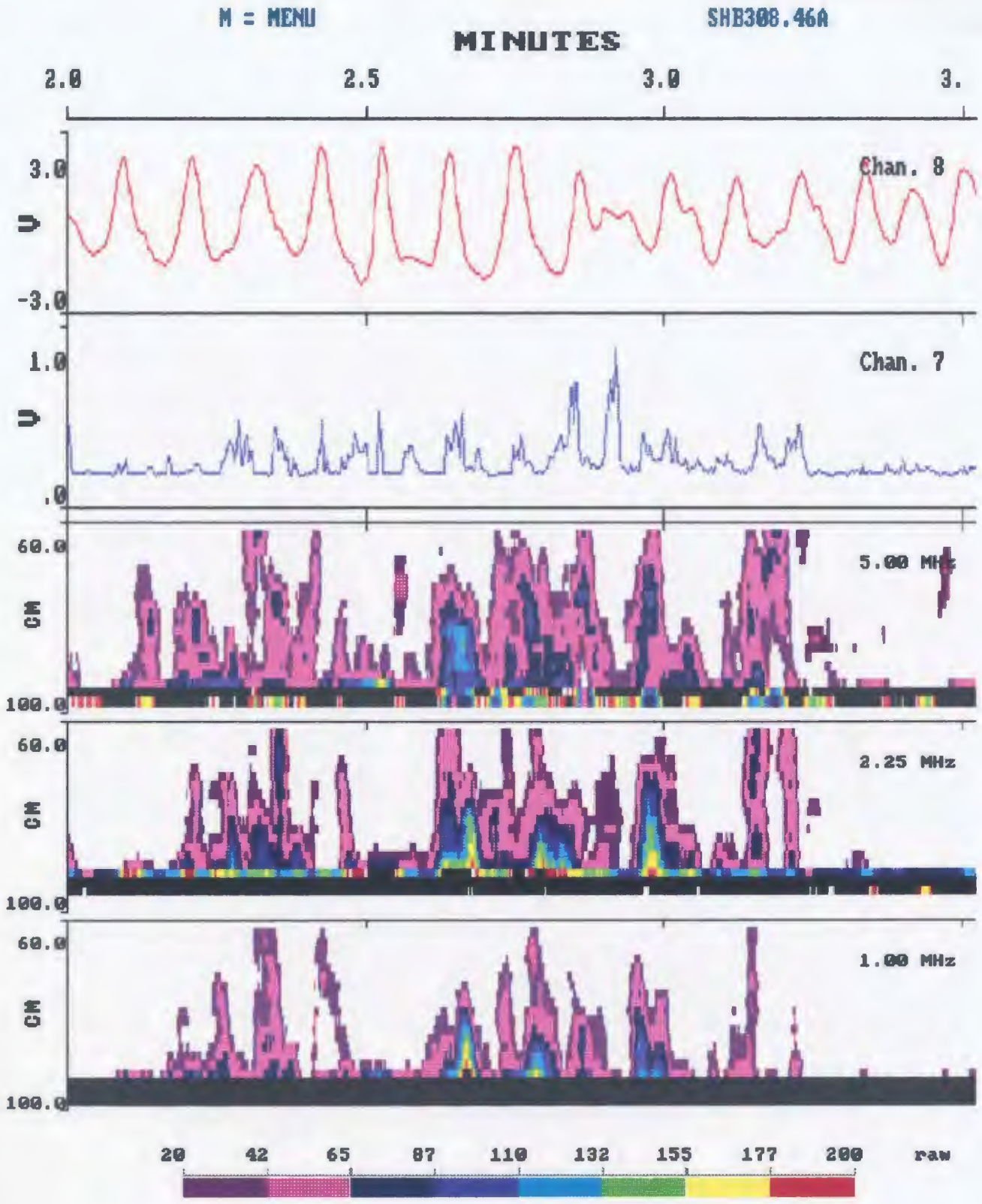

(a)

Figure 8.9. Color images of the filtered acoustic data in the high energy case for: (a) Window A and (b) Window B of SHB89308.046; (c) Window A and (d) Window B of SHB89308.047. Otherwise as in Figure 8.4.

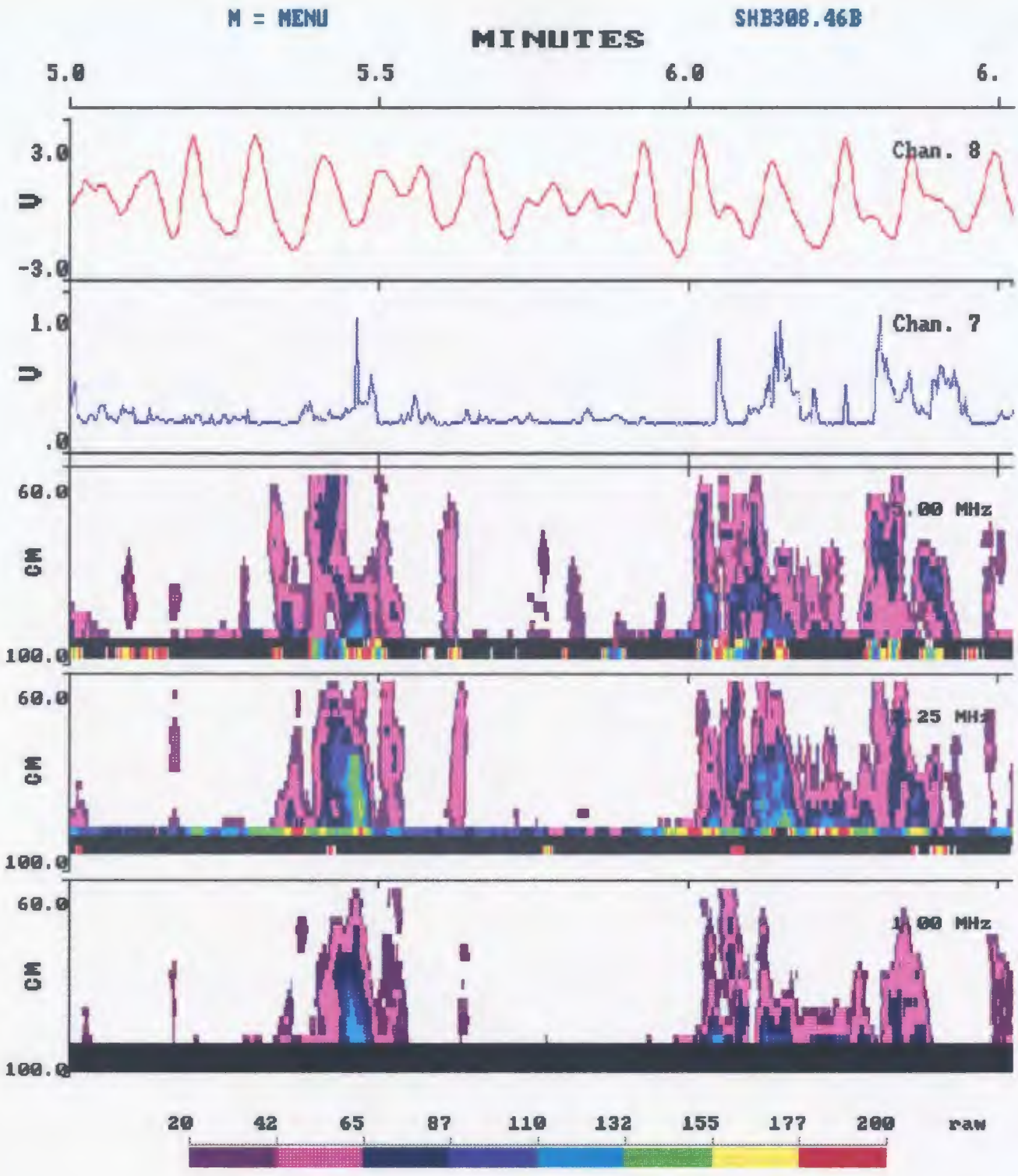

(b)

Figure 8.9. (continued)

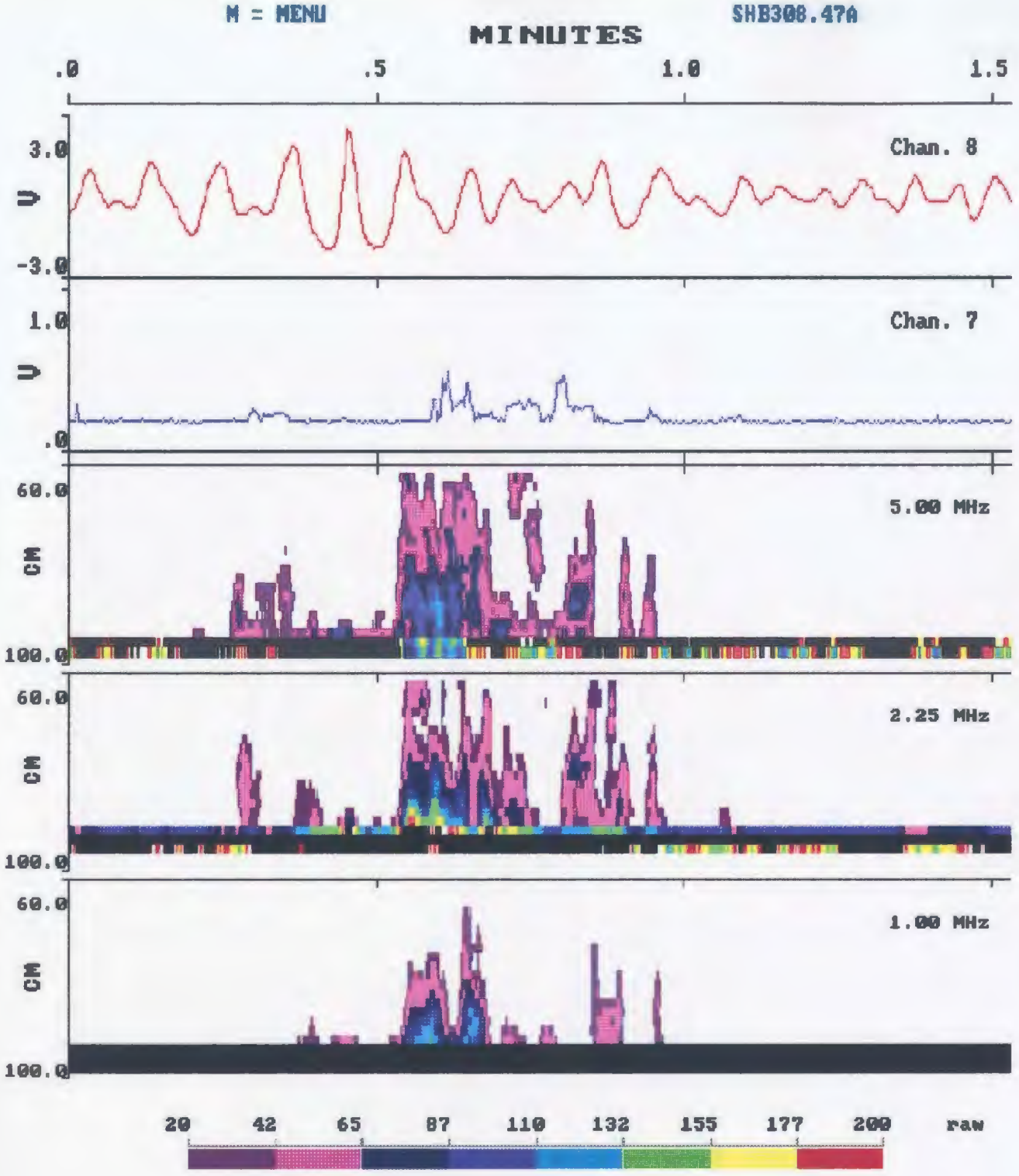

(c)

Figure 8.9. (continued)

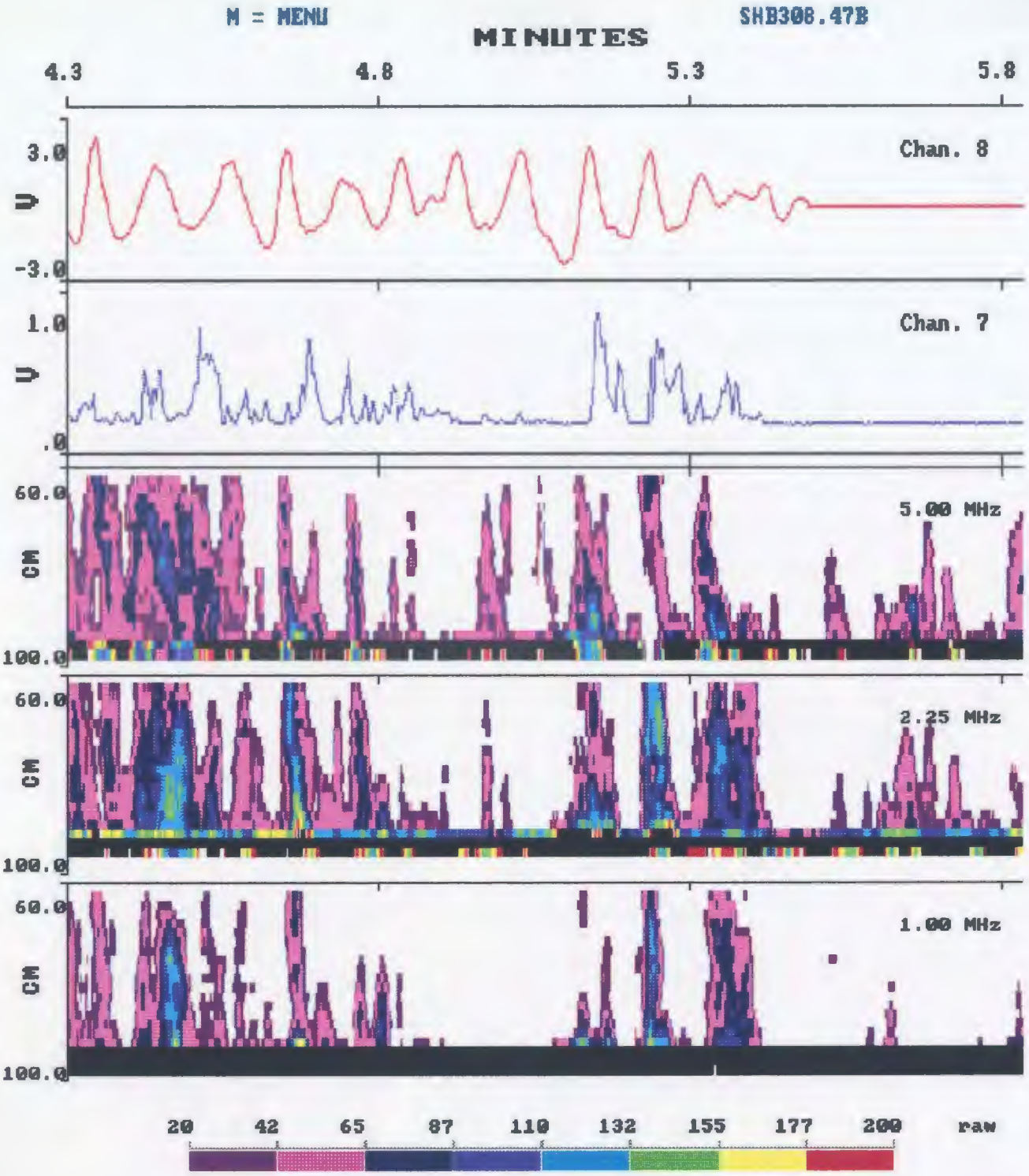

(d)

Figure 8.9. (continued)

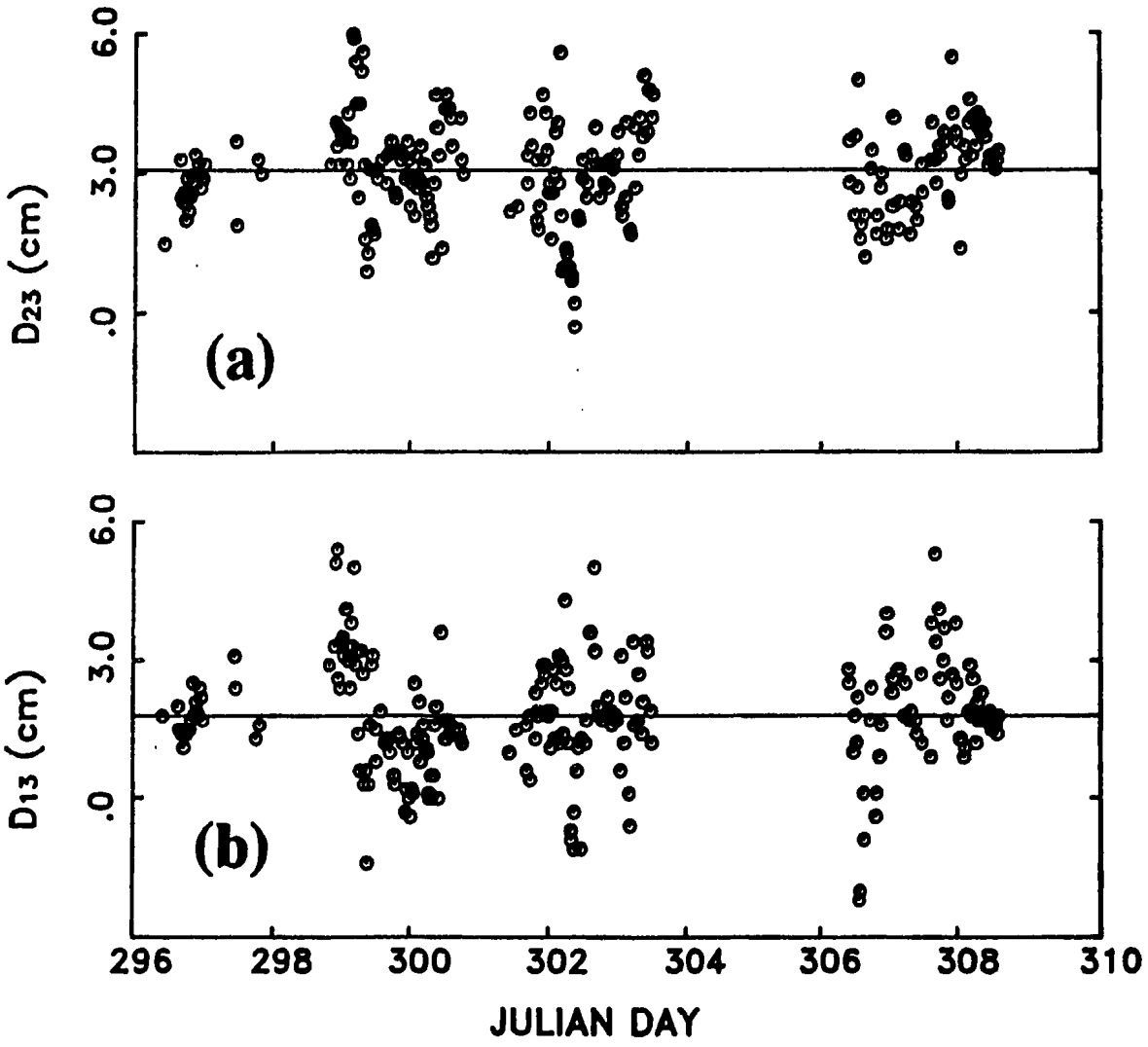

Figure 8.10. Depth differences between the pair of: (a) 2.25 and 5 MHz transducers; (b) 1 and 5 MHz transducers.

8.3 Color Images of Concentration and Size

By using the inversion method presented in Chapter 6 with the given value of $\sigma_g = 1.2$, which is nearest to σ_g for the natural SHB sand (1.25, see Table 5.1 and Figure 5.1), suspended particle concentration and diameter were extracted from backscatter data at the three different acoustic frequencies. Typical images of particle concentration and size are shown in Figures 8.11-8.13 for the three different wave energy cases, in which the curves in channels 7 and 8 are records of OBS and of cross-shore currents, respectively, as in Figures 8.4-8.6. Two color palettes are used in each figure, each serving as the scale for the color image immediately above the palette. The black color stripe near the bottom of each image indicates the bottom echo.

Color images in Figures 8.11-13 reveal considerable temporal and vertical variability of particle concentration and size. It is clear, from these images, that the strength of suspension events is associated with the energy level of the group of surface waves, rather than any individual wave, and that the resuspension of material from the bottom occurs only if the significant cross-shore velocity of the surface waves $U_{1/3}$ is large enough. It is very easy to determine the extent (the maximum height H_{max}) of each suspension event from the above figures. By choosing the maximum height to be the height above which the concentration is less than 1 g/l, then we have that H_{max} is about 10 cm in the low energy, 20 cm in the medium energy, and about 40 cm in the high energy case. It should be noted that the nearbed concentrations during strong resuspension events in Figures 8.11-8.13 are around 30 g/l or higher, which are of the same order as the near bed concentrations found by others using OBS's [e.g. Hanes and Huntley,

1986; Sternberg *et al.*, 1989].

It should be mentioned, however, that resuspension events were not always influenced solely by the groupness of the waves. A typical example is that at 0.3 to 0.6 minutes in Figure 8.13c, in which relatively little sediment suspension occurred in the whole water column during the passage of a group of large waves. The strong resuspension happened only after all big waves had passed.

Some discrete spots in the images of concentration are believed to be the contribution from high concentration eddies, seaweed, or other acoustic interference. The black near bottom of each image (see Figures 8.11-8.13), as before, is due to the sea bed, and signal amplitude in the first range bin above the bed may be affected by the migration of sand ripples.

From color images of suspended particle sizes shown in Figures 8.11-8.13, it can be seen that vertical variations of suspended particle size are much smaller than those of concentration, which is consistent with results obtained by Staub *et al.* [1984] from sediment suspension measurements in laboratory oscillatory flows. Most particle sizes in Figures 8.11-8.13 are in the range of 100 μm to 160 μm in diameter, which are slightly smaller than, or roughly equal to, the mean size of the bottom sediments d_0 =158 μm (see Table 5.1 for SHB sand, and Figure 5.1). Some spots with very large sizes, such as those at about 4.55 minutes and 78 cm range from the transducer in the low energy case (see Figure 8.11b), at about 2.35 minutes and 74 cm range in the medium energy case (see Figure 8.12b), and at many places in the high energy case, particularly at 4.5 and 5.35 minutes in the neighborhood of 75 cm in range from the transducer in Figure 8.13d, may be attributed to eddies or other aforementioned acoustic interference in the path of the sound beam.

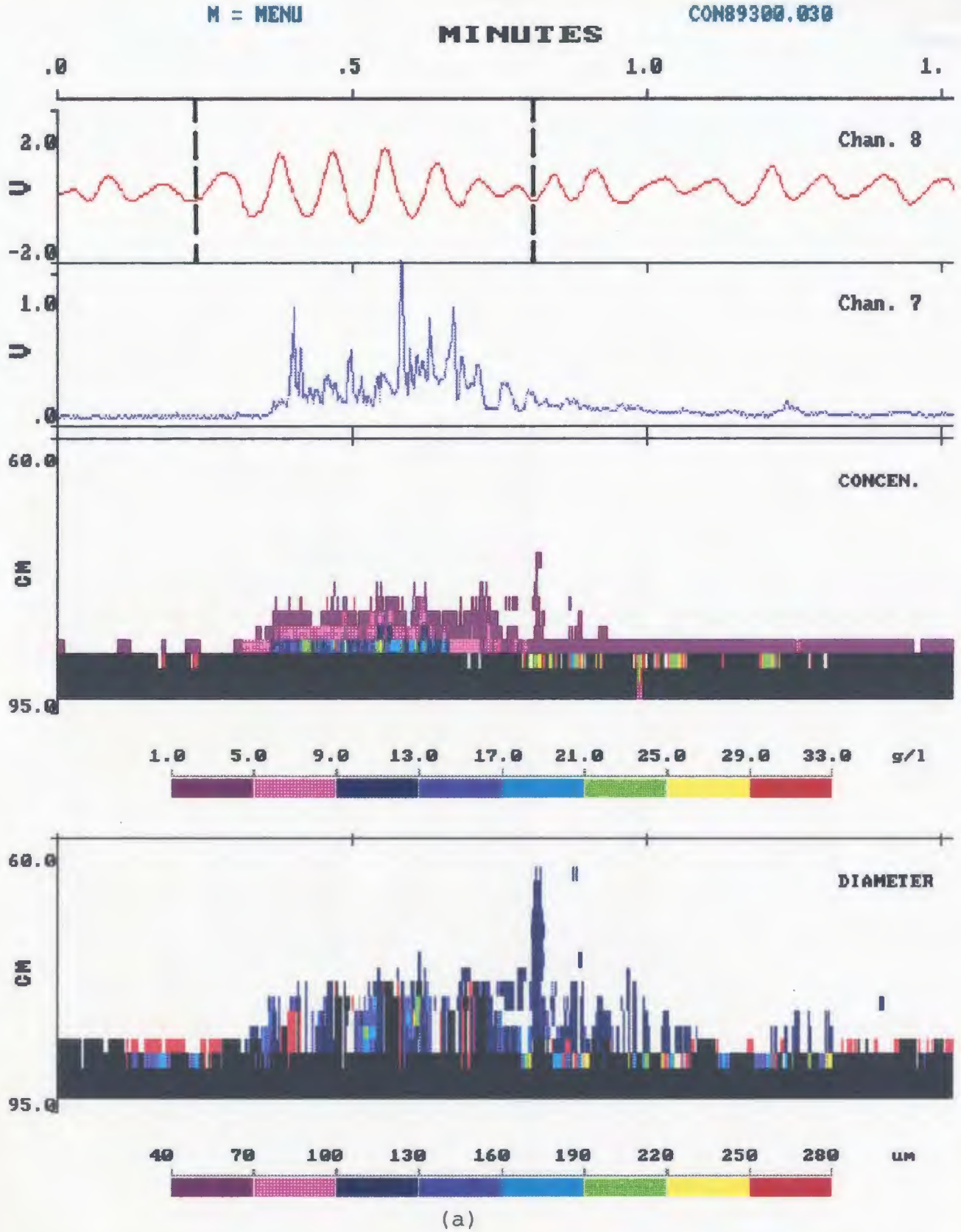

(a)

Figure 8.11. Color images of particle concentration and size inverted from multi-frequency acoustic data with records of the OBS and the flowmeter in the low energy case for: (a) Window A, dashed lines are boundaries of Event 1; (b) Window B, dashed lines are boundaries of Event 2.

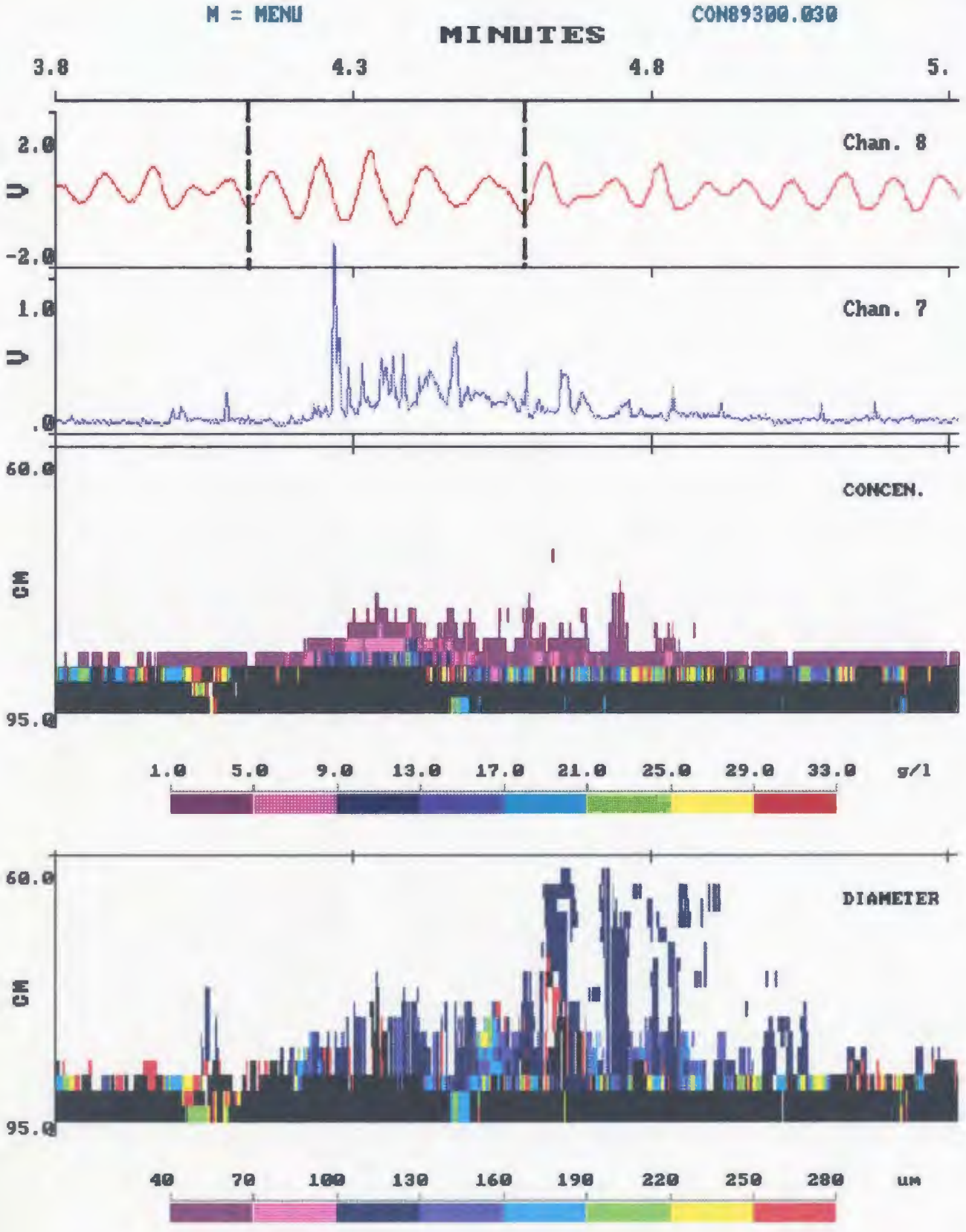

(b)

Figure 8.11. (continued)

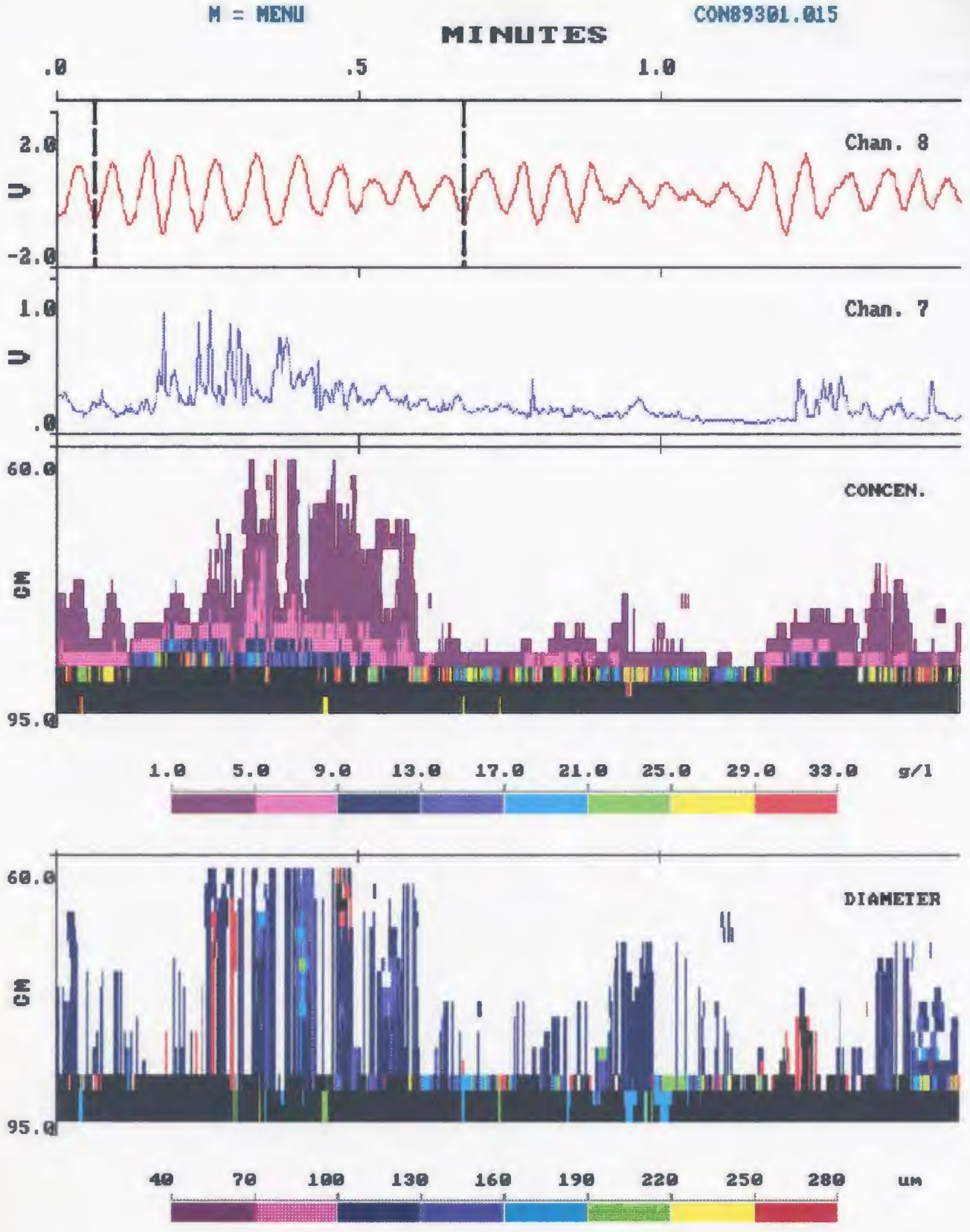

(a)

Figure 8.12. Color images of particle concentration and size inverted from multi-frequency acoustic data with records of the OBS and the flowmeter in the medium energy for: (a) Window A, dashed lines are boundaries of Event 1; (b) Window B, dashed lines are boundaries of Event 2; cb) Window C, dashed lines are boundaries of Event 3.

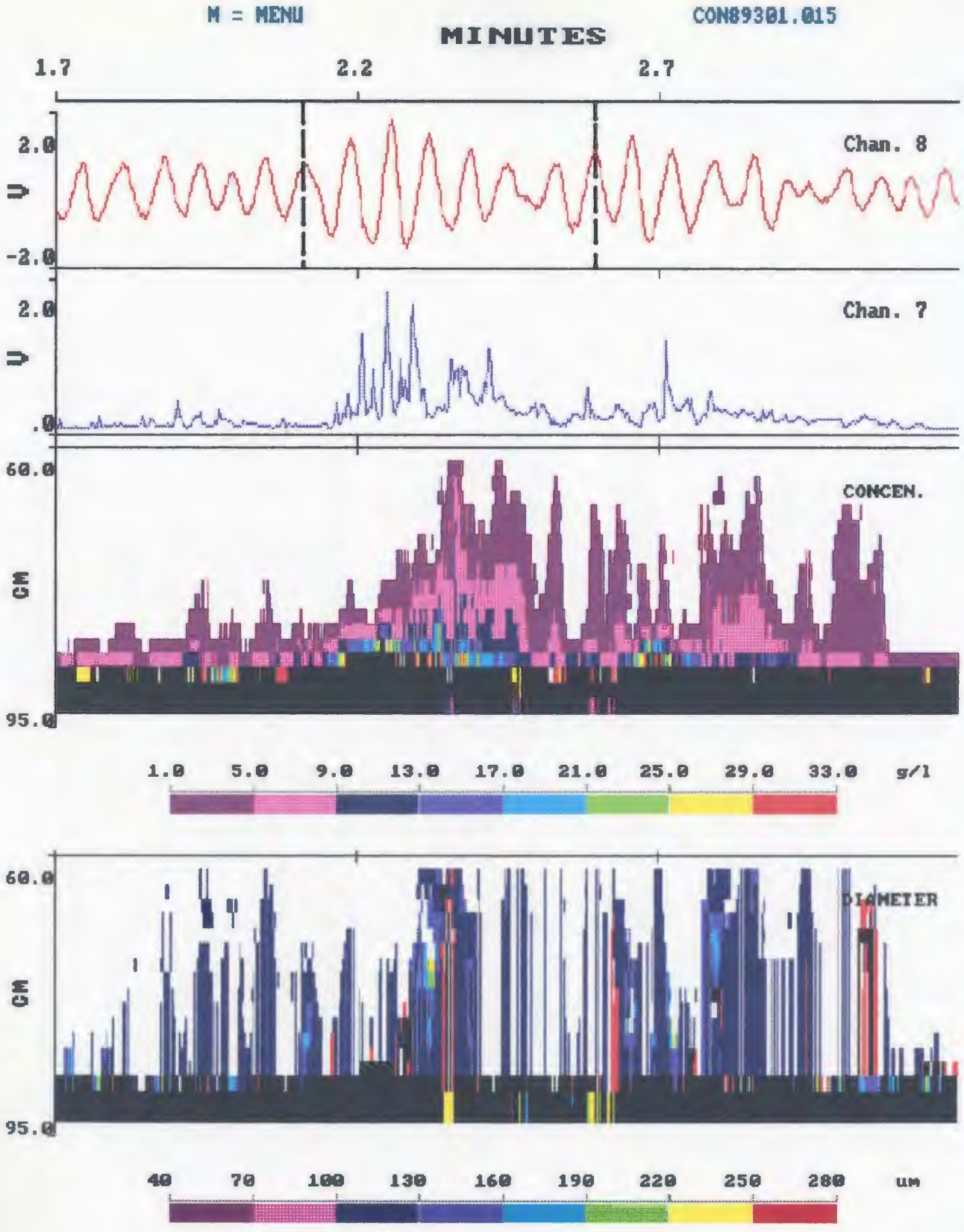

(b)

Figure 8.12. (continued)

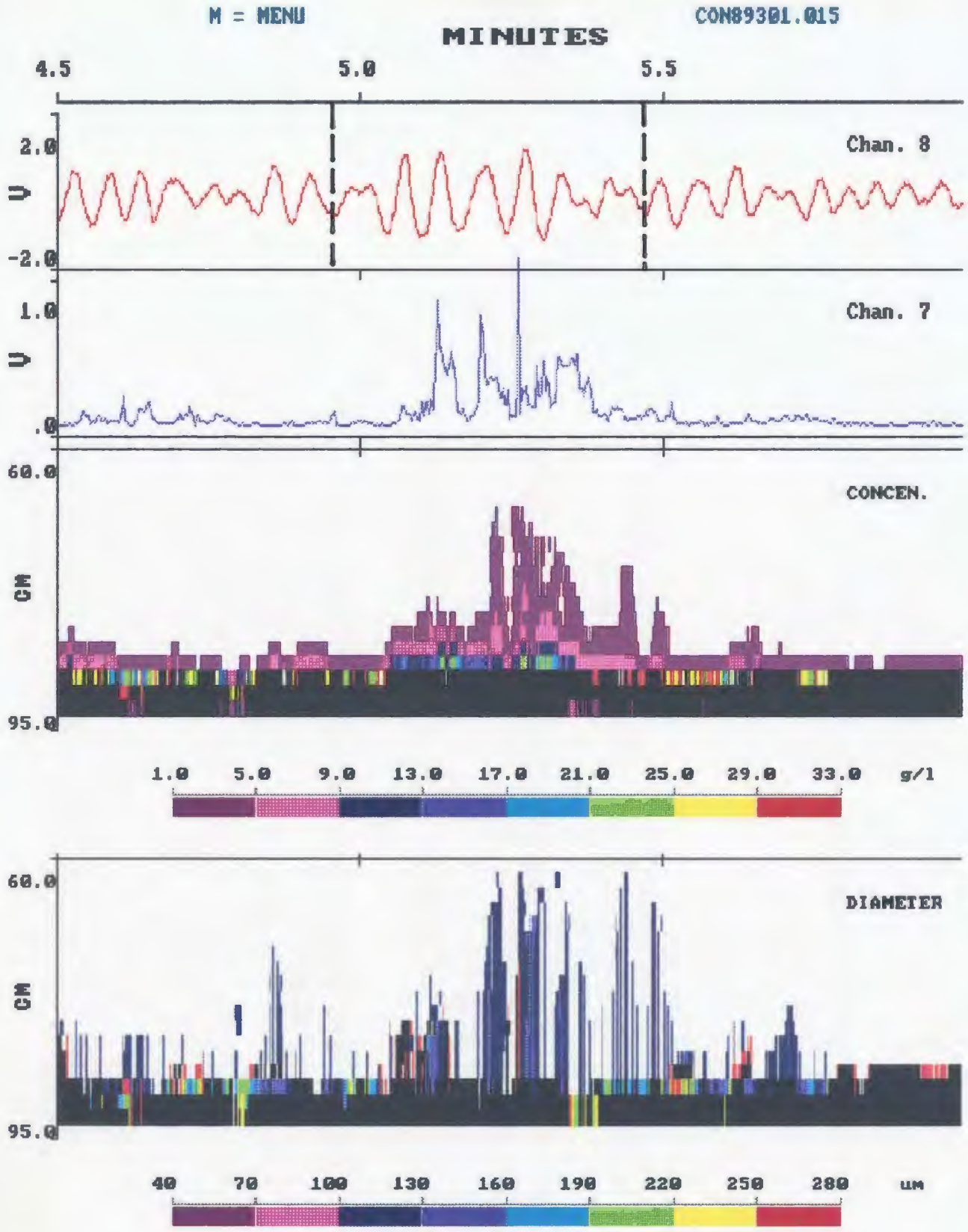

(c)

Figure 8.12. (continued)

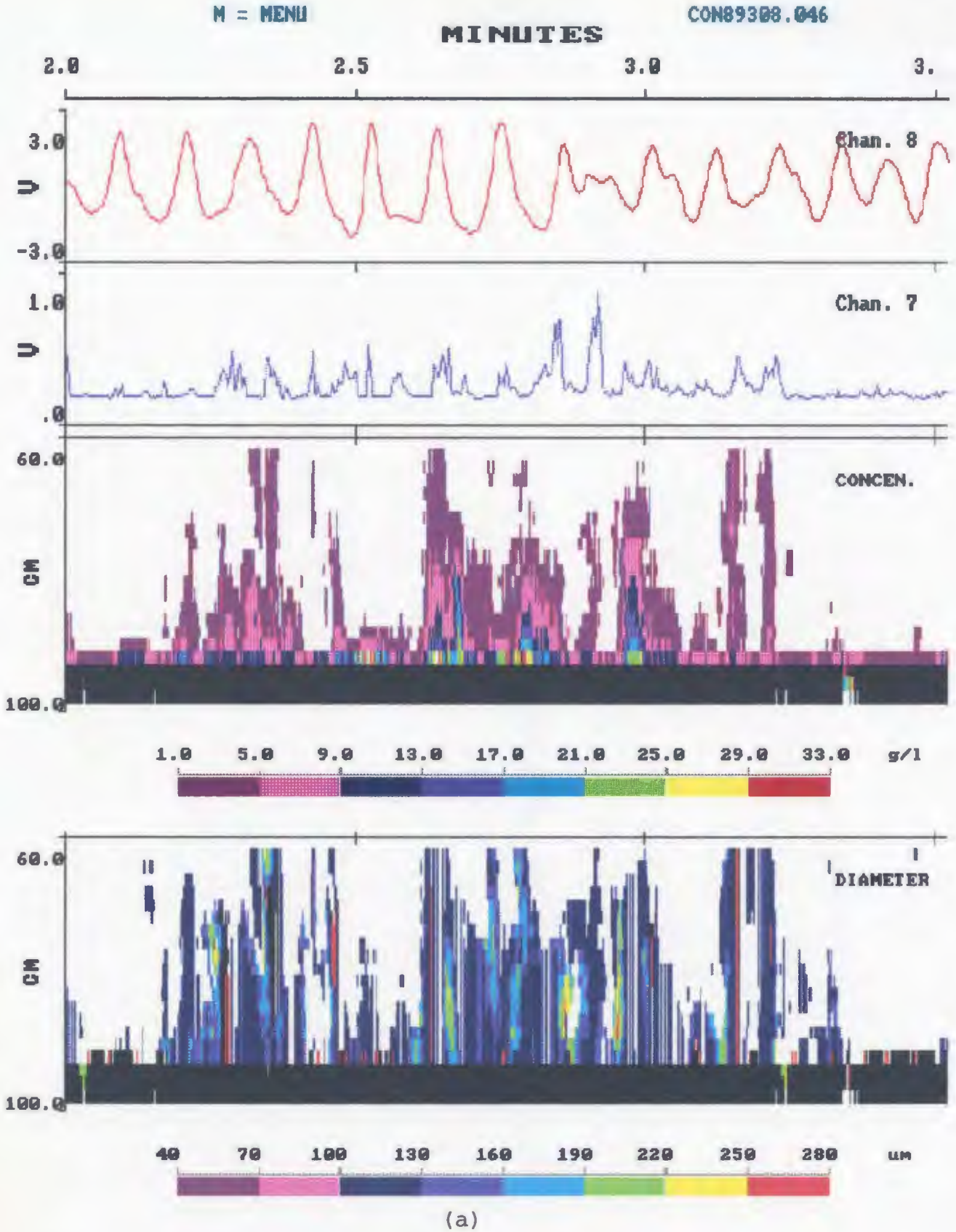

(a)

Figure 8.13. Color images of particle concentration and size inverted from multi-frequency acoustic data with records of the OBS and the flowmeter in the high energy case for: (a) Window A, and (b) Window B of SHB89308.046; (c) Window A, and (d) Window B of SHB89308.047.

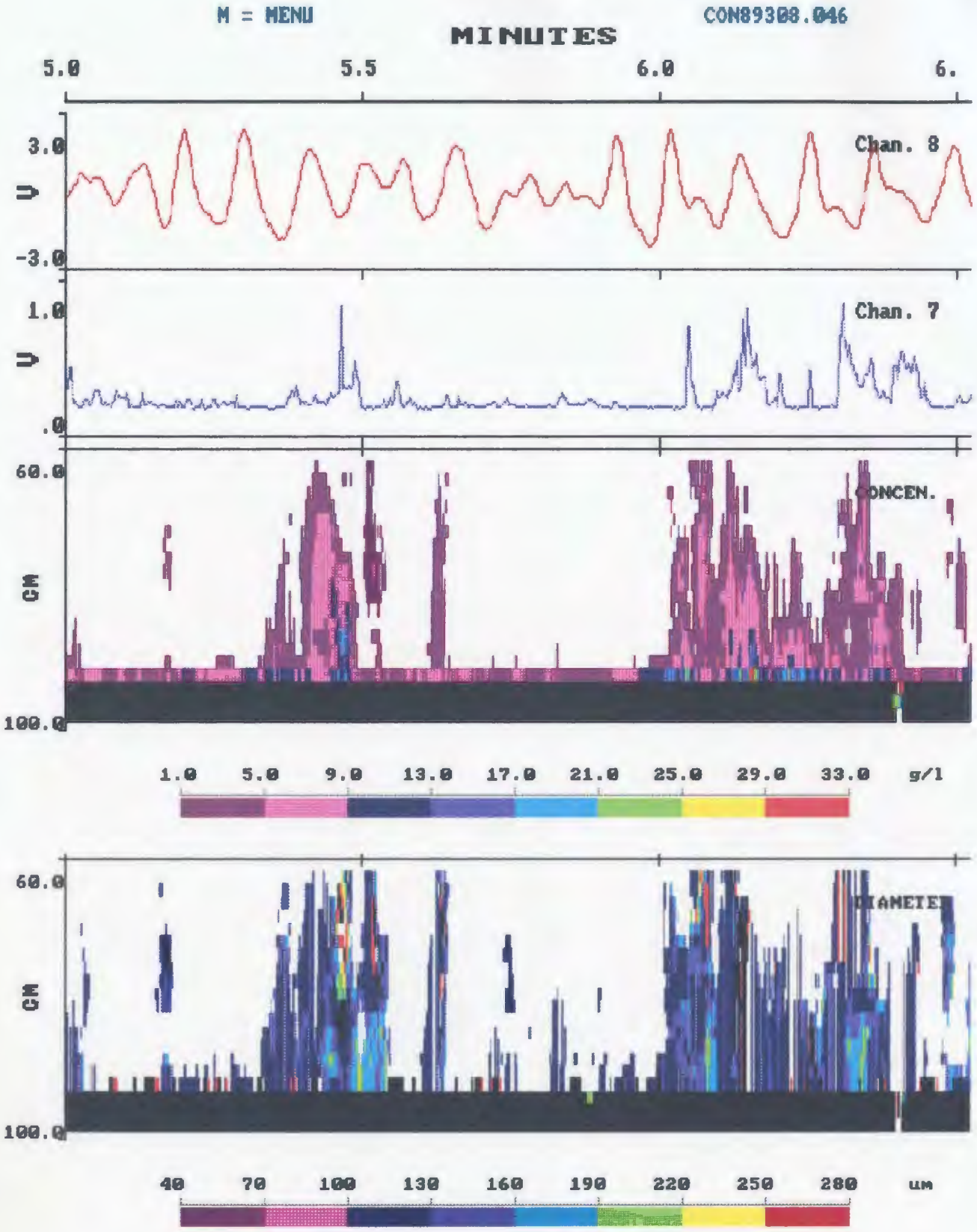

(b)

Figure 8.13. (continued)

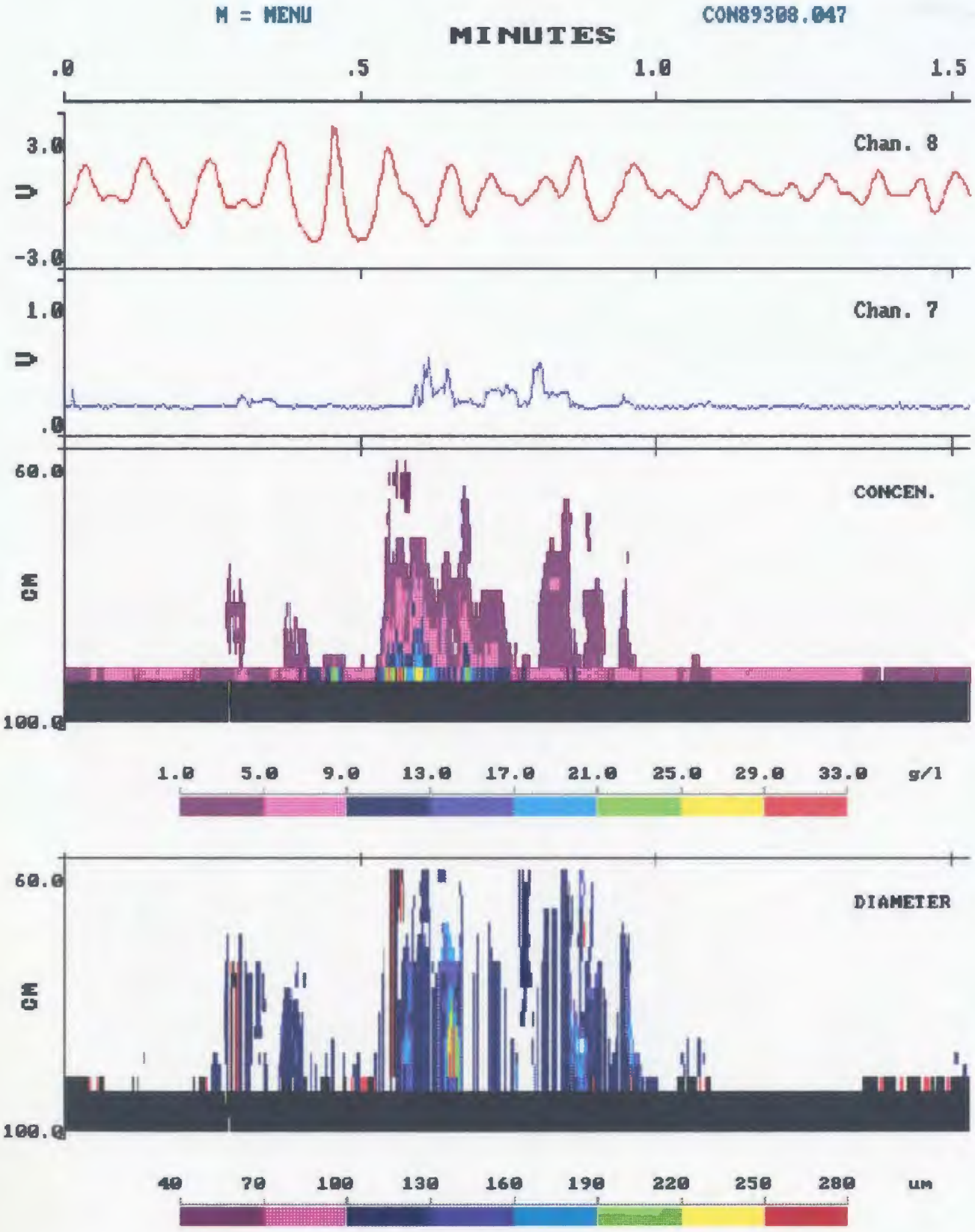

(c)

Figure 8.13. (continued)

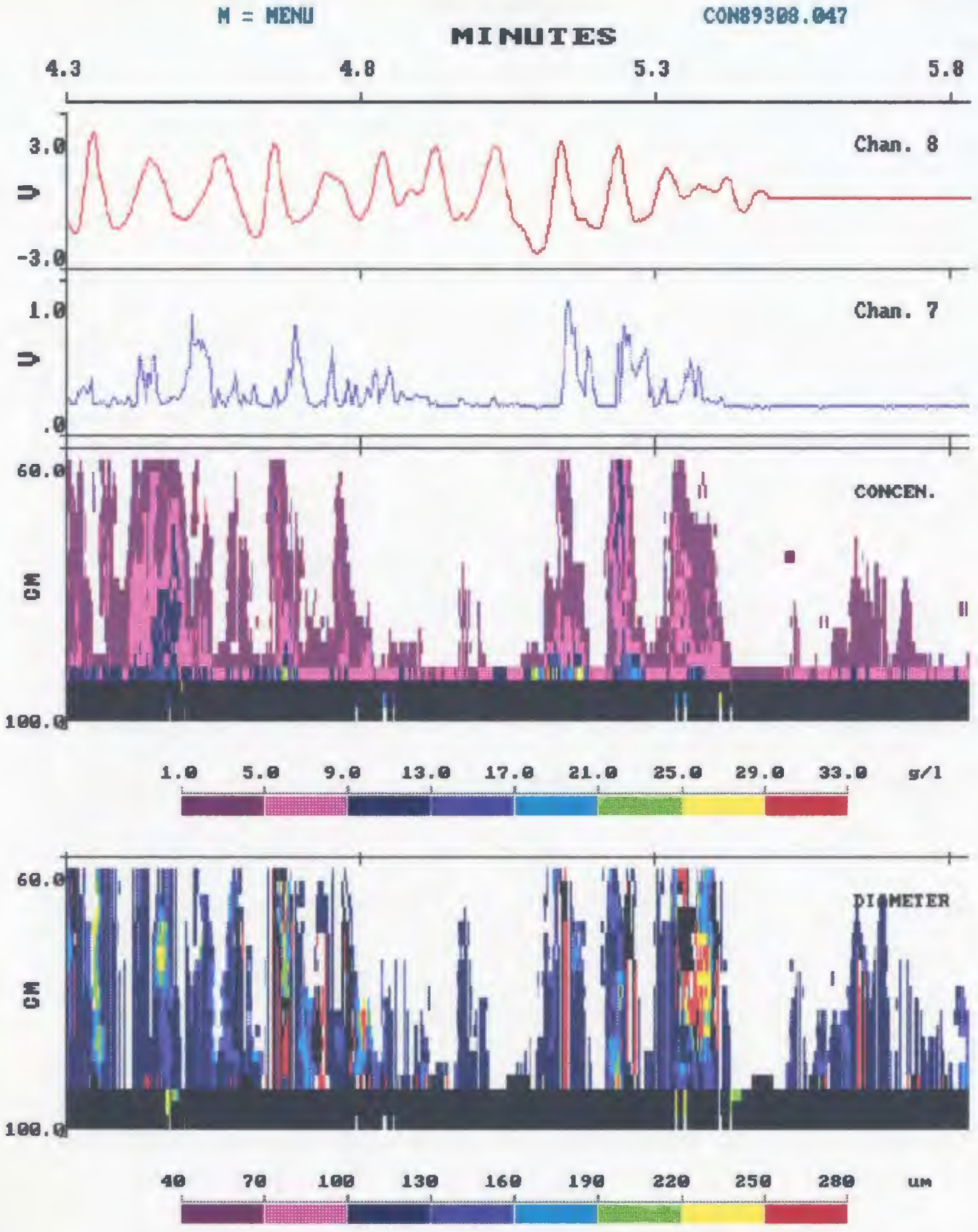

(d)

Figure 8.13. (continued)

8.4 Intercomparison between the OBS and RASTRAN data

The data from the laboratory jet experiments, which could be considered as a statistically-steady case, demonstrated that the present inversion method is adequate in estimating suspended particle concentration and size within a systematic error of +12% and -19% respectively. (Here the positive and negative signs denote respectively the overestimate of concentration and the underestimate of size by the inversion method). The effectiveness of the method for unsteady cases, such as the suspension stimulated by surface waves in the surfzone, however, is still unproved.

It has been discussed elsewhere [e.g. Hanes and Huntley, 1986] that the OBS, developed by Downing *et al.* [1981], is well suited to the measurement of suspended sediment concentrations up to 100 g/l at discrete, fixed points in the nearshore wave-dominated zone. In this section, we will present the intercomparisons of OBS data and RASTRAN data at the same depth.

It should be emphasized, however, that OBS records used here are those collected by the sensor located 1.6 meter shoreward of the cluster of three acoustic sounders (Figure 2.6). Therefore, point-by-point comparison of time series for the two systems is less meaningful due to the large spatial separation. Nevertheless, comparisons between concentrations averaged over many wave cycles during the same time interval can be made. The aforementioned three time segments are used in this section and in the following sections: the complete run of about 6.5 minutes, the entire window of about 1.5 minutes (600 sets, see Table 8.2, and Figures 8.11-8.13), and single events (see also Table 8.2, and Figures 8.11, 8.12), which are all longer than several surface wave cycles.

The beam pattern of the OBS is about 30° full width in the horizontal, 50° in the vertical, and 20 cm in maximum range (based on the manufacturer's specifications of OBS; see also Downing *et al.*, 1981). At 10 cm range, the optical beam therefore spans 9 cm in the vertical. It is desirable, therefore, to compare OBS data with vertically-averaged RASTRAN data. Since also the detected volume of the OBS is expected to decrease with increasing concentrations, because of increased attenuation, three averaging windows with widths of 1 range bin (or no vertical average), 2 range bins, and 3 range bins are used here. It should also be noted that the OBS data presented here are those converted through the calibration relation, which was obtained using the surficial sand collected from the deployment location of instruments in the field. It is therefore assumed, for the OBS, that the size of suspended sediments at any time and at any height is the same as that used in the laboratory calibration.

Time mean concentrations made by OBS (M_{OBS}) and those made by RASTRAN (M_R) are plotted in Figure 8.14 in the form of scatter diagrams, in which the different time segments are represented by different symbols. The cross denotes the mean value averaged over the complete run, the circle denotes the value over the entire window, and the triangle denotes the value over a single event. The solid lines in Figure 8.14 represent perfect agreement between OBS data and RASTRAN data, and the dashed lines are the linear regression lines constrained to pass through zero. R_{zy} is the linear correlation coefficient, and D_{yz} is the systematic difference between OBS data and RASTRAN data, which is defined by

$$D_{yz} = \sum_{i=1}^{I} \frac{1}{2} \frac{\left| M_R - M_{OBS} \right|}{M_R + M_{OBS}} \tag{8.1}$$

in which I is the total number of data points in the plot.

Figure 8.14 shows that the time-mean concentrations measured by the two systems over equal time intervals are well correlated whether or not the RASTRAN data are averaged in the vertical. Nevertheless, the 3-bin average gives the largest correlation coefficient (0.94). The linear regression line in the 3-bin average, however, is farthest from the perfect agreement line, while the linear regression line in the 2-bin average is closest to the perfect agreement line. Both above facts indicate that the RASTRAN data with the 2-bin average provide the best fit to OBS data, which is particularly true for $M_{OBS}>2$ g/l. The smallest correlation coefficient in the 2-bin average is mainly attributed to a great degree of scatter for the data with $M_{OBS}<2$ g/l (Figure 8.14). The systematic differences for all three vertical averages are similar and large, about 35-36%, which could be understandable considering the large separation of the two system, spatial variations of particle concentrations, and the unknown effects of changes in particle size and detected volume in the OBS signals. All above statistical parameters are also listed in Table 8.3.

Table 8.3. Some statistical coefficients of intercomparison between RASTRAN data and OBS data shown in Figures 8.14 and 8.15. The values in the parentheses are those calculated from the data for $M_{OBS}<2$ g/l.

Window Width	R_{yz}	D_{yz}	Slope
1 bin	0.91 (0.63)	36% (36%)	1.25 (1.02)
2 bins	0.87 (0.47)	35% (39%)	1.04 (0.86)
3 bins	0.94 (0.79)	36% (33%)	1.47 (1.19)

The data in Figure 8.14, but for M_{OBS} <2 g/l, are replotted in Figure 8.15. The corresponding statistical coefficients are tabulated in Table 8.3. It can be seen, from Figure 8.15, that the 3-bin average gives the highest correlation coefficient, and the smallest systematic difference, both of which indicate that the RASTRAN data with the 3-bin average provide the best fit to OBS data for M_{OBS} <2 g/l. Although the linear regression line in the 1-bin average (or no vertical average) is closest to the perfect agreement line, the data in this case exhibit a greater degree of scatter. The results with the 2-bin average, on the other hand, provide the worst fit to OBS data in the light of the correlation coefficient and the systematic difference (Table 8.3). It should be also noted that the linear correlation coefficients for all three averaging windows in Figure 8.15 are smaller compared with those in Figure 8.14, which are seen to be a possible artifact of the single high concentration point at M_{OBS} ~3.3 g/l.

The fact that the 2-bin average of RASTRAN data for M_{OBS} >2 g/l and the 3-bin average of RASTRAN data for M_{OBS} <2 g/l give the best fit to OBS data could perhaps be explained by considering the aforementioned fact that the detected volume of OBS is smaller when the particle concentration is higher, so that fewer range bins should be averaged in the RASTRAN data for purpose of comparison.

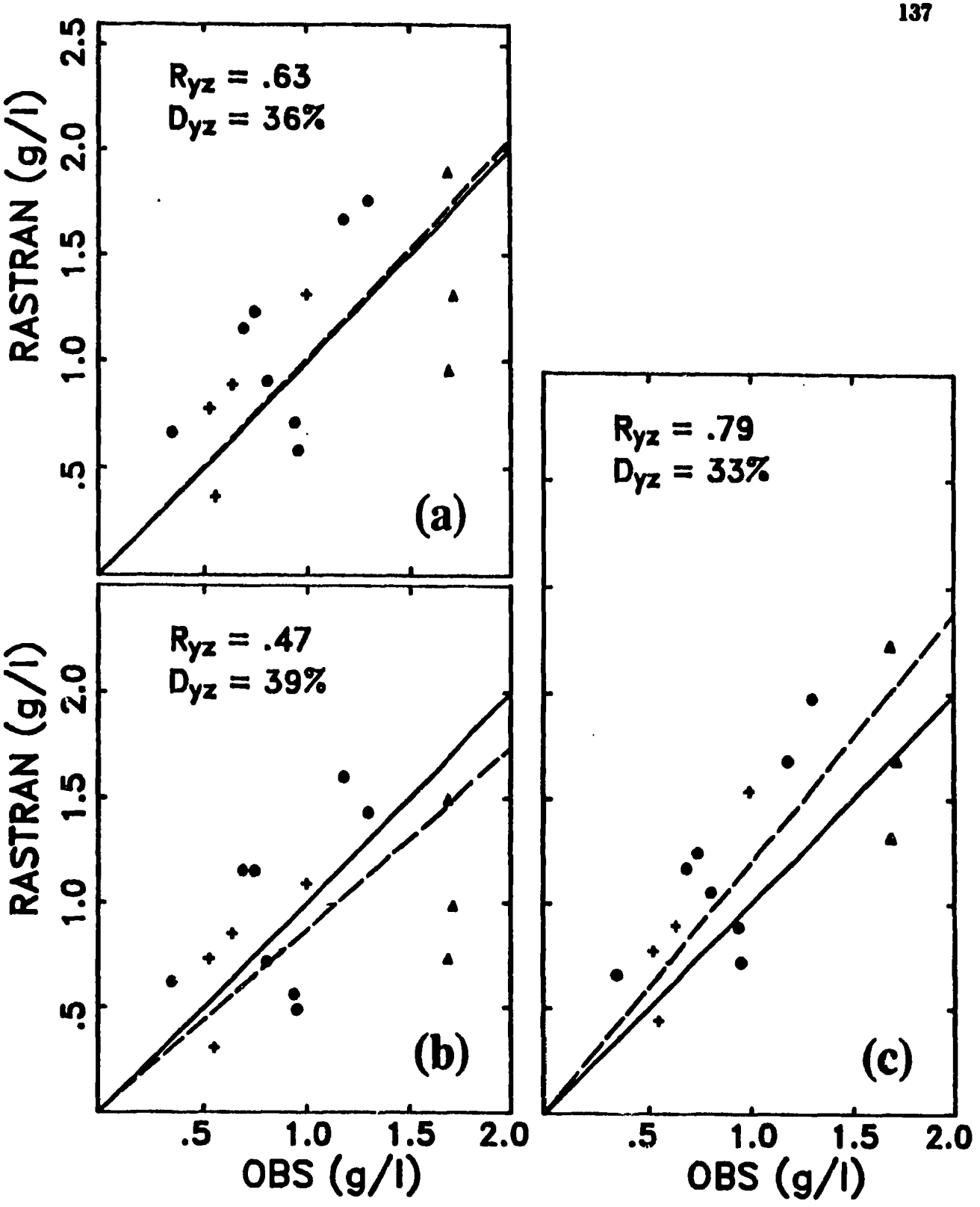

Figure 8.15. Intercomparison of mean concentrations over the same time periods between OBS data and RASTRAN data for $M_{OBS} < 2$ g/l in the case of (a) no vertical average; (b) the 2-bin average; (c) the 3-bin average.

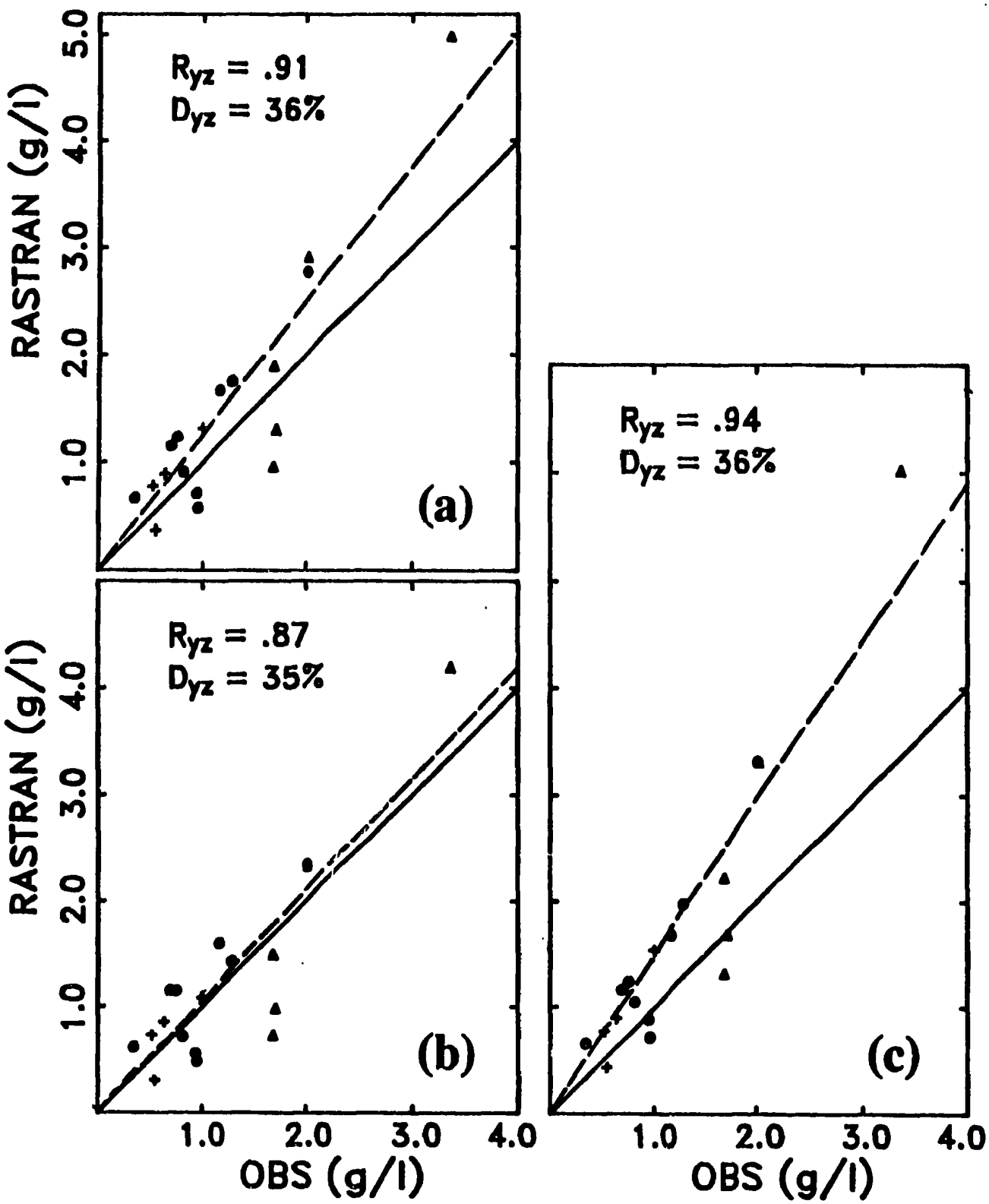

Figure 8.14. Intercomparison of mean concentrations over the same time periods between OBS data and RASTRAN data at the same depth in the case of (a) no vertical average; (b) the 2-bin average; (c) the 3-bin average.

Figures 8.16-8.18 show time series of OBS and RASTRAN data at the same depth with the velocity records appearing at the top of the plots. The RASTRAN data are those averaged over 3 range bins. The similarity in the low-frequency variations of the OBS and RASTRAN time series in the low and high energy cases (Figures 8.16-8.18) further demonstrates the ability of the RASTRAN system and the inversion method in measuring sediment transport in natural dynamic environments. In the medium energy case shown in Figure 8.17, however, the low-frequency variations of RASTRAN data in three resuspension events, i.e. in periods of 0.1 to 0.5 minutes, 2.2 to 2.7 minutes, and 5.0 to 5.4 minutes, are larger than those of OBS data, and the difference in the second event, particularly, is very noticeable. These large differences in the low-frequency values between OBS and RASTRAN data in the medium energy case are the main cause for the large discrepancy in the high concentration points in Figure 8.14. It should also be noted there exist large differences in the high-frequency variations between OBS and RASTRAN data (see Figures 8.16-8.18), which are probably due to the large spatial separation of the two systems.

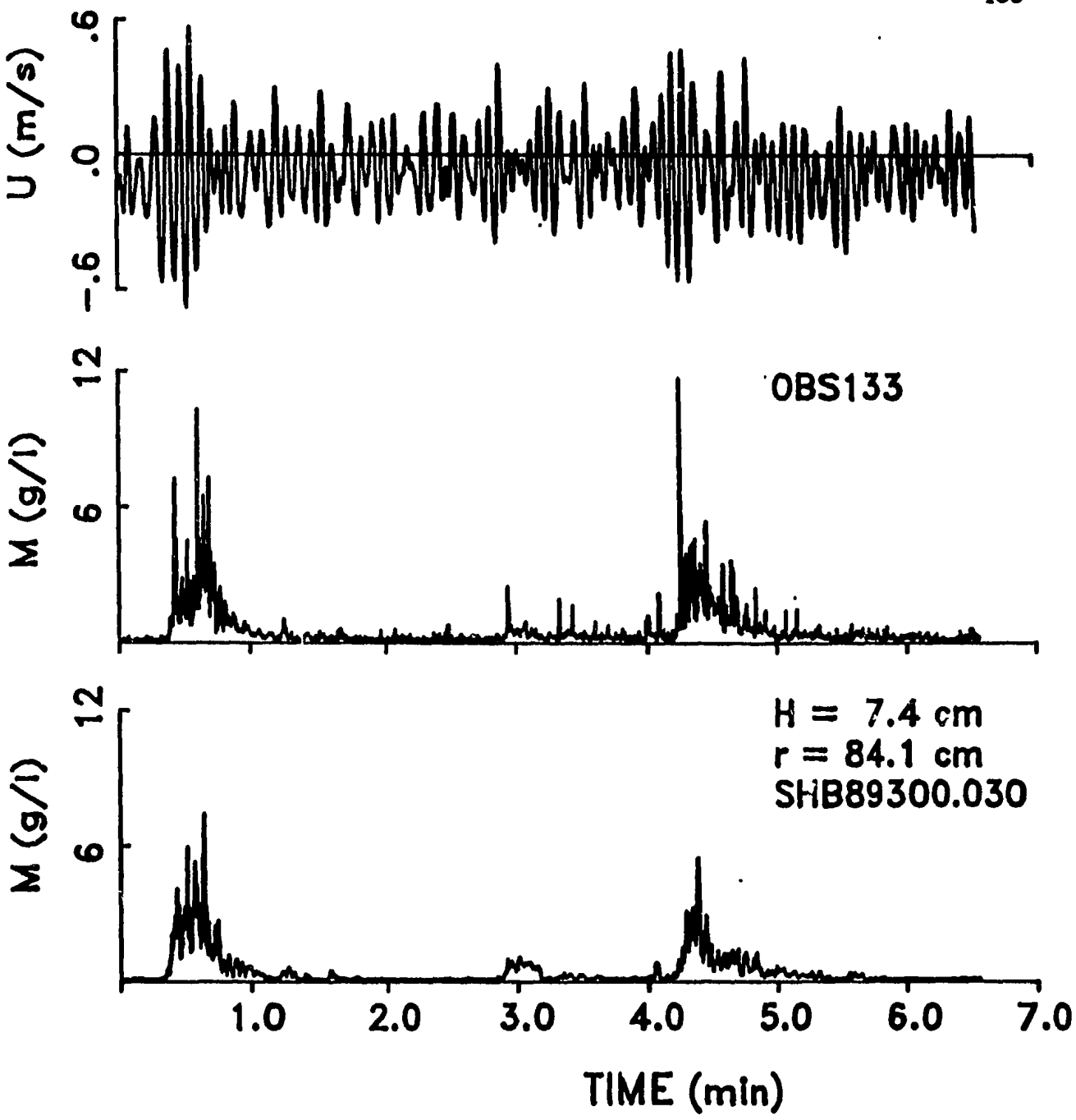

Figure 8.16. Time series of concentrations measured by the two systems in the low energy case. The curve appearing on the top of the plot is the cross-shore currents, converted from raw data through 1 V = 0.6 m/s. The second one is the concentration measured by OBS converted from raw data through 1 V = 10 g/l. The curve on the bottom of the plot is the concentration inverted from RASTRAN data at the selected range, in which both H, the height of the range bin from the bed, and r, the distance of the range bin from the transducer, were used to indicate where the RASTRAN data are selected to be plotted here.

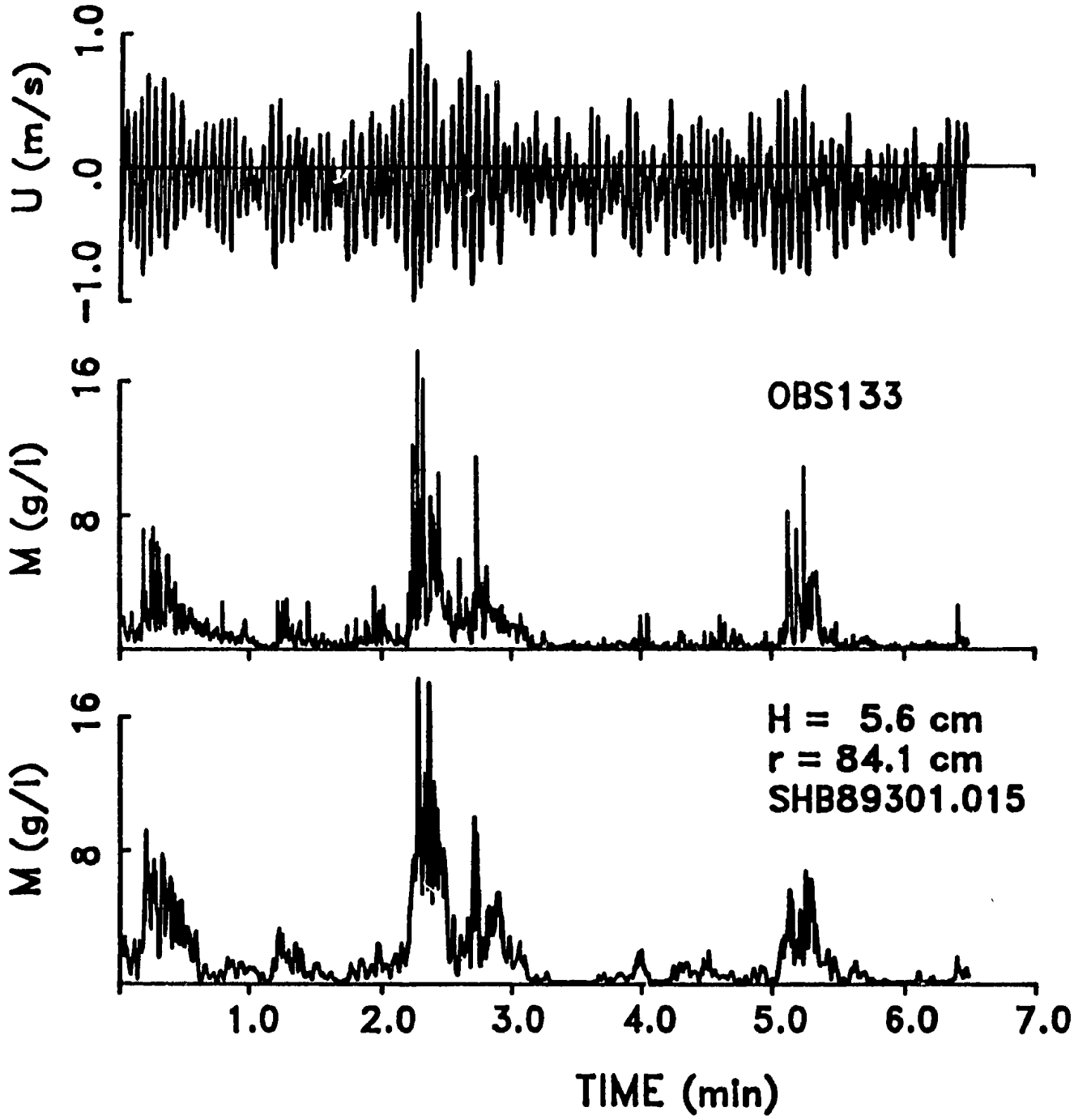

Figure 8.17. Time series of concentrations measured by the two systems in the medium energy case. Otherwise as in Figure 8.16.

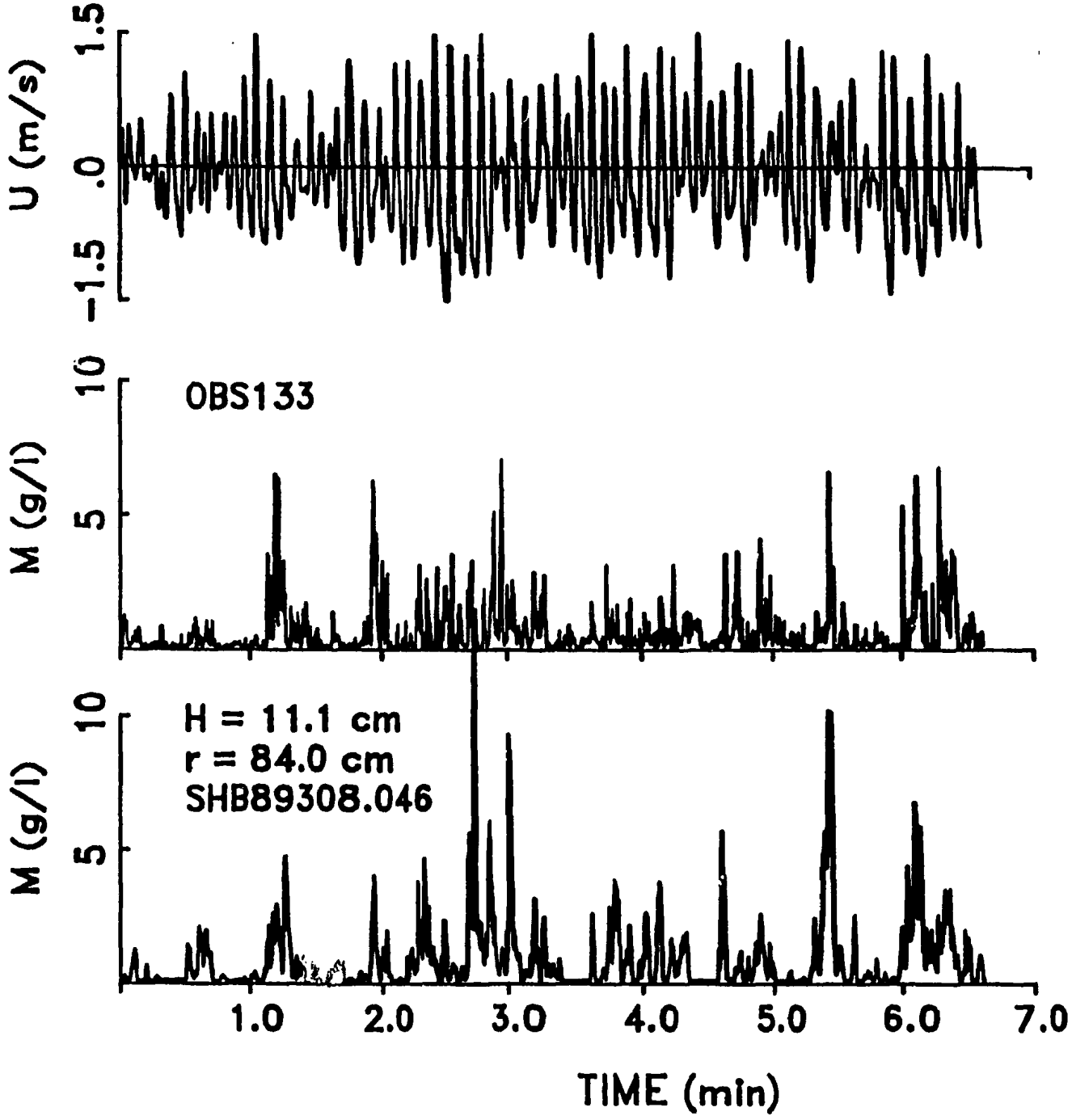

(a)

Figure 8.18. Time series of concentrations measured by the two systems in the high energy case for two consecutive runs: (a) SHB89308.046, (b) SHB89308.047. Otherwise as in Figure 8.16.

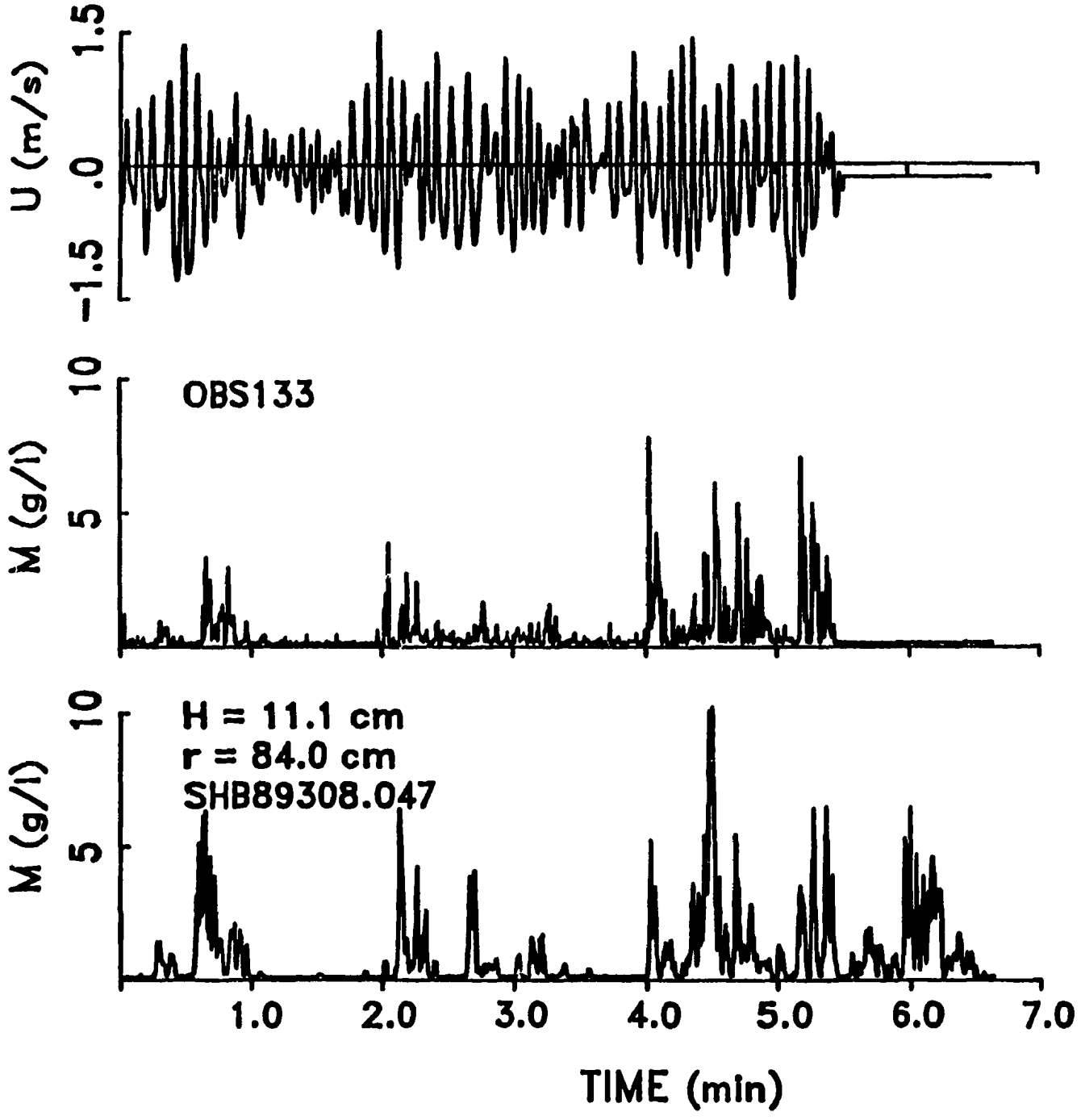

(b)

Figure 8.18. (continued)

8.5 Averaged Vertical Profiles of Concentration and Size

Time-averaged profiles of particle concentration and size were calculated over three different time intervals: the complete run of about 6.5 minutes, the entire window of about 1.5 minutes, and single events of about 30 seconds (see Table 8.2).

Figure 8.19a shows time-averaged profiles of particle concentration over the complete run for three cases of wave energy in the form of a semilogarithmic diagram. It can be seen that the averaged maximum height H_{max} of sediment suspension over the entire data run strongly depends on the wave energy. By choosing the maximum height H_{max} to be the height above which the time-averaged concentration is less than 0.2 g/l, then we get H_{max} is about 8 cm in the low energy, 25 cm in the medium energy, and 35 cm in the high energy case, which are comparable to those obtained from the color images in Section 8.3 (where the instantaneous concentration of 1 g/l was chosen as the criterion). It should be noted that the inverted particle concentrations and sizes for heights above about 15 cm in the low energy, 38 cm in the medium energy, and 45 cm in the high energy case are not shown in Figure 8.19a, since the time-averaged concentrations are very small and change very slowly with height as well, and particle sizes dropped to the minimum resolvable value (80 μm in diameter), which could indicate that the acoustic data at these heights were mainly due to background scatterers, such as very fine particles, or biological objects in water.

The concentration profiles in Figure 8.19a indicate that in the near bed region suspension concentrations decrease with height, but the vertical profiles

can not be fitted by a straight line, which means that concentration profiles in this region are not exponential. For heights above the near bed region, however, mean concentrations do decrease approximately exponentially with height in all three energy cases, although it could be a little ambiguous in the low energy case due to the small number of data points available for heights above 10 cm. The thicknesses of the near bed region are also different: about 10 cm in the low energy; 15 cm in the medium energy; and 5 cm in the high energy case. Figure 8.19a shows that at heights below 8 cm from the bed, time-averaged particle concentrations over the same time period increase with wave energy when surface waves change from the low to medium energy condition, and then decrease with wave energy when surface waves change from the medium to high energy. At heights over 8 cm from the bed suspension concentrations always increase with wave energy for these data.

Time-averaged profiles of particle size in three energy cases are also shown in Figure 8.19a. It should be noted, however, that the time-mean value of particle size at each range bin is the average over only the sets with nonzero values of particle size, while the time mean concentration was obtained by averaging over all sets available in the given time interval. Since there are no direct measurements of particle sizes available, it is rather difficult to indicate quantitatively how the accuracy the inversion method could be in estimating particle sizes. Nevertheless, on the basis of the laboratory measurements, any variation of greater than 15% in the time-averaged particle sizes could be significant.

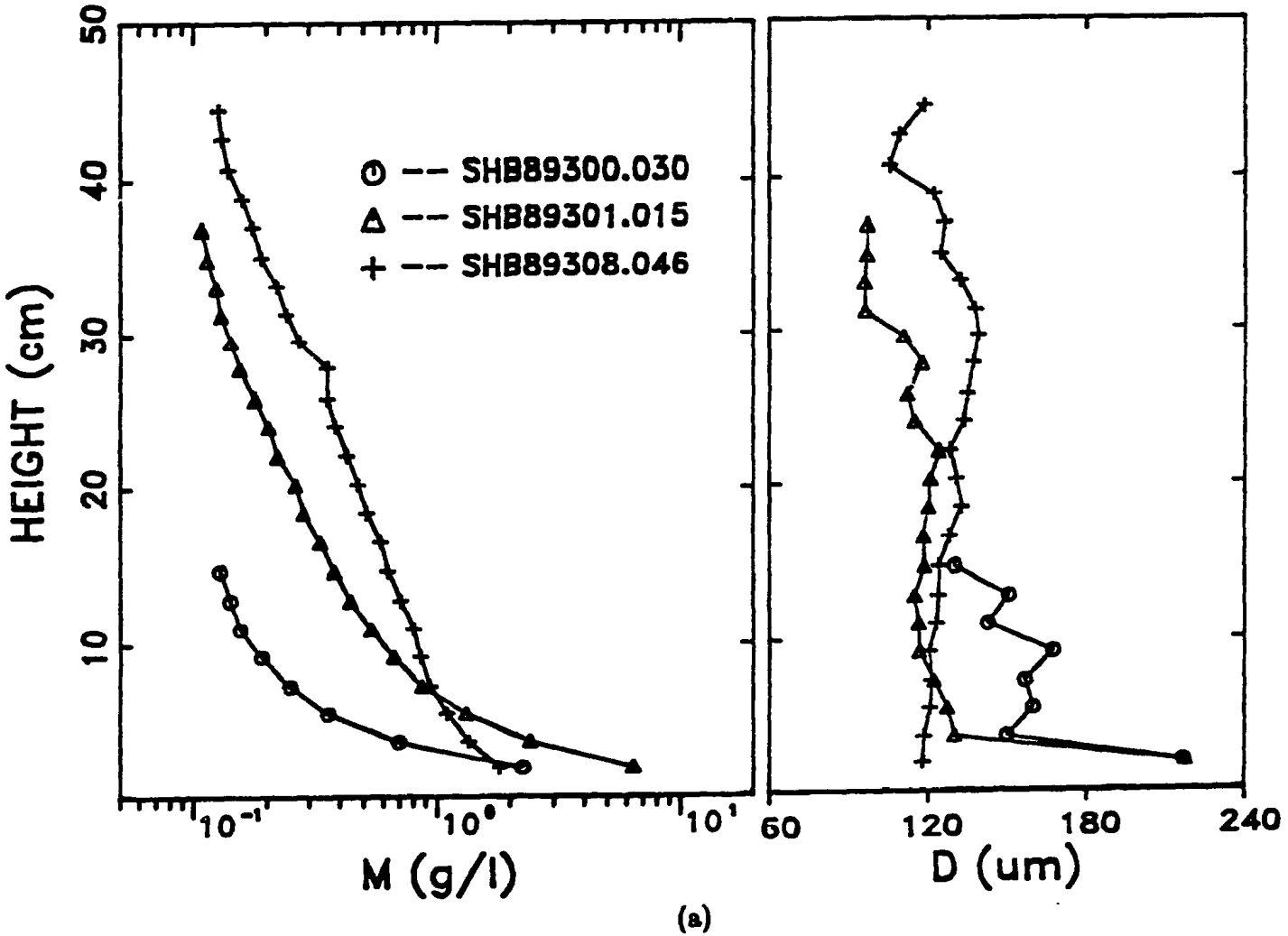

Figure 8.19. (a) Time-averaged profiles of particle concentration and size over the complete run in the three energy cases. Concentration profiles are plotted in the form of a semilogarithmic diagram. (b) Vertical profiles of particle concentration are plotted in the form of a log-log diagram.

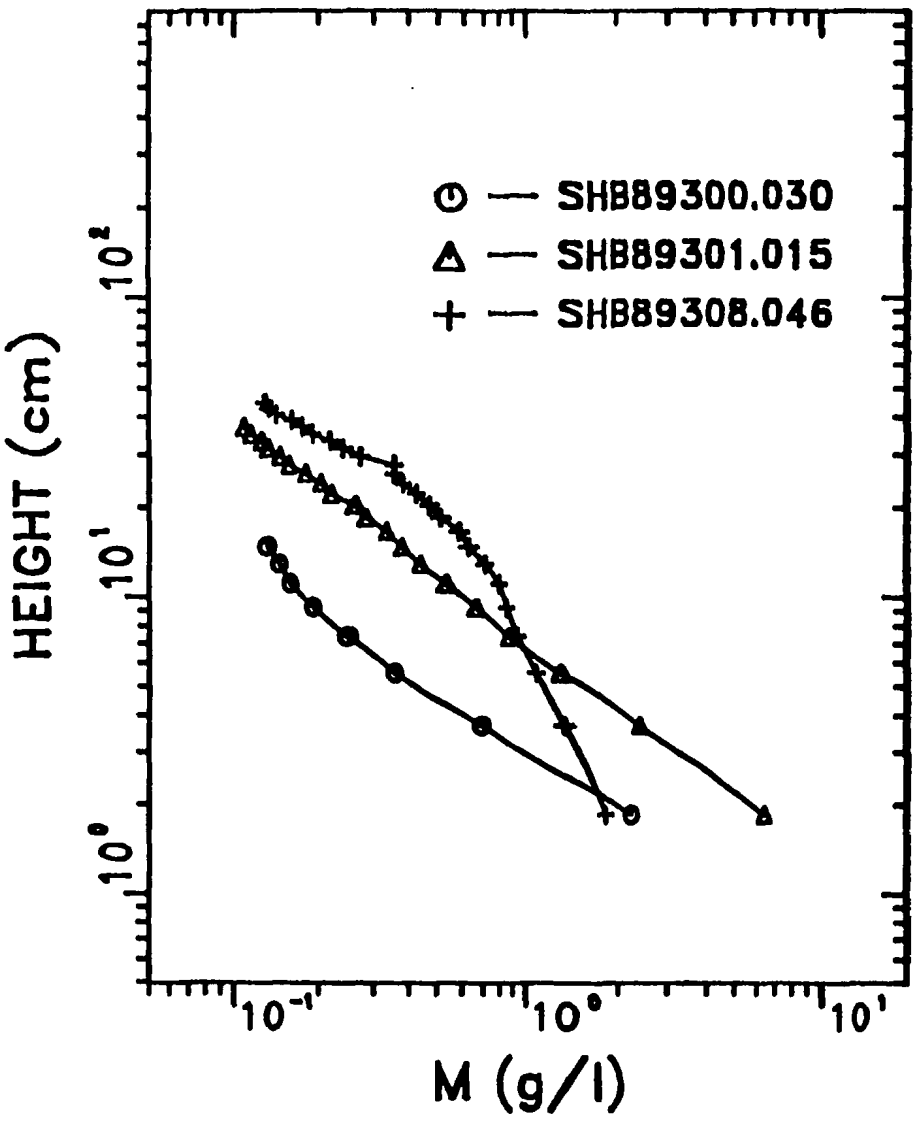

(b)

Figure 8.19. (continued)

It can be seen, from Figure 8.19a, that variations in size with height are really quite small, especially compared to variations in concentration with height, which is comparable to the laboratory results obtained by Staub *et al.* [1984]. Except for the first range bin above the bed, particle sizes for the three energy cases are almost uniform up to a minimum height, which varies with energy: about 12 cm in the low energy case; 28 cm in the medium energy case; and 35 cm in the high energy case. It appears, in Figure 8.19a, that suspended sediments in the low energy case have the largest particle sizes, while particle sizes are comparable in the medium and high energy cases for heights below about 25 cm from the bed. From Figure 8.19a, it can be also noticed that particle size at the first range bin next to the bed in the low and medium energy cases is greatest, roughly twice as large as those at other range bins, which could be due to the low accuracy of the inversion method in estimating particle size at this range bin, otherwise, may indicate that coarse suspended sediments were restrained only within the thin layer. Finally, the particle sizes in the near bottom bins immediately above this level, are comparable to, or less than, the medium size of the bottom sediments (Figure 5.1, Table 5.1).

An alternative way in displaying concentration profiles in the three energy cases is to use a fully logarithmic diagram. By doing so, characteristics of the vertical profiles of particle concentration in the near bed region could be determined. Time mean concentration profiles averaged over the entire run in different energy cases are plotted in Figure 8.19b in the form of a log-log diagram. It can be seen that the concentration profiles can be fitted well by straight lines in the near bed region, which suggests a power law relationship with height. For heights above the near bed region, concentration profiles can not be fitted by straight

lines in the log-log diagram shown in Figure 8.19b, which further demonstrates that there exist two distinct regions in the vertical profiles of particle concentration.

The above characteristics of time-averaged profiles of particle concentration and size are also observable in those averaged over shorter time segments, such as entire windows and single events. It will be seen, however, that there is more fine structure in the mean vertical profiles for shorter time segments.

Figure 8.20a shows profiles of particle concentration and size averaged over two selected windows listed in Table 8.2 (see also Figure 8.11) in the low energy case. It can be seen that there are no significant differences in vertical concentration profiles between the two windows, which is concordant with the fact that the significant wave velocities $U_{1/3}$ near the bed in both windows are comparable (see Table 8.2). For heights below about 10 cm, particle concentrations can not be expressed by an exponential function, while particle concentrations are small for heights above 10 cm from the bed. Vertical profiles of size in Figure 8.20a demonstrate that suspended particle sizes, except the value in the range bin nearest the bed, are approximately uniform at heights below 10 cm from the bed. The mean size in Window A (about 170 μm) is slightly greater than the mean size in Window B (about 140 μm) at these heights. For heights above 10 cm from the bed, particle sizes in Window A are also roughly uniform, but about 55% smaller than those at heights below 10 cm, while particle sizes in Window B decrease with height almost continuously. It can also be noted, from Figure 8.20a, that in both windows the particle size at the near bed range bin is larger than any other, similar to Figure 8.19a.

Time mean profiles averaged over two selected single events in the low energy case (Table 8.2, see also Figure 8.11) are shown in Figure 8.20b. It can be seen that particle concentrations in the same range bin are comparable for both events, and concentration profiles are not exponential for heights below about 12 cm from the bed, similar to Figure 8.20. The difference in particle size between the two events, however, is noticeable. Particle sizes in Event 1 are roughly uniform at heights below and above 10 cm from the bed, but the mean particle size for heights below 10 cm is about twice as large as the mean particle size for heights above 10 cm from the bed. The particle sizes in Event 2 are also nearly uniform for heights below 10 cm from the bed, but there is a peak in particle size at a height of about 10 cm, and below this height the sizes are smaller than those for Event 1.

Figure 8.21a displays time mean profiles over three selected windows in the medium energy case (Table 8.2, see also Figure 8.12), in which two distinct regions in the vertical concentration profiles can also be distinguished. Particle concentrations at heights below about 15 cm from the bed decrease with height, but are non-exponential. For heights over 15 cm from the bed concentration profiles can be fitted reasonably well by straight lines. By considering that the significant wave velocity $U_{1/3}$ in Window B is 0.71 m/s, which is the largest for these three windows; and $U_{1/3}$ in Window C is 0.51 m/s, which is smallest (see Table 8.2), it can be concluded, from Figure 8.21a, that the time-mean concentrations averaged over the same period increase with wave energy, similar to the complete run averages in Figure 8.19a. The vertical profiles of size for heights below 8 cm from the bed in Figure 8.21a also reveals features similar to those in Figure 8.19a, i.e., particle sizes in Window C, which has the lowest significant

wave velocity $U_{1/3}$, are largest, while particle sizes in other two windows are very comparable at heights between 4 cm to 15 cm from the bed. Figure 8.21a also indicates that time variations in suspended particle size are large at heights between 15 and 30 cm.

Time mean profiles over three events (Table 8.2, see also Figure 8.12) extracted from the above windows are given in Figure 8.21b, from which it can be seen that some of the features of the concentration profiles in Figure 8.21a are again present, except there is small amplitude fine structure superposed on the mean concentration profiles. Particle sizes in the three events are approximately uniform for heights below 8 cm from the bed, for which particle sizes are largest in Event 3 (about 155 μm), and smallest in Event 1 (about 120 μm). For heights between 10 cm to 30 cm from the bed, particle sizes in Event 3 are nearly uniform, but 50% smaller than those at heights below 8 cm, while particle sizes in Event 1 and Event 2 are roughly uniform (about 130 μm). For heights above 30 cm from the bed, particle sizes in both Event 1 and Event 2 drop to minimum values (about 90 μm).

Vertical profiles averaged over two selected windows in the high energy case (Table 8.2, and also see Figure 8.12) are shown in Figure 8.22 for two consecutive runs: SHB89308.046 (Figure 8.22a), and SHB89308.047 (Figure 8.22a). It can be seen from Figure 8.22a that the non-exponential region of vertical concentration profiles in the semi-log diagram is confined to very small heights from the bed, roughly about 5 cm. The time-averaged concentrations in the two windows in Figure 8.22a are comparable, which is also consistent with the similar values of the significant wave velocity $U_{1/3}$ in both windows (difference in $U_{1/3}$ between

the two windows is less than 5%, Table 8.2). Particle sizes in both windows in Figure 8.22a are also similar: they increase slightly with height up to about 25 cm in height, then decrease with height. The variations in particle size for heights below 20 cm are not significant, and the tendency for size to decrease toward the bottom could be attributed to the precision of the inversion method because of accumulated errors in the scattering attenuation correction. Particle sizes below 20 cm from the bed in Figure 8.22a, therefore, may be considered to be uniform with height. From Figure 8.22b, it can be seen that the basic features of the vertical concentration profiles in Figure 8.22a are also revealed. Particle concentrations at the same range bin in Window B are larger that those in window A in Figure 8.22b, which is consistent with the fact that the significant wave velocity $U_{1/3}$ in Window B is about 13% larger than that in Window A (Table 8.2). Vertical profiles of particle size in Figure 8.22b indicate that particle sizes are nearly uniform for heights below 20 cm in Window A, and for heights between 18 cm and 30 cm in Window B, while particle sizes increase quite rapidly with height for heights between 20 cm and 40 cm in Window A, and for heights below 18 cm from the bed in Window B. These unusual profiles of particle size in Figure 8.22b could be understandable by referring to acoustic images of particle size in Figures 8.13c and 8.13d, from which it can be seen that there are several spots at intermediate heights in the size images with relatively higher values, specifically at about 5.3 minutes and 75 cm range in Figure 8.13d, which have significant effects on the time-averaged profiles of particle size.

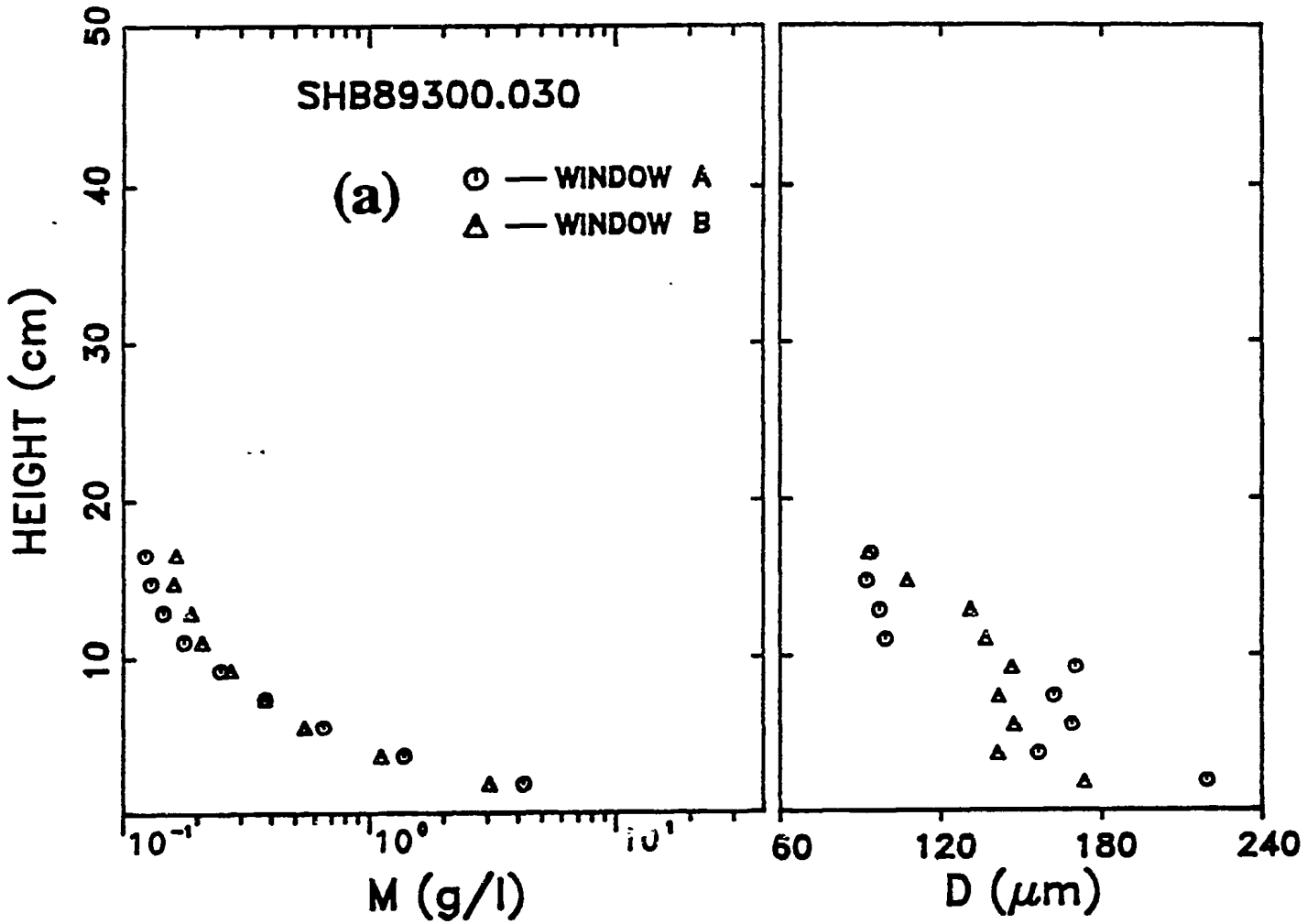

(a)

Figure 8.20. Time-averaged profiles of particle concentration and size over: (a) entire windows; (b) single events in the low energy case.

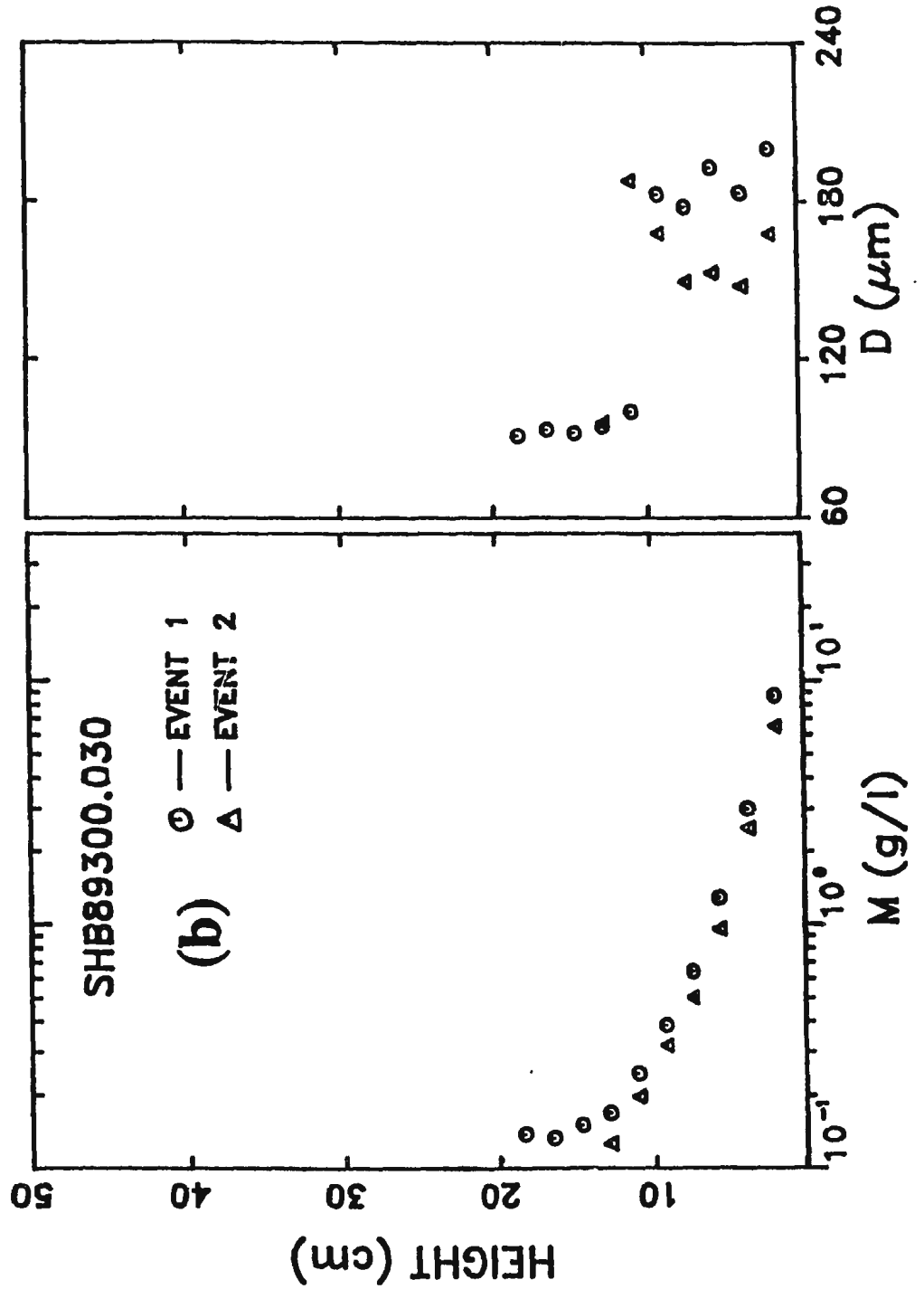

(b)

Figure 8.20. (continued)

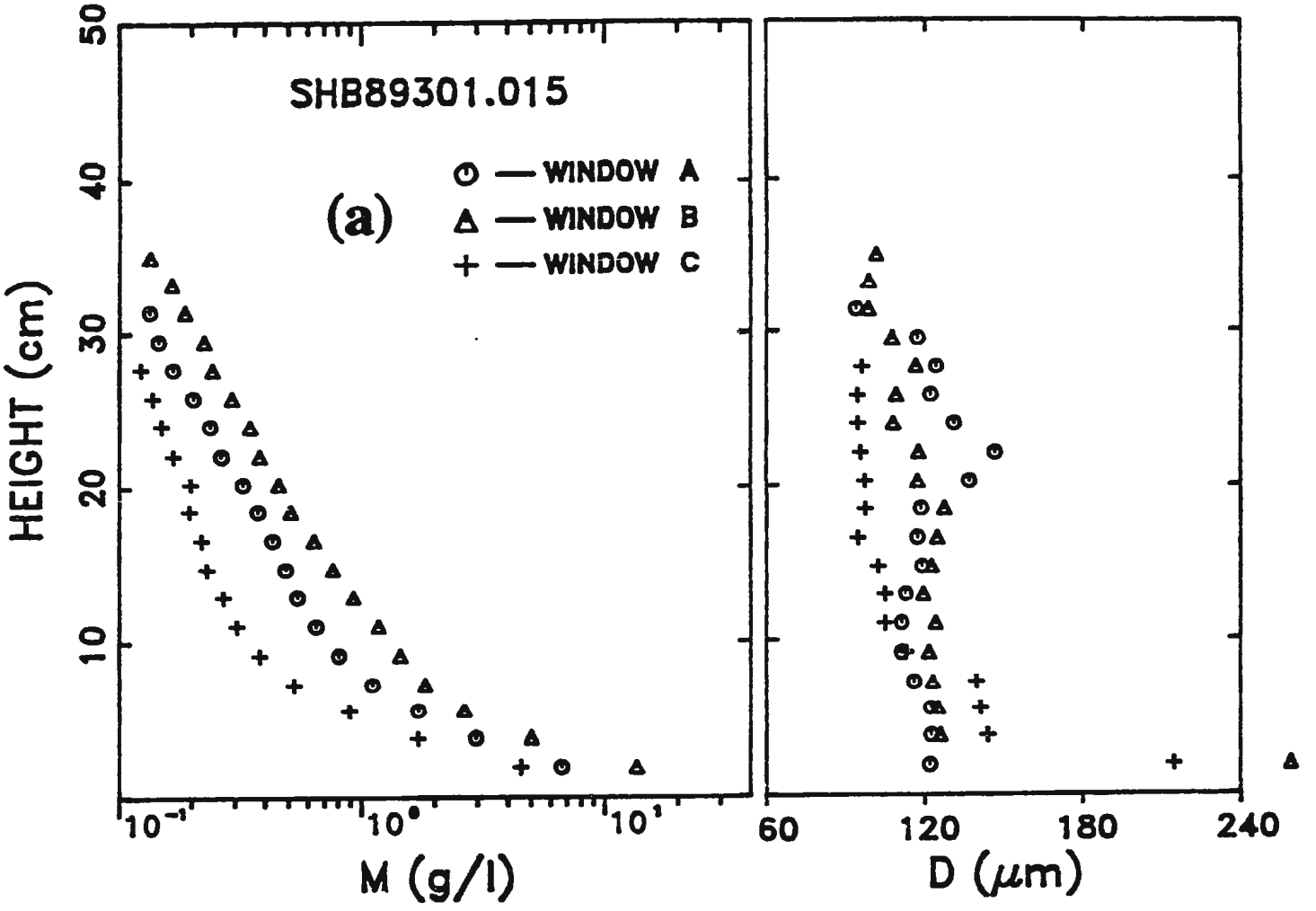

(a)

Figure 8.21. Time-averaged profiles of particle concentration and size over: (a) entire windows; (b) single events in the medium energy case.

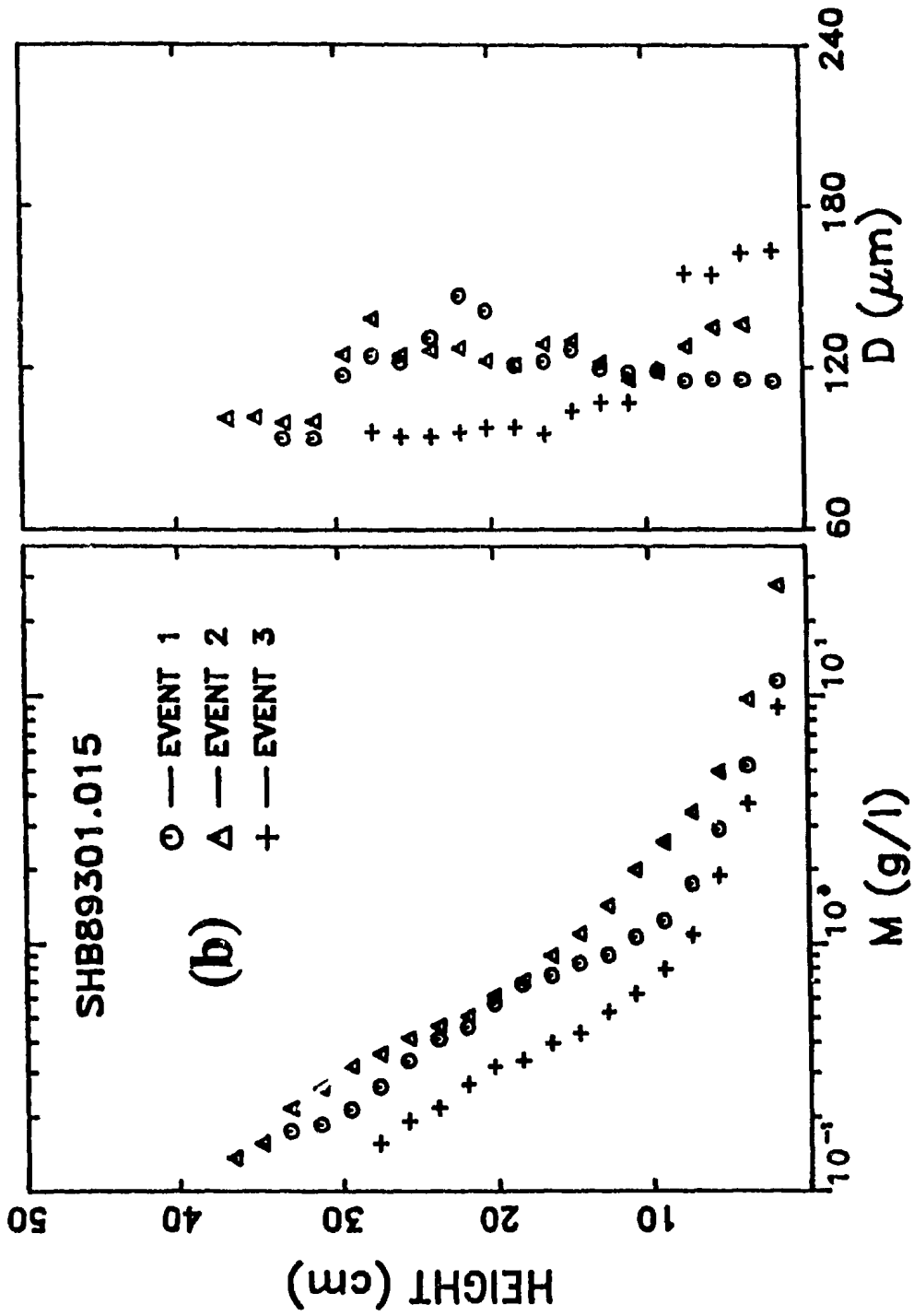

(b)

Figure 8.21. (continued)

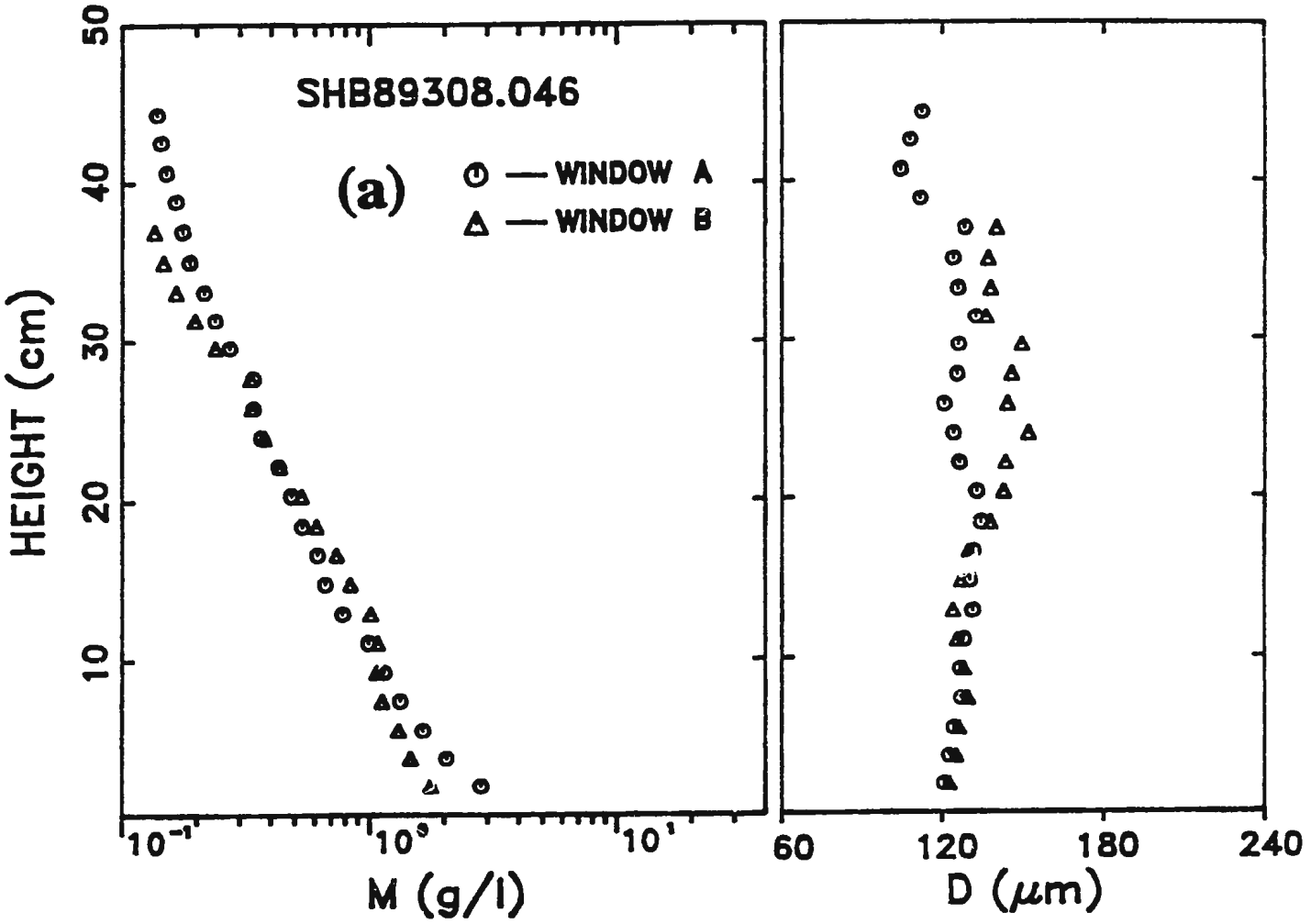

(a)

Figure 8.22. Time-averaged profiles of particle concentration and size over windows in the high energy case for consecutive runs: (a) SHB89308.046, (b) SHB89308.047.

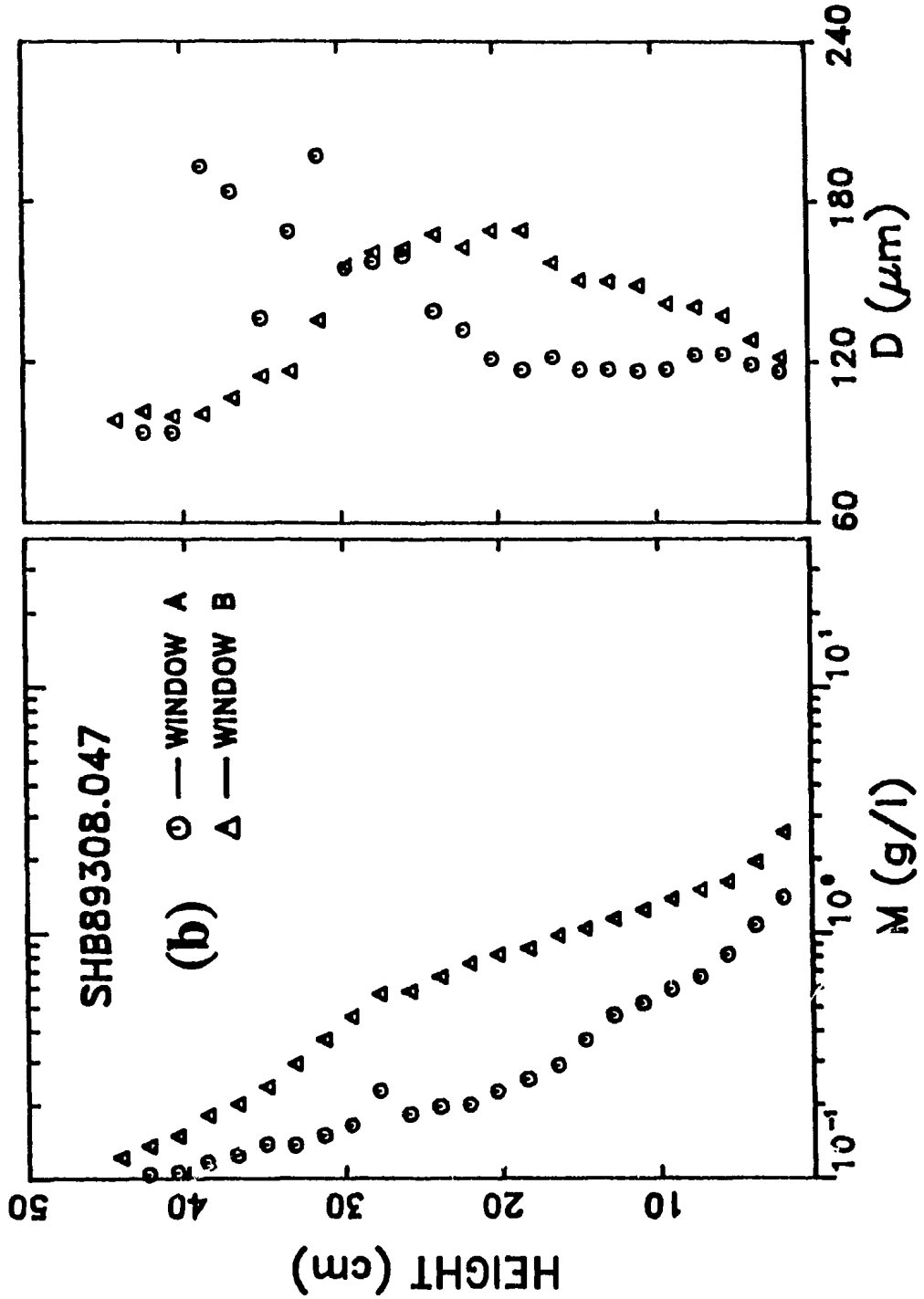

(b)

Figure 8.22. (continued)

8.6 Vertical Profiles of Eddy Diffusivity

Sediment suspension in wave-current conditions can be mathematically treated as a diffusion-dispersion process. The complete diffusion coefficient equation can be expressed by [Wang and Liang, 1975]

$$\frac{\partial M}{\partial t} + \nabla\cdot(M\,\mathbf{U}_s) = \nabla\cdot(K_\mu \nabla M), \tag{8.2}$$

where M and $\mathbf{U}_s$ are the instantaneous concentration and particle velocity vector, respectively, and K_μ is the molecular diffusivity. The z-axis is upward with $z=0$ at the bed.

The instantaneous concentration M and velocity $\mathbf{U}_s$ in the wave-current field can both be decomposed into three components [Kennedy and Locher, 1971]

$$\begin{cases} M = \overline{M} + M_w' + m \\ \mathbf{U}_s = \overline{\mathbf{U}} + \mathbf{U}_w' + \mathbf{u}, \end{cases} \tag{8.3}$$

where $\overline{M}$ and $\overline{\mathbf{U}}$ are the time mean values, M_w' and $\mathbf{U}_w'$ the wave induced components, and m and $\mathbf{u}$ the turbulent fluctuations. Substituting Eq. (8.3) into Eq. (8.2), and taking the time average over a time interval longer than many wave cycles yields

$$\nabla\cdot\left[\overline{M}\,\overline{\mathbf{U}} + \overline{M_w'\mathbf{U}_w'} + \overline{m\,\mathbf{u}} - K_\mu\nabla\overline{M}\right] = 0. \tag{8.4}$$

since $\overline{\frac{\partial M}{\partial t}}=0$ by definition. Here the overbar represents the time average. For sand particles the molecular diffusion is very small, compared with other three, so the term $K_\mu\nabla\overline{M}$ can be neglected without substantial loss of generality. Hence,

Eq (8.4) can be expressed in the terms of three components

$$\frac{\partial}{\partial x}\left[\overline{M}\overline{U}+\overline{M_w' U_w'}+\overline{mu}\right]+\frac{\partial}{\partial y}\left[\overline{M}\overline{V}+\overline{M_w' V_w'}+\overline{mv}\right]+ \\ +\frac{\partial}{\partial z}\left[\overline{M}\overline{W}+\overline{M_w' W_w'}+\overline{mw}\right]=0, \tag{8.5}$$

where the x-axis is directed onshore, and the y-axis is directed alongshore. In Eq. (8.5) $(\overline{U},\overline{V},\overline{W})$ are three components of $\overline{\mathbf{U}}$; (U_w',V_w',W_w') three components of $\mathbf{U}_w'$; and (u,v,w) three components of $\mathbf{u}$. Since the average is taken over many wave cycles, the horizontal gradients may be assumed small compared to vertical gradients. Therefore, terms of the form $\frac{\partial}{\partial x}[\ ]$ and $\frac{\partial}{\partial y}[\ ]$ will be dropped from Eq. (8.5), which then reduces to

$$\frac{\partial}{\partial z}\left[\overline{M}\overline{W}+\overline{M_w' W_w'}+\overline{mw}\right]=0, \tag{8.6}$$

it can be integrated once, with the result

$$\overline{M}\overline{W}+\overline{M_w' W_w'}+\overline{mw}=C, \tag{8.7}$$

C is the constant of integration, which can be determined by considering that at the maximum height H_{max} that the sediment could reach, all terms in the left hand side of Eq. (8.7) equal zero. Therefore, we get $C=0$. Rearranging Eq. (8.7), we have

$$W_s\overline{M}=\overline{M_w' W_w'}+\overline{mw}. \tag{8.8}$$

in which $\overline{W}=-W_s$ has been used, where W_s is the particle settling velocity, which is defined as the terminal fall velocity of the particle when the drag forces are balanced by the immersed weight of the particle [Dyer, 1986, Chapter 4], and the negative sign indicates downward direction of the particle settling velocity.

The terms on the right-hand side of the above equation represent the effects of vertical displacement due to waves and turbulent diffusion, respectively. By further assuming that

$$\begin{cases} \overline{M_w' W_w'} = -K_w \dfrac{d\overline{M}}{dz} \\ \overline{mw} = -K' \dfrac{d\overline{M}}{dz} \end{cases}, \tag{8.9}$$

where K_w and K' are, respectively, the eddy diffusivities due to wave particle motion and turbulence. We finally have [Taylor and Dyer, 1977]

$$-W_s \overline{M} = K_s \frac{d\overline{M}}{dz}, \tag{8.10}$$

where K_s is called the sediment eddy diffusivity [e.g. Taylor and Dyer, 1977, Vincent and Green, 1990], which is given by

$$K_s = K_w + K'. \tag{8.11}$$

The expression given by Eq. (8.10) indicates that the vertical profile of the sediment diffusivity can be obtained from the mean concentration profile and its gradient. For discrete data points, K_s can be calculated by

$$K_{s,i+\frac{1}{2}} = \frac{\Delta z}{2} \frac{W_{s,i+1}\overline{M}_{i+1} + W_{s,i}\overline{M}_i}{\overline{M}_{i+1} - \overline{M}_i} \tag{8.12}$$

in which the subscript i denotes the ith range bin.

It is clear, from Eq. (8.12), that the settling velocity W_s of sand particles is quantitatively required to estimate the sediment eddy diffusivity from a vertical concentration profile. Based on Gibbs et al. [1971], the settling velocity of a

spherical particle in still water is given by

$$W_G = \frac{-3\mu + \sqrt{9\mu^2 + gd^2\rho(\rho_s'-\rho)(0.003869+0.024801d)}}{\rho(0.011607+0.074405d)} \tag{8.13}$$

in which d is the diameter of a spherical particle, and μ is the molecular shear viscosity of water, which can be calculated by [Weast, et al., 1985, P37]

$$\log_{10}\mu = \begin{cases} \dfrac{1301}{998.333+8.1855(T-20)+0.00585(T-20)^2} - 1.30233 & T \leq 20^\circ\,\mathrm{C} \\ \log_{10}\mu_{20} + \dfrac{1.3272(20-T)-0.001053(T-20)^2}{T+105} & T > 20^\circ\,\mathrm{C} \end{cases} \tag{8.14}$$

Since the shape of sand particles is very irregular, errors may result when Eq. (8.13) is used to find the settling velocity for sand particles. Baba and Komar [1981] obtained an empirical formula for the settling velocity of natural sand particles in water based on the expression Eq. (8.13), that is

$$W_s = 0.977\, W_G^{0.913}. \tag{8.15}$$

The settling velocity of the sand particle, therefore, can be calculated from the time-averaged size profile obtained in Section 8.5 through Eqs. (8.13) and (8.15). For the range of sand sizes we are interested in, the calculated values of W_G and W_s based on Eqs. (8.13) and (8.15) are plotted in Figure 8.23, in which the solid line is the settling velocity of a spherical particle, and the dashed line is for the sand particle, both with grain density ρ_s'=2700 kg/m^3. It can be seen that the settling velocity is in the order of 1-3 cm/s, and the maximum difference in the settling velocities given by Eq. (8.13) and Eq. (8.15) is about 10% at d=250 μm.

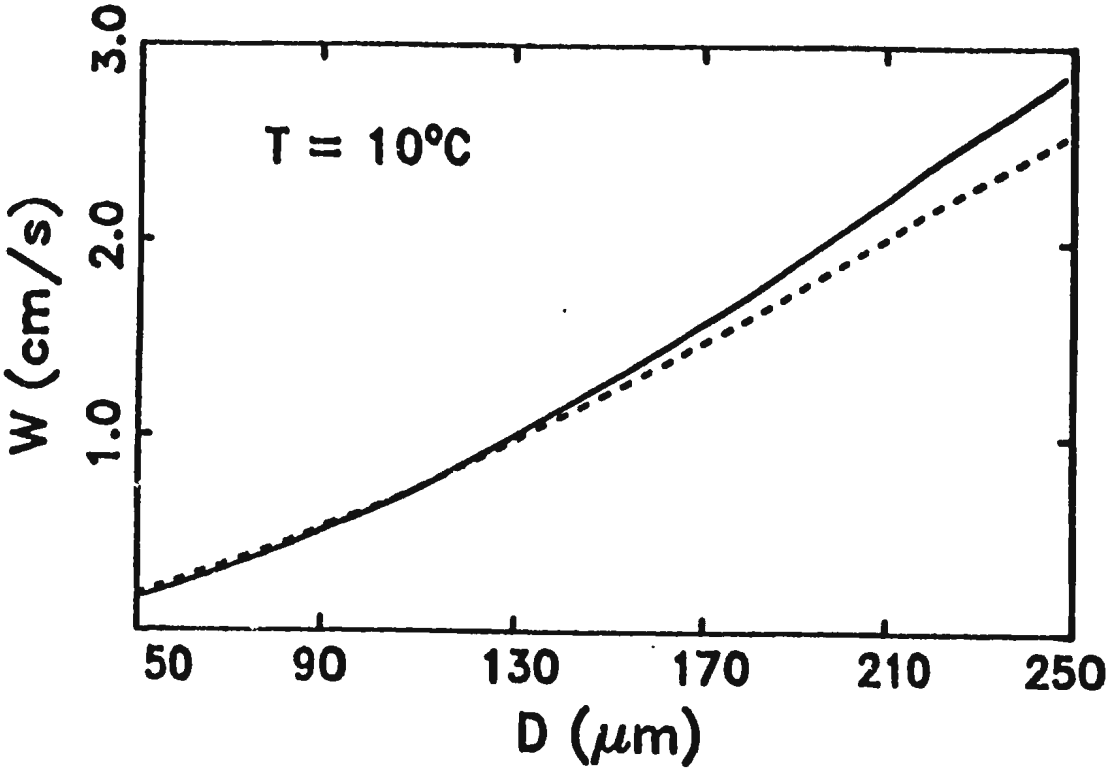

Figure 8.23. The settling velocity of spherical quartz particles and of natural sand in water at T = 10 °C. The dashed line is results for the natural sand particles and the solid line is results for spherical quartz particles.

The sediment eddy diffusivity can now be estimated from time mean profiles of inverted concentration and size through Eqs. (8.12), (8.13) and (8.15). It should be noted that the data to be presented are those obtained by using a smoothing filter 3 bins wide in the vertical to remove the small scale variations.

By presenting the vertical profiles of K_s estimated from time-mean profiles of particle concentration and size averaged over the complete run (Figure 8.19) for the three wave energy cases, as shown in Figure 8.24, it can be seen that K_s increases approximately linearly with height in the near bed region. After reaching some maximum value, the eddy diffusivity then decreases slightly with height.

The thickness of the linear region, or the near bed region, moreover, is different for different surface wave energies: at least 10 cm at low energy, about 15 cm at medium energy, and 8 cm at high energy. The rate of increase of K_s with height in the linear region is smaller for medium than for low energies, but becomes larger again at high energies. The maximum estimated eddy diffusivity is about 13 cm^2/s at low energy, 15 cm^2/s at medium energy, and 23 to 28 cm^2/s at high energy. It must be emphasized that the linear behavior of vertical profiles of sediment eddy diffusivity in the near bed region illustrated by Figure 8.24 appears to be universal [e.g. Smith and McLean, 1977a; Taylor and Dyer, 1977; Glenn and Grant, 1987].

Vertical profiles of sediment diffusivity in the low energy case are shown in Figure 8.25a, in which the data are those estimated from time-mean profiles of particle concentration and size averaged over entire windows and the complete run (Figure 8.20a). From Figure 8.25a, it can be seen that eddy diffusivities increase almost linearly with height up to about 10 cm in Window A, and up to about 12 cm from the bed in Window B. For heights above about 12 cm from the bed eddy diffusivities in Window B increase nonlinearly with height for heights above 12 cm, and reach a maximum value at about 15 cm height. It should be noted, however, that the accuracy of K_s at heights near the top of the suspension is lower, since the small values of concentration, and small and less accurate concentration gradients at these heights, can introduce large errors in the estimate of K_s. From Figure 8.25a, it can also be seen that for heights below 8 cm from the bed the estimated diffusivity profiles in the near bed region in both windows are very comparable, which is encouraging because the difference in $U_{1/3}$ between the two windows is very small, less than 3% (see Table 8.2).

The vertical profiles of eddy diffusivity calculated from time-mean profiles of particle concentration and size averaged over two single events in the low energy case (Figure 8.20b) are presented in Figure 8.25b, from which it can be seen that eddy diffusivities in Event 1 increase approximately linearly with height in the near bed region, reach a maximum at a height of about 8 cm height, then decrease with height up to 12 cm height. The eddy diffusivity at the top point of Event 1 is large, of which the accuracy, however, may be low. We do not attempt to analyze the vertical profile of eddy diffusivity in Event 2 in Figure 8.25b, since there are only two points available, which makes less meaningful in the statistical point of view.

Vertical diffusivity profiles computed from time-mean profiles of particle concentration and size averaged over three entire windows and the complete run in the medium energy case (Figure 8.21a) are shown in Figure 8.26a, from which it can be seen that the eddy diffusivities increase approximately linearly with height up to 15 cm height, then slightly decrease with height after reaching a maximum value in the neighborhood of 20 cm height. By examining the data points in Figure 8.26a, it can be also seen that comparable vertical profiles of eddy diffusivity in windows A and C correspond well to the equivalent values of $U_{1/3}$ in these two windows (the difference is less than 4%, see Table 8.2). The significant wave velocity $U_{1/3}$ near the bed in Window B is 34% larger than those in windows A and C, and the eddy diffusivity in Window B shown in Figure 8.26a is smaller than those in other two windows at intermediate heights. Except for one isolated data point in Window C, for which the estimated value of the diffusivity is about 20 cm^2/s, all estimated profiles of eddy diffusivity in Figure 8.26a demonstrate the common feature of K_ϵ: a linear increase with height first, a maximum value,

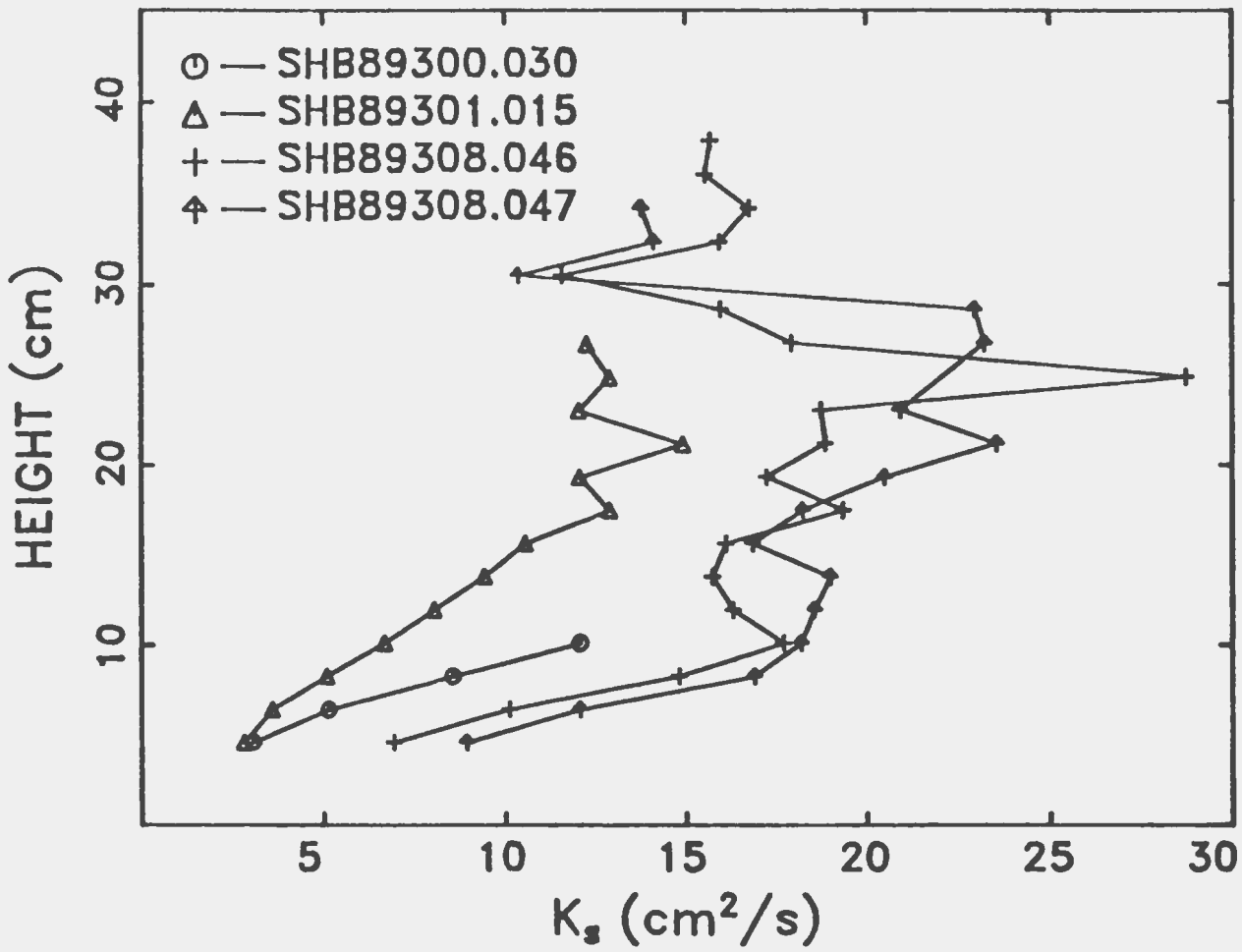

Figure 8.24. Vertical profiles of sediment diffusivity calculated from time-mean profiles of particle concentration and size averaged over the complete run (Figure 8.19) in three wave energy cases.

and then a slight decrease with height.

Vertical profiles of K_s estimated from time-mean profiles of particle concentration and size averaged over three single events in the medium energy case (Figure 8.21b) are shown in Figure 8.26b, in which the data exhibit a greater degree of scatter compared to those in Figure 8.26a. This may be due to the shorter time interval used to obtain these profiles. Nevertheless, the same trend as that in Figure 8.26a is apparent, especially for events 2 and 3. An interesting feature indicated by Figure 8.26b, however, is that there is a peak in the estimated value of K_s at a height of 15 cm in Event 1, 25 cm in Event 2, and 18 cm in Event 3. The big jump occurs in the transition between linear and nonlinear regions of K_s, similar to the second model suggested by Christoffersen and Jonsson [1985].

Vertical profiles of diffusivity calculated from time-mean profiles of concentration and size averaged over selected windows in the high energy case (Figure 8.22) are shown in Figure 8.27, in which the general feature of vertical diffusivity profiles is a more complex vertical structure than those in lower energy cases. The thickness of the linear region is about 5 to 7 cm, which is also smaller than those in the lower energy cases. Although the significant wave velocities $U_{1/3}$ near the bed for the two windows in Figure 8.27a are comparable (Table 8.2), there are significant differences in the vertical profiles of eddy diffusivity for both windows, specifically at heights between 5 and 15 cm from the bed. Figure 8.27a shows that eddy diffusivities in Window A increase slightly with height superposed by some small-scale vertical variations for heights above the linear region. While eddy diffusivities in Window B in Figure 8.27a also increase with height, there is

a large peak at the value of K_s at a height of about 10 cm, similar to those shown in Figure 8.26b for the medium energy case, but closer to the seabed. Vertical profiles of eddy diffusivity in Figure 8.27b are also considerably different from those shown in Figure 8.27a. It can be seen, from Figure 8.27b, that eddy diffusivities in Window B first increase almost continuously with height up to 10 cm from the bed, then decreases with height after reaching a maximum in the neighborhood of 18 cm height. Eddy diffusivities in Window A in Figure 8.27b, on the other hand, increase linearly with height up to about 8 cm height, then decrease with height, and then increase with height again after reaching a minimum value in the neighborhood of 15 cm height. It is also interesting to note, from Figure 8.27b, that the eddy diffusivity at the same range bin in Window A is smaller than that in Window B for heights below 20 cm from the bed, which corresponds well to the fact that the significant wave velocity $U_{1/3}$ in Window A is about 12% smaller than that in Window B.

In order to understand further the vertical structure of sediment eddy diffusivity for the different energy cases, the characteristic of sand ripples needs to be specified. It was found [Grant and Madsen, 1986] that the thickness of the linear region is not only dependent on the energy level of surface waves, but also on the presence of ripples. For a rippled bed, the thickness of this region increases with wave energy until the ripple steepness approaches a maximum. After that stage, the ripples are obliterated by the flow, and the thickness of the region decreases [Grant and Madsen, 1986]. The ripple steepness can be represented by the vertical-form index, which is defined by [Allen, 1982]

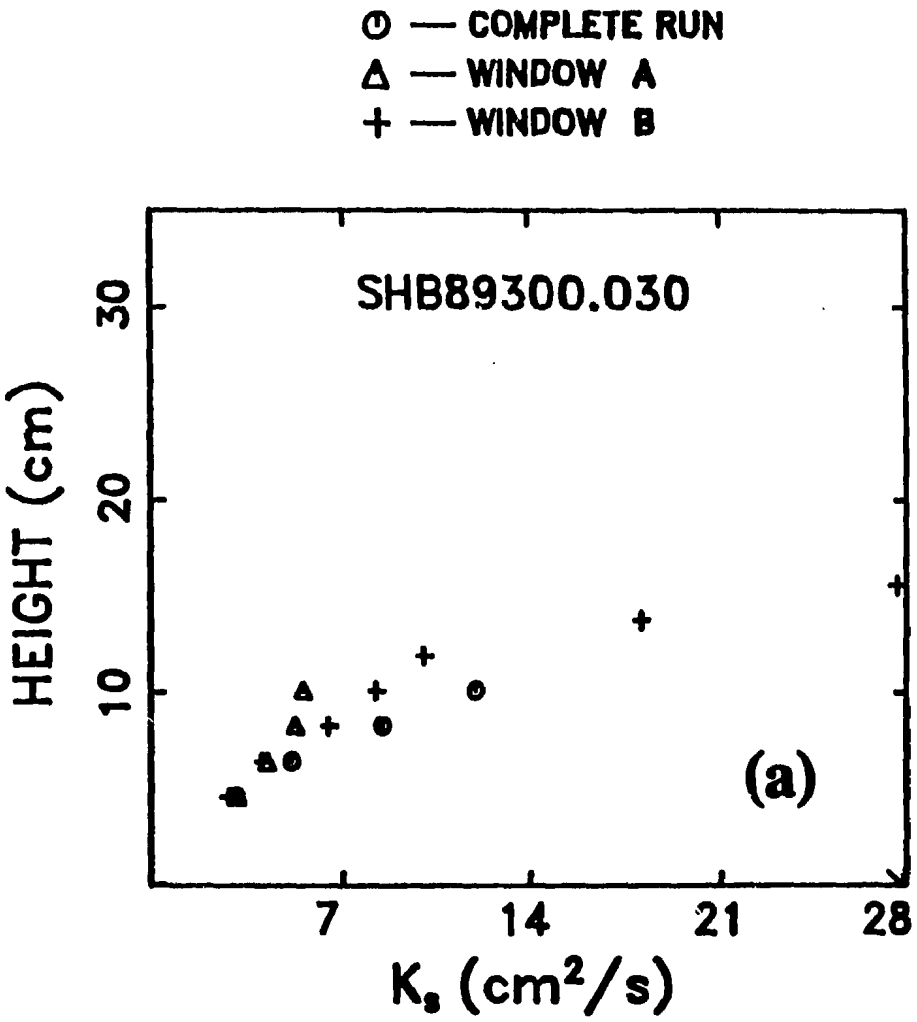

(a)

Figure 8.25. Vertical profiles of sediment diffusivity calculated from time mean profiles of particle concentration and size averaged over: (a) two entire windows and the complete run; (b) two single events in the low energy case.

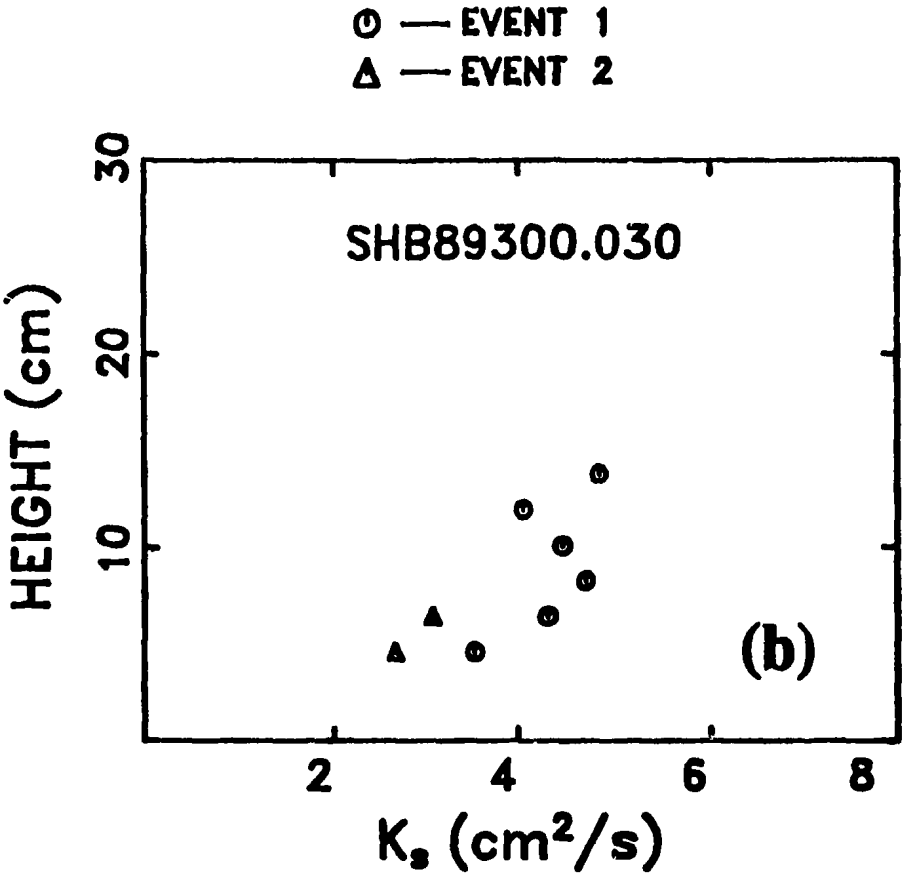

(b)

Figure 8.25. (continued)

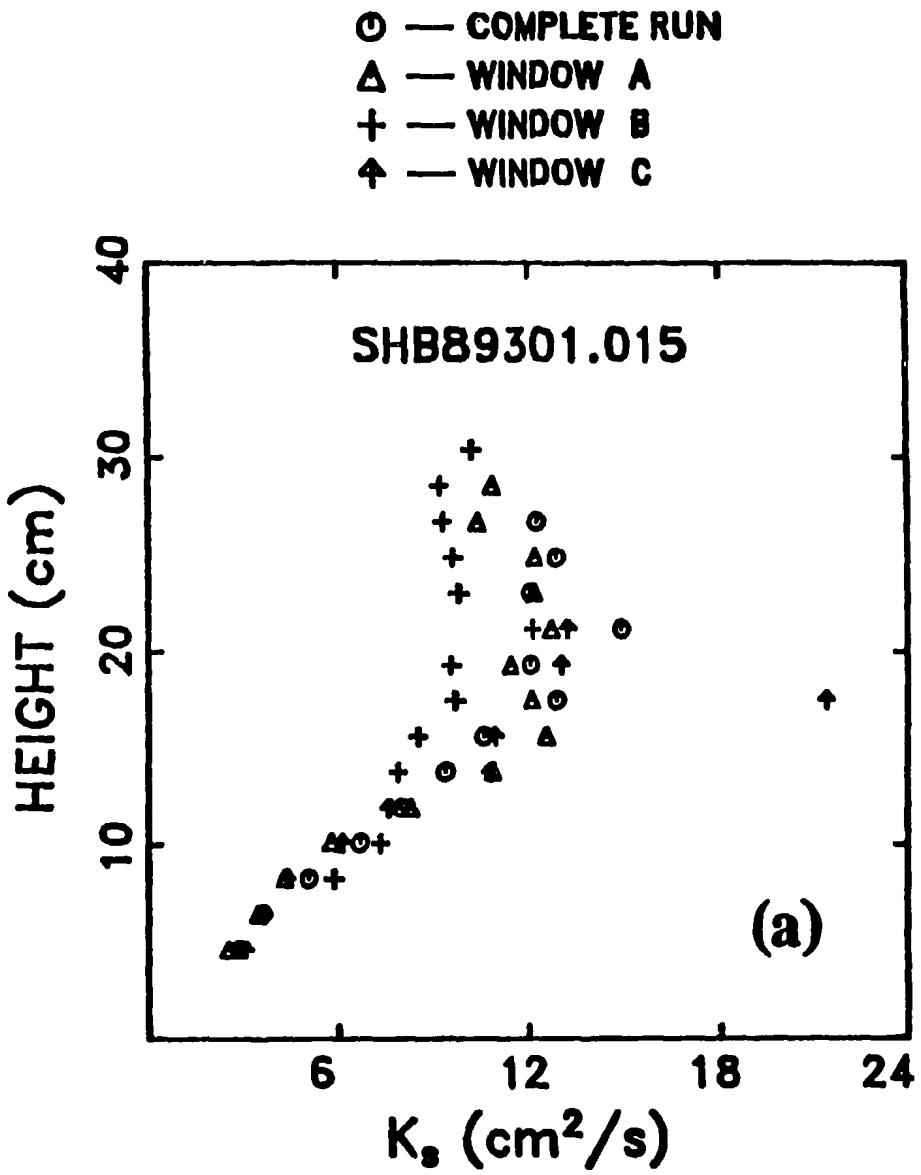

(a)

Figure 8.26. Vertical profiles of sediment diffusivity calculated from time-mean profiles of particle concentration and size averaged over: (a) two entire windows and the complete run; (b) single events in the medium energy case.

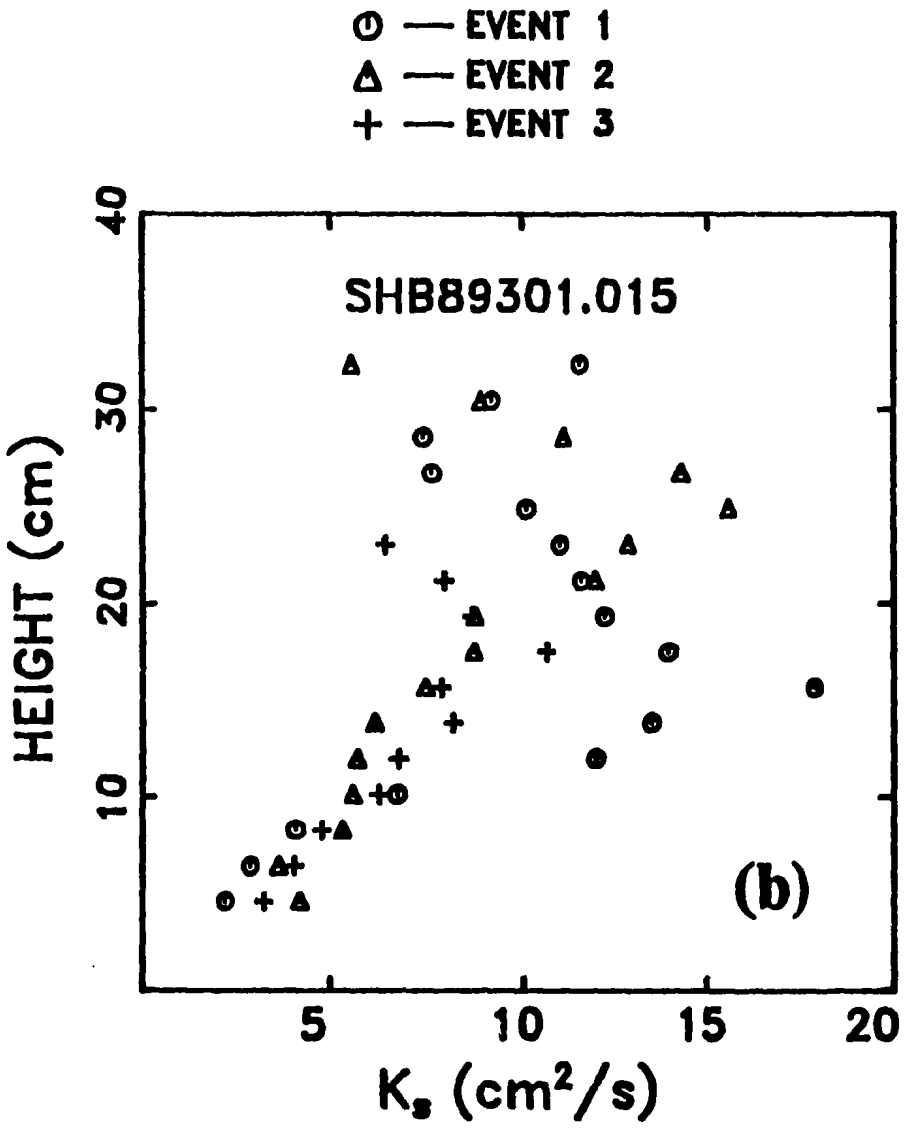

(b)

Figure 8.26. (continued)

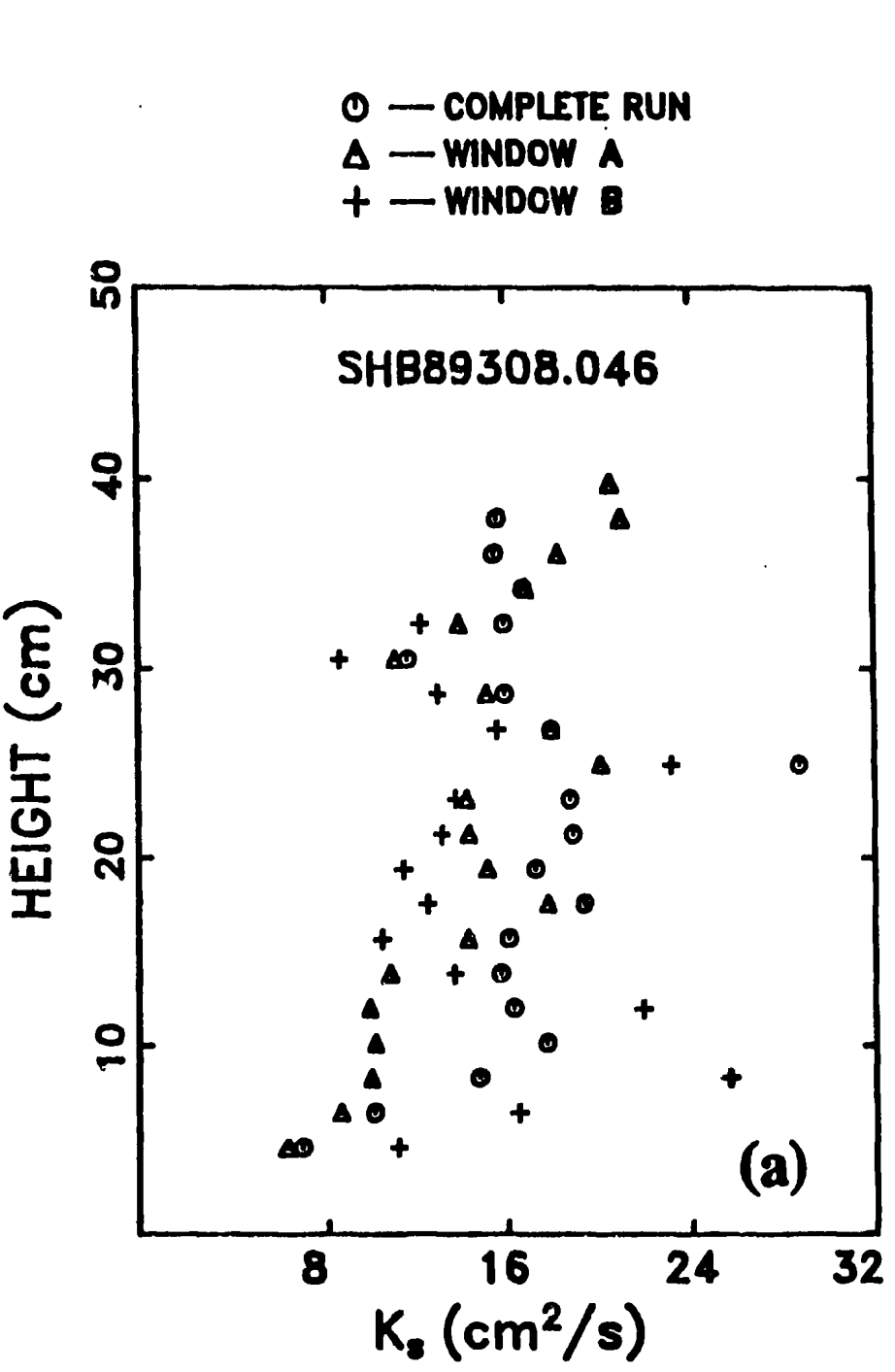

(a)

Figure 8.27. Vertical profiles of the sediment diffusivity calculated from time-mean profiles of particle concentration and size averaged over two entire windows and the complete run for: (a) SHB89308.046; (b) SHB89308.047 in the high energy case.

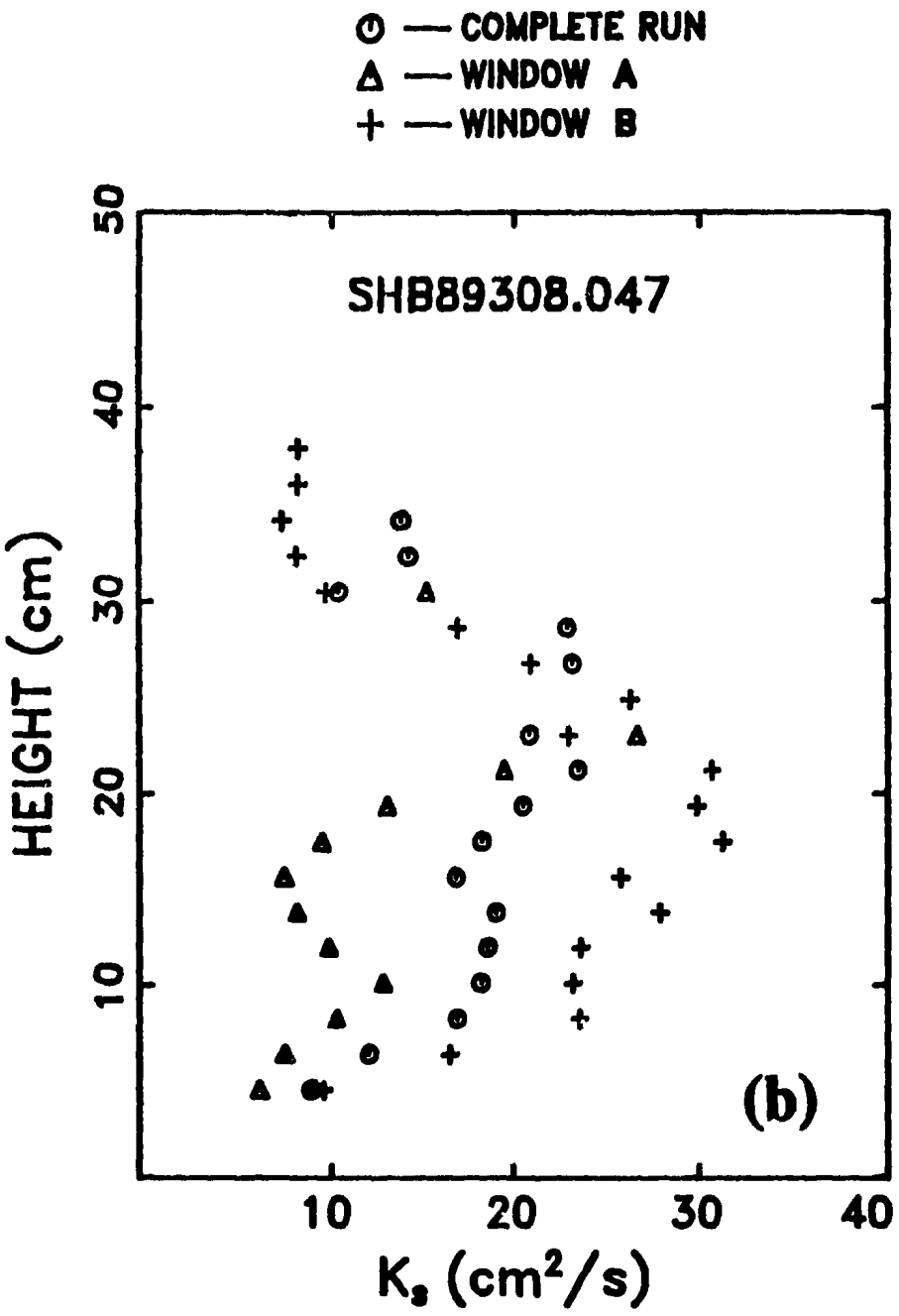

(b)

Figure 8.27. (continued)

$$\text{VFI} = \frac{\text{Ripple Wavelength}}{\text{Ripple height}}, \tag{8.16}$$

then the ripple steepness is equal to VFI^{-1}. No direct measurements of VFI are available for the Stanhope experiment at this time, except occasional diver observations. Hence, the diagram developed by Allen [1982, p.444] is used here, and is shown in Figure 8.28. Care must be taken when using Allen's diagram. Since it was mainly based on laboratory results, the maximum orbital velocity in Figure 8.28 should be that for regular waves. In order to estimate the vertical-form index from Figure 8.28 for irregular surface waves, the significant wave velocity near the bed $U_{1/3}$ is used. For example, the medium size of bottom sand at the RASTRAN location was about 158 μm (see Table 5.1, and Figure 5.1), and the significant wave velocity close to the bed $U_{1/3}$ is about 0.35 m/s in the low energy case (Table 8.2). From Figure 8.28, we get $VFI \leq 7.5$, which indicates the appearance of ripples on the bed, and the ripple wavelength on the bed should be equal to, or smaller than, 7.5 multiplying by the ripple height.

To quantitatively determine ripple heights, bed positions measured using the LeCroy 9400 digital oscilloscope shown in Figure 8.10 are re-analyzed here. Figure 8.29a shows temporal variations in bed positions during the period of 10 hours in the low energy case after removing the mean and linear trend from the data by using least squares procedures [Bendat and Piersol, 1971, p.289]. The maximum variation in Figure 8.29a, roughly about 3 cm peak to peak, is associated with the typical ripple height. Suppose the ripple height is equal to the maximum variation in Figure 8.29a (3 cm), then the ripple wavelength should have been equal to, or smaller than, 22.5 cm in the low energy case, using $VFI \leq 7.5$. It should be noted, however, that since the width of the transducer beam pattern

was about 6 to 8 cm at the sea bottom, the actual ripple height could be greater than the maximum variation shown in Figure 8.29a. The *in situ* measurements made by divers on the same day (at 1600 h) indicated that the ripple height was about 3 cm and the ripple length about 15 cm, which, it can be seen, compares reasonably well with the values estimated above.

The significant wave velocity near the bed $U_{1/3}$ is about 0.55 m/s in the medium energy case (Table 8.2). From Figure 8.28, we have $VFI \leq 20$, which is about 3 times larger than that in the low energy case, or in the other words, the maximum possible ripple steepness in this case should have been 3 times smaller than in the low energy case. The temporal variations in bed positions in the medium energy case are shown in Figure 8.29b, again with mean and linear trend removed. The maximum variation in Figure 8.29b is about 2.5 cm peak to peak, the same order but a little less than that in the low energy case. Suppose again the ripple height is equal to the maximum variation in Figure 8.29b (2.5 cm), then the typical ripple length in the medium energy case should have been equal to, or smaller than, 50 cm in the medium energy case.

The significant wave velocity near the bed $U_{1/3}$ in the high energy case is about 1.06 m/s (Table 8.2). According to Figure 8.28, the bed in this case should have been plane, which indicates that all ripples at the bottom were swept away by large surface waves. The temporal variations in the bed positions, after removing the mean and linear trend, are shown in Figure 8.29c. It can be seen, from Figure 8.29c, that the maximum variation in this case is very small, about 0.3 cm, which supports the existence of plane bed conditions in this case.

The feature of vertical profiles of eddy diffusivity in the three energy cases

shown in Figure 8.24 could now be explained by using above characteristics of the sand ripples. The ripple height in the medium energy case is of the same order as that in the low energy case, similar bottom roughness in both cases can be expected. For the same bottom roughness, the linear region could be thicker for the greater significant wave velocity $U_{1/3}$, based on the Davies-Soulsby's modeling output [Davies *et al.*, 1988]. Since $U_{1/3}$ in the medium energy case is about 60% larger than that in the low energy case (Table 8.4), the thickness of the linear region in the medium case, therefore, should be larger than that in the low energy. The sand ripples in the high energy case, on the other hand, were wiped out by surface waves, therefore, the bottom roughness is much smaller, and the linear region should be thinner, compared to both the low and medium energy cases. The values of $U_{1/3}$, VFI and the thickness of the linear region and the estimated ripple height for three cases of wave energy are listed in Table. 8.4.

Finally it should be pointed out that the linear dependence of eddy diffusivities on the height in the near bed region further demonstrates that particle concentrations in this region follow a power law. By letting

$$K_s = \gamma z \tag{8.17}$$

in the near bed region, in which γ is dependent on the wave energy and the bottom roughness, but independent of z. By further assuming that the variation of the settling velocity W_s of sand particles in this region is not significant, then we have

$$\overline{M} = \overline{M}_o \left[\frac{z}{z_o}\right]^{-\frac{W_s}{\gamma}} \tag{8.18}$$

by integrating Eq. (8.9). $\overline{M}_a$ in the above expression is the time mean particle concentration at the reference height z_a. Eq. (8.18) indicates that particle concentrations vary as a reciprocal power of height above bottom, which is consistent with existing suspended sediment transport theories [Smith, 1977; Dyer, 1986].

It should be also be noted that for $K_z \approx$constant the exponential distribution of $\overline{M}$ with respect to height can be also obtained through Eq. (8.9).

Table 8.4. Values of significant cross-shore wave velocity near the bed $U_{1/3}$, vertical-form index VFI, the ripple height h_{ripple}, and the thickness of the linear region in the profile of diffusivity δ_{linear} in three energy cases.

Energy	File	$U_{1/3}$ (m/s)	h_{ripple} (cm)	VFI	δ_{linear} (cm)
Low	SHB89300.030	0.35	3.0	≤ 7.5	8
Medium	SHB89301.015	0.55	2.5	≤ 20	15
High	SHB89308.046 SHB89308.047	1.06	0.3	$\rightarrow\infty$	6

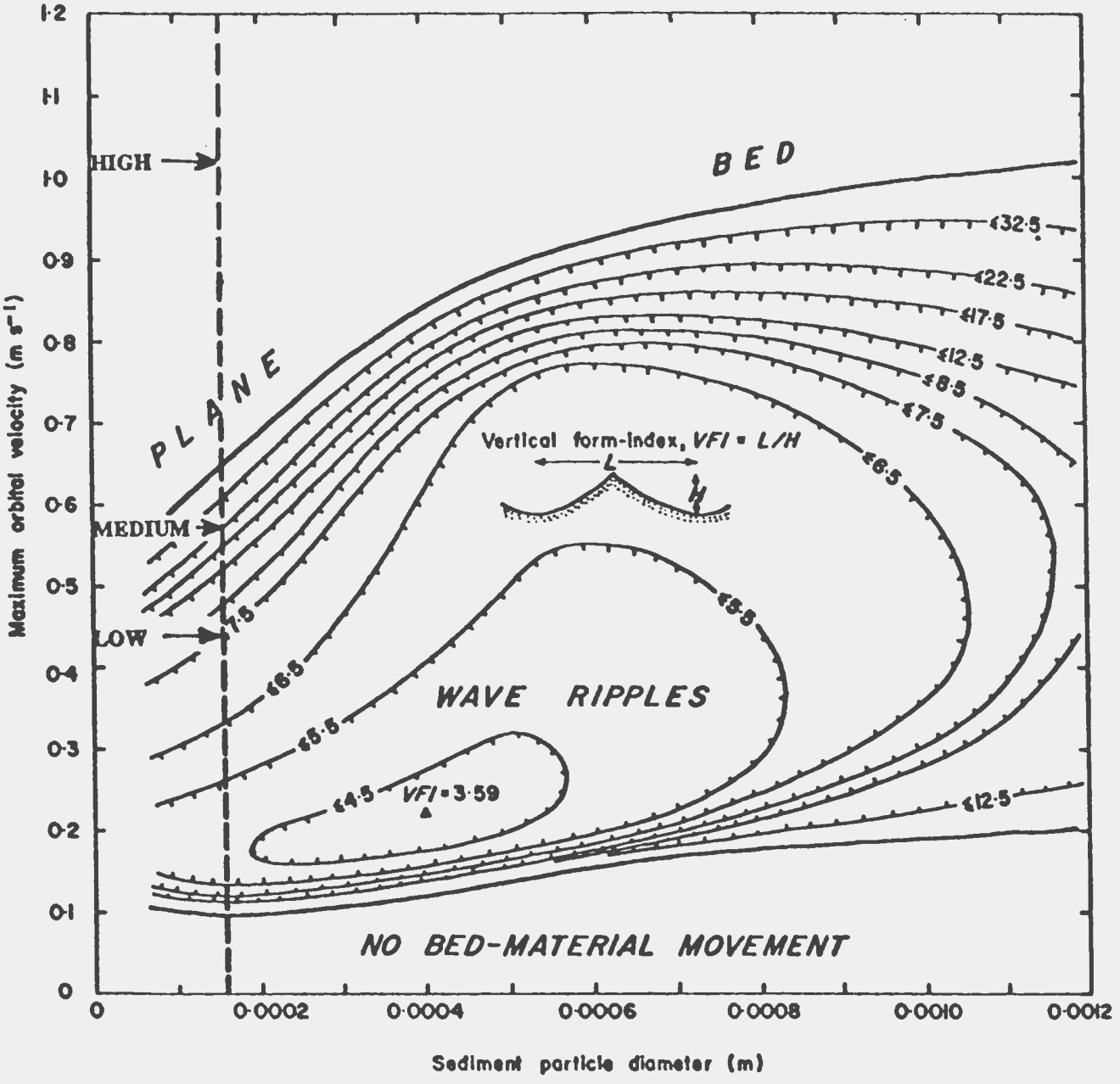

Figure 8.28. The vertical form-index of wave ripple marks as a function of the maximum orbital velocity near the bed and sediment diameter [adopted from Allen, 1982].

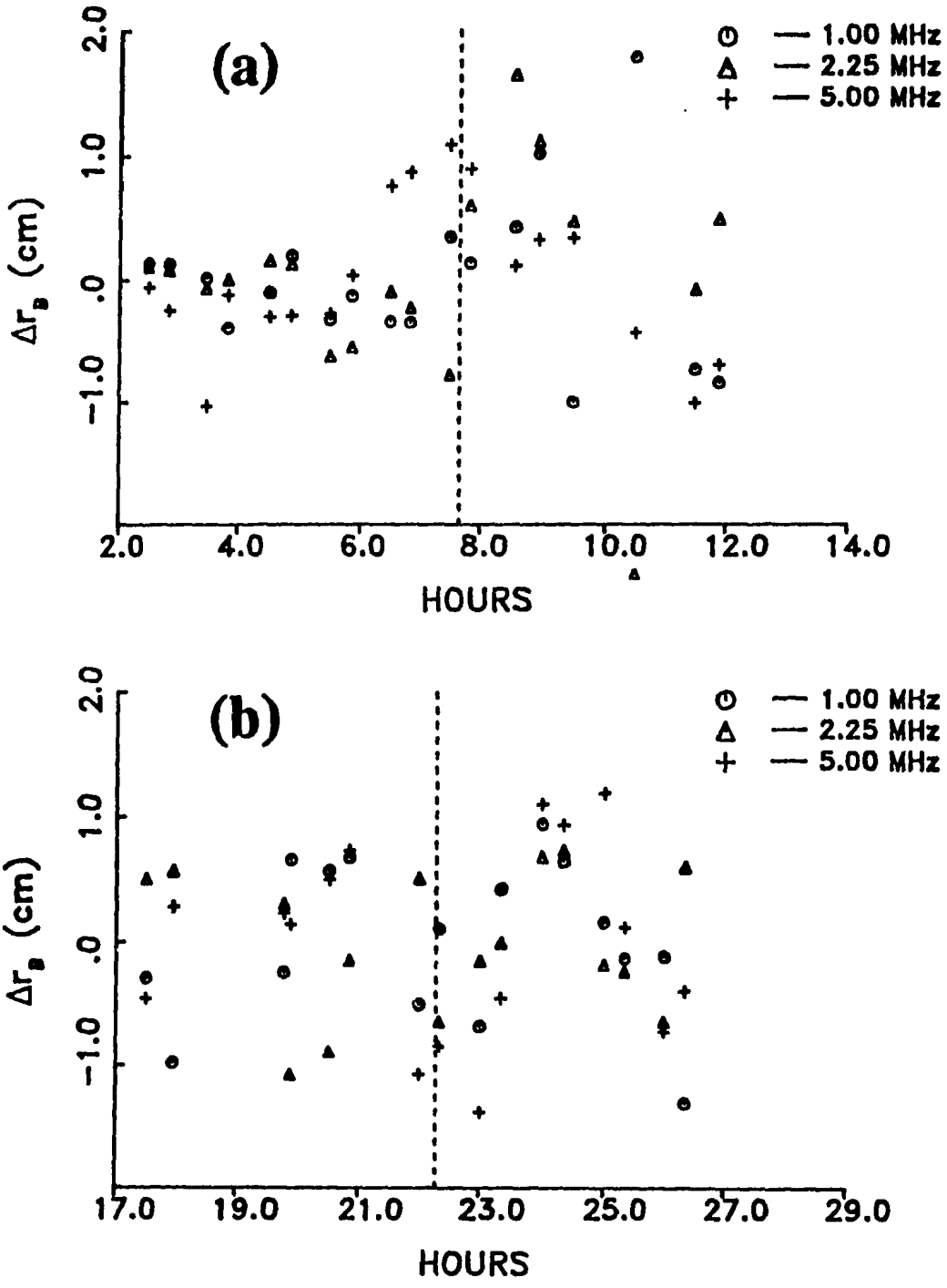

Figure 8.29. The temporal variations in bed positions measured by the digital oscilloscope in the case of: (a) the low energy; (b) the medium energy; (c) the high energy.

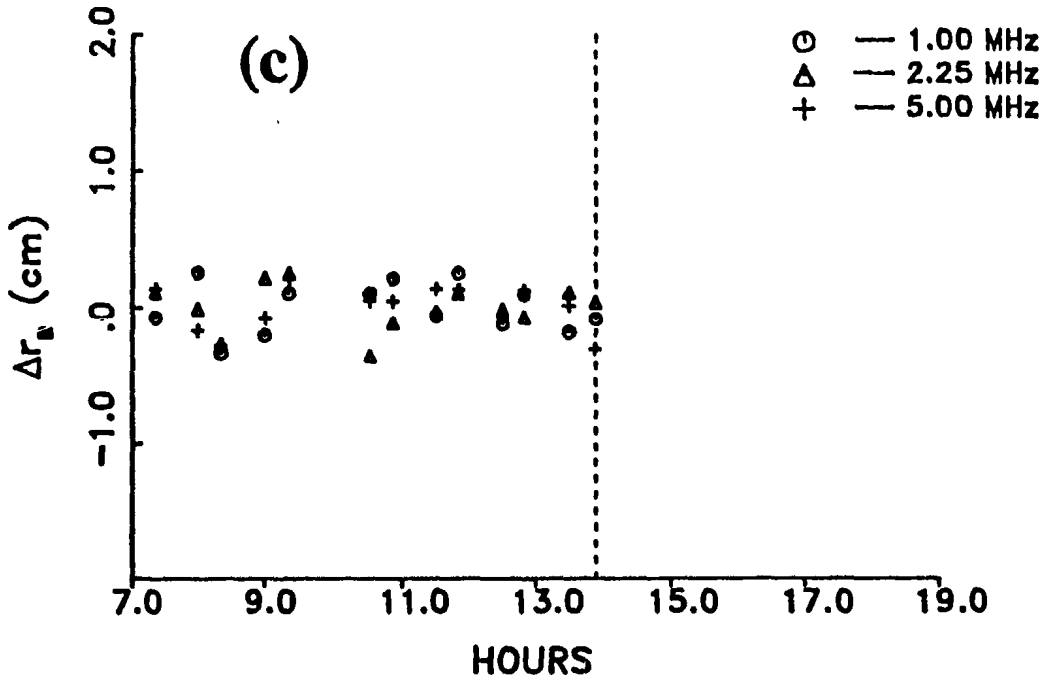

Figure 8.29. (continued)

8.7 Suspended Sediment Flux Profiles and Suspended Sediment Transport Rates

Assuming that the suspended sediment travels across the shore at the same velocity as the cross-shore current, the suspended sediment transport rate in the cross-shore direction is given by

$$q_t = \int_0^{H_{max}} M \cdot U dz \tag{8.19}$$

in which M and U are respectively the instantaneous particle concentration and cross-shore component of velocity, and can be divided individually into three parts: the mean value, the oscillatory term due to waves, and the fluctuation term, as in Eq. (8.3). The fluctuation terms m and u have both been removed by using the low pass filter in time (1.2 s running average), therefore, we have

$$\begin{cases} M = \overline{M} + M_w' \\ U = \overline{U} + U_w' \end{cases} \tag{8.20}$$

By using Eq. (8.20) in Eq. (8.19), then taking the time average, we have

$$q = \overline{q_t} = \int_0^{H_{max}} \overline{MU} dz = \overline{q} + q_w \tag{8.21}$$

with

$$\begin{cases} \overline{q} = \int_0^{H_{max}} \overline{M} \cdot \overline{U} dz \\ q_w = \int_0^{H_{max}} \overline{M_w' U_w'} dz \end{cases} \tag{8.22}$$

where q is the total suspended sediment transport rate, $\overline{q}$ the transport rate by

the mean flow, and q_w the transport rate due to wave orbital motion. Likewise, $\overline{MU}$ is the total suspended sediment flux, $\overline{M}\cdot\overline{U}$ the mean flux, and $\overline{M_w' U_w'}$ the (horizontal) wave flux.

Similar to $\overline{M}$ in Section 8.6, the mean velocity $\overline{U}$ can be obtained by averaging the records of the flowmeter over a certain time period. It should be mentioned that, unlike the mean value of M, there are two main uncertainties in estimating $\overline{U}$. One is that the measured mean on-offshore velocity is about 5-10 cm/s. While this value is consistent with other measurements in the nearshore zone [e.g. Haines, 1985; Huntley and Hanes, 1987], it is in the range of generally accepted uncertainty in mean flows measured by the Marsh-McBirney electromagnetic flow meters [A. J. Bowen and D. Hazen, personal communication]. Therefore, it is difficult at this time to assess the accuracy of the measured mean values of $\overline{U}$. Another is that velocity measurements used here are those detected by the flowmeter, which was mounted at about 20 cm from the bed. Since the bed is movable, the height of flowmeter's location from the bed was variable. Although a number of possible theories can be used to extrapolate the mean velocity at a single point to any height, considering the large uncertainty in the mean measured value of velocity $\overline{U}$, it is simply assumed in the following discussion that the velocity is uniform in the whole depth. It is obvious that this assumption will overestimate $\overline{M}\cdot\overline{U}$ near the bed. It is reasonable to assume, on the the other hand, that the horizontal wave velocity U_w' is independent of height by using the shallow water theory [Bowden, 1983, p.81]. The mean water depth in the deployment location of instruments is about 2.2 m with the maximum tidal variation of less than 1 m in magnitude, and the typical wave period t_w is 3.6 to 5.4 seconds

for the four selected segments of field data (Table 8.2). The typical wavelength of the surface waves is about 16 to 24 m long using wavelength=$t_w \sqrt{gH}$ based on the shallow water theory [Bowden, 1983, p.81], which, it can be seen, is much greater than the mean water depth. Nevertheless, the purpose of the discussion in this section is to emphasize the shapes of the sediment flux profiles obtained by the RASTRAN system, rather than total suspended sediment transport rates.

Profiles of sediment flux averaged over the complete run are plotted in Figures 8.30-8.32 for the low, medium and high energy cases, respectively. From left to right in the plots are the profiles for the total flux, the mean flux, and the wave flux, respectively.

For the case of low energy, the wave flux $\overline{M_w' U_w'}$ is quite small, except that in first range bin above the bed (Figure 8.30), for which the uncertainties associated with the calculation, however, are large. The total flux is mainly contributed from the mean flux, and is in the seaward direction. The sediment transport rates are also calculated, and listed in Table 8.5. It can be seen, from Table 8.5, that the wave transport rate q_w is small, and the total transport rate q can be roughly represented by the mean transport rate $\overline{q}$. The seaward direction of the wave flux at heights near the bed can be understood by referring to color images in Figures 8.11a and b, from which it can be found that the concentration maxima of RASTRAN data at the range bins near the bed in the two noteworthy suspension events (Figures 8.11a and b) are associated mainly with nearly maximum seaward velocities.

For the case of medium energy, the mean flux is in the offshore direction, as in Figure 8.30, but the wave flux is now shoreward, in the opposite direction with

the mean flux (Figure 8.31). The total flux is in the same direction as the mean flux (seaward), but its magnitude is smaller than that of the mean flux. The wave transport rate q_w is not small, about 43% of the mean transport rate $\overline{q}$ (Table 8.5), and q_w and $\overline{q}$ are also out of phase. The total transport rate q is about 60% smaller than that of the mean transport rate $\overline{q}$ (Table 8.5). From the color images in Figure 8.12, it can be found that the concentration maxima at heights near the bed in the three suspension events (Figure 8.12), particularly in Event 3, are indeed associated mainly with the shoreward velocities, which further proves the shoreward direction of sediment flux shown in Figure 8.31.

Figure 8.32a shows profiles of sediment flux for the run SHB89308.046 in the high energy case. The mean sediment flux is in the seaward direction, as in the other two energy cases. The most interesting feature, which can be found from Figure 8.32a, is that the direction of the wave flux relative to that of the mean flux varies with height, which is consistent with results obtained by Vincent and Green [1990]. It can be seen from Figure 8.32a that the wave flux and the mean flux are both directed offshore for heights below 20 cm from the bed, but they are in opposite direction for heights above 20 cm though the wave flux at these heights is not very large. The wave transport rate q_w is of the same order, but about 30% smaller than the mean transport rate $\overline{q}$. The total transport rate q is about 75% larger than the mean transport rate $\overline{q}$. The seaward wave flux near the bed can be further proved by examining color images in Figure 8.13a and b, from which it can be seen that the RASTRAN concentration maxima at the range bins near the bed are correlated mainly with seaward velocities.

The feature shown in Figure 8.32a is even more pronounced in Figure 8.32b

for the run of SHB89308.047. It can be seen, from Figure 8.32b, that the wave flux and the mean flux are both offshore for heights below 10 cm, but the wave flux is onshore for heights above 10 cm from the bed. It is also interesting to note that the magnitude of the wave flux at heights above 20 cm from the bed is larger than the mean flux. The wave transport rate is shoreward, out of phase with the mean transport rate. The total transport rate q is seaward, in the same direction as the mean transport rate $\overline{q}$, but its magnitude is 40% smaller than that of the mean transport rate. The profile of sediment flux shown in Figure 8.32b can also be verified by analyzing the correlation between concentration maxima and the wave-induced cross-shore velocities from the color images shown in Figures 8.13c and d. It can be found that the concentration maxima at heights near the bed are mainly correlated with seaward velocities. It must be pointed out, however, that the concentration maxima at these heights do not correlate with maximum seaward velocities, but rather with the seaward velocities of smaller amplitudes. For heights above 20 cm from the bed, the concentration maxima, specifically in Window B of SHB89308.047 (Figure 8.13d), are mainly correlated with shoreward velocities.

It is clear from Figures 8.30-8.32 that the contribution from the horizontal sediment wave flux to the total sediment transport is not negligible [Vincent and Green, 1990], especially considering the fact that the effects of bottom friction on the mean flow have been ignored. Moreover, the sediment transport due to wave motion can dominate at some heights and at some wave energies. The relative direction of the horizontal wave flux and mean flux not only varies with wave energy, but also with height.

Table 8.5. Sediment transport rates averaged over the complete run for three cases of wave energy, in which q is the total transport rate, $\overline{q}$ the transport rate due to the mean flow, and q_w the transport rate due to wave motion.

Energy	File	$\overline{U}$ (cm/s)	Transport Rate (kg/m^{2}s)		
			$\overline{q}$	q_w	q
Low	SHB89300.030	-7.4	-0.385	-0.020	-0.405
Medium	SHB89301.015	-12.1	-1.885	0.813	-1.072
High	SHB89308.046	-8.0	-1.075	-0.799	-1.874
	SHB89308.047	-8.3	-0.044	0.380	-0.563

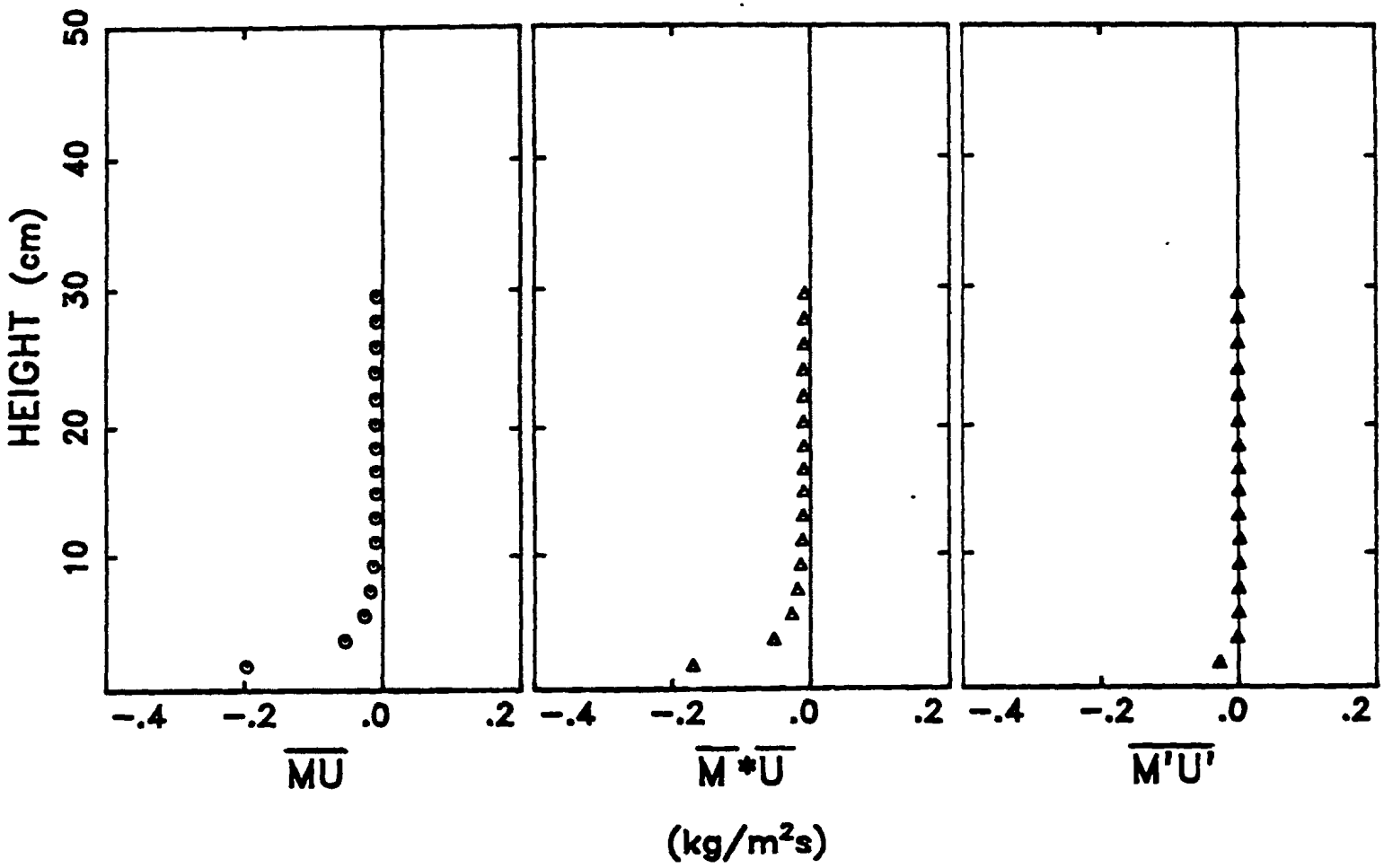

Figure 8.30. Time-averaged profiles of sediment flux over the complete run in the low energy case. $\overline{MU}$ is the total flux, $\overline{M}\cdot\overline{U}$ the mean flux, and $\overline{M_w' U_w'}$ the wave flux.

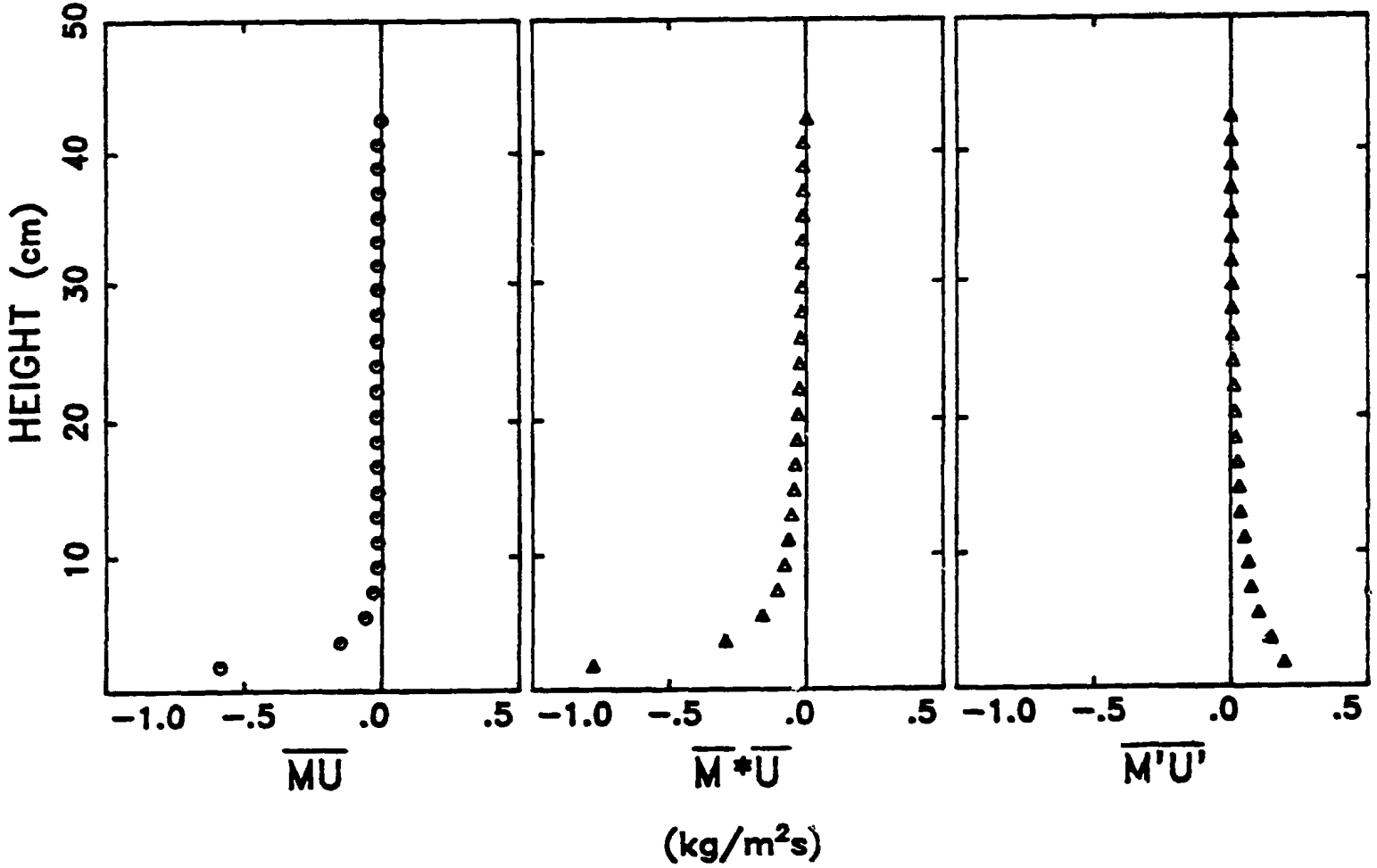

Figure 8.31. Time-averaged profiles of sediment flux over the complete run in the medium energy case. $\overline{MU}$ is the total flux, $\overline{M}\cdot\overline{U}$ the mean flux, and $\overline{M_w' U_w'}$ the wave flux.

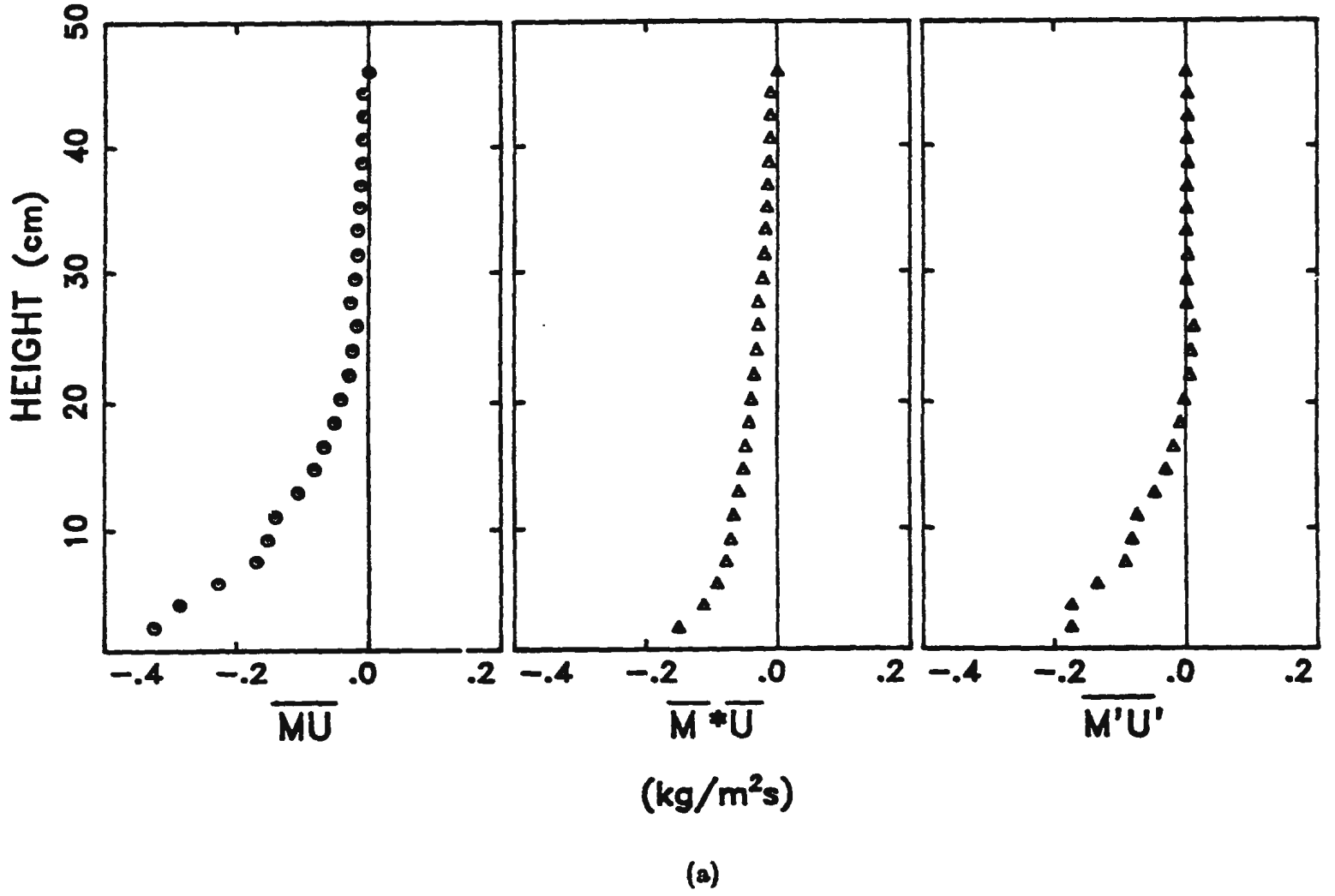

(a)

Figure 8.32. Time-averaged profiles of sediment flux over the complete run in the high energy case for: (a) SHB89308.046; (b) SHB89308.047. $\overline{MU}$ is the total flux, $\overline{M}\cdot\overline{U}$ the mean flux, and $\overline{M'U'}$, the wave flux.

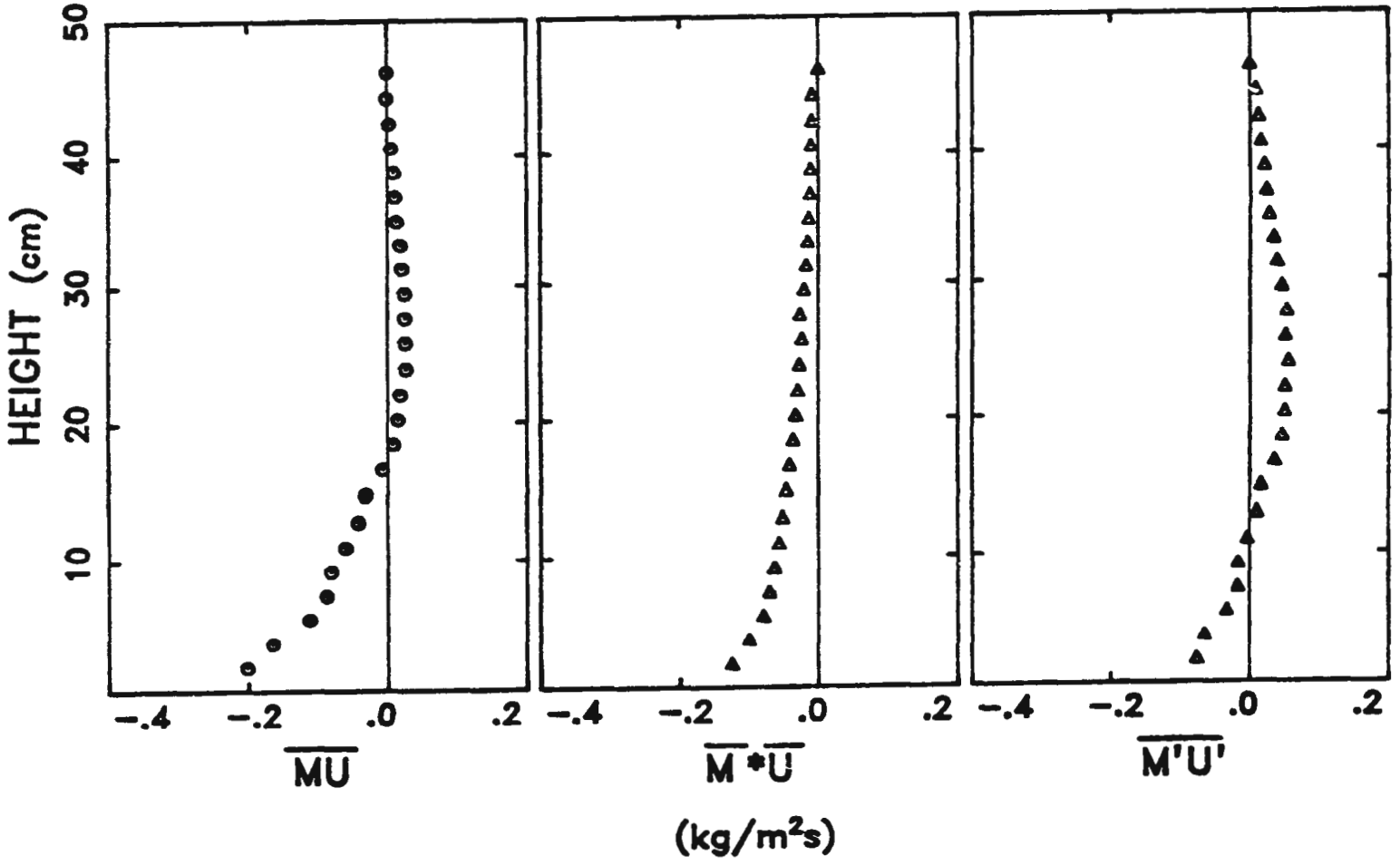

(b)

Figure 8.32. (continued)

8.8 Profiles of Eddy Diffusivity due to Turbulence

The relation between sediment eddy diffusivity K_s and eddy viscosity K_m [e.g. Taylor and Dyer, 1977] has attracted a lot of attention in the past. The linear dependence of K_s on K_m was proposed under steady flow conditions [Dyer, 1986]. Caution must be taken, however, when it is extended to the situation in which sediments are suspended mainly by surface waves, since K_s is affected by the vertical wave flux $\overline{M_w' W_w'}$, based on Eq. (8.11). It is the eddy diffusivity due to turbulence K' that is analogous to the eddy viscosity K_m.

By solving K' from Eq. (8.11) and also using Eqs. (8.9) and (8.10), we have

$$K' = K_s + \frac{\overline{M_w' W_w'}}{\frac{d\bar{M}}{dz}} \tag{8.23}$$

from which it can be seen that the vertical wave flux $\overline{M_w' W_w'}$ is quantitatively required in order to estimate K' from vertical profiles of particle concentration and K_s. No direct measurements of W_w', however, were made at Stanhope Beach. Therefore measurements of U_w' will be used here to evaluate W_w'. Since the mean water depth in the deployment location of the RASTRAN system (2.2 m) is much smaller than the typical wavelength (16 to 24 m, see Section 8.7), by ignoring nonlinear terms in the first order approximation, then the theory for surface gravity waves of small amplitude in shallow water can be applied. By setting the x-axis to be in the shoreward direction, which is also assumed to be the direction of wave propagation, and the z-axis to be upward with $z=0$ at the seabed, we have [Bowden, 1983, p. 81]

$$W_w' = \frac{z}{\sqrt{gH}} \frac{\partial U_w'}{\partial t} \tag{8.24}$$

in which U_w' is independent of z, as in Section 8.6, and H is the water depth. Eq. (8.24) indicates that W_w' is linearly dependent on height, and W_w' is zero at the seabed ($z=0$). The water depth H varied with time by tides and storm setup. It was estimated from tide gauge measurements at about 180 m from the baseline (Figure 2.5a), and is listed in Table 8.6. A rectangular running average 7 sets in width was applied to the time series of U_w' to filter out high-frequency variations. The central difference scheme was then used to estimate W_w' from the filtered records of U_w' through Eq. (8.24). Finally the rectangular running average 7 sets in width was again applied on the estimated time series of W_w' to remove some high-frequency variations due to differencing. The results for W_w' at two selected heights ($z=10$ cm, and $z=$H) in three cases of wave energy are presented in Appendix C.

The vertical profiles of wave flux $\overline{M_w' W_w'}$ are calculated from the estimated vertical velocities W_w' and particle concentrations inverted from the multi-frequency acoustic data (Section 8.3). As before, a low-pass filter 3 bins wide is also used to remove small-scale variations on the vertical $\overline{M_w' W_w'}$ profile. Figure 8.33 shows time-mean profiles of $\overline{M_w' W_w'}$ averaged over the complete run for the three wave energy cases. It can be seen, from Figure 8.33, that the wave flux $\overline{M_w' W_w'}$ in the low energy case is small and slightly decreases with height. It was found that the wave flux in this case mainly has negligible effects on the sediment suspension. In the medium energy case, $\overline{M_w' W_w'}$ decreases with height up to 10 cm in height, similar to that in the low energy case. For heights above 10 cm, however, $\overline{M_w' W_w'}$ in the medium energy case increases with height. For both high energy cases, $\overline{M_w' W_w'}$ mainly decreases with height in the near bed region, similar

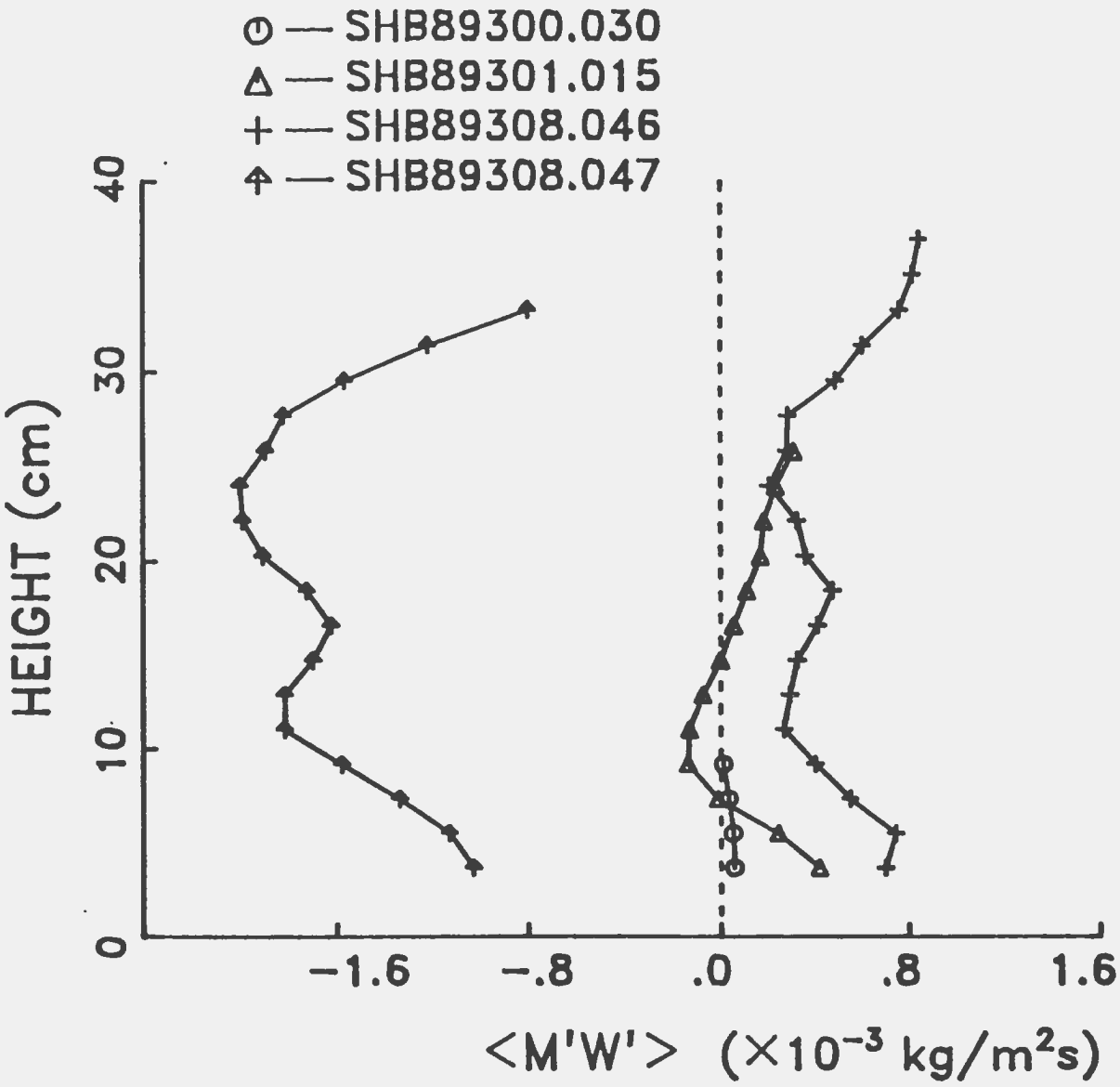

Figure 8.33. Time-averaged vertical profiles of wave flux $\overline{M_w' W_w'}$ over the complete run in three wave energy cases.

to the medium energy case. For heights between 12 cm and 16 cm from the bed $\overline{M_w' W_w'}$ increases with height after reaching a minimum in the neighborhood of 12 cm in height, also analogous to that in the medium energy case. It appears, however, that $\overline{M_w' W_w'}$ in the high energy case has more than one minimum on its vertical profile. By examining Figure 8.33, it can be seen, the second minimum of $\overline{M_w' W_w'}$ is at around 23 cm in height. There also exists a significant difference in the magnitude of $\overline{M_w' W_w'}$ between the two consecutive runs in the high energy case: $\overline{M_w' W_w'}$ in the first run (SHB89308.046) is positive, while $\overline{M_w' W_w'}$ in the second run (SHB89308.047) is negative at all heights inside the suspension cloud.

Although the exact causes for the vertical structure of $\overline{M_w' W_w'}$ shown in Figure 8.33 are not investigated in detail here, the tendency for $\overline{M_w' W_w'}$ to decrease with height in the near bed region can be understood by considering that W_w' increases linearly with height, but M_w' decreases with height at a faster rate. Consequently, the product of W_w' and M_w' in the near bed region must decrease with height. It should be noted that positive or negative values of $\overline{M_w' W_w'}$ in this region are mainly determined by the phase relationship between the maxima of particle concentration and surface wave velocity.

The effects of vertical wave flux on the sediment suspension, on the other hand, are rather easy to be determined. It can be seen, according to Eq. (8.8), that the wave flux $\overline{M_w' W_w'}$ affects the time-mean concentration $\overline{M}$ in such a way that the sediment resuspension will be strengthened by wave motion if M_w' and W_m' are in phase (or $\overline{M_w' W_w'}>0$), and the resuspension will be weakened by wave motion if M_w' and W_m' are out of phase (or $\overline{M_w' W_w'}<0$). Moreover, the slope of vertical $\overline{M_w' W_w'}$ profile determines whether the effects of wave motion on $\overline{M}$

increase or decrease with height. For $\overline{M_w' W_w'} > 0$, a positive slope indicates that strengthening effects of wave motion on $\overline{M}$ increase with height, while a negative slope represents that the strengthening effects decrease with height. For $\overline{M_w' W_w'} < 0$, likewise, a positive slope denotes that weakening effects of wave motion on $\overline{M}$ increase with height, while a positive slope intimates that the weakening effects decrease with height.

The main feature of vertical $\overline{M_w' W_w'}$ profiles shown in Figure 8.33, that is: $\overline{M_w' W_w'}$ decreases with height first, then reaches a minimum, finally increases with height, and there is more than one extremum in the profiles for higher wave energy, can be also found from time-mean $\overline{M_w' W_w'}$ profiles averaged over shorter time segments (Appendix C).

The eddy diffusivity due to turbulence K' is calculated from vertical profiles of particle concentration $\overline{M}$ and wave flux $\overline{M_w' W_w'}$ through Eq. (8.23). Figure 8.34 shows vertical K' profiles averaged over the complete run for the three cases of different wave energy. From Figure 8.34, we can see that in the near bed region K' increases approximately linearly with height, in the same way as K_s (Figure 8.24). Moreover, the slope of K' in the near bed region is also approximately equal to the slope of K_s in Figure 8.24, except for the SHB89308.047 run, for which the slope of K' is slightly larger than that of K_s. For heights above the near-bed region, however, K' is considerably different from K_s, in the medium and high energy cases. After reaching a maximum in the neighborhood of 20 cm height, K' decreases with height faster than K_s for the case of medium energy. The same tendency can be also found in both runs of the high energy case (SHB89308.046-047). The behavior of K' in the second run of the high

energy case (SHB89308.047), however, is different from others in that K' is always greater than K_ε for all heights inside the suspension cloud (Figure 8.34).

It should be pointed that the errors in the values of K' may be greater for heights above the near-bed region, partially due to the small values of concentration and less accurate concentration gradients at these heights, as mentioned before, and partially due to larger errors in estimated values of W_w' since the nonlinear terms, which become increasingly important with increasing z, were ignored.

The above feature of vertical K' structure can be also recognized on the time-mean K' profiles averaged over shorter time segments. The vertical K' profiles averaged over two selected windows in the low energy case (Table 8.2, see also Figure 8.11) are shown in Figure 8.35a, from which, by comparing with K_ε in Figure 8.25a, it can be seen that there are no significant differences between K' and K_ε in either window for heights below 10 cm from the bed, and K' (or K_ε) increases linearly with height at these heights. For heights between 10 and 16 cm K' in Window B increases with height slightly faster than K_ε, which is caused by the negative wave flux at these heights (Figure 8.34a). The thickness of the linear region for K' is roughly same as that for K_ε in Figure 8.25a. It should be noted the thickness of the linear region in Window A is questionable since there are no data points for heights above 10 cm in this window, as before. Vertical K' profiles averaged over two events in the low energy case (Table 8.2, also see Figure 8.11) are shown in Figure 8.35b. Compared with those in Figure 8.25b, it can be seen that there are no significant differences between K' and K_ε in the two events.

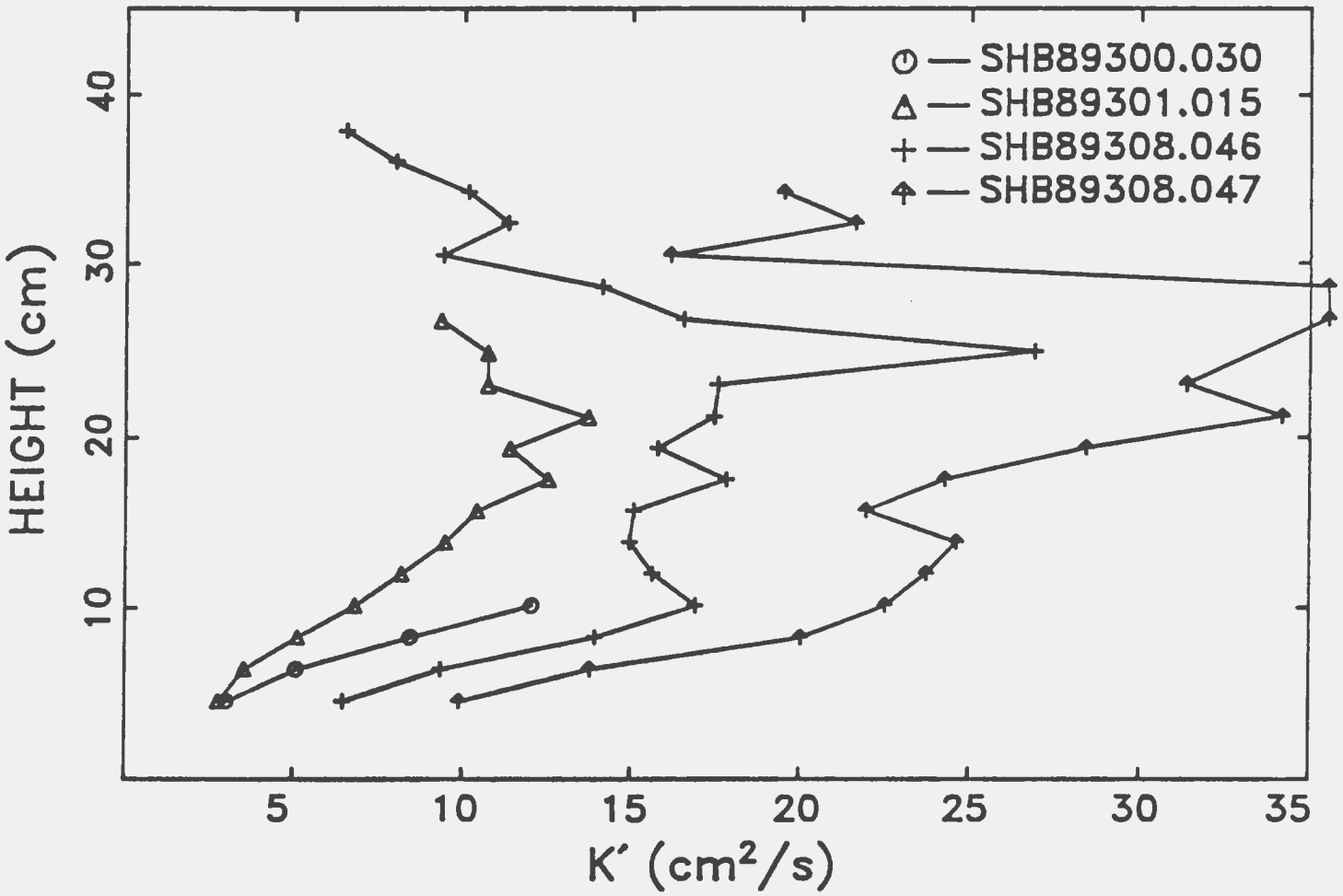

Figure 8.34. Vertical profiles of eddy diffusivity K' calculated from time-mean profiles of K_s and $\overline{M_w' W_w'}$ averaged over the complete run in three wave energy cases.

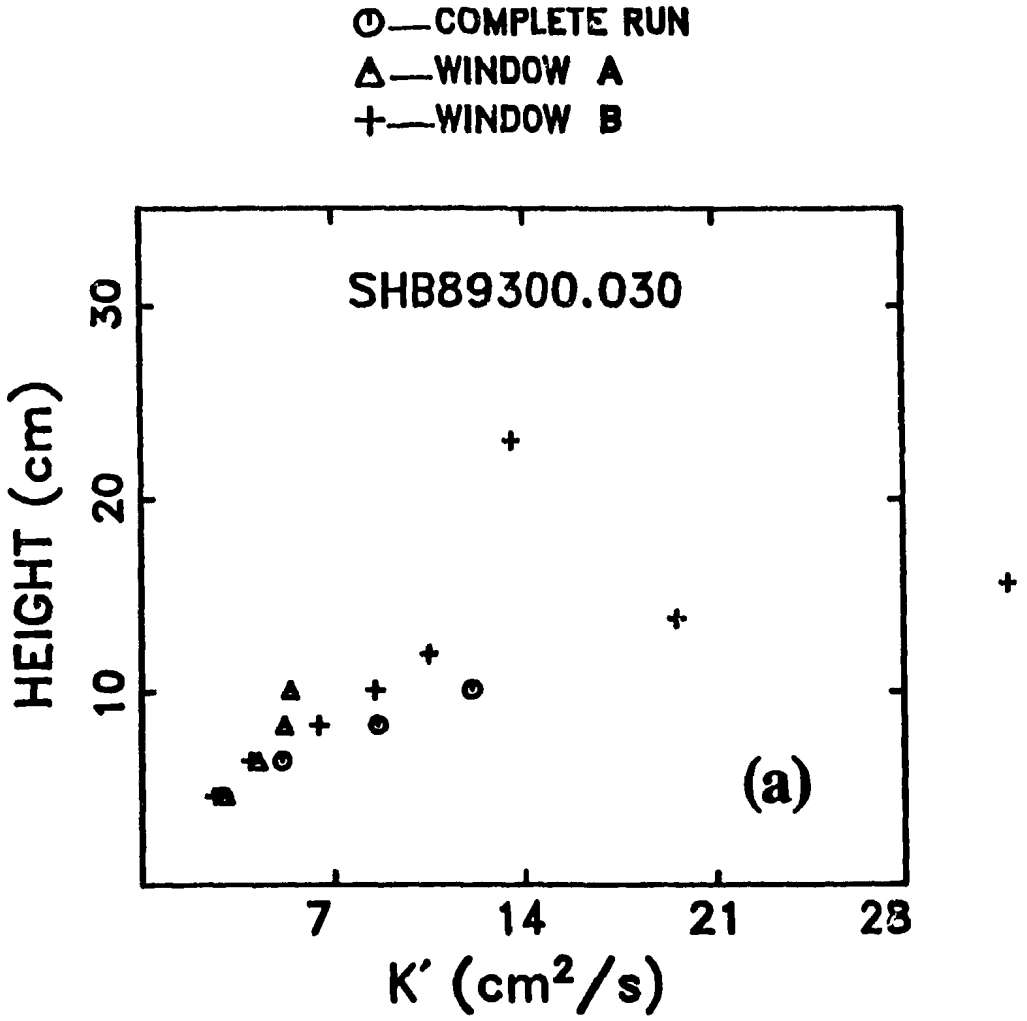

Figure 8.35. Vertical profiles of eddy diffusivity K' calculated from time-mean profiles of K_e and $\overline{M'_w W'_w}$ averaged over: (a) two entire windows and the complete run; (b) two single events in the low energy case.

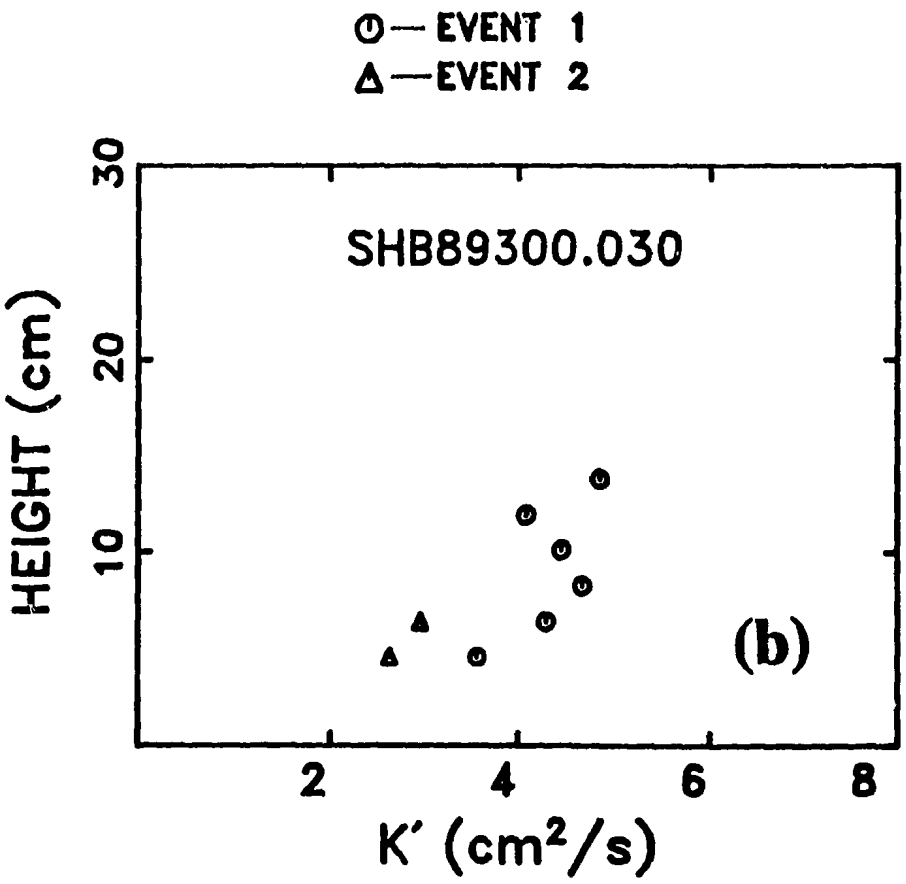

Figure 8.35. (continued)

Figure 8.36a shows vertical K' profiles averaged over three selected windows in the medium energy case (Table 8.2, also see Figure 8.12). In comparison with K_t in Figure 8.26a, K' in Figure 8.36a is mainly the same as K_t for heights below 8 cm in all three window. K' is slightly larger than K_t for heights between 8 cm and 18 cm in windows A and C, and between 8 to 12 cm in Window B, which is due to the effects of $\overline{M_w' W_w'}$ (Figure C.6). The values of K' in all three windows are smaller and decrease more rapidly with height than K_t for heights above 18 cm from the bed. Figure 8.36b displays vertical K' profiles averaged over three events in the medium energy case (Table 8.2, also see Figure 8.12). It can be seen, by comparing with Figure 8.26b, that there are no significant differences between K' and K_t at heights below 10 cm. Again K' decreases with height faster than K_t after reaching a maximum. It appears that data for heights above 18 cm from the bed in Figure 8.36b are less scattered, compared with data in Figure 8.26b. It should be noted that the negative values of K' at heights above 30 cm from the bed in Event 2 (Figure 8.36b) are mainly due to overestimates of vertical wave flux $\overline{M_w' W_w'}$ at these heights.

Vertical K' profiles averaged over two selected windows in the high energy run SHB89308.046 (Table 8.2, see also Figures 8.13 a and b) are shown in Figure 8.37a. Compared with K_t in Figure 8.27a, K' in Window A in Figure 8.37a is roughly same as K_t for heights below 14 cm, but larger than K_t for heights between 14 cm and 33 cm. Again, the most noticeable effect is that K' becomes much smaller and decreases faster with height than K_t for heights above 33 cm from the bed. K' in Window B, however, is slightly smaller than K_t for heights below 7 cm, then becomes larger than K_t for heights between 7 cm and 18 cm,

finally is much smaller than K_s for heights above 18 cm from the bed. Vertical K' profiles in the second high energy run SHB89308.047 are shown in Figure 8.37b. By comparing with K_s in Figure 8.27b, it can be seen that K' for both windows is larger than K_s at all heights inside the suspension cloud, and the slope of vertical profiles in the linear near bed region becomes larger than that in Figure 8.27b. This is due to the large negative vertical wave flux (Figure C.7b).

By assuming now that K' is linearly related with K_m [e.g. Dyer, 1986, p.159], we have

$$K' = \beta_K K_m \tag{8.25}$$

in which β_K is constant, and K_m can be written as [e.g. Dyer, 1986, p.159]

$$K_m = k u_* z \tag{8.26}$$

in the linear region. In the above expression k is von Karman's constant, which is about 0.4, and u_* is the bottom friction velocity. Let us consider the simplification $\beta_K = 1$. Then it is clear that the bottom friction velocity u_* can be estimated from the vertical K' profiles shown in Figure 8.34. From Figure 8.34, and these values are listed in Table 8.6. By comparing with $u_* \approx$4-10 cm/s used by Taylor and Dyer [1977], 6.0 cm/s found by Soulsby and Wainwright [1987], 2.71-5.41 cm/s obtained by Cacchione *et al.* [1987], 5.6 cm/s used by Davies *et al.* [1988], and 2.4-3.7 cm/s by Vincent and Green [1990], it can be seen that the values of u_* listed in Table 8.6 are of the same order as the values obtained by others.

The thickness of the wave boundary layer may be estimated by [Grant and Madsen, 1986]

$$\delta_b = \frac{k u_{*,max} t_w}{2\pi} \tag{8.27}$$

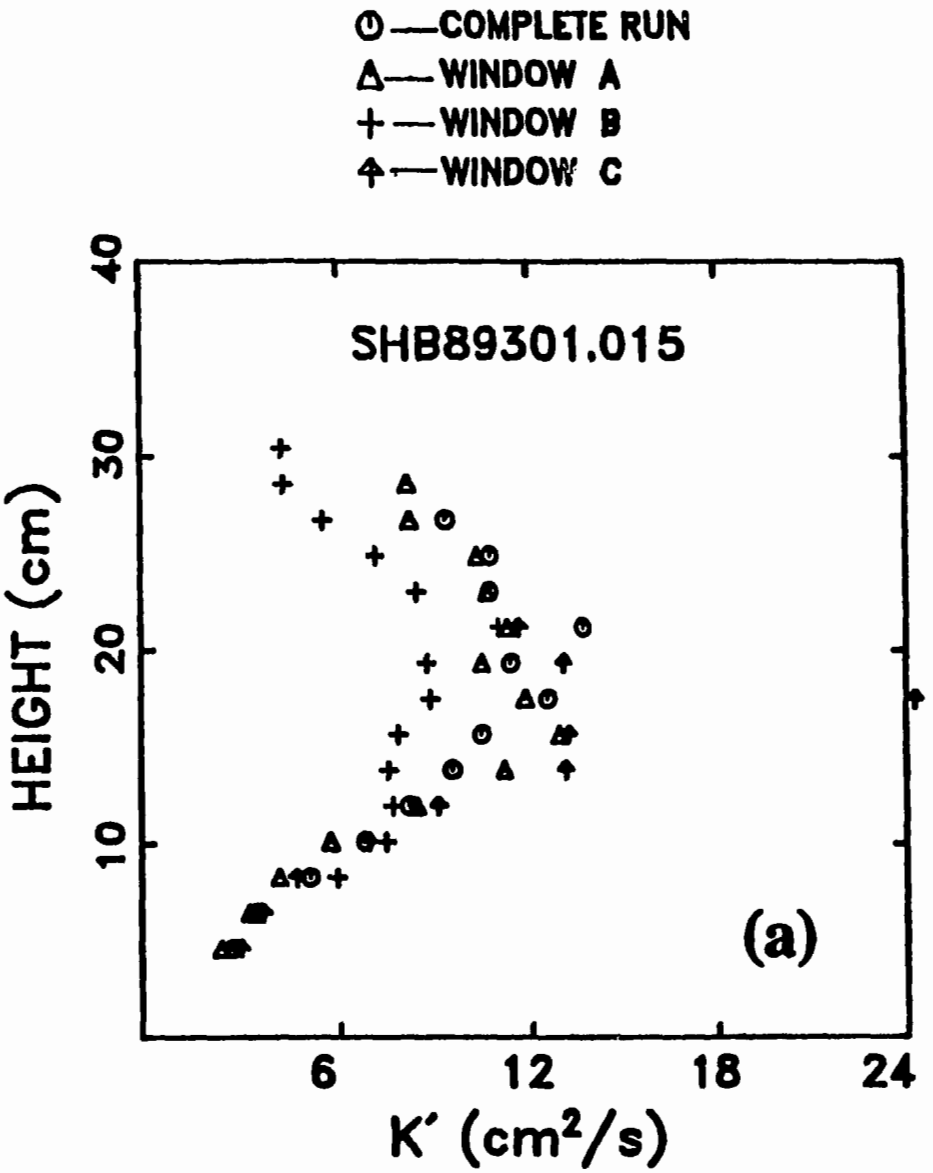

Figure 8.36. Vertical profiles of eddy diffusivity K' calculated from time-mean profiles of K_e and $\overline{M_w' W_w'}$ averaged over: (a) three entire windows and the complete run; (b) three single events in the medium energy case.

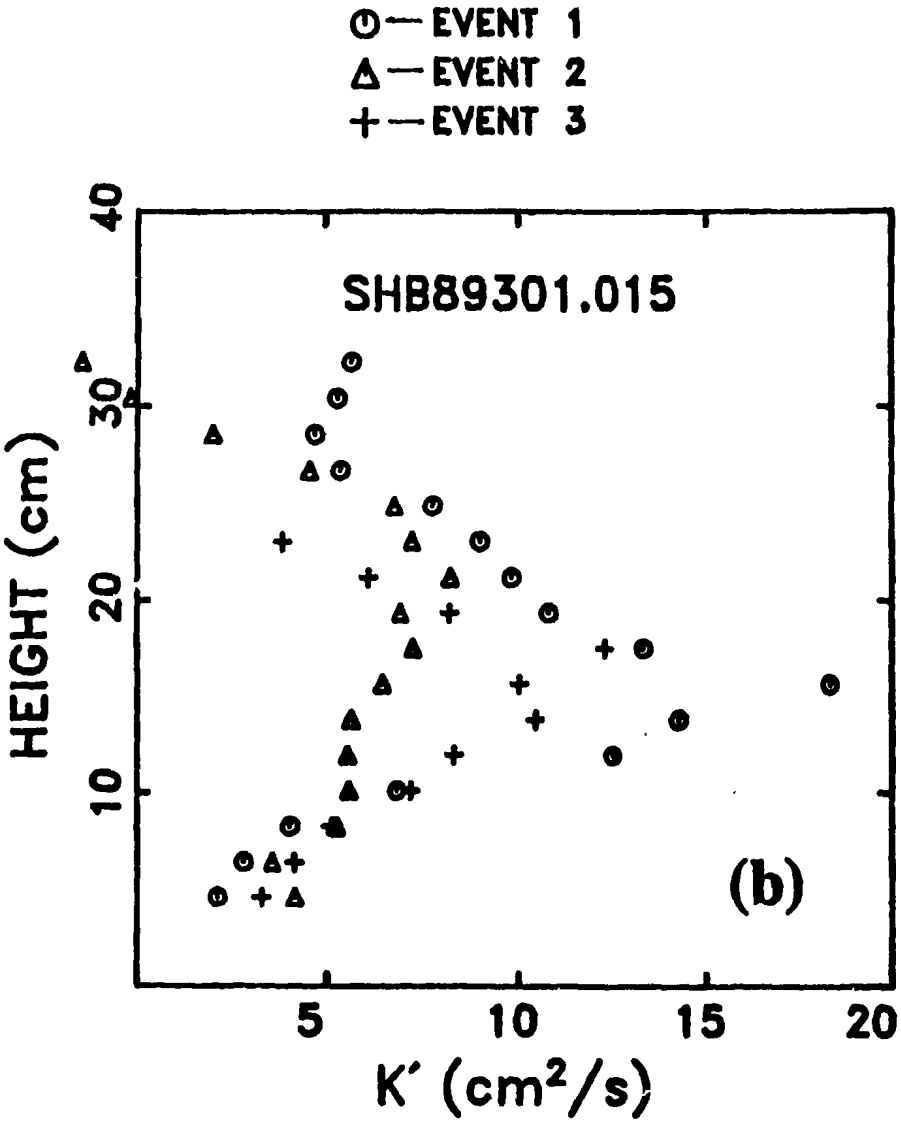

Figure 8.36. (continued)

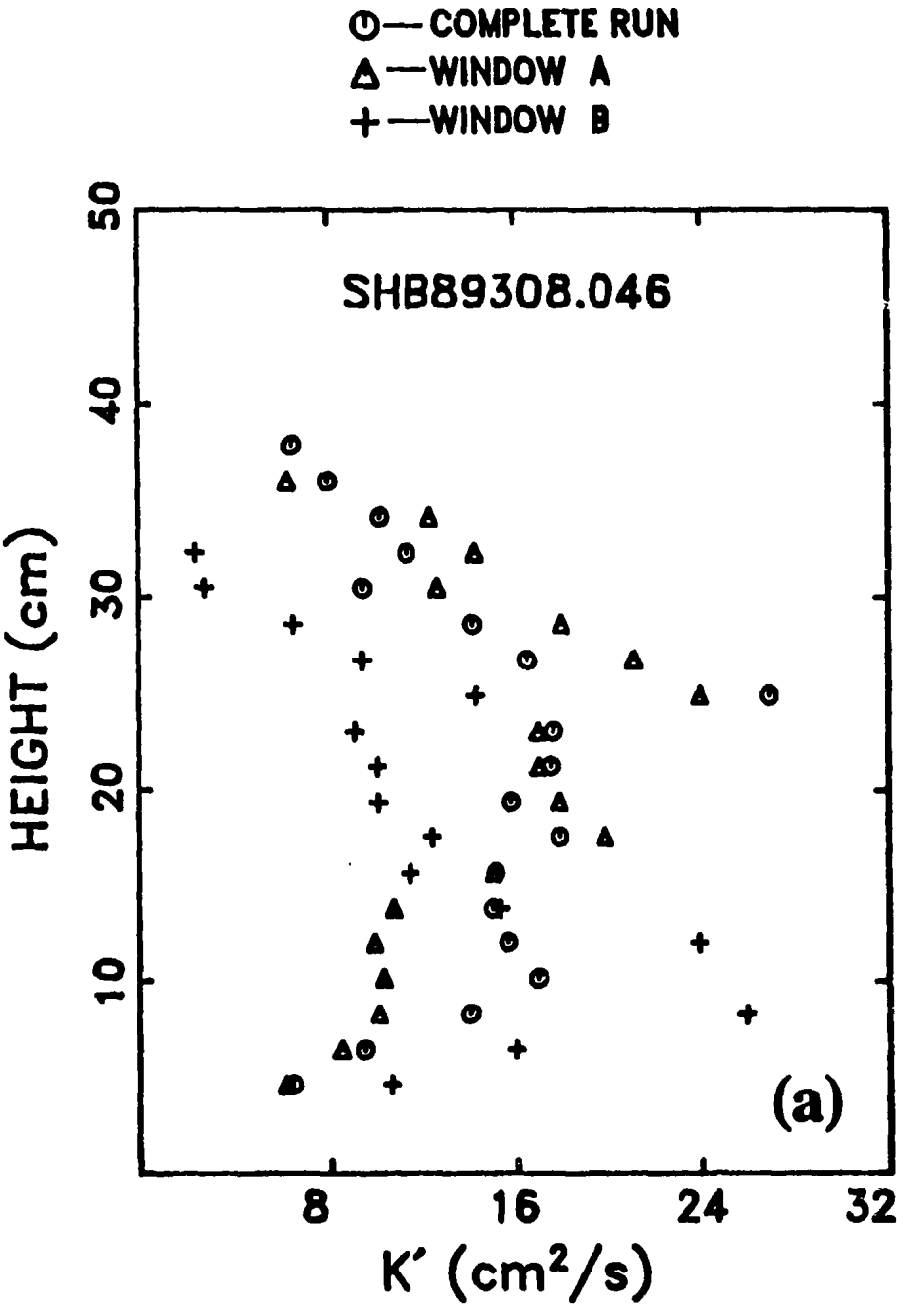

Figure 8.37. Vertical profiles of eddy diffusivity K' calculated from time-mean profiles of K_z and $\overline{M_w' W_w'}$ averaged over two entire windows and the complete run for: (a) SHB89308.046; (b) SHB89308.047 in the high energy case.

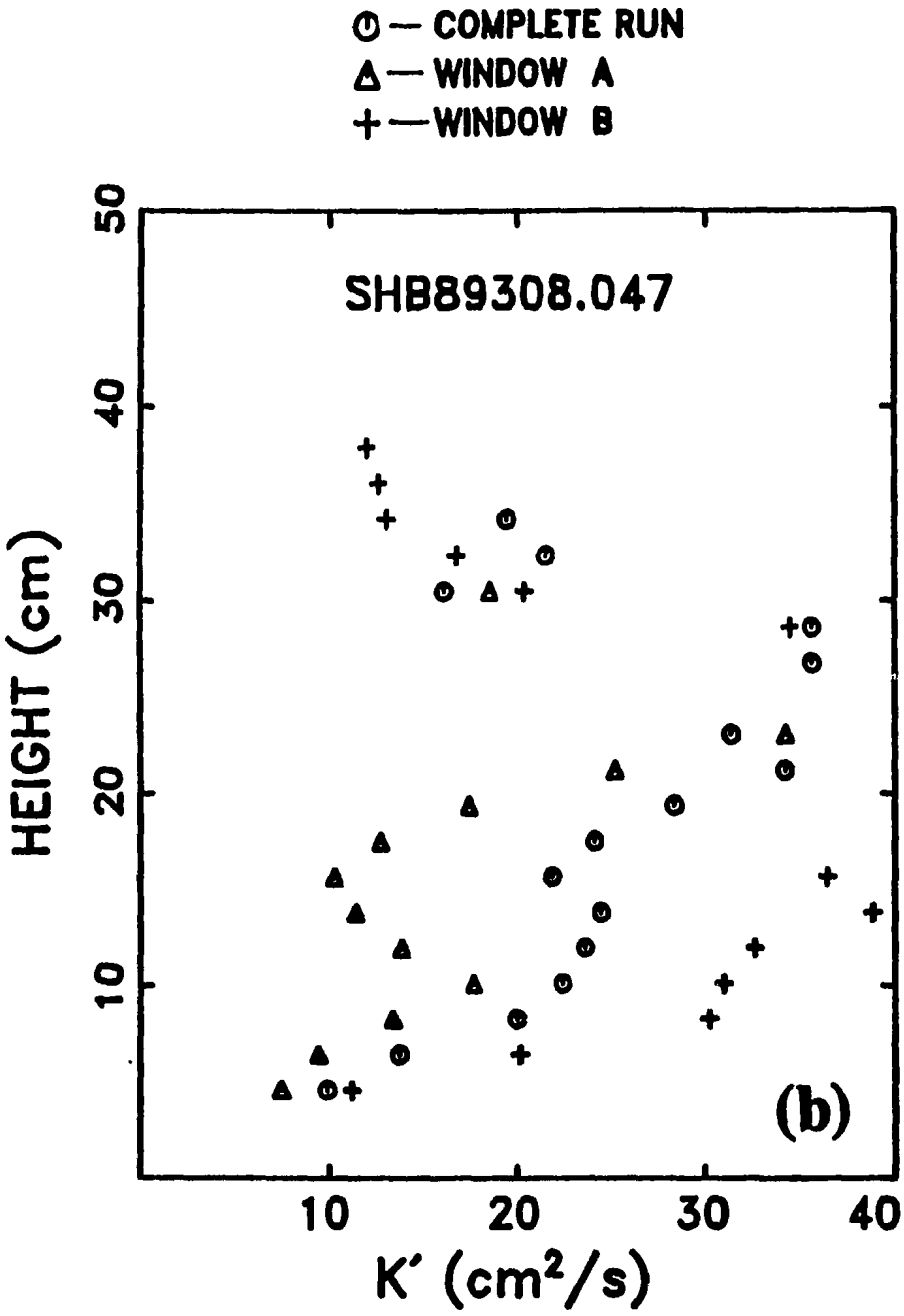

Figure 8.37. (continued)

in which $u_{*,max}$ is the maximum friction velocity, and t_w is the typical surface wave period. The values of $u_{*,max}$ in Eq. (8.27) for the Stanhope data are not available. Hence, we attempt to estimate δ_b by using the time-averaged friction velocity u_* listed in Table 8.6, instead of $u_{*,max}$. It is found that δ_b is about 1.4 cm in the low energy case, 0.4 cm in the medium energy case and 1.6-2.0 cm in the high energy case (Table 8.6), smaller than those estimated from temporal variations of bed positions (δ_{linear} in Table 8.4), which clearly emphasize the importance of using $u_{*,max}$ in Eq. (8.27) if reasonable estimates of δ_b is to be calculated.

Finally, the data in Figure 8.34 are normalized by the factor ku_*H, as suggested by Smith and McLean [1977a], and are replotted in Figure 8.38. It can be seen, in comparison with Figure 8.34, that the values of K'/ku_*H obtained for the three cases of different wave energy collapse together, especially for $z/H \leq 0.05$ and for $z/H > 0.11$. The linear dependence of K'/ku_*H on z/H for very small values of z/h and the parabolic shape for $z/H > 0.05$ appear to be universal and are very similar to the normalized eddy viscosity K_m/ku_*H found by others [e.g. Townsend, 1951; Klebanoff, 1955; Smith and McLean, 1977a; Taylor and Dyer, 1977; Glenn and Grant, 1987]. By examining Figure 8.38, it can be seen that the thickness of the linear region of K'/ku_*H is different for different surface wave energies (normalized values): at least 0.04 at low energy; about 0.08 at the medium energy; and 0.04 at the high energy, which are distinct from K_m/ku_*H discussed by Smith and McLean [1977a]. The variant vertical extent of the linear regions in different wave energy cases is attributed to the combined effects of bottom roughness and surface wave energies (Section 8.6), which may

also be the main reason why the data at intermediate heights ($0.04 \leq z/H \leq 0.11$) in Figure 8.38 appear to be a great degree of scatter. It can be seen from Figure 8.38 that the maximum normalized eddy diffusivity K'/ku_*H is about 0.088 at $z/H \sim 0.1$ in the medium energy case; 0.065 at $z/H \sim 0.18$ in the high energy run SHB89308.047; and 0.04 at $z/H \sim 0.09$ in the high energy run SHB89308.046. By considering that the maximum normalized eddy viscosity K_m/ku_*H is about 0.165 at $z/H \sim 0.3$ [Smith and McLean, 1977a], it is apparent that the maximum value of K'/ku_*H (Figure 8.38) are 2 to 4 times smaller than the maximum value of K_m/ku_*H [Smith and McLean, 1977a]. Since the normalized heights z/H corresponding to the maximum values on the profile of K'/ku_*H is also 2 to 4 times smaller than that for K_m/ku_*H, the difference in the maximum values between K'/ku_*H and K_m/ku_*H could be simply due to the normalized factor H. Finally, the vertical profiles of K'/ku_*H shown in Figure 8.38 could be affected by the possible alongshore currents as well, of which the measurements, however, are not available.

Table 8.6. Water depth H estimated from tidal measurements, the time-mean bottom friction velocity u_* estimated from vertical K' profiles shown in Figure 8.34, and calculated values of boundary thickness δ_b replacing $u_{*,max}$ in Eq. (8.27) by u_* in three wave energy cases.

Energy	File	t_w (s)	$U_{1/3}$ (m/s)	H (m)	h_{ripple} (cm)	u_* (cm/s)	δ_b (cm)
Low	SHB89300.030	5.3	0.35	2.18	3.0	4.1	1.4
Medium	SHB89301.015	3.6	0.55	2.15	2.5	1.8	0.4
High	SHB89308.046	5.0	1.15	2.22	0.3	5.0	1.6
	SHB89308.047	5.1	0.97			6.1	2.0

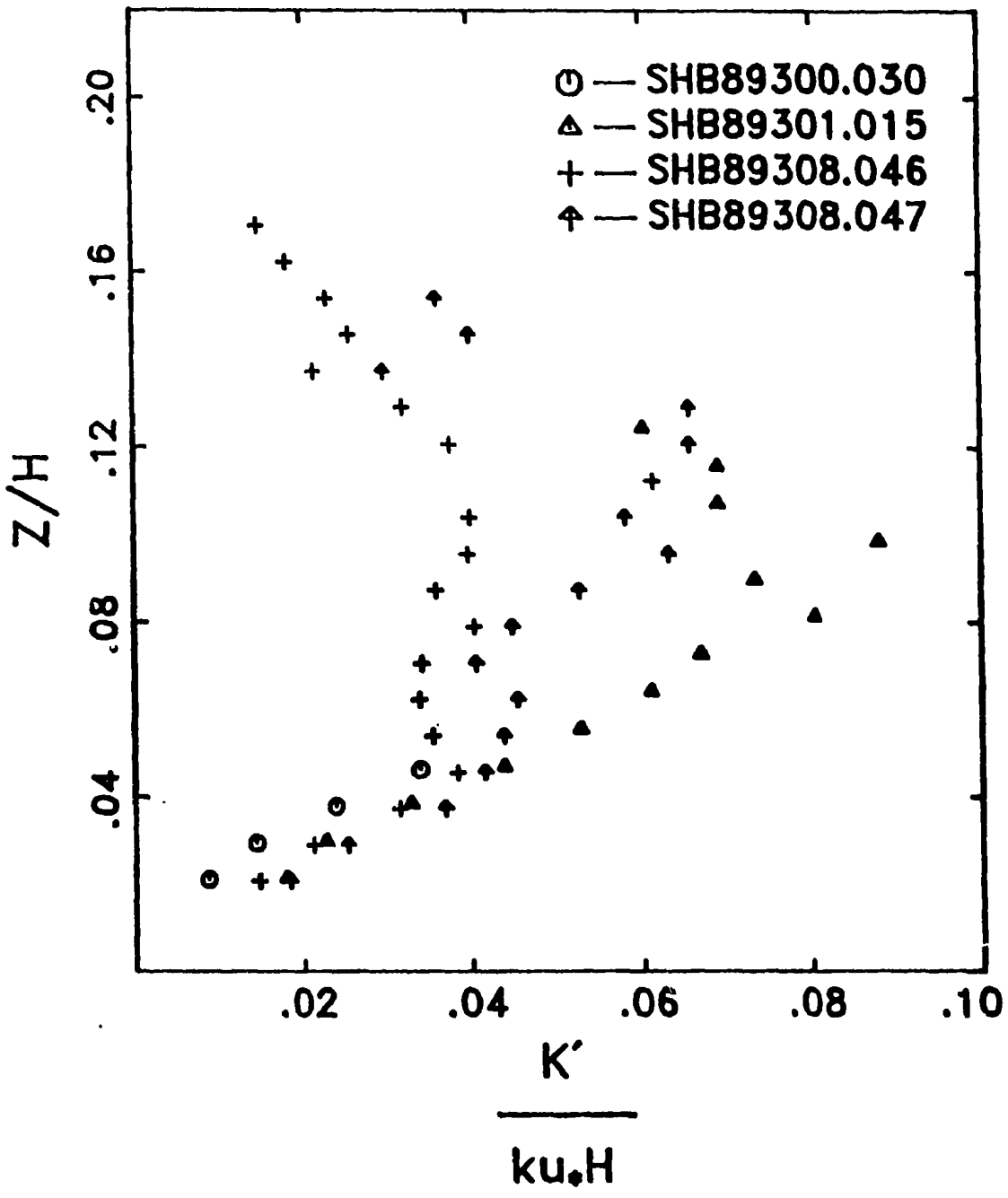

Figure 8.38. Normalized eddy diffusivity K' profiles in three wave cases.

CHAPTER 9 CONCLUSIONS

RASTRAN System 1 [Hay *et al.*, 1988] was successfully used both in laboratory jet experiments and in nearshore sediment transport experiments. Acoustic backscatter signals at three different frequencies (1, 2.5 and 5 MHz) were collected at a 4-ping ensemble-averaged profile acquisition rate of 6.6 Hz and 1.8 cm resolution in range. The results obtained here demonstrate that a multi-frequency acoustic profiling system can be used to obtain suspended sediment concentration and size remotely, given the transducer sensitivities and sand scattering cross sections.

To determine system sensitivity at each frequency, standard targets (straight stainless steel wires) were used. This problem was addressed by beginning with the theoretical investigation of acoustic backscattering from a cylinder of finite length in a pulsed monostatic system with narrow beamwidth. Theoretical results revealed that the scattered pressure linearly increase with the effective length L of the cylinder when L is much smaller than the diameter of the first half-period Fresnel zone $\sqrt{2r\lambda}$. For $L >> \sqrt{2r\lambda}$, on the other hand, the scattered pressure is independent of L. Backscatter measurements from wires with four different radii were made in the test tank by placing wires at seven different ranges from the transducers. It was illustrated that the measured size/frequency variations of the form factor $|f_w(x_w)|$ agree well with the theory for a straight elastic cylinder. The predicted variations of scattered pressure at different ranges were also verified by measurements. System sensitivities were finally evaluated from detected voltages by using the theoretical results of $|f_w(x_w)|$ and $|\Gamma|$. It was

found, however, that estimated values of sensitivity from wire measurements are about $\sqrt{2}$ times larger than those obtained using other standard targets, such as turbulent suspensions of spherical glass beads [Hay, 1991]. It is interesting to note that the factor $\sqrt{2}$ is equivalent to converting the wire signals from rms amplitudes peak amplitudes. Wire measurements were also made at the field site before deploying the system. The field site calibration indicated that system sensitivities were roughly the same as those obtained in the laboratory for 1 and 2.25 MHz transducers. For the 5 MHz transducer, however, the sensitivity was found to be 40% larger than that estimated in the laboratory. Since measured data for this unit were very scattered, the large variation may be due to the presence of bubbles.

Based on scattering cross sections (i.e. the form factor $|f_\infty(x)|$) for natural sand measured in the test tank, a semi-empirical expression for non-uniform sand scattering cross sections was constructed by using theoretical results for a rigid movable spherical scatterer, and by assuming that the size distribution of natural sands follows a log-normal distribution.

It was shown that concentrations and sizes obtained by inverting the three-frequency measurements made in the laboratory compare well with siphoned concentrations and known sizes in the sediment jet experiments: with an average error of +12% for concentration, and -19% for size (the positive sign indicates overestimates and the negative sign indicates underestimates by the inversion method). The larger error for size may be due to the sorting characteristics of the sediment jet. It was found visually that for the finer size fractions the vertical extent of the suspension cloud in the capture cone was greater, which may cause

the size of suspended sediment at the centerline of the jet to be somewhat larger than that of the injected material. For coarser size fractions, on the other hand, the size of suspended sediment at the center of the jet may be somewhat finer since the largest particles can preferentially settle out in horizontal sections of the circuit. The larger variation in particle size is also attributed to the lower accuracy of some runs with low jet centerline concentrations.

Measurements made by Optical Backscatter Sensors (OBS) provide the valid independent check on the accuracy of the inversion method for the field data. It was found that the suspended sediment concentrations obtained from RASTRAN were in reasonable agreement with OBS measurements of concentration at a point 1.6 m shoreward. In the low suspension case RASTRAN field data averaged over 3 range bins provided the best fit to the OBS data, while in the higher concentrations averaging over 2 range bins provide the best fit. It is suggested that this could be due to the decrease in the OBS detected volume with increasing concentration.

To deal with an enormous quantity of acoustic data, color coded images of the detected voltage, or the concentration, or the size, were created. The temporal and vertical variabilities of particle concentration and size are clearly revealed in the acoustic images, from which the suspension strength and vertical extent can also be determined. It was illustrated that the vertical extent of sediment suspension varied with surface wave energy: 10 cm for the low energy; 20 cm for the medium energy; and 40 cm for the high energy. The particle sizes were more uniform vertically than concentration. Discrete spots containing large particles were observed at intermediate heights in some of the images, particularly

those at high surface wave energy.

Time-averaged profiles of particle concentration and size were calculated over three different time intervals: complete data sets (about 6.5 minutes), entire windows (about 1.5 minutes), and single events (28 to 36 seconds), which are all longer than several surface wave periods (about 4 to 5 seconds). It was found that in the near bed region, mean particle concentration profiles follow a power law. Above that region, mean particle concentrations decrease with height approximately exponentially. The dependence of concentration on the wave energy is quite interesting: for heights greater than 8 cm from the bed, concentration is larger for higher energy; for heights below 8 cm from the bed, however, the concentration in the medium energy case was largest, while the concentration in the low energy case was smallest.

It was shown that time mean suspended particle sizes are nearly uniform with height, especially for mean concentration $\geq$ 0.2 kg/m^3, but vary with time during deployment. The particle sizes in the near bottom bins immediately above this level are comparable to, or less than, the medium size of the bottom sediments. While there are no field measurements of size profiles available, the above results are very promising and demonstrate the value of measuring size as well as concentration.

Sediment eddy diffusivities K_s were calculated from the vertical profiles of particle concentration and size, by assuming a balance between the vertical diffusion and settling. It was found that in the near bed region sediment eddy diffusivities increase linearly with the height, which is in correspondence with the power distribution of concentration profiles in this region. Above the near bed

region, eddy diffusivities decrease slightly with height, which is consistent with the fact that concentration profiles in this region can be approximately expressed by exponential functions.

The bottom roughness was characteristized by the ratio of ripple wavelength to ripple height: *VFI* [Allen, 1982], and the ripple heights. The former was obtained from the Allen's diagram by using significant cross-shore wave velocities near the bed, while the latter were estimated from variations of measured values of the depth from transducers by using an oscilloscope. It was found that the thickness of the near bed region depends on both surface wave energy and bottom roughness. For similar bottom roughness, the linear region becomes thicker for higher energy. When the bottom changes from the rippled bed to a plane one, the region becomes thinner.

It was demonstrated that the contribution of the on-offshore wave flux to the total sediment transport rate is not negligible, sometimes it becomes the main component. The relative directions of the on-offshore wave flux and the flux due to the mean flow not only vary with the wave energy, but also with height.

In order to compare the sediment eddy diffusivity with the eddy viscosity K_m, it is necessary to eliminate the effects of wave motion from the sediment eddy diffusivity K_s by estimating the vertical wave flux $\overline{M_w' W_w'}$ using shallow water theory. It was found that the eddy diffusivity due to turbulence K' increases linearly with height in the near bed region, after reaching a maximum, it decreases parabolically with height, which appear to be universal and very similar to the eddy viscosity K_m found by others [e.g., Smith and McLean, 1977a]. It was shown that the variant vertical extent of the linear region of the

normalized eddy diffusivity K'/ku_*H for different wave energies is mainly caused by the combined effects of the bottom roughness and surface wave energy, which are also the main reason why K'/ku_*H at the intermediate heights appear to be a great degree of scatter. By estimating the slope of the K' profile in the near bed region, and assuming K' is identical to K_m, then bottom friction velocity was estimated and found to be of the same order as suggested by others.

The currently proposed inversion method, however, can only resolve the mean size of suspended particles, which is limited by characteristics of $F(x)$-ratios for the particle size of 30 μm to 300 μm. To determine completely particle size distribution, an acoustic system with more than three different frequencies, or a broad band frequency technique, is required.

REFERENCES

Abramowitz, M., and I. A. Stegun, *Handbook of Mathematical Functions.* National Bureau of Standards, Applied Mathematics Series, Dover, 55, 437-478, 1968.

Adams, C.E., and G. L. Weatherly, Some effects of suspended sediment stratification on an oceanic bottom boundary layer. *J. Geophys. Res., 86,* 4161-4172, 1981.

Albers, V. M., *Underwater Acoustic Handbook - II,* The Pennsylvania State University, 356 pp., 1965.

Allen, J. R. L., *Sedimentary Structures, Their Character and Physical Basis.,* Developments in Sedimentology 30 A, Elsevier, New York, 663 pp., 1982.

Andreeva, I. B., and V. G. Samovol'kin, Sound scattering by elastic cylinders of finite length. *Sov. Phys. Acoust. 22,* 361-364, 1977.

Baba, J., and P. D. Komar, Measurements and analysis of settling velocities of natural quartz sand grains. *Jour. Sed. Petrology, 51,* 631-640, 1981.

Bendat, J. S., and A. G. Piersol, *Random Data: Analysis and Measurement procedures.* John Wiley & Sons, New York, 407 pp., 1971.

Bedford, K. W., R. VanEvra III, and H. Valizadeh, Ultrasonic measurement of sediment resuspension. In *Applying Research to Hydraulic Practice,,* P. Smith, ed. ASCE Press, 575-580, 1982.

Bowden, K. F., *Physical Oceanography of Coastal Waters,* John Wiley & Sons, New York, 302 pp., 1983.

Bosman, J. J., T. J. M. Elsbeth, V. D. Velden, and H. Cornelis, In *Proc. of Coastal Engineering, 11,* 353-370, 1987.

Brenninkmeyer, S. J., In situ measurements of rapidly fluctuating, high sediment concentrations. *Mar. Geol., 20,* 117-128, 1976.

Cacchione, D. A., and D. E., Drake, A new instrument system to investigate sediment dynamics on continental shelves. *Mar. Geol., 30,* 299-312, 1979.

Cacchione, D. A., W. D. Grant, D. E., Drake, and S. M. Glenn, Storm-dominated bottom boundary layer dynamics on the Northern California Continental Shelf: Measurements and Predictions. *J. Geophys. Res., 92* 1817-1827, 1987.

Carver, R. E., *Procedures in Sedimentary Petrology,* John Wiley & Sons, New York, 653 pp., 1971.

Christoffersen, J. B., and I. G. Jonsson, Bed friction ad dissipation in a combined current and wave motion. *Ocean Engng., 12,* 387-423, 1985.

Clarke, S. P., *Handbook of Physical Constants,* Geol. Soc. Am. Mem., 97, revised ed., 197-201, 1966.

Clay, C. S., and H. Medwin, *Acoustical Oceanography,* John Wiley & Sons, New York, 544 pp., 1977.

Chow, V. T., The log-probability law and its engineering applications. *Am. Soc. Civil Engineering Proc., Separate no. 536,* 25, 1954.

Dally, W. R., and R. G. Dean, Suspended sediment transport and beach profile evolution. *J. Waterway, Port, Coastal and Ocean Engineering, 110,* 15-33, 1984.

Davies, A. G., R. L. Soulsby, and H. L. King, A numerical model of the combined wave and current bottom boundary layer. *J. Geophys. Res., 93,* 491-508, 1988.

Downing, J. P., R. W. Sternberg, and C. R. B. Lister, New instrumentation for the investigation of sediment suspension processes in the shallow marine environment. *Mar. Geol., 42,* 19-34, 1981.

Drake, D. E., Suspended sediment and thermal stratification in Santa Barbara Channel, California. *Deep-Sea Research, 18,* 763-769, 1971.

Drake, D. E., D. A. Cacchione, R. D. Muench, and C. H. Nelson, Sediment transport in Norton Sound, Alaska. *Mar. Geol., 36,* 97-126, 1980.

Drake, D. E., and D. A. Cacchione, Estimates of the suspended sediment reference concentration (C_a) and resuspension coefficient (γ_o) from near-bed observations on the California shelf. *Continental Shelf Research, 9,* 51-64, 1989.

Dyer, K. R., *Coastal and Estuarine sediment Dynamics,* John Wiley & Sons, New York, 342 pp., 1986.

Dyer, K. R., and R. L. Soulsby, Sand transport on the continental shelf. *Ann. Rev. Fluid. Mech., 20,* 295-324, 1988.

Einstein, H. A., Bed load movement in mountain creek. *U.S. Dept. Agr., Soil Conserv. Serv., SCS-TP-55,,* 54 pp., 1944.

Einstein, H A., The bed-load function for sediment transportation in open channel flows. *U.S. Dept. Agr., Soil Conserv. Serv., Tech. Bull. 1026,* 78 pp., 1950.

Faran, J. J. Jr., Sound scattering by solid cylinders and spheres. *J. Acoust. Soc. Amer., 23,* 405-418, 1951.

Fisher, F. H., and V. P. Simmons, Sound absorption in sea water. *J. Acoust. Soc. Am., 62,* 558-564, 1977.

Flammer, G. H., Ultrasonic measurement of suspended sediment. *Geological Survey Bulletin No. 1141-A,* US Government Printing Office, Washington, 1962.

Forbes, D. L, Shoreface sediment distribution and sand supply at C^2S^2 sites in the southern Gulf of St. Laweence. In *Coastal Sediments, 87,* ASCE, 694-709, 1987.

Gibbs, R. J., M. D. Matthews, and D. A. Link, The relationship between sphere size and settling velocity. *Jour. Sed. Petrology, 41,* 7-18, 1971.

Glenn, S. M., *A continental shelf bottom boundary layer model: The effects of waves, currents, and a moveable bed.* ScD thesis. Mass. Inst. Technol., Cambridge. 275 pp., 1983.

Glenn, S. M., and W. D. Grant, A suspended sediment stratification correction for combined wave and current flows. *J. Geophys. Res. 92,* 8244-8264, 1987.

Gradshteyn, I. S., and I. M. Ryzhik, *Table of Integrals, Series, and Products.* Academic Press, New York, 1160 pp., 1980.

Grant, W. D., and O. S. Madsen, Combined wave and current interaction with a rough bottom. *J. Geophys. Res. 84,* 1797-1808, 1979.

Grant, W. D., and O. S. Madsen, Moveable bed roughness in unsteady oscillatory flow. *J. Geophys. Res. 87,* 469-481, 1982.

Grant, W. D., and O. S. Madsen, The continental-shelf bottom boundary layer. *Ann. Rev. Fluid Mech., 18* 265-305, 1986.

Haines, J. W., Steady flows in the nearshore zone. In *Proc. 19th Coastal Engineering Conf.,* Houston, Texas, ASCE, New York, 2280-2292, 1985.

Hanes, D. M., and D. A. Huntley, Continuous measurements of suspended sand concentration in a wave dominated nearshore environment. *Continental Shelf Research, 6,* 585-596, 1986.

Hanes, D., and C. E. Vincent, Detailed dynamics of nearshore suspended sediment. In *Coastal Sediments, 87,* ASCE, 285-299, 1987.

Hanes, D. M., C. E. Vincent, D. A. Huntley, and T. L. Clarke, Acoustic measurements of suspended sand concentration in the C^2S^2 experiment at Stanhope lane, Prince Edward Island. *Mar. Geol., 81,* 185-196, 1988.

Hatch, T. and S. P. Choate, Statistical description of size properties of non-uniform particulate substances. *Franklin Inst. Jour., 207,* 369-387, 1929.

Hay, A. E., On the remote acoustic detection of suspended sediment at long wavelengths. *J. Geophys. Res., 88,* 7525-7542, 1983.

Hay, A. E., and D. Heffler, Design considerations for an acoustic sediment transport monitor for the nearshore zone. *Canadian Coastal Sediment Study, Report No. 4,* 37 pp., 1983.

Hay, A. E., L. Huang, E. B. Colbourne, J. Sheng, and A. J. Bowen, A high speed multi-channel data acquisition system for remote acoustic sediment transport studies. In *Proc. Ocean '88,* 413-418, 1988.

Hay, A. E., and A. S. Schaafsma, Resonance scattering in suspensions. *J. Acoust. Soc. Amer., 85,* 1124-1138, 1989.

Hay, A. E., Sound scattering from a particle-laden turbulent jet. *J. Acoust. Soc. Amer.,* (accepted) 1991.

Hazen, D. G., D. A. Huntley, and A. J. Bowen, UDATS: A system for measuring nearshore process. In *Proc. Oceans'87,* 993-997, 1987.

Hom-ma, M., K. Horikawa, and R. Kajima, A study on suspended sediment due to wave action. *Coast. Eng. Jap., 8,*85-103, 1965.

Hess F. R., and K. W. Bedford, Acoustic backscatter system (ABSS): the instrument and some preliminary results. *Mar. Geol., 66* 357-380, 1985.

Huntley, D. A., In situ sediment monitoring techniques: a survey of the state of the art in U. S. A. *Canadian Coastal Sediment Study, Report No. 1,* 35 pp., 1982.

Huntley, D. A., and D. M. Hanes, Direct measurement of suspended sediment transport. In *Coastal Sediments 87,* ASCE, 723-737, 1987.

Huntley, D. A., and A. J. Bowen, Modeling sand transport on continental shelves. In *Modeling Marine System, Vol.1,* A. M. Davies, ed., CRC Press, 221-254, 1989.

Huff, L., and D. C. Friske, Development of two sediment transport instrument system. In *Proceeding, Seventeenth International Conference on Coastal Engineering,* ASCE, New York, 1980.

Jansen, R. H. J., An ultrasonic Doppler scatterometer for measuring suspended sand transport. In *Ultrasonic International '79, UI79,* Graz, Austria, 366-369, 1979.

Kajima, R, and H. Katori, Sediment transport rate. In *Nearshore Dynamics and Coastal Processes,* K. Horikawa, ed., University of Tokyo Press, 522 pp., 194-217, 1988

Kennedy J. K., and F. A. Locher, Sediment suspension by water waves. In *Waves on Beaches*, R. E. Meyer, ed., Academic Press, New York, 249-298, 1972.

Klebanoff, P. S., Characteristics of turbulence in boundary layer with zero pressure gradient. *Nat. Adv. Aeronaut. Rep. No. 1247*, 1955.

LeBond, P. H., and L. A. Mysak, *Waves in the Ocean*, Elsevier, New York, 602 pp., 1978.

Lesht, B. M., T. L. Clarke, G. L. Freeland, D. J. P. Swift, and R. A. Young, An empirical relationship between the concentration of resuspended sediment and near-bottom wave orbital velocity. *Geophys. Res. Lett., 2*, 1049-1052, 1980.

Li, T, and M. Ueda, Analysis of echoes from a cylinder that includes the directivity of the transmitter and receiver. *J. Acoust. Soc. Am., 87*, 1880-1884, 1990.

Libiciki, C. L., K. D. Bedford, R. VanEvra III, and J. F. Lynch, A 3 MHz acoustic sediment profiling system. In *Proc. of Coastal Sediments, 87*, 237-249, 1987.

Libiciki, C. L., K. D. Bedford, and J. F. Lynch, The interpretation and evaluation of a 3-MHz acoustic backscatter device for measuring benthic boundary layer sediment dynamics. *J. Acoust. Soc. Am., 85*, 1501-1511, 1989.

Lynch, J. F., T. F. Gross, C. Libiciki, and K. W. Bedford, Deepwater sediment concentration profiling in HEBBLE using a one megahertz acoustic backscatter system. In *Coastal Sediments '87*, ASCE, 250-259, 1987.

Moody, J. A., B. Butman, and H. Bothner, Near-bottom suspended matter concentration on the Continental Shelf during storms: estimates based on in situ observations of light transmission and a particle size dependent transmissometer calibration. *Continental Shelf Research, 7*, 609-628, 1987.

Nakato, T. F., F. A. Locher, J. R. Glover, and J. F. Kennedy, Water entrainment of sediment from rippled beds. In *Proc. ASCE. 103, No. WW1*, 83-99, 1977.

Press, W. H., B. P. Flannery, B. P. Teukolsky, and W. T. Vetterling, *Numerical Recipes: The Art of Scientific Computing.* Cambridge University Press, Cambridge, 818 pp., 1986.

Orr M. H., and F. R Hess, Remote acoustic monitoring of natural suspensate distributions, active suspensate resuspension, and slope/shelf water intrusions. *J. Geophys. Re., 83*, 4062-4068, 1978.

Rayleigh, Lord (J. W. Strutt), *Theory of Sound.* 2nd Ed., Dover, New York, 504 pp., 1945.

Renger, E., New technology and automation of continuous sediment concentration measurement. In *Transport of Suspended Solids in Open Channels*, W. Bechteler, ed., Balkema, Netherlands, 221-231, 1986.

Schaafsma, A. S., and W. J. G. J. der Kinderen, Ultrasonic instruments for the continuous measurement of suspended sand transport. In *Proc. IAHR-Symposium on Measuring Technique in Hydraulic Research*, Delft, 11 pp., 1986.

Sheng, J., and A. E. Hay, An examination of the spherical scatter approximation in aqueous suspensions of sand. *J. Acoust. Soc. Amer., 83*, 598-610, 1988.

Sheng, Y. P., and C. Villaret, Modeling the effect of suspended sediment stratification on bottom exchange processes. *J. Geophys. Res., 94*, 14429-14444, 1989.

Skudrzyk, E., *The Foundations of Acoustics*. Springer, New York, 790 pp., 1971.

Sleath, J. F. A., The suspension of sand by waves. *J. Hydraulic Research, 20*, 439-452, 1982

Smith, J. D., and T. S. Hopkins, Sediment transport on the continental shelf off of Washington and Oregon in light of recent current measurements. In *Shelf Sediment Transport*. D. J. P. Swift, D. B. Duane, and O. H. Pikey, eds., Dowden, Hutchison & Ross, Stroudsburg, 143-180, 1972.

Smith, J. D., Modeling of sediment transport on continental shelves. In *The Sea: Ideas and Observations on Progress in the Study of the Seas*, E. G. Goldberg, ed., John Wiley & Sons, New York, 539-576, 1977.

Smith, J. D., and S. R. McLean, Spatially averaged flow over a wavy surface. *J. Geophys. Res., 82*, 1735-1476, 1977(a).

Smith, J. D., and S. R. McLean, Boundary layer adjustments to bottom topography and suspended sediments. In *Bottom Turbulence*. J. C. J. Nihoul, ed., Elsevier, New York, 123-152, 1977(b).

Soulsby, R. L., and B. L. S. A. Wainwright, A criterion for the effect of ssuspended sediment on near-bottom velocity profiles. *J. Hydr. Res., 25*, 341-356, 1987.

Spinrad, R. W., J. R. Zaneveld, and J. C. Kiychen, A study of the optical characteristics of the suspended particles in the benthic nepheloid layer of the Scotian Rise. *J. Geophys. Res., 88*, 7641-7645, 1983.

Stanton, T. K., Sound scattering by cylinders of finite length. I. fluid cylinders. *J. Acoust. Soc. Amer., 83*, 55-63, 1988(a).

Stanton, T. K., Sound scattering by cylinders of finite length. II. elastic cylinders. *J. Acoust. Soc. Amer., 83*, 64-67, 1988(b).

Staub, C., I. G. Josson, and I. A. Svendsen, Variation of sediment suspension in oscillatory flow. In *Coastal sediments '84*, ASCE, 2310-2321, 1984.

Sternberg, R. W., N. C. Shi, and J. P. Downing, Suspended sediment measurements. In *Nearshore Sediment Transport*. R. L. Seymour, ed, Plenum, New York, 231-257, 1989.

Sundermann, J., and R. Klocker, Sediment transport modeling with applications to the North Sea. In *North Sea Dynamics*, J. Sundermann and W. Lenz, Eds., Springer, Berlin, 1983.

Taylor, P. A., and K. R. Dyer, Theoretical models of flow near the bed and their implications for sediment transport. In *The Sea: Ideas and Observations on Progress in the Study of the Seas*, E. G. Goldberg, ed., John Wiley & Sons, New York, 579-601, 1977.

Thornton, E. B., and W. D. Morris, Suspended sediments measured within the surf zone. In *Coastal Sediments '77*, ASCE, New York, 655-668, 1978.

Townsend, A. A., The structure of the turbulent boundary layer. *Proc. Cambridge Phil. Soc., 47*, 375-395, 1951.

Urick, R. J., The absorption of sound in suspensions of irregular particles. *J. Acoust. Soc. Am., 20*, 283-289, 1948.

Varadan, V. K., V. N. Bringi, V. V. Varadan, and Y. Ma, Coherent attenuation of acoustic waves by pair-correlated random distributions of scatters with uniform and Gaussian distributions. *J. Acoust. Soc. Am., 73*, 1941-1947, 1983.

Vincent, C. A., R. A. Young, and D. J. P. Swift, The relationship between bedload and suspended sand transport on the inner shelf, Long Island, New York. *J. Geophys. Res., 87*, 4163-4170, 1982.

Vincent, C. A., D, Hanes, T. Tamura, and T. L. Clarke, The acoustic measurement of suspended sand in the surf-zone. In *Measuring Techniques*, Landon, England, 443-451, 1986.

Vincent, C. A., and M. O. Green, Field measurements of the suspended sand concentration profiles and fluxes, and of the resuspension coefficient over a rippled bed. *J. Geophys. Res., 95*, 11591-11601, 1990.

Wang, H., and S. S. Liang, Mechanics of suspended sediment in random waves. *J. Geophys. Res., 80*, 3488-3494, 1975.

Weast, R. C., M. J. Astle, and W. H. Beyer, *Handbook of Chemistry and Physics*, CRC Press, Boca Raton, F-37, 1985.

Welch, P. D., The use of Fast Fourier Transform for the estimation of power spectra: method based on time averaging over short, modified periodo-

grams. In *Modern Spectrum Analysis*, D. G. Childers, ed., New York, IEEE Press, 17-20, 1978.

Willis, D. H., The Canadian coastal sediment study: An overview. In *Coastal Sediments '87*, ASCE, 682-693, 1987.

Wu, J., Bubble population and spectra in near-surface ocean: Summary and review of field measurements. *J. Geophys. Res.*, *86*, 457-463, 1981.

Young, R. A., J. T. Merrill, T. L. Clarke, and J. R. Proni, Acoustic profiling of suspended sediments in the marine bottom boundary layer. *Geophysical Res. Lett.*, *9*, 175-178, 1982.

APPENDIX A. ANALYTICAL RESULTS OF Γ IN TWO EXTREME CASES

The expression for $|\Gamma|$ in the extreme cases of $\psi \to 0$ and $\psi \to \infty$ can be obtained analytically. For simplicity, we consider a very narrow beam system, which means $\beta_m \ll 1$. We have

$$\begin{cases} \csc\beta \approx 1+\dfrac{\beta^2}{2} \\ \sin\beta \approx \beta \qquad\qquad (\text{for } \beta_m \ll 1), \\ \tan\beta_m \approx \sin\beta_m \approx \beta_m \end{cases} \tag{A.1}$$

Similarly, ψ in Eq. (3.52) can be approximately by

$$\psi \approx \sqrt{\frac{k_c\, r}{\pi}}\,\beta_m \tag{A.2}$$

Using Eqs. (A.1) and (A.2) in Eq. (3.55), and ignoring any terms with higher order than β^2 in the exponential part of Eq. (3.55), we have

$$\Gamma = \sqrt{\frac{2k_c\, r}{\pi}}\, e^{-i\frac{\pi}{4}} \int_0^{\beta_m} D^2 \exp\left[ik_c\, r\, \beta^2\right] d\beta, \tag{A.3}$$

For a very narrow beam system $\beta_m \ll 1$, the farfield theoretical directivity D given in Eq. (3.17) can be also approximated by [Abramowitz and Stegun, 1968, p.370]

$$D \approx \frac{2J_1\left(3.832\dfrac{\beta}{\beta_m}\right)}{3.832\dfrac{\beta}{\beta_m}} \approx 1 - 1.834\left(\frac{\beta}{\beta_m}\right)^2 \qquad (\text{for } \beta \le 0.783\beta_m) \tag{A.4}$$

The approximation for D in the range of $0.783\beta_m < \beta \leq \beta_m$ also needs to be specified. Considering D^2 in the aforementioned range (i.e. $0.783\beta_m < \beta \leq \beta_m$) is less than -13 dB, the expression given by Eq. (A.4) can be assumed to be valid in the whole range $0 \leq \beta \leq \beta_m$. Substituting Eq. (A.4) into Eq. (A.3), we get

$$\Gamma = \sqrt{\frac{2k_c r}{\pi}} e^{-i\frac{\pi}{4}} \int_o^{\beta_m} \left[1 - 3.668\left(\frac{\beta}{\beta_m}\right)^2 + 3.363\left(\frac{\beta}{\beta_m}\right)^4\right] \exp\left[ik_c r \beta^2\right] d\beta, \qquad (A.5)$$

For $\psi \to 0$, the exponential $\exp\left[ik_c r \beta^2\right]$ can be replaced by unity for the first order of approximation. Hence, Γ in Eq. (A.5) can be written as

$$\Gamma = \sqrt{\frac{2k_c r}{\pi}} e^{-i\frac{\pi}{4}} \int_o^{\beta_m} \left[1 - 3.668\left(\frac{\beta}{\beta_m}\right)^2 + 3.363\left(\frac{\beta}{\beta_m}\right)^4\right] d\beta \quad (\text{for } \psi \to 0). \qquad (A.6)$$

After integrating, Γ can be expressed by

$$\Gamma = 0.450\sqrt{2}\psi e^{-i\frac{\pi}{4}} = \frac{0.450L}{\sqrt{r\lambda}} e^{-i\frac{\pi}{4}} \quad (\text{for } \psi \to 0), \qquad (A.7)$$

which indicates Γ is a linear function of ψ (or L), and Θ tends to -45^0 when $\psi \to 0$.

For $\psi \to \infty$, variations due to $\exp\left[ik_c \beta^2\right]$ is dominant in the main lobe of the directivity pattern. By letting $\chi = \sqrt{k_c r}\,\beta$, Eq. (A.5) becomes

$$\Gamma = \sqrt{\frac{2}{\pi}} e^{-i\frac{\pi}{4}} \int_o^{\chi_o} \left[1 - \frac{3.668\chi^2}{\chi_o^2} + \frac{3.363\chi^4}{\chi_o^4}\right] e^{i\chi^2} d\chi \qquad (A.8)$$

in which $\chi_o = \sqrt{k_c r}\,\beta_m$. After integrating by parts, we have

$$\int_0^{\chi_o} \chi^2 e^{i\chi^2} d\chi = -\frac{i\chi_o}{2} e^{i\chi_o} + \frac{i}{2}\int_0^{\chi_o} e^{i\chi^2} d\chi \tag{A.9}$$

and

$$\int_0^{\chi_o} \chi^4 e^{i\chi^2} d\chi = -\frac{i\chi_o^3}{2} e^{i\chi_o} + \frac{3\chi_o}{4} e^{i\chi_o} - \frac{3}{4}\int_0^{\chi_o} e^{i\chi^2} d\chi \tag{A.10}$$

Substituting Eqs. (A.9) and (A.10) into Eq. (A.8), Γ takes the form

$$\Gamma = \sqrt{\frac{2}{\pi}} e^{-i\frac{\pi}{4}} \left[\left(1 - \frac{1.834i}{\chi_o^2} - \frac{2.522}{\chi_o^4} \right) \int_0^{\chi_o} e^{i\chi^2} d\chi + \right.$$
$$\left. + \left(0.153i + \frac{2.522}{\chi_o^2} \right) \frac{e^{i\chi_o^2}}{\chi_o} \right] \tag{A.11}$$

From Gradshteyn and Ryzhik [1980, p.395], we have

$$\int_0^{\infty} e^{i\chi^2} d\chi = \int_0^{\infty} \cos(\chi^2) d\chi + i\int_0^{\infty} \sin(\chi^2) d\chi = \frac{\sqrt{\pi}}{2} e^{i\frac{\pi}{4}}. \tag{A.12}$$

Since $\chi_o = \sqrt{k_c r}\, \beta_m = \sqrt{\pi}\psi$, $\chi_o \to \infty$ when $\psi \to \infty$. Hence

$$\Gamma = \sqrt{\frac{2}{\pi}} e^{-i\frac{\pi}{4}} \lim_{\chi_o \to \infty} \left[\left(1 - \frac{1.834i}{\chi_o^2} - \frac{2.522}{\chi_o^4} \right) \int_0^{\chi_o} e^{i\chi^2} d\chi + \right.$$
$$\left. + \left(0.153i + \frac{2.522}{\chi_o^2} \right) \frac{e^{i\chi_o^2}}{\chi_o} \right] = \frac{1}{\sqrt{2}} \quad (\text{for} \quad \psi \to \infty). \tag{A.13}$$

which indicates that, for a very large value of ψ, $|\Gamma|$ tends to a constant $1/\sqrt{2}$ and Θ tends to zero degree.

APPENDIX B. RESULTS OF JET MEASUREMENTS

The measured and inverted jet-centerline concentrations (M) and sizes (a) with the centerline voltages (V) detected by three sounders are listed in this Appendix, where V_1, V_2 and V_5 are respectively the centerline voltage for 1, 2.25 and 5 MHz. M_o is the centerline concentration measured by the suction method, and a_o is the midpoint of each sieved interval for the uniform sand particles or the geometric mean radius for the natural sands. M_i and a_i are the values converted from multi-frequency acoustic data using the inversion method in Chapter 6. The run identification was made in such a way that the first three characters represent the sand type: "USS" indicates the uniformly sized sand particles; "PEI" the Stanhope Beach sand; "BWB" the Bluewater Beach sand; "QLB" the Queensland Beach sand, the following five characters denote the year and Julian Day when the file was collected, and the extension is the sequential run number.

Run	V_1	V_2 (mV)	V_5	M_o (kg/m^3)	M_i	a_o (μm)	a_i
USS89201.002	28.3	48.8	38.9	0.65	0.46	49.0	64.7
USS89201.005	34.4	62.8	42.2	0.86	0.79	57.8	62.9
USS89201.008	37.3	66.0	39.1	0.69	0.72	68.8	69.6
USS89201.011	47.5	78.9	53.7	0.94	1.12	82.5	70.4
USS89201.014	60.7	86.8	71.7	1.01	1.32	98.0	76.7
USS89201.017	70.7	77.9	68.8	0.92	1.00	115.5	94.1
USS89201.020	85.5	77.2	66.3	0.96	1.02	137.5	107.8
USS89201.023	91.5	85.1	57.6	0.87	1.05	163.8	125.7
USS89201.026	102.5	109.5	54.5	1.01	1.38	195.0	156.6
USS89201.029	100.5	119.2	52.5	1.11	1.54	231.3	142.3
PEI89222.002	28.5	37.7	23.0	0.18	0.17	79.0	86.1
PEI89222.004	37.6	56.7	36.8	0.41	0.47	79.0	71.3
PEI89222.006	55.6	83.6	55.6	1.26	1.07	79.0	71.2
PEI89222.008	76.2	129.5	85.1	2.65	3.28	79.0	60.9

PEI89222.010	113.0	189.1	116.8	6.08	6.81	79.0	61.9
PEI89222.012	134.9	225.0	128.6	9.44	9.87	79.0	62.1
PEI89222.014	158.5	262.9	141.9	12.27	13.74	79.0	61.7
PEI89222.016	184.3	303.2	151.2	16.65	20.29	79.0	60.9
PEI89222.018	200.2	313.7	153.7	19.61	21.57	79.0	63.4
PEI89222.020	213.8	335.6	154.1	23.06	25.18	79.0	62.2
PEI89228.008	38.7	63.2	40.9	0.62	0.66	79.0	64.9
PEI89228.010	57.2	94.6	63.3	1.35	1.62	79.0	62.4
PEI89228.012	78.6	129.8	84.3	2.82	3.12	79.0	63.0
PEI89228.014	97.4	168.0	103.1	4.37	5.21	79.0	61.8
PEI89228.016	112.8	193.0	115.0	6.03	6.95	79.0	61.4
PEI89228.018	140.3	233.2	135.3	9.40	10.56	79.0	62.4
PEI89228.020	157.9	256.3	144.1	12.19	13.29	79.0	63.0
PEI89228.022	174.0	275.0	147.8	14.51	14.60	79.0	64.2
PEI89228.024	186.1	293.7	156.0	16.17	18.13	79.0	62.3
PEI89228.026	195.7	311.3	158.4	18.59	20.86	79.0	62.5
PEI89228.028	207.1	318.4	150.9	20.40	21.63	79.0	65.5
BWB89230.004	30.9	46.4	25.8	0.30	0.28	68.0	72.6
BWB89230.006	40.9	66.6	39.5	0.72	0.71	68.0	63.4
BWB89230.008	50.9	87.0	49.6	1.27	1.18	68.0	61.4
BWB89230.010	71.2	122.2	70.4	2.66	2.55	68.0	60.2
BWB89230.012	86.3	152.6	85.0	4.13	4.23	68.0	58.0
BWB89230.014	98.3	180.9	98.5	5.75	6.43	68.0	55.9
BWB89230.016	108.7	196.2	109.6	7.47	7.62	68.0	54.7
BWB89230.018	119.4	212.5	116.5	9.04	9.08	68.0	54.7
BWB89230.020	129.4	227.0	118.9	10.25	9.82	68.0	56.8
BWB89230.022	137.2	247.5	125.6	11.95	12.43	68.0	54.3
BWB89230.024	149.3	259.7	133.5	14.00	14.36	68.0	56.1
BWB89230.026	152.9	269.8	134.3	15.81	15.24	68.0	54.8
BWB89230.028	166.1	288.1	139.4	18.59	17.93	68.0	56.0
BWB89230.030	192.8	323.0	156.0	22.30	23.24	68.0	55.8
QLB89230.004	33.6	39.6	17.4	0.12	0.13	175.0	136.7
QLB89230.006	41.8	50.9	23.0	0.21	0.23	175.0	150.2
QLB89230.008	55.8	71.8	32.5	0.50	0.47	175.0	150.6
QLB89230.010	92.2	116.8	53.1	1.17	1.32	175.0	149.1
QLB89230.012	126.5	158.4	72.6	2.48	2.58	175.0	144.2
QLB89230.014	155.2	184.1	86.0	3.47	3.66	175.0	138.7
QLB89230.016	211.4	250.7	113.4	6.26	7.44	175.0	135.0
QLB89230.018	244.5	289.6	125.4	9.02	10.71	175.0	133.6
QLB89230.020	273.0	316.8	137.1	10.49	12.89	175.0	134.8
QLB89230.022	338.9	371.1	149.5	15.59	22.37	175.0	122.9

APPENDIX C. VERTICAL WAVE VELOCITY AND VERTICAL WAVE FLUX

Sea-level variations due to tides in the surfzone of Stanhope Beach were measured by the tide gauge at about 180 m from the baseline (Figure 2.5a) at the interval of 5 minutes during the period of the RASTRAN deployment (roughly 2 weeks). The high-frequency variations on the records are filtered out by using a rectangular running average of 50 minutes wide in the time domain. Relative sea-level changes caused by tides, for the first order of approximation, are then obtained by subtracting the filtered tide gauge measurements from their mean value. By assuming the relative sea-level changes due to tides at the RASTRAN site (at about 247 m from the baseline) are same as those at the tide gauge site (at about 180 m), the water depth H at the RASTRAN site can then be represented by the summation of the aforementioned relative sea-level changes caused by tides and the mean water depth ($\approx$2.2 meter). The time series of water depth at the RASTRAN site is shown in Figure C.1, from which the water depth for four selected periods of field data is obtained, and listed in Table 8.6.

The wave-induced vertical velocities W_w' at the depth of $z=10$ cm and $z=H$ (see Table 8.6) calculated from horizontal velocities gradients through Eq. (8.24) are shown in Figure C.2 for the low energy case, in Figure C.3 for the medium energy case, and in Figure C.4 for the high energy case with the records of U_w' appeared on the top of the plot. It should be noted, as mentioned before, both U_w' and W_w' have been filtered using a running average of 7 sets (about 1.1 sec) in width to remove high-frequency variations from U_w' and W_w'. From

Figures C.2-4, it can be noticed that the maximum magnitude of vertical velocity W_w' at $z=10$ cm above the bed is about 2 cm/s in the low energy case, 3 cm/s in the medium energy case, and 4 cm/s in the high energy case. The maximum magnitude of W_w' at the surface (i.e. $z=H$) is about 80% in the low energy case, 75% in the medium energy case, and 65% in the high energy case smaller than the maximum magnitude of horizontal velocity U_w'.

The vertical $\overline{M_w' W_w'}$ profiles averaged over the complete run for the three wave energy cases were shown in Figure 8.32. The results to be presented are those averaged over shorter time segments, from which the common feature of vertical $\overline{M_w' W_w'}$ profiles, that is a decrease with height first, a negative extremum, and then a increase with height, can also be seen, except that there is more fine structure appearing in the mean vertical profiles. It should be noted that data presented in Figures C.5-C.7 are those averaged over 3 range bins in vertical, same as those in Figure 8.32.

Vertical $\overline{M_w' W_w'}$ profiles averaged over two selected windows in the low energy case (Table 8.2, see also Figure 8.11) are shown in Figure C.5a, from which it can be seen that the variation of $\overline{M_w' W_w'}$ in Window A is small, and can be mainly considered as uniform with height. The value of $\overline{M_w' W_w'}$ in Window B, on the other hand, decreases continuously up to about 16 cm height, around which $\overline{M_w' W_w'}$ reaches a negative extremum, and it finally decreases in magnitude for heights greater than 16 cm from the bed. It can be noticed that the shape of $\overline{M_w' W_w'}$ in Window B is very similar to that in the medium energy case shown in Figure 8.32, except the position of the minimum value of $\overline{M_w' W_w'}$ in Window B (Figure C.5a) is slightly higher.

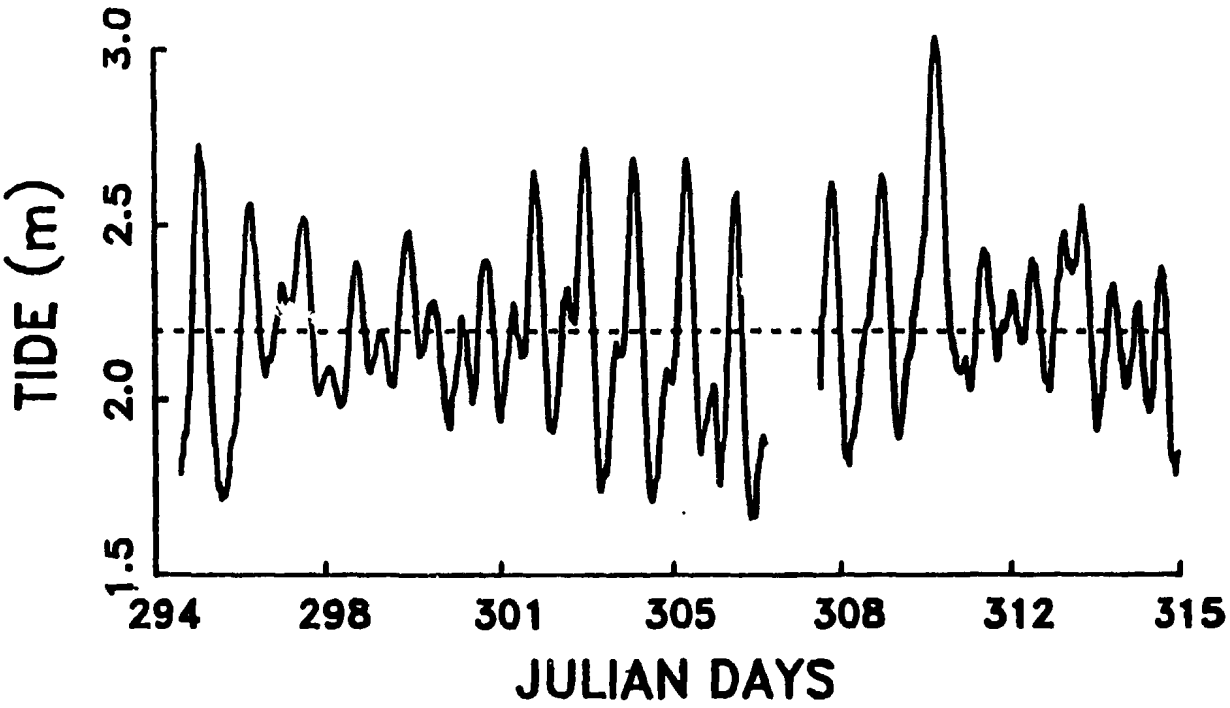

Figure C.1. Time series of water depth at the RASTRAN site.

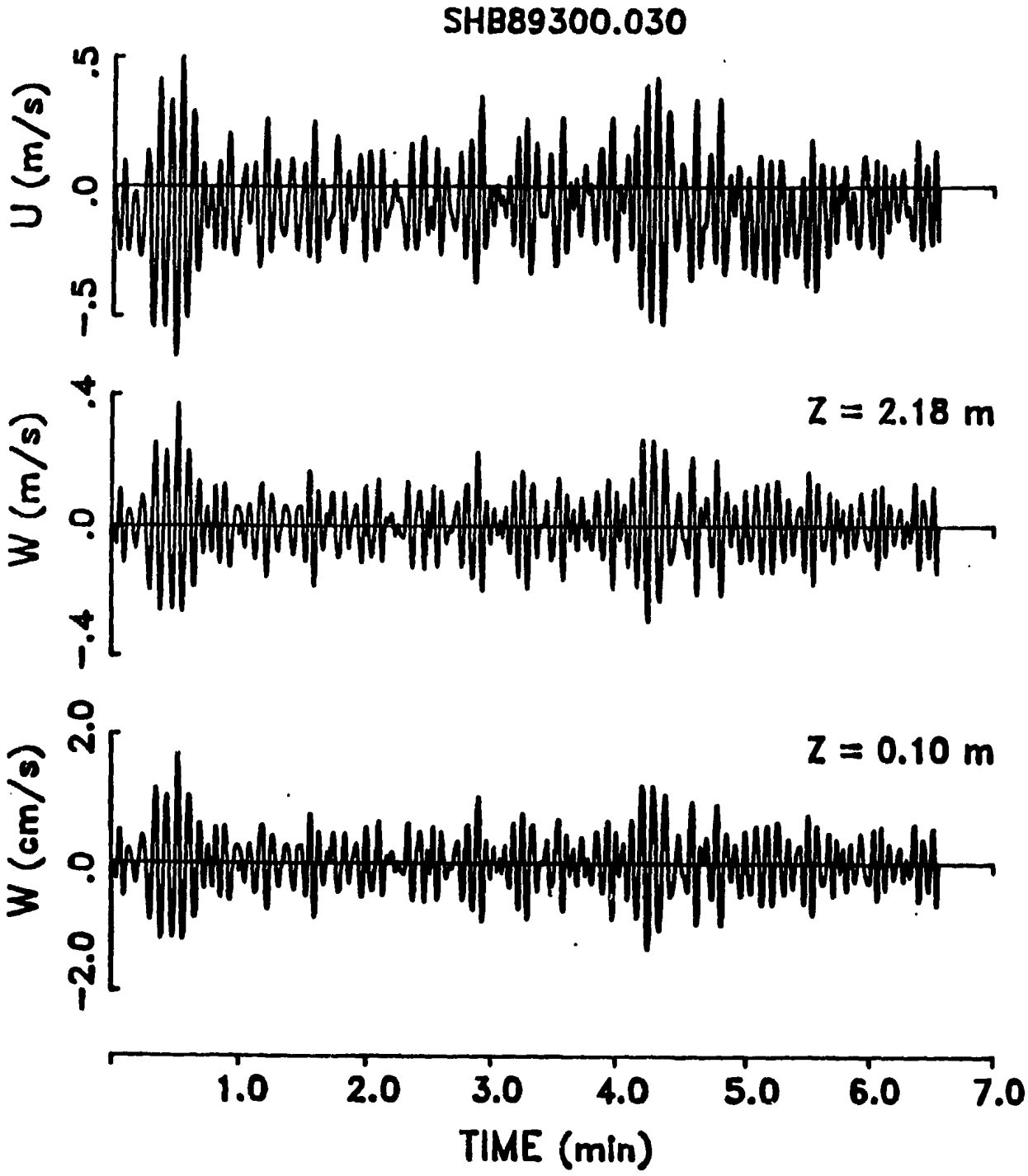

Figure C.2. Time series of horizontal velocity U_w', and vertical velocity W_w' at $z=0.1$ m and $z=H=2.10$ m in the low energy case.

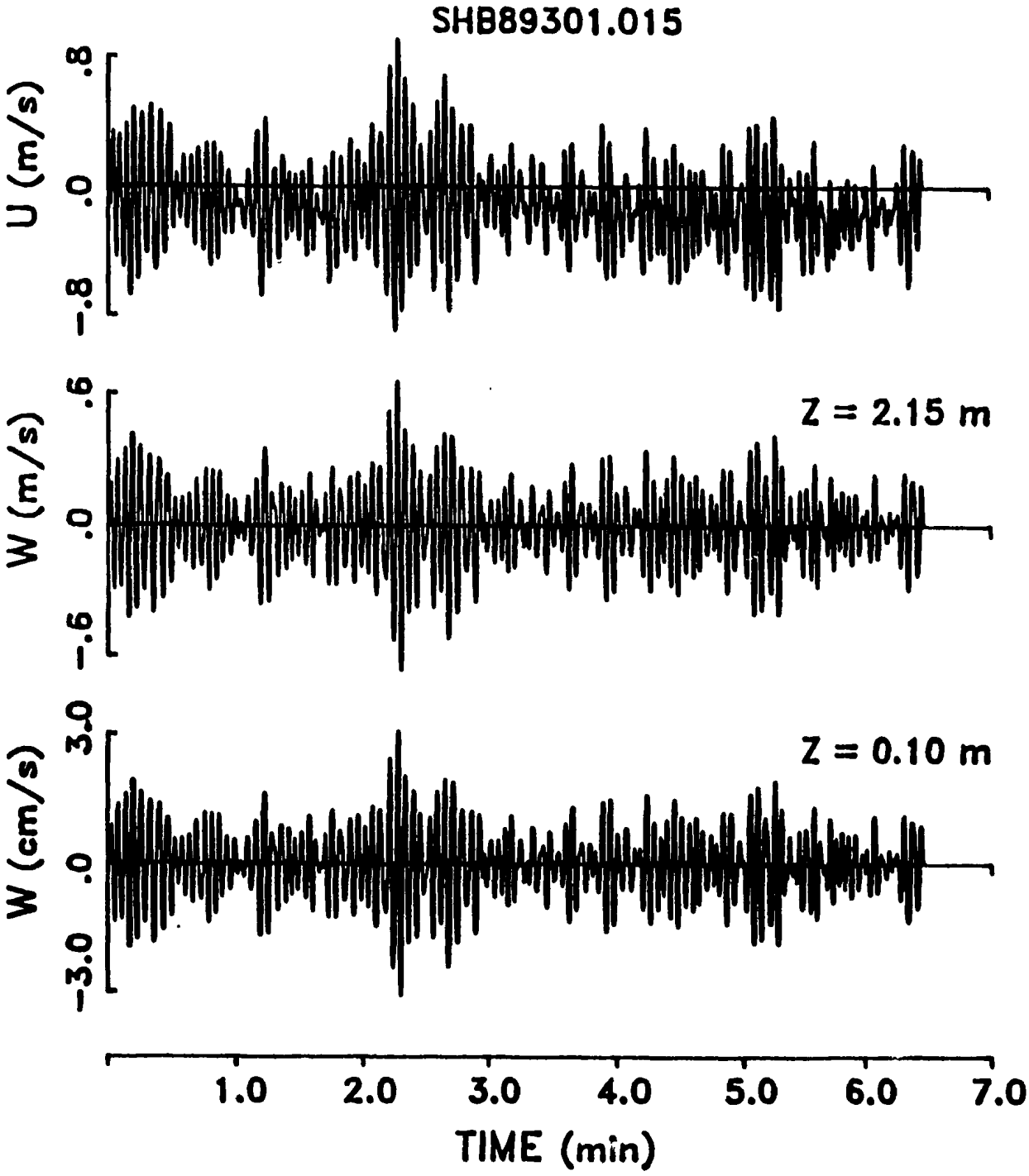

Figure C.3. Time series of horizontal velocity U_w', and vertical velocity W_w' at $z=0.1$ m and $z=H=2.15$ m in the medium energy case.

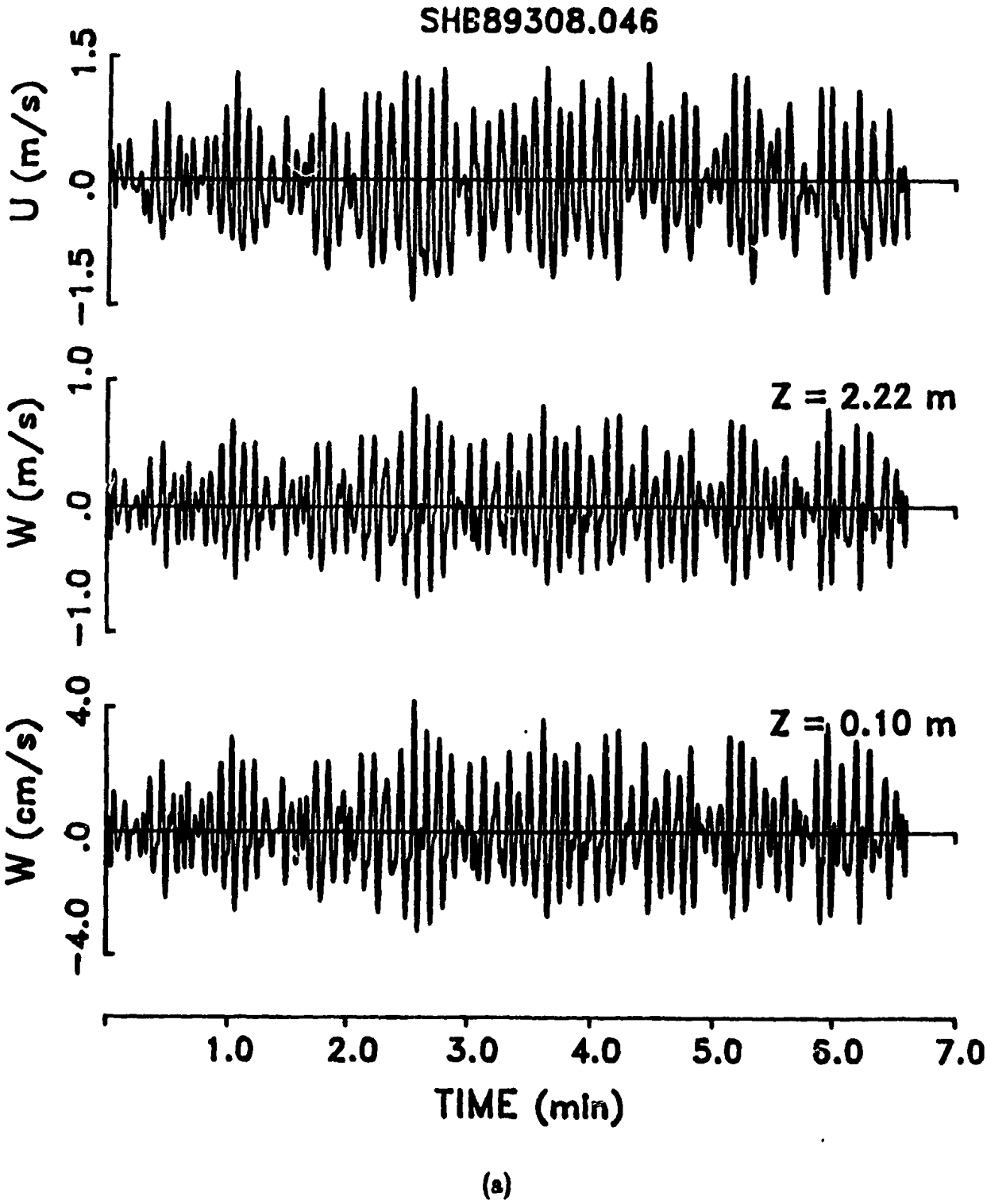

Figure C.4. Time series of horizontal velocity U'_w, and vertical velocity W'_w at $z=0.1$ m and $z=H=2.22$ m in the high energy case for two consecutive runs: (a) SHB89308.046; (b) SHB89308.047.

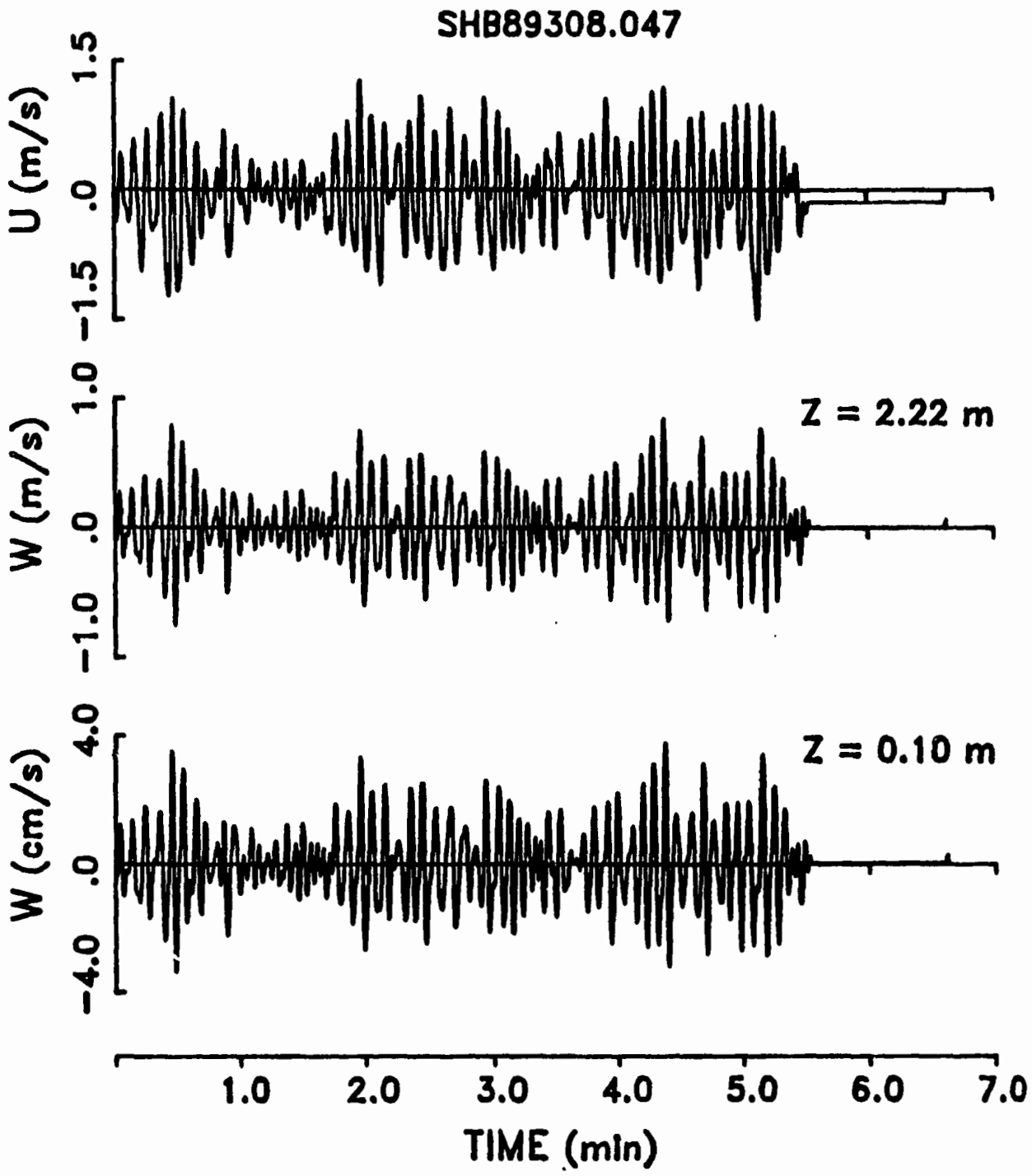

(b)

Figure C.4 (continued)

Vertical $\overline{M_w' W_w'}$ profiles averaged over two noteworthy events in the low energy case (Table 8.2, see also Figure 8.11) are shown in Figure C.5b. It can be seen, from Figure C.5b, that for heights below 10 cm from the bed $\overline{M_w' W_w'}$ in both events decreases with height. The rate of decrease in Event 2 is much higher than that in Event 1, and the value of $\overline{M_w' W_w'}$ in Event 2 at a height of 4 cm is much larger (about 12 times larger) than that in Event 1 at the same height. This large positive value of $\overline{M_w' W_w'}$ at a height of 4 cm in Event 2 is attributed to strong correlations between sediment suspensions at this height and surface waves. By examining the color images shown in Figure 8.11b, we can see that the maxima of particle concentration in Event 2 at the range bins closer to the bed are strongly correlated with the nearly maximum first derivative of seaward velocity U_w', so that W_w' and M_w' are in phase, $\overline{M_w' W_w'}>0$.

Vertical $\overline{M_w' W_w'}$ profiles averaged over three selected windows in the medium energy case (Table 8.2, see also Figure 8.12) are shown in Figure C.6a, from which, it can be found that $\overline{M_w' W_w'}$ in all three windows decreases with height in the near bed region, reaches a minimum at a height of about 13 cm in Window A, 11 cm in Window B, and 9 cm in Window C, and then increases with height. It is interesting to note that $\overline{M_w' W_w'}$ in Window B has two minima on its vertical profile, one at about 9 cm, and one around 22 cm from the bed, analogous to the shapes of vertical $\overline{M_w' W_w'}$ profiles in the high energy case shown in Figure 8.32. By considering that $U_{1/3}$ in Window B is about 40% larger than $U_{1/3}$ in Window A or $U_{1/3}$ in Window C, the profiles in Figure C.6a may further demonstrate the dependence of vertical $\overline{M_w' W_w'}$ structure on the wave energy, i.e., there are more than one extremum on the profile for higher wave energy.

Vertical $\overline{M_w' W_w'}$ profiles averaged over three events in the medium energy case (Table 8.2, see also Figure 8.12) are shown in Figure C.6b. It can be noticed that the shape of vertical $\overline{M_w' W_w'}$ profile in each event is very similar to that in the window from which the data for the event are extracted. The very large positive values of $\overline{M_w' W_w'}$ at heights of around 25 cm in Event 2 are mainly attributed to strong correlations between particle concentrations and the upward vertical velocity W_w' at these heights. From the color images shown in Figure 8.12b, it can be observed that most sediment suspension around 25 cm in height occurred when the first derivative of cross-shore velocities are almost maxima, so that large positive values of $\overline{M_w' W_w'}$ at these heights should be obtained.

For the case of high energy, the vertical profiles averaged over two windows (see Table 8.2, also see Figures 8.13a and b) in the first run (SHB89308.046) are shown in Figure C.7a, from which the feature of the vertical $\overline{M_w' W_w'}$ profile suggested previously is seens: $\overline{M_w' W_w'}$ in both windows decreases with height in the near bed region, and there are two minima on each profile above near-bed region. There exist significant differences, however, in the positions of the minima between the two windows. It can be seen, from Figure C.7a, that the first minimum is located at about 9 cm in Window A, about 14 cm in Window B, while the second minimum is located at about 21 cm in Window A, and about 27 cm in Window B. It can be also noted that the second minimum is dominant in Window A, while the minimum of $\overline{M_w' W_w'}$ near the bed is dominant in Window B. The vertical profiles of $\overline{M_w' W_w'}$ averaged over two windows (Table 8.2, see also Figures 8.13c and d) in the second run (SHB89308.047) are plotted in Figure C.7b. The shape of the vertical $\overline{M_w' W_w'}$ profile is similar to as those in Figure

C.7a. $\overline{M_w' W_w'}$ in the both windows decreases with height up to about 11 cm height. There are also two minima in each $\overline{M_w' W_w'}$ profile, as in Figure C.7a. The magnitude of the second minimum of $\overline{M_w' W_w'}$ in Window B (around 22 cm in height), however, is quite large, more than 10 times larger than that in the other three windows in Figure C.7. This very large negative value of $\overline{M_w' W_w'}$ around 22 cm in height is attributed to very strong correlations between particle concentrations at these heights and surface waves. By examining acoustic images shown in Figure 8.13d, it can be seen that maxima of particle concentration at mid-height in Window B of SHB89308.047 predominantly occurred during the periods when the cross-shore velocities had a minimum first derivative, which means W_w' and M_w' were mainly out of phase at these heights.

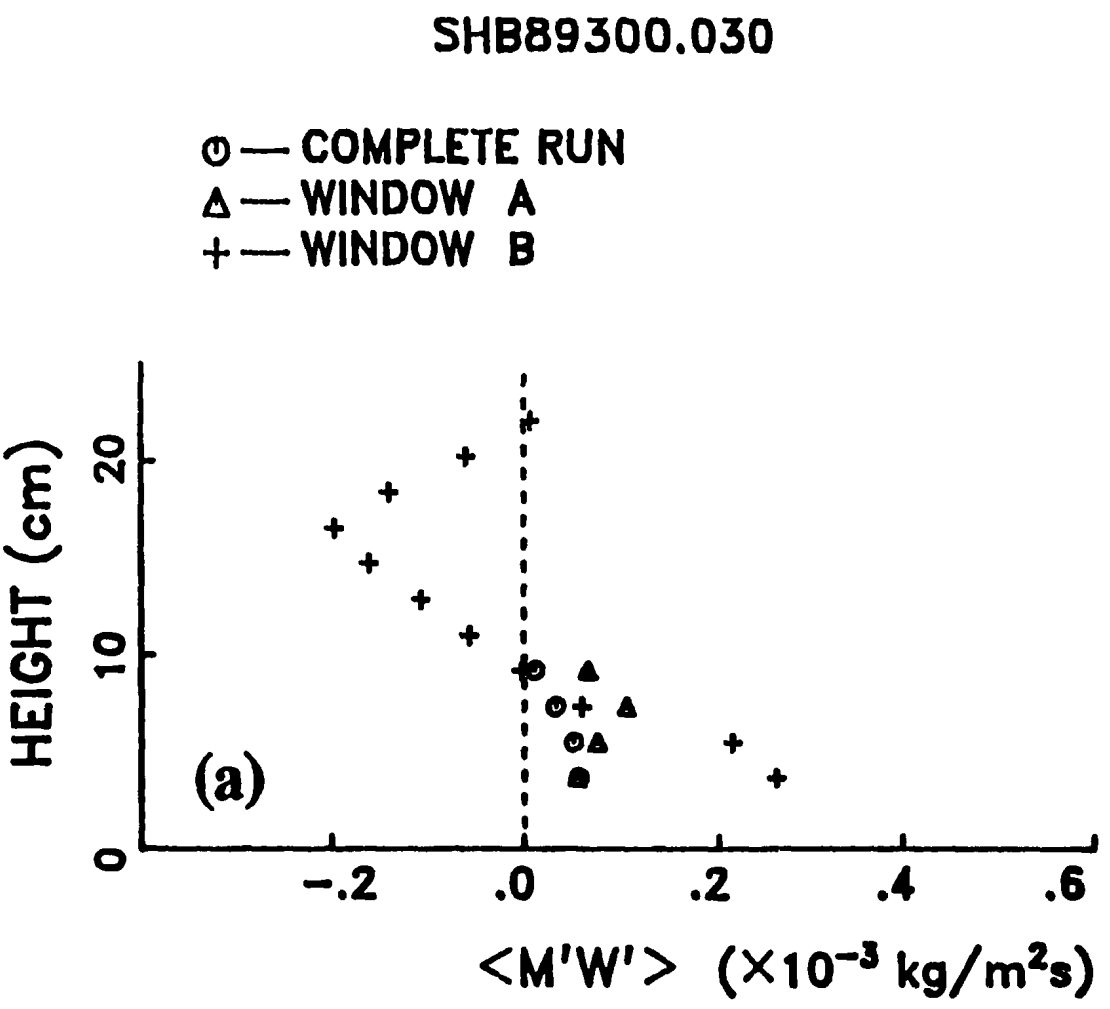

Figure C.5. Time-averaged vertical profiles of wave flux $\overline{M_w' W_w'}$ in the low energy case over: (a) two entire windows and the complete run; (b) two single events.

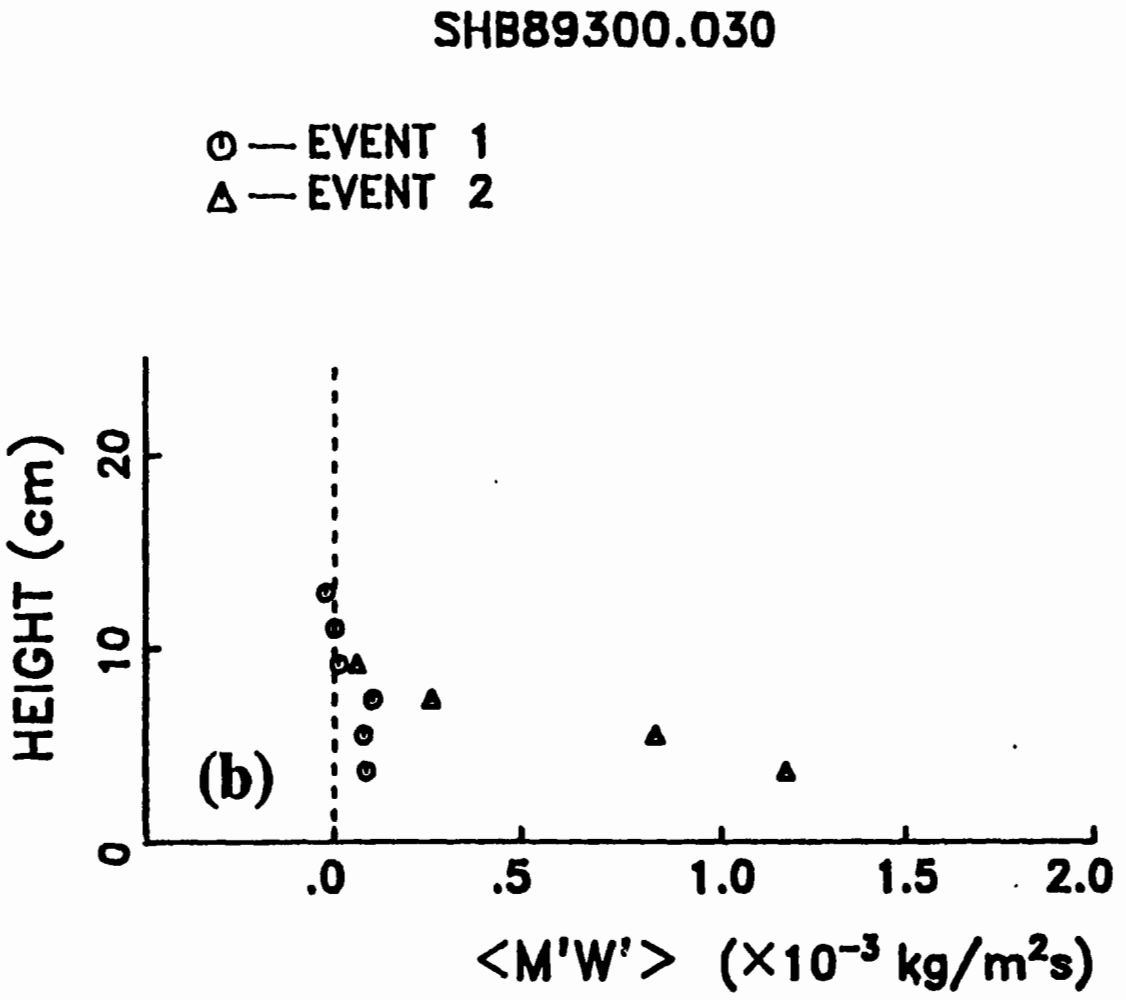

Figure C.5. (continued)

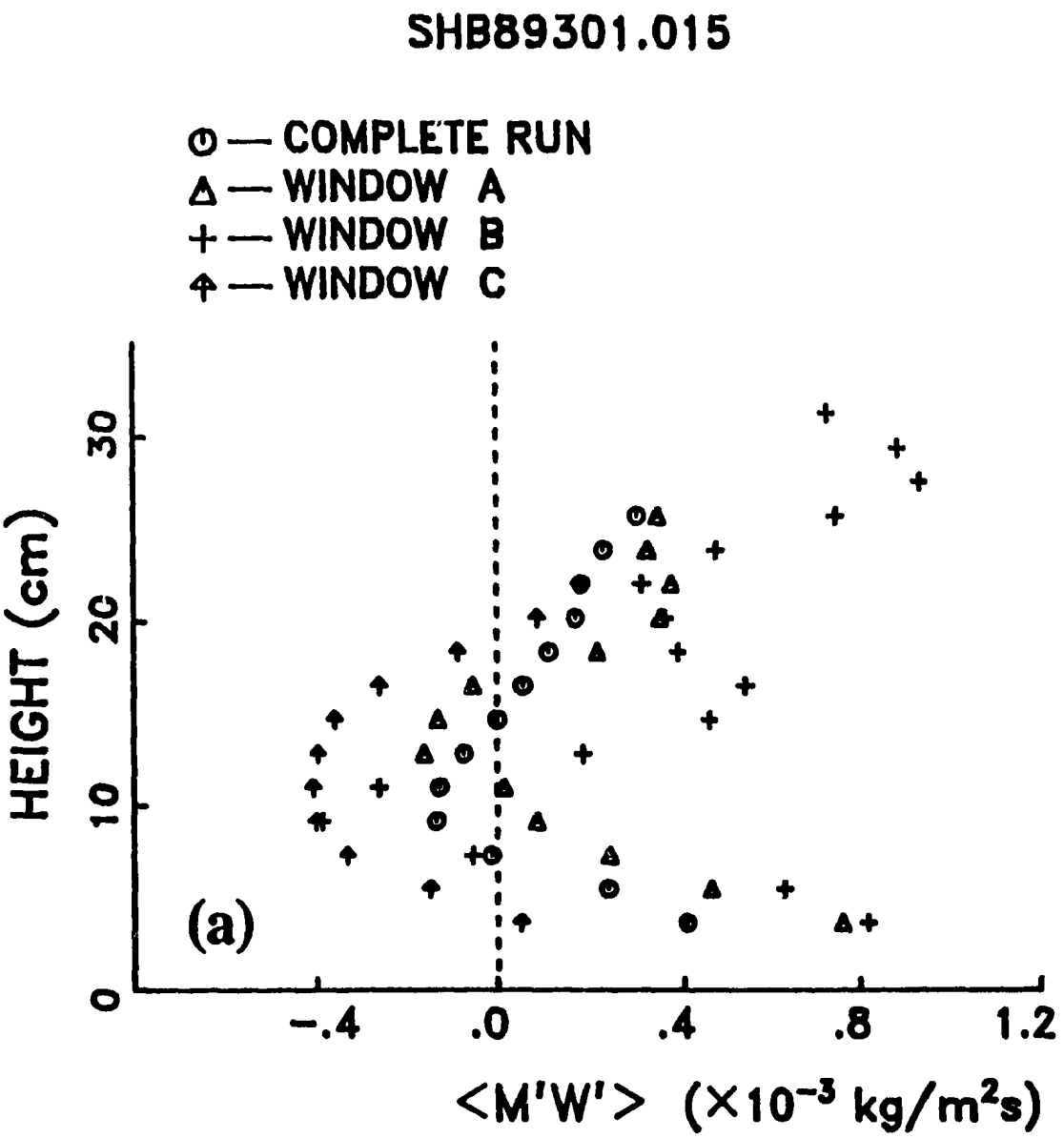

Figure C.6. Time-averaged vertical profiles of wave flux $\overline{M_w' W_w'}$ in the medium energy case over: (a) two entire windows and the complete run; (b) single events.

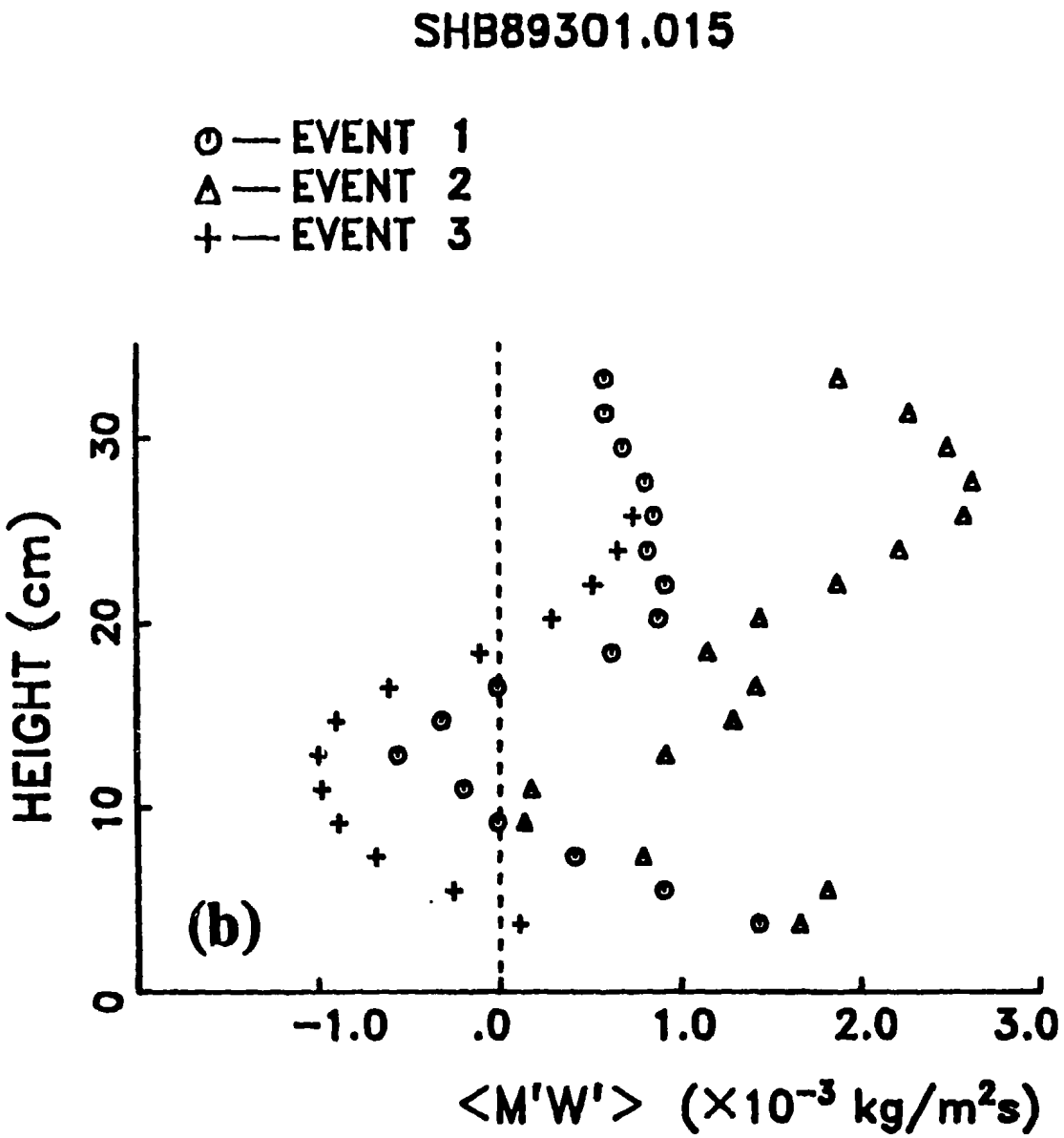

Figure C.6. (continued)

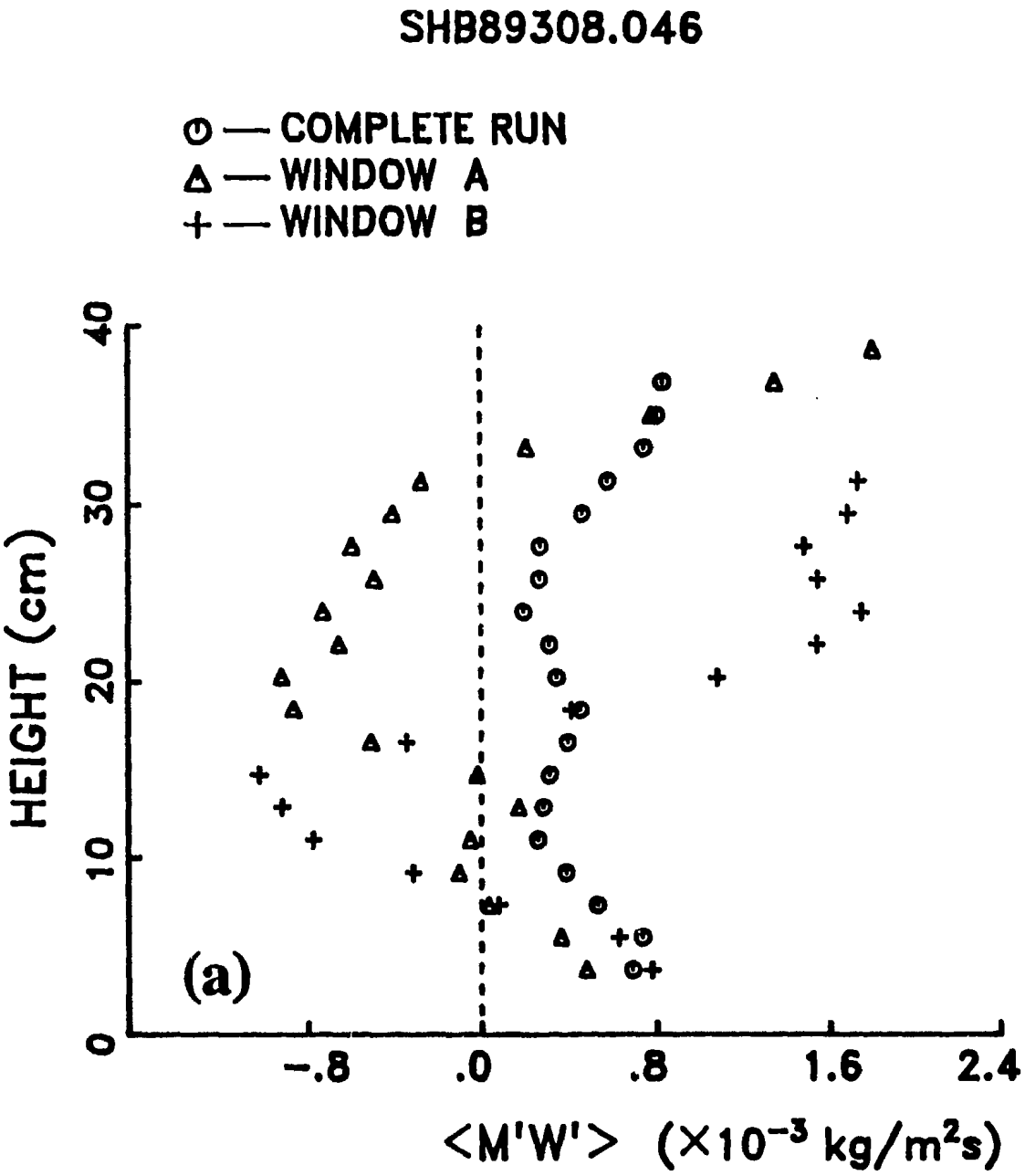

Figure C.7. Time-averaged vertical profiles of wave flux $\overline{M_w' W_w'}$ in the high energy case over two entire windows and the complete run for: (a) SHB89308.046; (b) SHB89308.047.

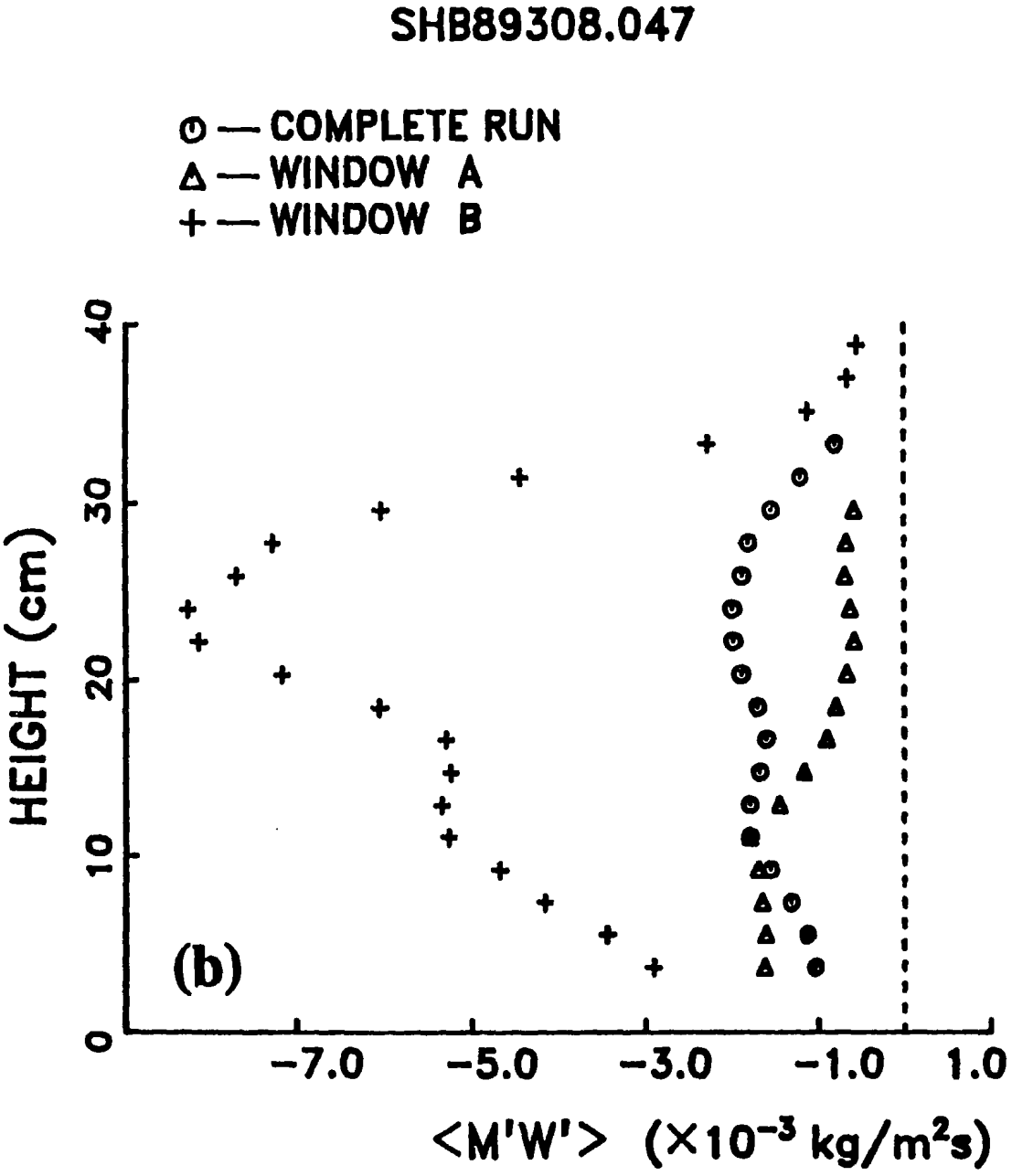

Figure C.7.(continued)

The time-mean profiles of wave flux $\overline{M_w' W_w'}$ shown in Figures C.5-C.7 are those averaged over 3 range bins. The purpose of applying running average for vertical $\overline{M_w' W_w'}$ profiles is to remove small-scale variations on the data. By doing so, however, some interesting features on the vertical $\overline{M_w' W_w'}$ profile could be unnecessarily smeared out. In this Appendix, time-mean profiles of $\overline{M_w' W_w'}$ without any bin average are presented. Figure C.8 shows time-mean profiles of $\overline{M_w' W_w'}$ over the complete run without any bin average in the three cases of wave energy. Compared with profiles in Figure 8.32, it can be seen that the small-scale variations on the vertical $\overline{M_w' W_w'}$ profile in Figure C.5 are obvious. Moreover, it is also interesting to note, from Figure C.8, that there is a peak in the value of $\overline{M_w' W_w'}$ at a height of about 5 cm on all profiles except the one for the run of SHB89308.047. This special feature on the vertical $\overline{M_w' W_w'}$ profile in the neighborhood of 5 cm in height can be also found from vertical $\overline{M_w' W_w'}$ profiles averaged over shorter time segments.

Figure C.9 shows vertical profiles of $\overline{M_w' W_w'}$ averaged over two entire windows and those averaged over two single events in the low energy case (Table 8.2, see also Figure 8.11). As in Figure C.8, profiles in Figure C.9 are those without any bin average. It can be seen, from Figure C.9, that there is a peak in the value of $\overline{M_w' W_w'}$ at about 4 cm above the bed on each vertical $\overline{M_w' W_w'}$ profile in Figure C.9, although variations of $\overline{M_w' W_w'}$ in Window A and $\overline{M_w' W_w'}$ in Event 1 are not significant.

Vertical $\overline{M_w' W_w'}$ profiles averaged over three selected windows and those averaged over three selected events in the medium energy case (Table 8.2, see also Figure 8.12) are shown in Figure C.10, from which it can be seen that there

is also a peak in the value of $\overline{M_w' W_w'}$ at a height of about 4 cm from the bed on the profile averaged over Window B and the profile averaged over Event 2. there are no obvious peaks, however, at heights near the bed on other profiles shown in Figure C.10.

Figure C.11a shows the time-mean $\overline{M_w' W_w'}$ profiles averaged over two selected windows in the high energy run SHB89308.046 (Table 8.2, see also Figure 8.13a and b). It can be noticed that there is a peak at about 4 cm in height on the profiles over two windows. The small-scale variations superposed in the profiles in Figure C.11a are significant. There are no peaks, however, near the bed on profiles averaged over two windows in the run of SHB89308.047 shown in Figure C.11b. The small-scale variations in Figure C.8b are also noticeable, same as in Figure C.11a.

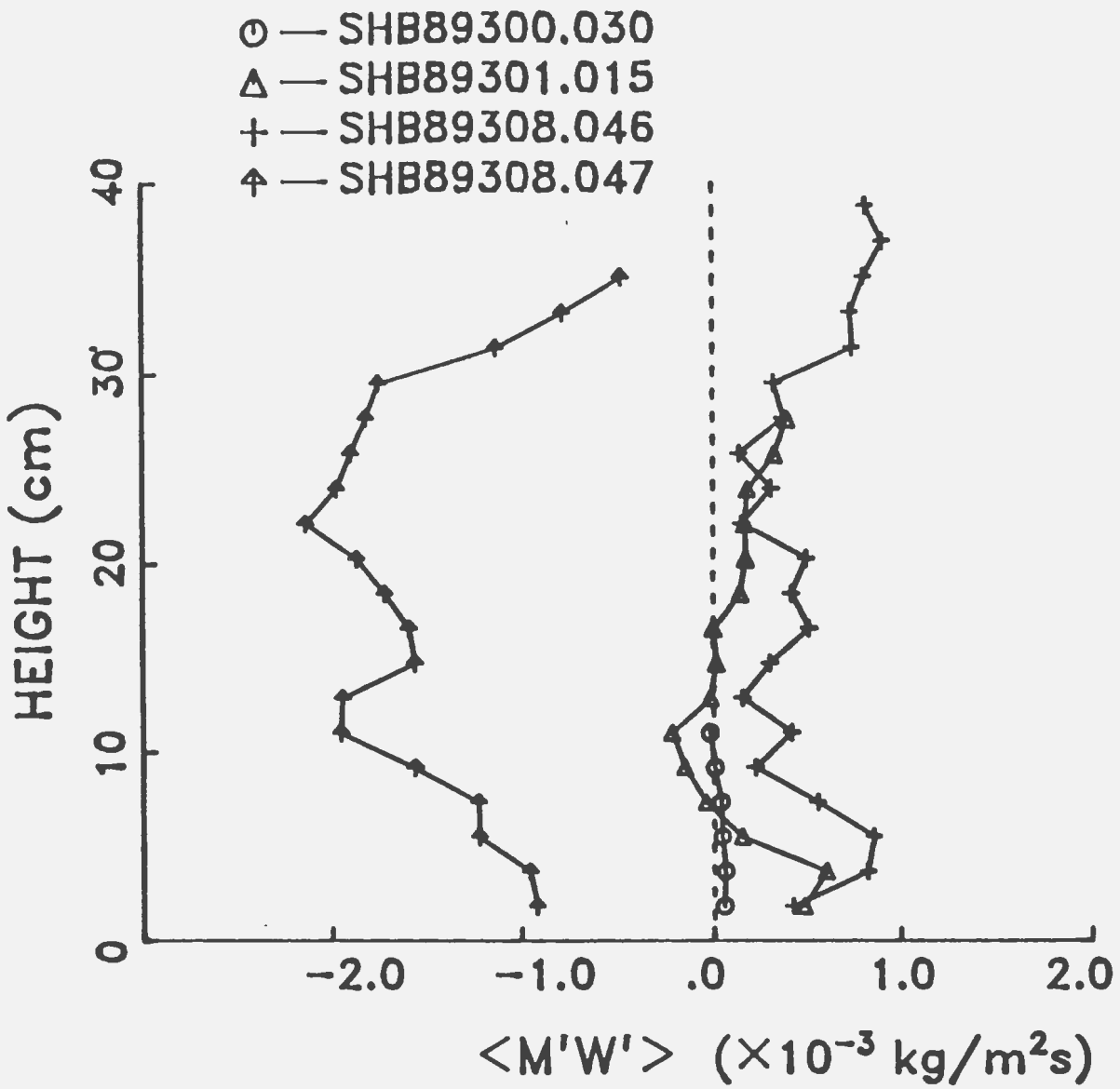

Figure C.8. Time-averaged vertical profiles of wave flux $\overline{M'_w W'_w}$ over the complete run without any bin average in three wave cases.

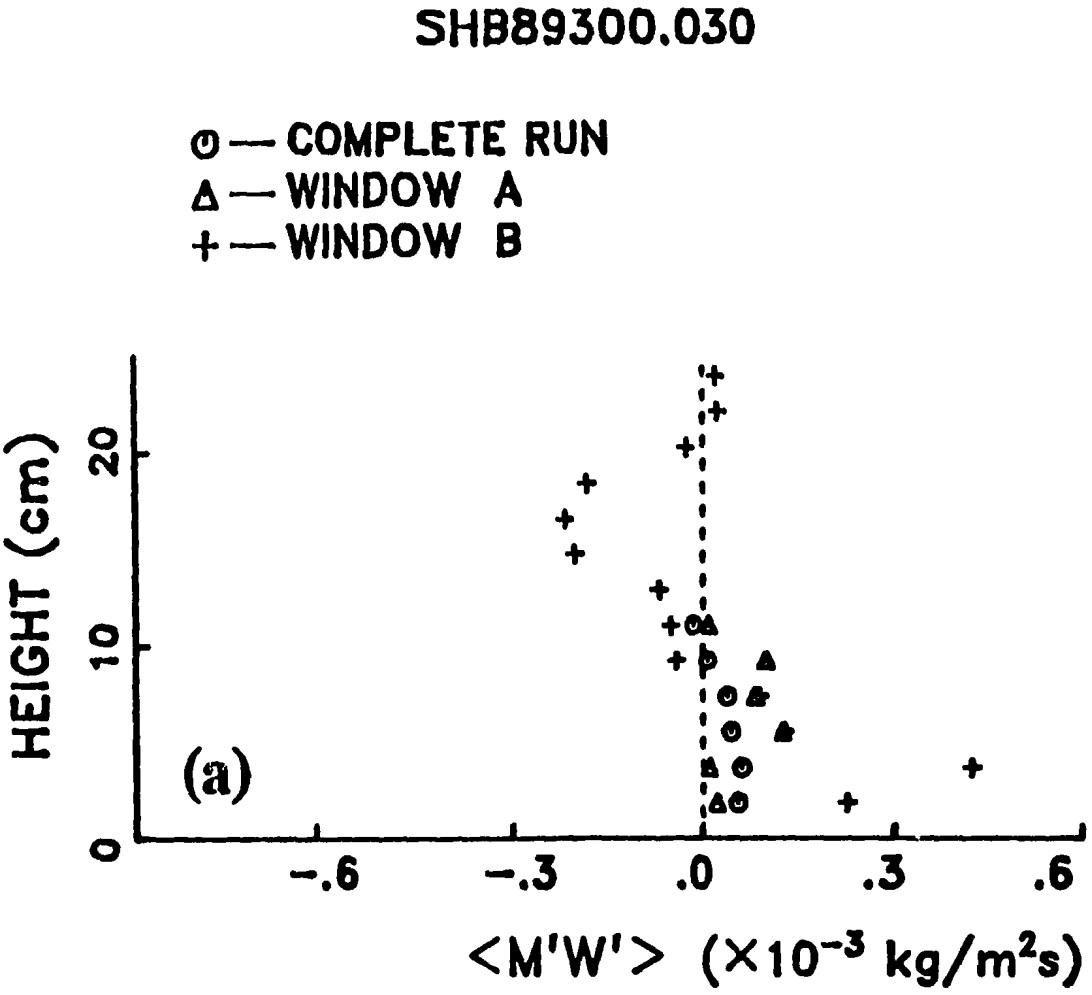

Figure C.9. Time-averaged vertical profiles of wave flux $\overline{M_w' W_w'}$ over: (a) two entire windows and the complete run; (b) two single events without any bin average in the low energy case.

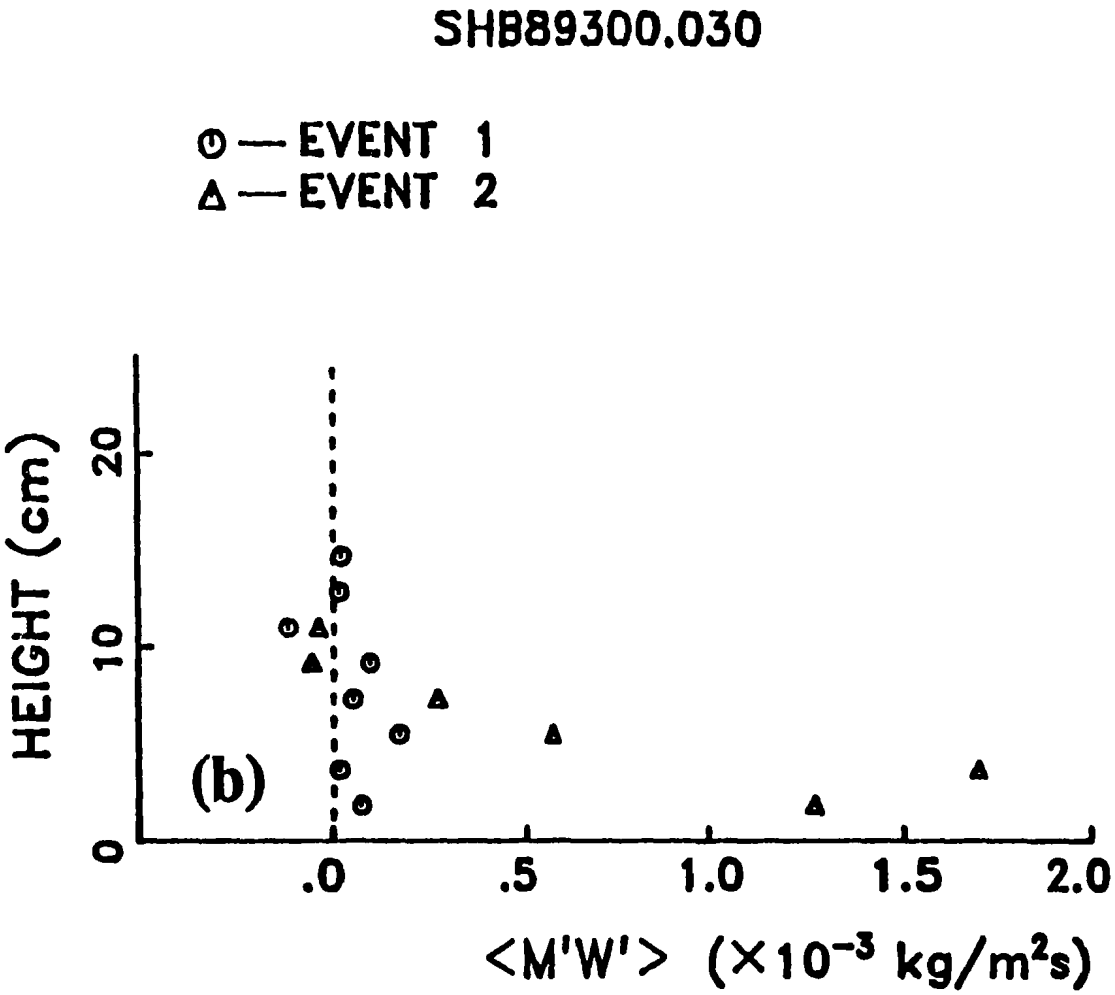

Figure C.9. (continued)

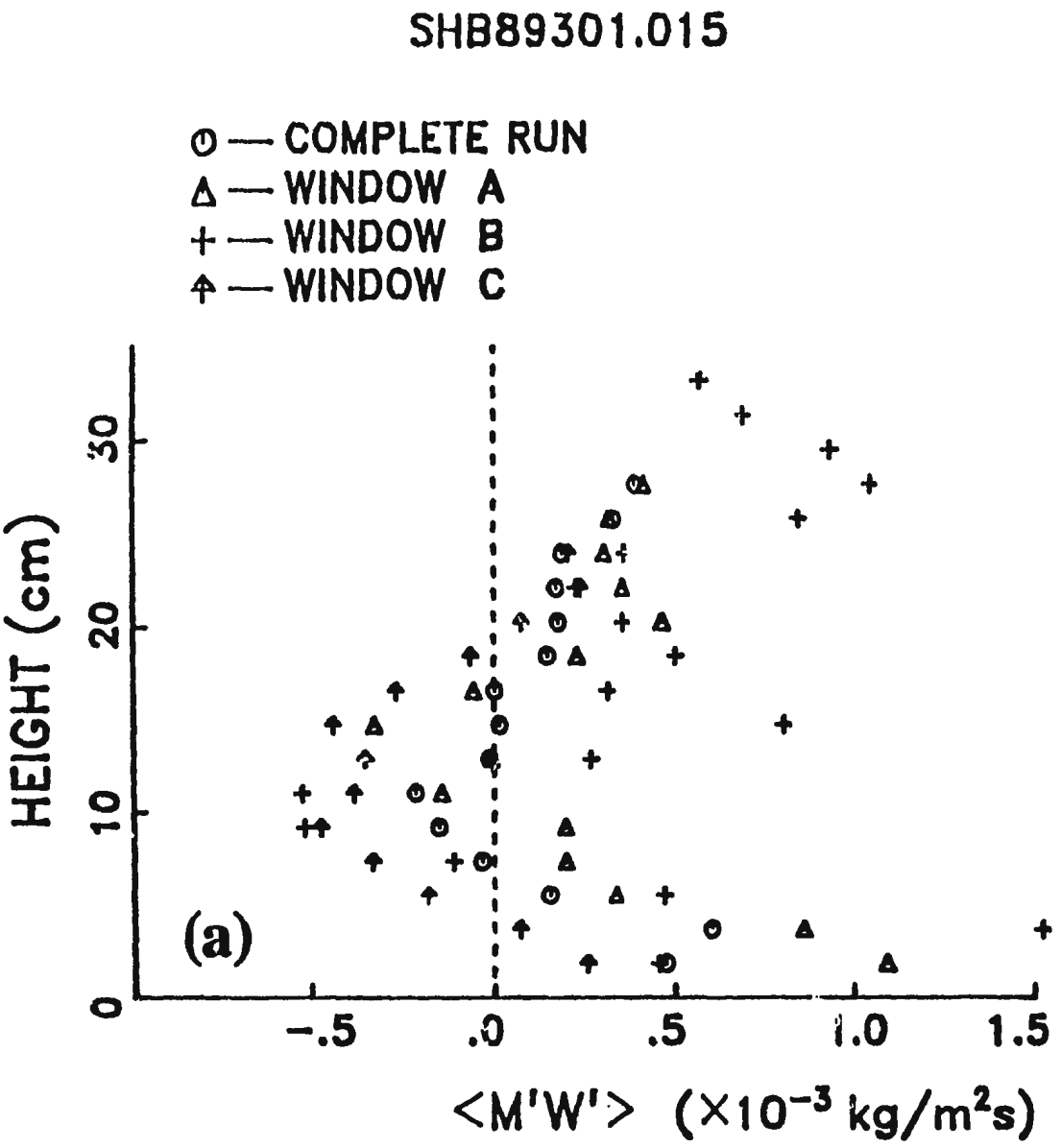

Figure C.10. Time-averaged vertical profiles of wave flux $\overline{M'_w W'_w}$ over: (a) three entire windows and the complete run; (b) three single events without any bin average in the medium energy case.

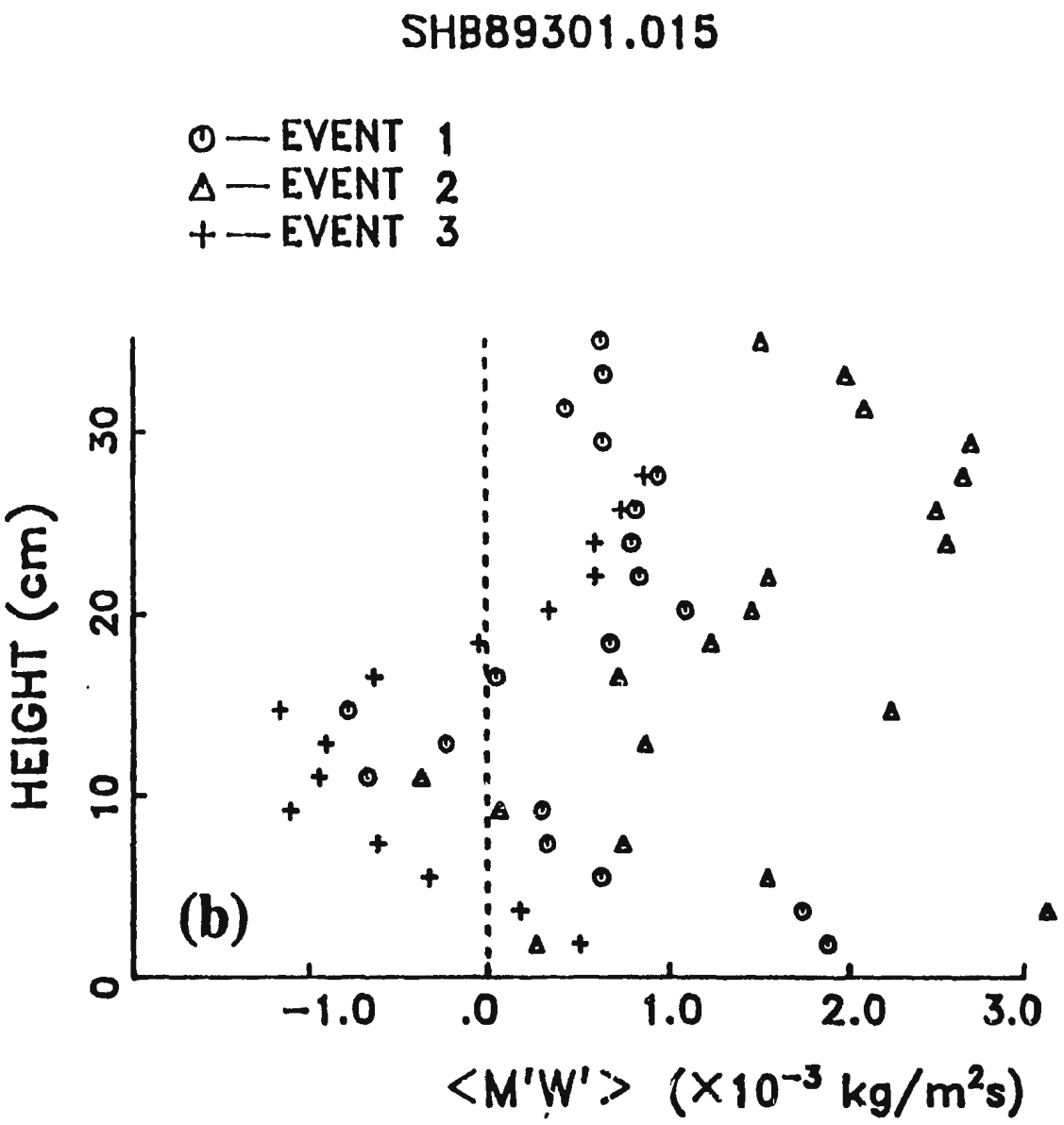

Figure C.10. (continued)

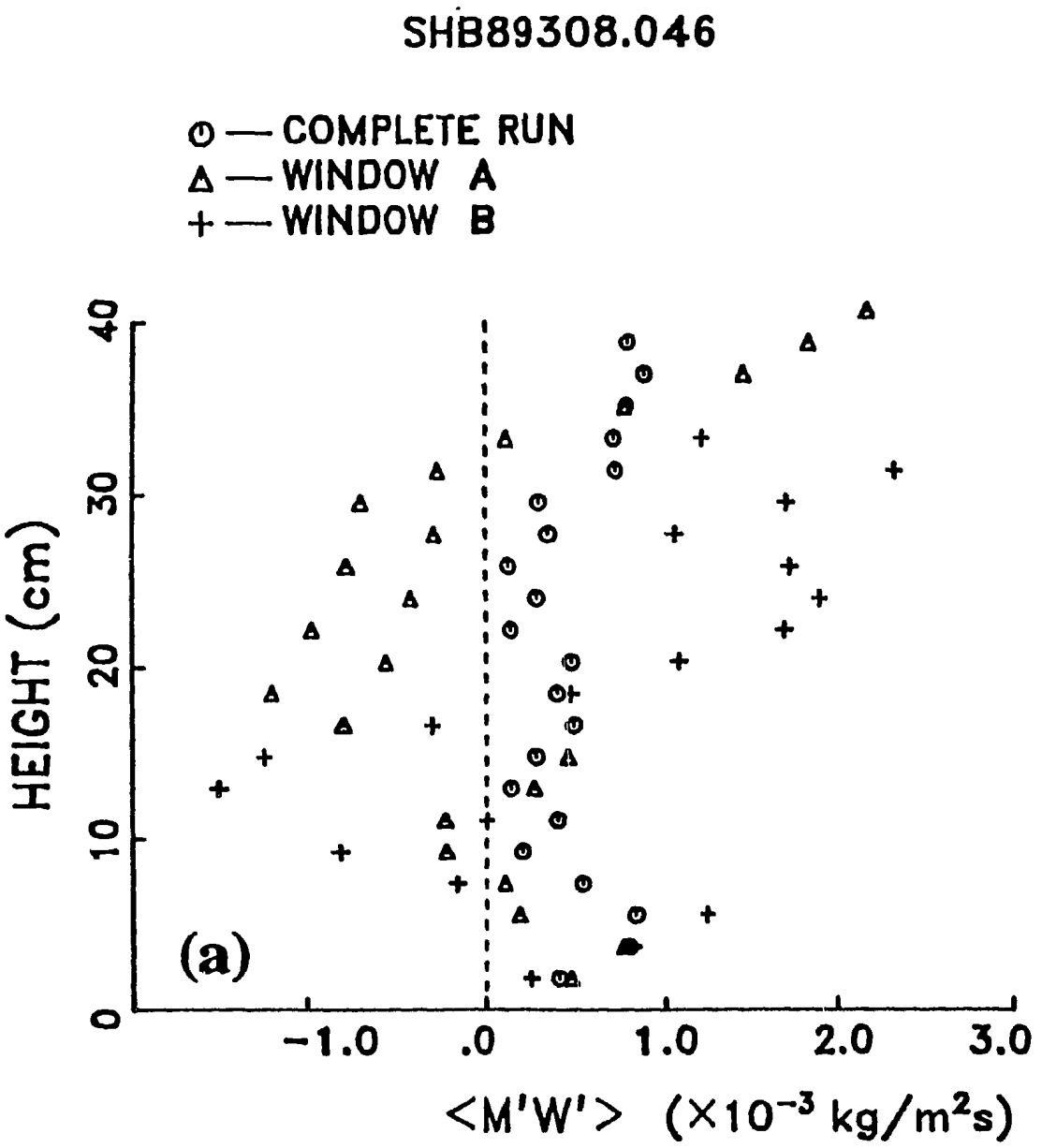

Figure C.11. Time-averaged vertical profiles of wave flux $\overline{M_w' W_w'}$ over two entire windows and the complete run without any bin average in the high energy case for: (a) SHB89308.046; (b) SHB89308.047.

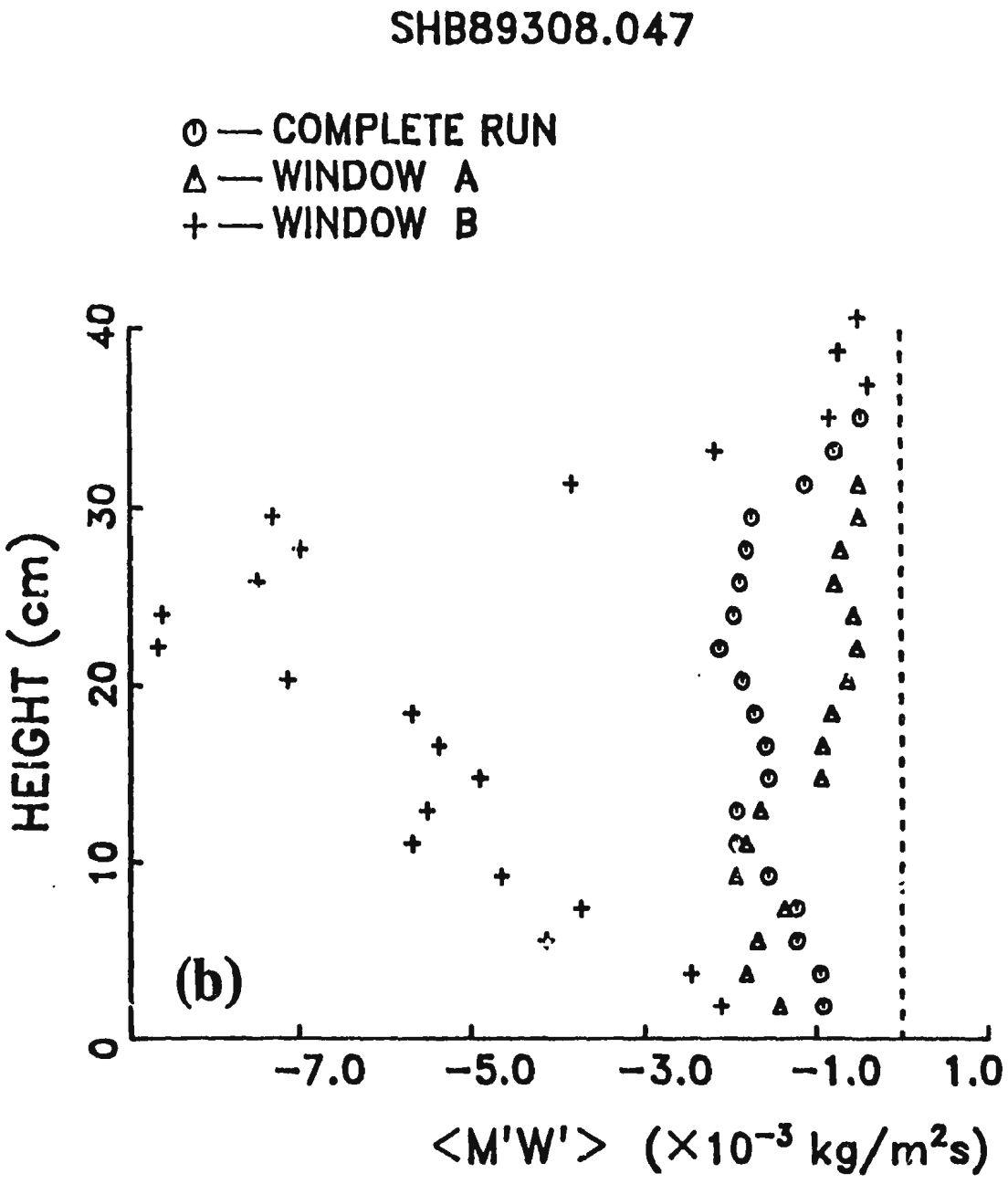

Figure C.11. (continued)